An Investigation Into the Tribology and Corrosion Barrier Performance of Thin Multilayer PVD Films

Jaimie Daure, BEng

School of Engineering

The University of Nottingham

June 2015

Thesis submitted to the University of Nottingham for the degree of Doctor of Philosophy

Abstract

As surface engineering develops, the methods of applying coatings and the materials used have improved significantly. One method of coating deposition that is becoming increasingly popular is physical vapour deposition (PVD). This research investigates PVD coatings of single layered systems, dual layered systems and multilayered systems with varying layer thicknesses. The properties of the coatings are investigated along with the dependence of those properties on the coating materials, the coating architecture, the hardness and surface finish of the substrates used as well as the deposition conditions. Tests were carried out on the coatings to investigate their tribological and corrosion resistant properties compared against industry standard benchmark coatings of electrodeposited chromium and nickel respectively. The base materials chosen were as follows: CrN (hard wearing) and Graphit-iC (low friction) for the durable and low friction coatings; corrosion resistant IN625 and chromium for the scratch and corrosion resistant coatings.

The results showed that multilayering can be an effective tool for increasing the hardness and scratch resistance of a coating system; however, no benefit was seen in terms of the wear and corrosion resistance of the selected coating systems through multilayering. In terms of corrosion behaviour of the coated systems, the coatings themselves were corrosion resistant, and therefore the system behaviour depends upon the barrier properties of the PVD films. PVD coatings contain growth defects which provide a route for exposure of the substrate to the corrosive media. Irrespective of the film architecture, the substrate surface finish was seen to play a significant role in determining defect density, resulting in a lower defect density for coatings deposited on substrates with a finer surface finish, which resulted in an improvement in the corrosion barrier properties of the resulting films.

Acknowledgments

The author would like to thank his supervisors, Dr K. Voisey and Prof P. Shipway for their help and continuous encouragement throughout this research.

He is also grateful to Joanne Hampshire, Joanne Stallard and Teer Coatings Ltd. for providing the coatings investigated in this research as well as carrying out hardness and scratch testing.

The author wishes to thank Dr D. Stewart and Rolls-Royce plc for financial support and the opportunity to carry out this research.

He would also like to thank Dr M. Fay for carrying out the TEM work and his technical advice.

The author would like to thank Dr N. Neate for the stress analysis using XRD and his support and advice over the years.

He would like to thank Keith Dinsdale, Tom Buss & Jason Grieves for their hard work maintaining equipment and their technical and practical advice throughout this research period.

Finally, he would like to thank his parents for their support and encouragement over the years.

Contents

Abstract i
Acknowledgments ii
List of tables and figures vii
1 Introduction 1
1.1 Aims & Objectives 5
2 Literature Review 7
2.1 Review of Physical Vapour Deposition (PVD) 7
2.1.1.1 PVD Processes 10
2.2 Review of the Microstructure of PVD Coatings and Properties 15
2.2.1 Introduction to the corrosion behaviour of PVD coatings 15
2.2.2 Growth defects and their effect on coating properties 16
2.2.3 Effect of deposition parameters on coating properties 21
2.2.4 Multilayers 23
2.2.5 Intermediate etching 27
2.2.6 Substrate surface roughness and the effect on coating properties 29
2.3 Review of Friction, Wear and Contact Mechanisms 33
2.3.1 Friction and contact mechanisms 34
2.3.2 Wear mechanisms 35
Abrasive wear 35
Fatigue wear 36
Sliding wear 36
2.3.3 Sliding wear behaviour of PVD coatings 38
2.4 Review of Coating Materials and Diamond-Like Carbon (DLC) 39
2.4.1 CrN 40
2.4.2 IN625 41
2.4.3 Introduction to carbon and diamond-Like Carbon 42
Properties of graphite and diamond 43
Diamond-like carbon 43
The effect of hydrogen on DLC properties 44
2.4.4 Graphit-iC™ and Dymon-iC™ (Teer Coatings Ltd) 47
2.4.5 DLC properties & surface roughness 49
2.4.6 Summary 51
3 Experimental Procedure 53
3.1 Introduction 53
3.2 Coating deposition 54

3.3 Substrate preparation 55
3.3.1 Optical emission spectroscopy 56
3.3.2 Coating methods and parameters 57
3.4 Sample preparation for characterisation 59
3.5 Characterisation of Materials 59
3.5.1 Scanning electron microscopy (SEM) 59
3.5.2 Energy Dispersive X-ray Spectroscopy (EDX) 60
3.5.3 X-ray Diffraction (XRD) 60
3.5.4 Transmission electron microscopy (TEM) 62
3.6 Tribological Behaviour 64
3.6.1 Wear testing 64
3.6.2 Scratch testing 68
3.6.3 Hardness testing 69
3.6.4 Corrosion testing 70
3.6.4.1 Salt spray testing 70
3.6.4.2 Potentiodynamic testing 71
3.7 Analysis of Tested Samples 73
3.7.1 Profilometry 73
3.7.2 Wear scar measurements 74
3.7.3 Ball wear scar measurements 75
3.7.4 Image analysis 76
4 Results 77
4.1 Introduction 77
4.2 Mechanical and Tribological Properties of Single and Multilayered PVD Coatings 78
4.2.1 Coating microstructure 78
..... 80
4.2.2 Effect of multilayering on the mechanical and tribological properties of coatings 81
4.2.2.1 Effect of multilayering on the mechanical properties of coatings 81
4.2.2.2 Effect of multilayering and substrate hardness on the tribological properties of coatings 85
4.2.3 Effect of multilayer architecture on the mechanical and tribological properties of coatings 97
4.2.3.1 Effect of multilayer architecture and substrate hardness on the mechanical properties of coatings 97
4.2.3.2 Effect of multilayer architecture on the tribological properties of coatings 100

4.2.4 Effect of ball type on the tribological properties of coatings 109
4.2.5 Summary 120
4.3 Mechanical and Corrosion Resistant Properties of Single and Multilayered PVD Coatings 121
4.3.1 Coating microstructure 121
4.3.2 Effect of multilayering on the mechanical properties of coatings 124
4.3.3 Effect of coating architecture on the corrosion barrier performance of coatings 128
4.3.4 Effect of growth defects on the structure of coatings 133
4.3.5 Effect of substrate surface roughness and deposition conditions on the structure of coatings 137
4.3.5.1 Effect of substrate surface finish and deposition conditions on the microstructure of coatings 140
4.3.5.2 Effect of substrate surface finish and deposition conditions on the mechanical properties of coatings 148
4.3.5.3 Effect of substrate surface finish and deposition conditions on the corrosion barrier performance of coatings 151
4.3.5.4 Effect of substrate surface finish and deposition conditions on the density of defects 153
4.3.5.5 Potentiodynamic testing 160
4.3.6 Summary 163
5 Discussion 165
5.1 Coatings Intended to be Durable and Low Friction 165
5.1.1 Effect of multilayering, multilayer architecture and substrate hardness on the hardness of coatings 165
5.1.2 Effect of multilayering, multilayer architecture and substrate hardness on the scratch resistance of coatings 167
5.1.3 Effect of multilayering and multilayer architecture on the microstructure of coatings 168
5.1.4 Effect of multilayering and multilayer architecture on the wear behaviour of coatings during sliding wear tests 169
5.1.5 Effect of substrate hardness on the wear behaviour of coatings during sliding wear tests 172
5.1.6 Effect of counterface ball material on the wear behaviour of coatings during sliding wear tests 173
5.2 Friction Coefficient 174
5.2.1 Effect of multilayering on the friction coefficients of coatings during sliding wear tests 174
5.2.2 Effect of multilayer architecture on the friction coefficient of coatings during sliding wear tests 175

5.2.3 Effect of substrate hardness on the friction coefficient of coatings during sliding wear tests 177
5.2.4 Effect of counterface ball material on the friction coefficient of coatings during sliding wear tests 178
5.2.5 Summary 179
5.3 Coatings Intended to be Corrosion and Scratch Resistant 181
5.3.1 Effect of multilayering, substrate surface finish and deposition conditions on the hardness of coatings. 181
5.3.2 Effect of multilayering, substrate surface finish and deposition conditions on the scratch resistance of coatings..... 182
5.3.3 Effect of multilayering, substrate surface finish and deposition conditions on the microstructure and residual stress of coatings 183
5.3.4 Effect of multilayering, substrate surface finish and deposition conditions on the corrosion barrier performance of coatings 184
5.3.5 Effect of multilayering, substrate surface finish and deposition conditions on the defect density in coatings 186
5.3.6 Summary 187
6 Conclusions 189
7 Future work 193
8 Appendix 194
9 References 196

List of tables and figures

List of figures:

Figure 2-1 Unbalanced magnetrons in a closed field arrangement (Field et al., 2004) **13**
Figure 2-2 Comparison of the ion current densities obtained by various magnetic arrangements (Laing et al., 1999) **14**
Figure 2-3 Plan view (a,b,c,d,h), cross-sectional SEM (e,g,i,j,k) and FIB images (f,l) of the following types of defects: (a) circular flat-topped morphological features at carbide inclusions in ASP30 tool steel (b) irregular flat-topped morphological features at carbide inclusions in D2 tool steel (c) nodular or flake defect (d) foreign particles preventing etching of the surface covered by them (e) cross-section of flake defect (f) FIB image of flake cross-section (g,h) through-voids or dish-like craters (i,j) cone-like defects (k) SEM image of pin-hole fracture cross-section (l) FIB image of pin-hole cross-section. (Panjan et al., 2009) **17**
Figure 2-4 Schematic representation of the influence of substrate temperature and argon pressure on the microstructure of metal coatings deposited using cylindrical magnetron sputtering sources (Thornton, 1977) **21**
Figure 2-5 SEM micrographs of cross sections of CrN coatings deposited by sputtering using varied N_2 flow rates of (a) 0 sccm, (b) 30 sccm, (c) 50 sccm, and (d) 70 sccm (Liu et al., 2002) **22**
Figure 2-6 (a) Thin hard coatings on a soft substrate generate lower stresses in the coating and at the coating/substrate interface compared to (b) a thicker coating with the same deflection (Holmberg et al., 1998) **24**
Figure 2-7 Optical microscope image of a multilayer lead/brass structure under load showing the shear occurring in the softer (lead) layers, the score lines were initially straight before loading (Matthews et al., 2001) **25**
Figure 2-8 Variation in the number of pinholes with surface roughness R_{max} of substrates for titanium single-layer films of 3 µm total thickness (Munemasa and Kumakiri, 1991) **31**
Figure 2-9 The effect of substrate surface roughness on the adhesion of CrN thin film (Lee et al., 1996) **33**
Figure 2-10 Macromechanical contact conditions for different mechanisms that influence friction when a hard spherical slider moves on a coated flat surface (Holmberg et al., 1998) **34**
Figure 2-11 Hybrised orbitals in carbon (Robertson, 2002) **42**
Figure 2-12 Graphitised transfer layer in sliding wear of DLC coatings (Holmberg et al., 2007). **46**
Figure 2-13 The specific wear rate of the counterface (a) AISI 306 ball (b) brass ball (Ohana et al., 2004) ... **50**
Figure 3-1 Schematic of CrN/Graphit-iC multilayer coatings with λ100 nm and multilayer ratios of (a) 1:1 (b) 3:1 and (c) 1:3 ..... **54**
Figure 3-2 Sample and sample holder outside the deposition chamber **58**
Figure 3-3 Inside the coating chamber **58**
Figure 3-4 Photograph of the wear rig **65**
Figure 3-5 Dimensions of the wear rig **66**
Figure 3-6 Potentiodynamic testing setup **71**
Figure 3-7 Tafel plot of IN625/Cr multilayer (λ100 nm) coating on a 1200 grit substrate **72**
Figure 3-8 Potential Vs current density plot for IN625/Cr multilayer (λ100 nm) coating on a polished substrate **73**
Figure 3-9 Schematic of profilometry measurements on samples after sliding wear tests **74**
Figure 3-10 Profilometry curve of a wear scar **75**
Figure 4-1 SEM micrograph of a CrN/Graphit-iC (λ600 nm) coating cross-section on a mild steel substrate **79**
Figure 4-2 Cross-sectional SEM micrographs of (a) CrN (b) CrN + Graphit-iC (c) CrN/Graphit-iC multilayer (λ100 nm) (d) CrN/Graphit-iC multilayer (λ20 nm) on mild steel substrates **79**

Figure 4-3 XRD patterns of (a) CrN, (b) CrN + Graphit-iC, (C) CrN/Graphit-iC multilayer (λ600 nm) (d) CrN/Graphit-iC multilayer (λ100 nm) (e) CrN/Graphit-iC multilayer (λ20 nm) coatings on 440C substrates **80**
Figure 4-4 SEM micrograph of chromium plate coating cross-section on a 440C substrate **81**
Figure 4-5 Effect of multilayering on the (a) hardness and (b) scratch resistance of coatings deposited on M42 substrates (HV = 946 ± 2 kg f mm^{-2}) in batch 1, error bars represent the equipment errors **82**
Figure 4-6 Scratch scar images of coatings on M42 substrates (a) CrN (b) CrN + Graphit-iC (c, d & e) CrN/Graphit-iC multilayer (c) λ20 nm & (d) λ100 nm & (e) λ600 nm **84**
Figure 4-7 Average wear depths on coatings on different substrates, deposited in batch 1, after sliding wear tests at (a) 10 N & (b) 40N normal load against a Ø3/8" WC-6%Co ball, error bars represent the standard deviation **87**
Figure 4-8 Specific wear rate of WC-6%Co counterface balls at (a) 10 N & (b) 40 N normal load against batch 1 coatings on different substrates, error bars represent the standard deviation **88**
Figure 4-9 Optical microscope images of WC-6%Co ball wear scars after sliding wear tests against batch 1 coatings on M42 substrates (a & b) CrN at (a) 10 N and (b) 40 N normal load (c & d) CrN/Graphit-iC multilayer λ20 nm at (c) 10 N and (d) 40 N normal load **89**
Figure 4-10 Optical microscope images of WC-6%Co ball wear scars after sliding wear tests against CrN + Graphit-iC coatings (a & b) on M42 substrates at (a) 10 N and (b) 40 N normal load and on 440C substrates (c & d) at (c) 10 N and (d) 40 N normal load **90**
Figure 4-11 Top surface SEM micrographs of the wear scars on the CrN + Graphit-iC coatings, deposited in batch 1, (a & b) on M42 substrates after sliding wear tests at (a) 10 N and (b) 40 N normal load (c & d) on a 440C substrate after sliding wear tests at (a) 10 N and (b) 40 N normal load (e & f) on a 304L substrate after sliding wear tests at (e) 10 N and (f) 40 N normal load against WC-6%Co balls **91**
Figure 4-12 Top surface SEM micrographs of wear scars on the CrN/Graphit-iC multilayer (λ20 nm) coatings, deposited in batch 1, on (a & b) M42 substrates after sliding wear tests at (a) 10 N & (b) 40 N (c & d) 440C substrates after sliding wear tests at (c) 10 N & (d) 40 N (e & f) 304L substrates after sliding wear tests at (e) 10 N & (f) 40 N normal load against WC-6%Co balls **92**
Figure 4-13 Example wear track profile showing smoothing on the CrN + Graphit-iC coating after sliding wear tests at 40 N normal load against a WC-6%Co ball on a 440C substrate, top surface images of the wear track can be seen in Figure 4-11 (d) **93**
Figure 4-14 Friction coefficients of coatings, deposited in batch 1, on 304L substrates (a) CrN (b) CrN/Graphit-iC (λ20 nm) (c) CrN/Graphit-iC (λ100 nm) (d) CrN + Graphit-iC at 10 N load against WC-6%Co balls **94**
Figure 4-15 Friction coefficients of coatings on different substrates, deposited in batch 1, during sliding wear tests at (a) 10 N & (b) 40 N normal load against a Ø3/8" WC-6%Co ball, error bars represent the standard deviation **96**
Figure 4-16 Effect of substrate hardness and multilayer architecture on the (a) hardness & (b) scratch resistance of CrN/Graphit-iC λ100 nm multilayer coatings deposited in batch 3, error bars represent the equipment errors **98**
Figure 4-17 Average wear depths on coatings, deposited in batch 3, on 440C substrates after sliding wear tests at (a) 10 N & (b) 40N normal loads against Ø3/8" WC-6%Co balls, error bars represent the standard deviation **101**
Figure 4-18 Specific wear rate of WC-6%Co counterface balls at (a) 10 N & (b) 40 N normal load against batch 3 coatings on 440C substrates, error bars represent the standard deviation **102**
Figure 4-19 Optical microscope images of WC-6%Co ball wear scars after sliding wear tests against CrN coatings on 440C substrates at (a) 10 N and (b) 40 N **103**
Figure 4-20 Optical microscope images of WC-6%Co ball wear scars after sliding wear tests against batch 3 coatings on 440C substrates (a & b) 440C substrate at (a) 10 N and (b) 40 N (c & d) CrN/Graphit-iC multilayer (λ100 nm (3:1)) at (c) 10 N and (d) 40 N normal load (e & f) CrN/Graphit-iC

multilayer (λ100 nm (1:1)) at (e) 10 N and (f) 40 N normal load (g & h) CrN/Graphit-iC multilayer (λ100 nm (1:3)) at (g) 10 N and (h) 40 N normal load **104**

Figure 4-21 Top surface SEM micrographs of the wear scars on the CrN/Graphit-iC λ100 nm multilayer coatings, deposited in batch 3, on 440C substrates after sliding wear tests (a & b) CrN/Graphit-iC multilayer (λ100 nm (3:1)) coating at (a) 10 N and (b) 40 N normal load (c & d) CrN/Graphit-iC multilayer (λ100 nm (1:1)) coating at (c) 10 N and (d) 40 N normal load (e & f) CrN/Graphit-iC multilayer (λ100 nm (1:3)) coating at (e) 10 N and (f) 40 N normal load against Ø3/8" WC-6%Co balls **105**

Figure 4-22 Friction coefficients of coatings, deposited in batch 3, on 440C substrates (a & b) CrN/Graphit-iC multilayer (λ100 nm (3:1)) at (a) 10 N and (b) 40 N normal load (c & d) CrN/Graphit-iC multilayer (λ100 nm (1:1)) at (c) 10 N and (d) 40 N normal load (e & f) CrN/Graphit-iC multilayer (λ100 nm (1:3)) at (e) 10 N and (f) 40 N normal load against Ø3/8" WC-6%Co balls **106**

Figure 4-23 Friction coefficients of coatings on 440C substrates, deposited in batch 3, at (a) 10 N & (b) 40 N normal load against Ø3/8" WC-6%Co balls, error bars represent the standard deviation **108**

Figure 4-24 Average wear depths on coatings, deposited in batch 3, on 440C substrates after sliding wear tests at (a) 10 N & (b) 40N normal load against Ø3/8" Stellite 20 and WC-6%Co balls, error bars represent the standard deviation **110**

Figure 4-25 Specific wear rate of Stellite 20 and WC-Co counterface balls at (a) 10 N & (b) 40 N normal load against batch 3 coatings on 440C substrates, error bars represent the standard deviation **111**

Figure 4-26 Optical microscope images of Stellite 20 ball wear scars after sliding wear tests against batch 3 coatings on 440C substrates (a & b) CrN/Graphit-iC (λ100 nm (1:3)) at (a) 10 N and (b) 40 N normal load (c & d) CrN/Graphit-iC (λ100 nm (1:1)) at (c) 10 N and (d) 40 N normal load (e & f) CrN/Graphit-iC (λ100 nm (3:1)) at (e) 10 N and (f) 40 N normal load **113**

Figure 4-27 Optical microscope images of Stellite 20 ball wear scars after sliding wear tests against uncoated 440C substrates at (a) 10 N and (b) 40 N normal load **114**

Figure 4-28 Top surface SEM micrographs of the wear scars on the CrN/Graphit-iC λ100 nm multilayer coatings, deposited in batch 3, on 440C substrates after sliding wear tests (a & b) CrN/Graphit-iC multilayer (λ100 nm (3:1)) coating at (a) 10 N and (b) 40 N normal load (c & d) CrN/Graphit-iC multilayer (λ100 nm (1:1)) coating at (c) 10 N and (d) 40 N normal load (e & f) CrN/Graphit-iC multilayer (λ100 nm (1:3)) coating at (e) 10 N and (f) 40 N normal load against Ø3/8" Stellite 20 balls **115**

Figure 4-29 Top surface SEM micrographs of the wear scars on the CrN and CrN + Graphit-iC coatings, deposited in batch 3, on 440C substrates after sliding wear tests (a & b) CrN coating at (a) 10 N and (b) 40 N normal load (c & d) CrN + Graphit-iC coating at (c) 10 N and (d) 40 N normal load against Ø3/8" Stellite 20 balls **116**

Figure 4-30 Friction coefficients of coatings, deposited in batch 3, on 440C substrates (a & b) CrN/Graphit-iC multilayer (λ100 nm (3:1)) at (a) 10 N and (b) 40 N normal load (c & d) CrN/Graphit-iC multilayer (λ100 nm (1:1)) at (c) 10 N and (d) 40 N normal load (e & f) CrN/Graphit-iC multilayer (λ100 nm (1:3)) at (e) 10 N and (f) 40 N normal load against Ø3/8" Stellite 20 balls **117**

Figure 4-31 Friction coefficient of coatings on 440C substrates, deposited in batch 3, against Ø3/8" WC-6%Co and Stellite 20 balls at (a) 10 N & (b) 40 N normal load, error bars represent the standard deviation **119**

Figure 4-32 Typical defects found in PVD coatings (a & b) IN625/Cr multilayer (λ100 nm) (c) IN625/Cr multilayer (λ20 nm) (d) IN625/Cr multilayer (λ600 nm) deposited on mild steel substrates **122**

Figure 4-33 XRD patterns of (a) IN625 (b) IN625 + Cr, (c) IN625/Cr multilayer (λ600 nm) (d) IN625/Cr multilayer (λ100 nm) (e) IN625/Cr multilayer (λ20 nm) coatings on 440C substrates **123**

Figure 4-34 SEM micrograph of nickel plate coating cross-section on a 440C substrate **124**

Figure 4-35 Effect of multilayering on the (a) hardness and (b) scratch resistance of coatings deposited on an M42 substrate (HV = 946 ± 2 kg f mm^{-2}) in batch 1, error bars represent the equipment errors **125**

Figure 4-36 Scratch scar images of coatings on M42 substrates (a) CrN (b) IN625/Cr λ600 nm (c) IN625/Cr λ100 nm (d) IN625/Cr λ20 nm **126**
Figure 4-37 FIB SEM cross-section of the scratch scar on the IN625/Cr λ100 nm coating on an M42 substrate **127**
Figure 4-38 Corrosion rate of coatings, deposited in batch 1, with different materials and architectures on mild steel substrates **128**
Figure 4-39 Top surface images of corroded batch 1 samples on mild steel substrates after 8 hours of salt spray testing (a) IN625 (b) IN625 + Cr (c) IN625/Cr multilayer (λ100 nm) (d) IN625/Cr multilayer (λ20 nm) **129**
Figure 4-40 Cross sectional SEM micrographs of IN625 + Cr coating, deposited in batch 1 on a mild steel substrate, after 18 hours of salt spray testing **130**
Figure 4-41 Cross sectional SEM micrographs of IN625/Cr multilayered (λ600 nm) coating, deposited in batch 1 on a mild steel substrate, after 18 hours of salt spray testing **130**
Figure 4-42 Top surface SEM micrographs of the IN625/Cr multilayered (λ100 nm) coating, deposited in batch 1 on a mild steel substrate, after 18 hours of salt spray testing **131**
Figure 4-43 EDX results taken on the corroded IN625/Cr multilayered (λ100 nm) coating, deposited in batch 1 on a mild steel substrate, after 18 hours of salt spray testing (a) at the coating substrate interface below the crack (b) at the coating away from the crack **132**
Figure 4-44 Cross sectional SEM micrographs of the as deposited IN625/Cr multilayer (λ20 nm) coating, deposited in batch 1 on a mild steel substrate **133**
Figure 4-45 Cross sectional SEM micrographs of the as deposited IN625/Cr multilayer (λ100 nm) coating, deposited in batch 1 on a mild steel substrate **134**
Figure 4-46 Cross sectional SEM micrographs of the as deposited IN625/Cr multilayer (λ600 nm) coating, deposited in batch 1 on a mild steel substrate **134**
Figure 4-47 Cross sectional SEM micrographs of cone like defects in the IN625/Cr multilayered (λ100 nm) coating, deposited in batch 1 on a mild steel substrate, after 18 hours of salt spray testing **135**
Figure 4-48 Cross sectional FIB micrograph of a defect within the IN625/Cr multilayered (λ100 nm) coating, deposited in batch 1 on a mild steel substrate, after 18 hours of salt spray testing **136**
Figure 4-49 Top surface SEM micrograph of as deposited IN625/Cr multilayered (λ100 nm) coating, deposited in batch 1 on a mild steel substrate **136**
Figure 4-50 Top surface BSE SEM micrographs of as deposited IN625/Cr multilayered (λ100 nm) coating, deposited in batch 1 on a mild steel substrate **137**
Figure 4-51 3D profilometry of 440C substrates with different surface roughnesses (a) workshop grind (b) 1200 grit (c) 6 μm polish **139**
Figure 4-52 XRD patterns of IN625 coatings on different surface finish substrates and under different deposition conditions (a) deposited on a workshop ground substrate (b) deposited on a 1200 grit substrate (c) deposited on a polished substrate (d) deposited under interrupted conditions (e) deposited under intermediate etch conditions, on 440C substrates **140**
Figure 4-53 XRD patterns of IN625/Cr multilayer (λ100 nm) coatings on different surface finish substrates and under different deposition conditions (a) deposited on a workshop grind substrate (b) deposited on a 1200 grit substrate (c) deposited on a polished substrate (d) deposited under interrupted conditions (e) deposited under intermediate etch conditions, on 440C substrates **141**
Figure 4-54 XRD patterns of IN625/Cr multilayer (λ20 nm) coatings on different surface finish substrates and under different deposition conditions (a) deposited on a workshop grind substrate (b) deposited on a 1200 grit substrate (c) deposited on a polished substrate (d) deposited under interrupted conditions (e) deposited under intermediate etch conditions, on 440C substrates **142**
Figure 4-55 Peak shift measurements at different ψ and ϕ tilts for IN625/Cr λ100 nm coating deposited on a 1200 grit substrate **143**

Figure 4-56 d-spacing vs. $\sin^2\psi$ for IN625/Cr λ100 nm coating deposited on a 1200 grit surface finish 440C substrate **143**
Figure 4-57 Compressive residual stresses in coatings deposited on different surface finish substrates and under different deposition conditions, error bars represent the standard deviation **144**
Figure 4-58 Cross-sectional (a) bright field (b) dark field transmission electron microscopy images of the IN625/Cr λ100 nm coating deposited on a 1200 grit, 440C substrate under intermediate etch conditions **145**
Figure 4-59 Cross-sectional (a) bright field (b) dark field transmission electron microscopy images of a crack within the IN625/Cr λ100 nm coating deposited on a 1200 grit, 440C substrate under intermediate etch conditions **146**
Figure 4-60 Cross-sectional high-resolution transmission electron microscopy **146**
Figure 4-61 Cross-sectional TEM images of a FIB-SEM lift-out of the as deposited IN625/Cr λ100 nm multilayer coating with an intermediate etch (a) selected area electron diffraction pattern from the area highlighted in (b) located in the upper region of the multilayers (c) a high-angle annular dark field image of the multilayers and intermediate etch position **147**
Figure 4-62 Effect of substrate surface roughness on the (a) hardness (b) scratch resistance of IN625 and IN625/Cr λ100 nm multilayer coatings, deposited in batch 2 on 440C substrates, error bars represent the equipment errors **149**
Figure 4-63 Effect of process conditions on the (a) hardness (b) scratch resistance of IN625 and IN625/Cr multilayered coatings deposited in batch 2, on 440C substrates, error bars represent the equipment errors **150**
Figure 4-64 Salt spray results of IN625 coatings, dotted lines show repeat tests **151**
Figure 4-65 Salt spray results of IN625/Cr multilayered (λ100 nm) coatings on 440C substrates, dotted lines show repeat tests **152**
Figure 4-66 Salt spray results of IN625/Cr multilayered (λ20 nm) coatings on 440C substrates, dotted lines show repeat tests **153**
Figure 4-67 Categories of defects on IN625/Cr multilayer (λ100 nm) and IN625 coatings, deposited in batch 2, on different substrate surface roughnesses (a) a >3 µm defect on an IN625/Cr multilayer (λ100 nm) coating on a WG substrate (b) a 1-3 µm defect on an IN625/Cr multilayer (λ100 nm) coating on a WG substrate (c) <1 µm defects on an IN625/Cr multilayer (λ100 nm) coating on a WG substrate (d) linear defects on an IN625/Cr multilayer (λ100 nm) coating on a WG substrate (e) a pit defect on an IN625 coating on a 6 µm polish substrate (f) cracks on an IN625 coating on a 6 µm polish substrate **154**
Figure 4-68 Average number of defects in a 4300 μm^2 area on IN625 and IN625/Cr multilayer coatings, deposited in batch 2, on different surface roughness 440C substrates and under interrupted and intermediate etch conditions, error bars represent the standard deviation **155**
Figure 4-69 Average number of defects in a 4300 μm^2 area on IN625 coatings, deposited in batch 2, on different surface roughness substrates and under different deposition conditions, error bars represent the standard deviation **156**
Figure 4-70 Average number of defects in a 4300 μm^2 area on IN625/Cr multilayer (λ100 nm) coatings, deposited in batch 2, on different surface roughness substrates and under different deposition conditions, error bars represent the standard deviation **157**
Figure 4-71 Average number of defects in a 4300 μm^2 area on IN625/Cr multilayer (λ20 nm) coatings, deposited in batch 2, on different surface roughness substrates and under different deposition conditions, error bars represent the standard deviation **158**
Figure 4-72 Top surface SEM micrographs of (a & b) (a) IN625 on a polished substrate (b) with an interrupted process (c & d) (c) IN625/Cr multilayer (λ20 nm) on a workshop grind substrate (d) with an intermediate etch (e & f) (e) IN625/Cr multilayer (λ100 nm) on a 1200 grit substrate (f) on a polish substrate **159**

Figure 4-73 Cracks generated by defects on an IN625 coating, deposited in batch 2, on a 6 µm polish substrate **160**
Figure 4-74 Potential-current density curves of IN625/Cr multilayer (λ100 nm) coatings deposited on different surface finishes, in 5 wt% NaCl solution **161**
Figure 4-75 Potential-current density curves of IN625/Cr multilayer (λ100 nm) coatings deposited under different deposition conditions, in 5 wt% NaCl solution **162**
Figure 4-76 Top surface photographs of IN625/Cr multilayer (λ100 nm) coatings after potentiodynamic testing (a) deposited on a 1200 grit substrate, (b) deposited on a polished substrate (c) deposited with an interrupted process **163**
Figure 5-1 Increase in hardness due to the presence of three different thicknesses of DLC on aluminium as a function of normalised indentation depth (Bull and Korsunsky, 1998) **166**
Figure 5-2 Cross-sectional schematic of coating and counterface ball during sliding wear tests **170**
Figure 5-3 Schematic of the point of contact of the counterface ball on the coating **171**
Figure 8-1 Variation in the mechanical properties (a) hardness (b) scratch resistance of repeat coatings deposited in different batches on M42 substrates (HV = 946 ± 2 kg f mm^{-2}) **195**

List of tables:

Table 2-1 Rate of corrosion of CrN films for different substrate surface roughnesses (Lee et al., 1996) **32**
Table 2-2 IN625 chemical composition range (wt %) (Rasmussen et al., 2008; Vesel et al., 2014) **41**
Table 3-1 Expected and intended properties of coatings deposited in this work **53**
Table 3-2 All PVD coatings and conditions requested **55**
Table 3-3 Average chemical compositions of 304L, 440C and M42 steel substrates (wt %) **56**
Table 3-4 Chemical composition of Stellite 20 balls (wt %) **65**
Table 4-1 All PVD coatings deposited in this research and their measured thicknesses **77**
Table 4-2 Effect of multilayering on the indentation depth, hardness, indentation modulus and H/E ratio of coatings **85**
Table 4-3 Effect of multilayer architecture and substrate hardness on the indentation depth, hardness, indentation modulus and H/E ratio of coatings **99**
Table 4-4 Batch 2 coatings deposited, different substrate surface roughnesses and deposition conditions used **138**
Table 4-5 Polarisation resistance (R_P), i_{corr} and E_{corr} values from potentiodynamic tests on IN625/Cr multilayer (λ100 nm) coatings deposited on different surface finishes and under different deposition conditions, in 5 wt% NaCl solution **162**

1 Introduction

In industry, many components are susceptible to wear due to contact with other components or through contact between moving parts within the component itself. Components are also often exposed to corrosive environments. The cost of wear to industry is very high as it can require components to be replaced, or the failure of a component could induce further damage to the overall system resulting in a greater overall cost. In our society, as well as the economic aspects stated, energy saving, environmental and safety aspects all determine the importance of controlling friction and wear in machinery and moving components. Oil lubrication is the most common method of reducing friction and wear. However, the use of oils and other liquid lubricants can present environmental problems as well as issues related to keeping the lubricant in the contact zone, ageing, storing and contamination. More significantly, some applications are not amenable to the use of lubricants. When such issues arise, coatings can be a suitable alternative (Holmberg et al., 2007).

Materials can be specifically designed to withstand the conditions of the application in which they are being deployed. However, these materials can also be of high cost and be difficult to machine; in addition, the properties required of the surface (which is exposed to the environment and to contact from other bodies) may conflict with those required of the core (e.g. the balance between hardness and toughness). Therefore, the development of protective coatings deposited onto less expensive and easily machinable materials is of high interest. This is known as surface engineering (Depner et al., 2011; Bobzin et al., 2012). Surface engineering generally consists of modifying the surface of the original component or applying a material to the surface to improve its lifecycle. Many engineering systems are now enhanced by (or may even be dependent upon) the use of such surface coatings as they can improve the functionality, durability and life-cycle performance of an engineering system. Examples include the modern aero-engine (which could not operate without the use of

strategically located coatings), modern cutting tools (which now provide longer and more predictable lifetimes even at an increased production rate) and medical prosthetic devices (many of which would not be able to achieve satisfactory performance without coatings which control their interactions with the bio-system in which they operate).

Wear is defined by the ASTM standard G40 as the "alteration of a solid surface by progressive loss or progressive displacement of material due to relative motion between that surface and a contacting substance or substances (ASTM, 2015)." This definition is not specific, but does indicate that this refers to attritive loss of material as opposed to (for example) loss of a coating associated with delamination at the coating-substrate interface, despite this latter being associated with the "relative motion between that surface and a contacting substance or substances". In this work, coatings will be subjected to tribologically aggressive conditions, and any means by which the coating is lost (e.g. attritive loss, coating break-up or large-scale coating delamination) will be deemed as a coating failure. To distinguish between these and the narrower concept of attritive wear, the term **coating durability** will be used to encompass all means by which the coating is removed.

The nuclear industry is one where corrosion and wear are significant issues where inspection and replacement of components is often more difficult and costly than in other (less hazardous) plant types. Alongside the complex issues associated with operation in the primary circuit, there are other issues associated with plants located in ocean-going vessels, where the aggressive marine conditions outside the plant add corrosion problems to the corrosion and wear problems encountered inside the systems. In such systems, surface engineering is generally employed to provide component lifetime enhancement, and given the nature of the systems being considered, decisions around the efficacy of a surface engineering solution will be dominated by this attribute, rather than upon costs of applying the surface engineering itself.

Within the nuclear industry, the current solutions for corrosion and scratch resistance are nickel and chromium (often termed *chrome*) electrodeposits respectively, with these solutions both being effective and having a long track-record; however, the production of such coatings by electrodeposition is coming under increasing pressure due to environmental concerns, with legislation (such as REACh (Regulation (EC) No 1907/2006, 2007)) putting the long term availability of these surface engineering solutions at risk. Therefore, the primary driver of this work is the replacement of chrome and nickel plate. For use in such situations, there is specific interest in:

- Coatings that combine durability and low coefficient of friction
- Coatings that combine scratch resistance and corrosion resistance

Although the nuclear industry is conservative, a number of new coating types (and associated methods for the deposition of such coatings) have been developed to high levels of maturity since the time when the selection of solutions for corrosion and wear resistant surfaces were made for current reactor technologies. As surface engineering has progressed over the years, significant improvements have been made to the materials used for (and methods of application of) thin films. Previously, wet bath technologies were favoured (such as electro- and electro-less deposition). However, coatings from these processes are in general much thicker and offer less control over structural and compositional profiles when compared with coatings deposited via more recently developed high performance dry coating methods such as physical vapour deposition (PVD), plasma-assisted chemical vapour deposition (PACVD) and chemical vapour deposition (CVD) (Matthews et al., 1998; Navinsek et al., 1999).

This research focusses on physical vapour deposited (PVD) coating solutions. Over the years, an important application of PVD coatings has been to improve the tribological properties of tools and machine parts. These properties include hardness, wear

resistance, scratch resistance, corrosion resistance and friction coefficient (McConnell et al., 1999). Since PVD coatings are typically only a few micrometres in thickness, these improvements are achieved with minimal change to the substrate dimensions.

The properties of PVD coatings are primarily controlled through the materials and deposition methods used, the coating architecture, the substrate material and the substrate surface finish. TiN and CrN PVD coatings are commonly used in industry for cutting and machining applications due to their high hardness and wear resistant properties as well as their ability to offer some corrosion protection. Due to their attractive and variable colours, PVD coatings are also frequently used for decorative applications such as watch cases, eye-glass frames and door plates. Nowadays, components in many applications require protection which the classic monolayered PVD coatings cannot provide; the coatings themselves have become more sophisticated, with significant enhancements in properties and performance being the goal. One development has been that of the use of multilayer PVD systems, where property and performance advantages have been associated with (i) the use of two different materials where each material confers a certain property to the system; (ii) the number of interfaces within the system which themselves influence the performance of the coating. Accordingly, multilayered and composite coatings are now of high interest, with applications being considered in a wide range of industry sectors (Jehn, 2000; Mendibide et al., 2004; Zhang et al., 2009; Oskouei and Ibrahim, 2011). The use of multilayer PVD coatings to provide alternative wear and corrosion resistant coatings for applications in marine-based nuclear reactor applications is an objective of this work. The broader aims include the development of an understanding of how the wear resistance, corrosion resistance and coefficient of friction of multilayer PVD coatings can be controlled by material selection and coating architecture.

1.1 Aims & Objectives

PVD coatings are favoured due to the benefits they confer, even when deposited at very low thicknesses (the coatings are often around 5 μm in thickness). The coatings are intended to be used in a nuclear environment where they must possess good wear, scratch and corrosion resistance. The application requires the coatings to be as thin as possible as the coatings are intended to be applied to an existing component for which change in any design features is undesirable.

The ability of multilayered coatings to provide more desirable wear and corrosion resistant properties compared to single and dual layered coatings is to be explored, along with development of an understanding of the factors which cause a difference in performance. The development of an understanding of the behaviour of such PVD coatings will itself underpin the development of new systems with improved properties through informed choice of materials and coating architecture design. The tests carried out on these coatings will be compared to benchmark coatings, these being commonly used nickel and chromium plate.

To investigate the effect of coating materials and coating architecture the following materials were chosen:

- CrN; this is an industry standard coating which is known to possess good wear and corrosion resistant properties.

- CrN + Graphit-iC and CrN/Graphit-iC multilayers; Graphit-iC is known for its low friction coefficient and CrN is known for its wear resistance; therefore, these coatings are intended to be durable and exhibit low friction. CrN/Graphit-iC multilayer coatings were also investigated using different ratios of the two materials in multilayer systems.

- IN625; this material is known to be corrosion resistant.

- IN625 + chromium and IN625/chromium multilayers; these material types are known to be corrosion resistant as well as exhibiting desirable wear resistance; therefore, these coatings are intended to be scratch and corrosion resistant.

Testing consisted of microstructural characterisation through the use of an SEM (incorporating EDX), TEM, XRD, sliding wear tests, hardness tests and scratch tests.

To investigate the effect of substrate hardness on the mechanical durability of coatings, three different hardness substrates were chosen: 304L (HV = 190 ± 5 kg f mm^{-2}), 440C (HV = 476 ± 7 kg f mm^{-2}) and M42 (HV = 946 ± 12 kg f mm^{-2}). Sliding wear tests, scratch tests and hardness measurements were carried out on coatings deposited on the different hardness substrates. Sliding wear tests were carried out against WC-6%Co balls as well as Stellite 20 balls to assess the effect of counterface type on the wear behaviour of coatings.

To investigate the effect of substrate surface finish and deposition conditions on the corrosion resistance, scratch resistance and hardness of coatings, IN625 and IN625/Cr multilayer (λ20 nm & λ100 nm) coatings were deposited onto 440C substrates of three different surface roughnesses: a rough workshop grind (126 ± 8 nm Ra), 1200 grit (78 ± 12 nm Ra) and 6μm polish (12 ± 4 nm Ra). Coatings deposited on a 1200 grit substrate were also deposited under different conditions, these being standard conditions, interrupted conditions and intermediate etch conditions. Testing consisted of microstructural characterisation through the use of an SEM (incorporating EDX), TEM, XRD, hardness tests, scratch tests, salt spray corrosion tests and potentiodynamic tests.

2 Literature Review

2.1 Review of Physical Vapour Deposition (PVD)

Physical vapour deposition is a process in which the atoms or molecules of a material are vaporised and transported through a vacuum or low pressure gaseous environment. The vapour is then condensed onto a substrate to form a coating. PVD coatings can be applied as (i) a single material, (ii) a multilayered composition (alternating layers of different materials with sharp interfaces between layers) or (iii) as layers with a graded composition (alternating layers of different materials with graded interfaces between layers) (Mattox, 2002).

PVD coatings generally range from a few nanometres to some microns in thickness and are commonly used for decorative, low friction, wear and corrosion resistant applications. PVD coatings are used on every day products such as CDs and DVDs, food packaging, mirrors, jewellery, accessories and fittings and they can provide an aesthetically pleasing finish as well as protection of the substrate from corrosion and wear (Bobzin et al., 2008). Hard coatings such as TiN and TiC have previously been used to extend the life of cutting tools, dies, punches and also to reduce wear on ball bearings (Ohring, 1992; Durst et al., 2009). Physical vapour deposition of thin films is a favoured technique in industry because the method of manufacture uses technology in which thousands of devices are produced at the same time, reducing manufacturing costs (Sree Harsha, 2006).

PVD is considered to be a technique which can provide not only metallic, but also alloyed and ceramic coatings with a virtually unlimited range of chemical compositions. The composition and architecture of the coating can be modified to give the required protective, mechanical and wear-resistant properties (Navinsek et al., 1999). Since the early 1980's, ceramic PVD coatings have been used in industry for many applications. In industry today, the most commonly used PVD coatings are TiN, Ti(C,N), (Ti,Al)N and CrN (Van Stappen et al., 1995; Holmberg et

al., 2007). In the 1990's, low friction diamond-like carbon (DLC) and MoS_2 coatings were developed and introduced into industry. In the 2000's, a considerable research effort has investigated the controlled modification of the coating structures including the development of nanostructured coatings such as gradient coatings, multilayered coatings and doped coatings, making the coatings more tailored to their environment (Matthews, 2003; Bobzin et al., 2008).

PVD coatings still face problems due to a lack of knowledge regarding the coating behaviour, with their corrosion resistance (or ability to protect the substrate from corrosion) remaining an ongoing issue in certain applications. Diamond-like carbon coatings are becoming increasingly popular as hard wearing, low friction coatings in industrial applications as more research is carried out and more is understood about the long-term tribological properties of the coatings (Van Stappen et al., 1995; Holmberg et al., 2007).

Through improvements of the plasma-based physical vapour deposition process, coatings can now be developed to have tribological properties which were previously unachievable. Some significant process innovations include ionization-enhancing systems such as thermionic assistance, arc evaporation, unbalanced magnetron sputtering and magnetic plasma confinement (Matthews, 2003). Before new and improved PVD processes became available, ion plating was the favoured PVD process for industrial use. Ion plating had limitations which new PVD processes do not; for example, the conventional "dc-diode" system that was used in ion plating did not provide sufficient levels of ionization to permit deposition of dense ceramic coatings with adequate mechanical properties (Matthews, 2003).

PVD coating technology can now be used to deposit coatings with mechanical and chemical properties similar to those deposited using old coating techniques, such as electroplating, and can thus be considered as a replacement coating technique. However, the coatings deposited by PVD are generally much thinner (often around 5 μm in thickness) and thus the chemical barrier properties and lifetime in a tribologically aggressive environment may be compromised. However, PVD coating

techniques do have advantages in this regard; the coatings themselves do not greatly increase the dimensions of the object being coated, meaning that a system does not need to be reconfigured to account for the coating thickness. PVD coatings can also be much more uniform than coatings deposited using more traditional techniques, and they can provide properties that are said to be highly repeatable, providing that there are good process controls in place (Hans et al., 2000; Mattox, 2001; Lüdecke et al., 2013).

This research looks into the tribology and corrosion resistance of selected PVD coatings. The tribology and corrosion resistance of PVD coatings is determined by many factors including the coating materials, architecture, deposition methods, the cleanliness of the deposition conditions, the environment in which the coating is being employed (or tested), substrate morphology and material. The effect of substrate surface roughness on coating properties is discussed in section 2.2.6. The substrate has a large effect on the behaviour of the coating. For example, a very hard, brittle coating on a soft substrate would not generally give desirable properties as the coating would tend to fracture.

One of the main interests in PVD coatings is the ability to tailor the properties of the coatings through design of the architecture of the coating itself. PVD coatings can be deposited as systems with multiple layers of alternating (or otherwise different) materials as outlined in section 2.2.4. Depending on the materials used and the thickness of the layers, coatings can be developed to have specific properties. Another significant factor affecting the properties of PVD coatings are growth defects which occur during deposition, outlined in section 2.2.2. Their density is affected by various factors including the substrate and deposition conditions. The current research programme aims to investigate single and multilayered systems in order to understand the properties that can be achieved; attention is also given to how the architecture of the coatings dictates these properties, as well as trying to minimize the density of growth defects.

2.1.1.1 PVD Processes

There are many different techniques used to deposit PVD coatings, namely vacuum evaporation, sputter deposition, ion plating, arc vapour deposition and closed field unbalanced magnetron sputter ion plating (CFUBMSIP).

Vacuum evaporation (or vacuum deposition) is a process in which a material is vaporised through thermal vaporisation. The vapour is transported through a vacuum environment to the substrate (Mattox, 1998; 2002). The source material may be a solid in any form or purity and high vaporisation rates can be achieved. However, many alloy compounds can be difficult to deposit due to differing vapour pressures of the alloying elements. Vacuum evaporation is used to create films which are used in applications such as optical interference coatings, mirror coatings, decorative coatings, electrically conducting films, corrosion resistant coatings, and on flexible packaging materials such as food packaging to provide a permeation barrier (Mattox, 2002).

Sputter deposition is a non-thermal vaporisation process. Surface atoms of the target are physically ejected by momentum transfer from an atomic, energetic bombarding particle. The bombarding atom can be supplied in a number of ways, such as from a plasma, an ion gun, an accelerator or by a radioactive material which emits alpha particles. During sputter deposition, the particles are ejected from a target surface by the physical sputtering process and then deposited onto the substrate.

The physical sputtering process is driven by momentum exchange which is due to collisions between the ions and atoms in the materials. The sputtering of a surface atom from a target material involves the atom gaining enough energy, through ion bombardment, to cause it to vibrate and transfer energy to nearby atoms. This increase in energy causes collisions between the ions and atoms in the material. If a surface atom gains enough energy, then that atom can be ejected (sputtered) from the target surface.

Sputtering allows the deposition of alloy compositions which cannot be thermally evaporated due to the differing vapour pressures of the different alloying elements. In the sputtering process, each solid surface layer is removed consecutively; therefore, the composition of the vapour flux leaving the surface will be the same as the composition of the material being sputtered, providing there is no significant diffusion (Mattox, 2002). Sputter deposition has been used to create: energy controlling coatings on architectural glass, transparent conductive coatings on glass, reflective coatings for compact disks, magnetic films, decorative coatings and films to provide wear resistance and dry film lubrication (Mattox, 2002).

Ion plating is a process in which the atoms or molecules of coating material are evaporated from a hot source into a glow discharge. Unlike other PVD deposition methods, the vaporisation source for ion plating can be one of many, including evaporation, sputtering and arc erosion (an arc struck against a solid source material). Some of the vapour atoms become ionised and are accelerated toward the substrate which is held at a negative potential; other atoms move under their thermal velocities. Ion plating can be achieved in either a plasma or vacuum environment. In a plasma environment, the ions for bombardment are provided by the plasma, whereas in a vacuum environment, the ions are formed in a separate ion gun. This type of ion plating is known as ion beam assisted deposition (IBAD) (Hutchings, 1992; Mattox, 2002). Ion plating is commonly used to deposit hard compound coatings, such as metal coatings with good adhesion, optical coatings with high densities and coatings for surfaces with complex structures (Mattox, 2002).

One of the most effective PVD processes has been proven to be arc evaporation due to high ionization levels achievable (Matthews, 2003). In arc vapour deposition, the vapour is formed from the anode (anodic arc vaporisation) or cathode (cathodic arc vaporisation) of a low voltage high current DC arc in a low pressure gaseous environment. Cathodic arc vaporisation is the most common arc vaporisation process and it involves a high current density arc moving over a solid cathode. This causes local heating and in turn, vaporisation. The arc movement can be steered using a

magnetic field and multiple cathodic arc sources may be used to give deposition over a large area. Cathodic arc vaporisation also allows the evaporation of alloy materials with ease. (Mattox, 2002). Films deposited through cathodic arc vapour deposition are commonly used for wear resistant decorative coatings which have a functional purpose, such as plumbing fixtures and door handles (Mattox, 2002).

2.1.1.1.1 Closed field unbalanced magnetron sputter ion plating (CFUBMSIP)

Closed Field Unbalanced Magnetron Sputter Ion Plating (CFUBMSIP), developed by Teer Coatings Ltd, is recognised as a state of the art technique and is now established as a versatile method for high rate deposition of high quality metal, alloy or ceramic coatings and is the method of coating deposition used in this research. A key factor of the process is its ability to transport high ion currents to the substrate, enhancing the formation of fully dense coatings at relatively low temperatures (Kelly et al., 1996; Kelly and Arnell, 1997; Kelly and Arnell, 2000). Magnetron sputtering has become widely used in industry for a range of applications such as hard, wear-resistant coatings, low friction coatings, corrosion resistant coatings, decorative coatings and coatings with specific optical or electrical properties. In a variety of cases, magnetron sputtering can produce coatings which outperform thicker films deposited by older PVD techniques discussed earlier in section 2.1.1.1 (Kelly and Arnell, 2000).

A magnetron consists of a permanent magnet arrangement which is positioned behind the target. It was developed to increase the sputtering rate by confining the plasma at the target surface and enhancing the ionisation efficiency by using electric and magnetic fields. In unbalanced magnetron sputtering, the outer magnets of the magnetron are made much stronger than the central magnet. This allows electrons produced from sputtering to follow the magnetic field lines away from the target and towards the substrate (Stallard, 2005).

In the early 1970's, the balanced magnetron system was introduced, followed by the unbalanced magnetron in the late 1980's. The introduction of the unbalanced

magnetron into multi-source closed field systems transformed the capabilities of the technique, allowing it to be more suitable for a wider range of industrial applications (Kelly and Arnell, 2000). In a closed field arrangement, the magnetrons are arranged so that at least one pair of neighbouring magnetrons are of opposite magnetic polarity. In this arrangement the magnetic field is essentially closed meaning electrons from the outer poles are contained within the closed field, thus trapping the plasma region as shown in Figure 2-1 (Field et al., 2004).

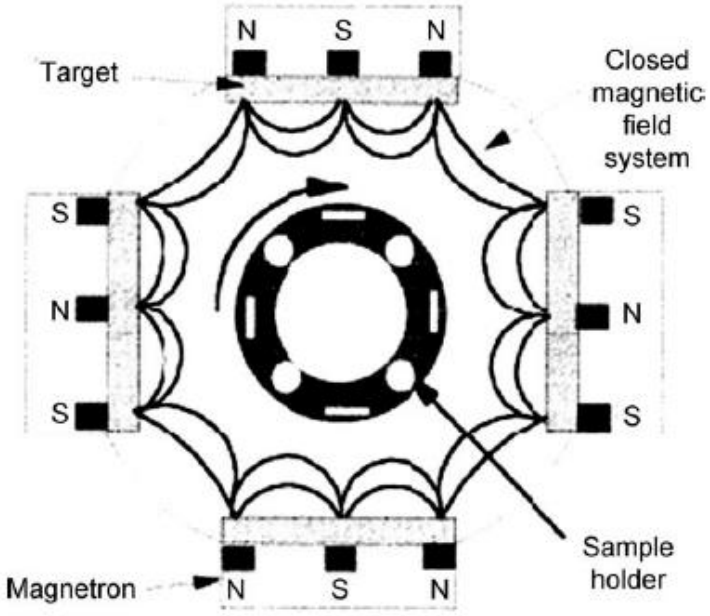


Figure 2-1 Unbalanced magnetrons in a closed field arrangement (Field et al., 2004)

This configuration prevents the loss of ionising electrons so that deposition occurs under high density bombardment by low energy ions. These have been shown to be the best conditions to grow dense films; Figure 2-2 shows the increase in ion current achieved by Teer Coatings Ltd through the use of a closed field unbalance magnetron arrangement. (Laing et al., 1999; Cooke et al., 2004).

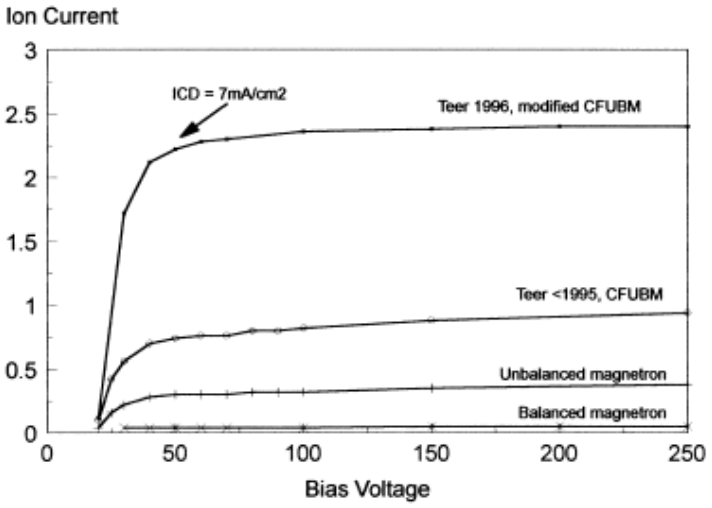


Figure 2-2 Comparison of the ion current densities obtained by various magnetic arrangements (Laing et al., 1999)

CFUBMSIP allows the rapid and reliable deposition of multilayer coatings, and can be used to easily deposit complex alloy structures from multiple sources or a single metal target, either directly or by reactive methods. Typical industrial coating units now have up to six magnetron sources. The process has proven effective in depositing coatings to be used in critical applications such as cutting and forming tools, components designed for wear resistance and optical systems (Voevodin et al., 1995; Cooke et al., 2004).

CFUBMSIP is the method used to deposit coatings in this research, and derives its beneficial aspects from the retention of plasma within the deposition environment which, compared to classic magnetron sputtering techniques, produces a higher ion current density. This produces high quality coatings with excellent adhesion (Camino et al., 1999; Cooke et al., 2004). This process is commonly used to deposit a commercially available coating, using carbon and chromium targets, known as Graphit-iC (which will be used in this research programme). Other commercially available coatings deposited by CFUBMSIP include commonly used hard coatings such as TiN, CrN, TiAlN, TiCN, CrTiAlN, corrosion resistant Al/Mg supersaturated alloy

coatings and wear resistant molybdenum disulphide (MoS_2)-based MoST coatings (Kelly and Arnell, 2000; Jianxin et al., 2008; Aihua et al., 2012; Yang et al., 2012).

2.2 Review of the Microstructure of PVD Coatings and Properties

The mechanical properties of PVD coatings are to a large extent dependent on their microstructure which is characterized as a columnar structure with local defects (Cunha and Andritschky, 1999; Cunha et al., 1999; Dörfel et al., 1999; Mendibide et al., 2006). The microstructure of PVD coatings is dependent on the deposition methods, deposition parameters and source material used although slight variations in the film composition can have a large effect on the microstructure. The morphology and cleanliness of the substrate and deposition chamber are also very important factors in determining the microstructure of coatings. Growth defects can occur within PVD coatings and their main causes are dust particles on the substrate surface prior to or during deposition, and pits or asperities on the substrate surface. In this section, the microstructure of PVD coatings is discussed, including growth defects and their effect on corrosion resistance and coating properties. The effect of deposition conditions, coating architecture, intermediate etching and substrate surface finish are discussed.

2.2.1 Introduction to the corrosion behaviour of PVD coatings

The corrosion resistance of PVD coatings is determined by many factors such as the chemical composition, architecture, deposition parameters, thickness, surface roughness, through-coating porosity and substrate properties (Liu et al., 2002). The architecture of coatings can be designed to help increase the coatings corrosion resistance through methods such as multilayering. It has been argued that the multiple layers increase the corrosion resistance of a coating by blocking or disrupting

the pinhole defects within the coating, thereby reducing the chance of exposure of the substrate to corrosive material (Liu et al., 2002). It has been said (Jehn, 2000; Liu et al., 2001) and observed that, only a relatively limited number of studies exist investigating the corrosion resistance and methods of improving the corrosion resistance of PVD coatings. PVD coatings contain pores and pinhole defects, often growth related, which act as channels to the substrate therefore lowering their corrosion resistance (Liu et al., 2001; Liu et al., 2002; Merl et al., 2004).

2.2.2 Growth defects and their effect on coating properties

The properties of PVD coatings are determined by many factors such as the deposition methods used, coating materials and architecture. But even with carefully selected parameters, PVD coatings may not perform to their full potential predicted from the properties of materials used. This is due to growth defects which can occur from a variety of sources such as substrate surface finish and foreign particle contamination. Whilst PVD coating materials themselves generally exhibit a high corrosion resistance, the coating-substrate systems may exhibit corrosive attack of the substrate due to these defects. These growth defects can cause local loss of adhesion, higher friction, voids, pitting corrosion and can act as stress raisers (Brandl and Gendig, 1996; Ries et al., 1997; Cunha and Andritschky, 1999; Jehn, 2000; Lewis et al., 2006; Altun and Sen, 2007; Čekada et al., 2007; Panjan et al., 2009; Hoche et al., 2011; Panjan et al., 2012; Panjan et al., 2013). Growth defects are non-uniformly distributed over the volume of the coating, suggesting that the formation of growth defects is sporadic and spatially localised. Their form, size and density depend on the deposition time, deposition techniques, deposition parameters, substrate position in the vacuum chamber, substrate orientation and rotation mode, the surface conditions of the substrate, type of coating material and target material (Panjan et al., 2009; Depner et al., 2011; Panjan et al., 2013).

Panjan et al. (2009) have identified various different types of defects and characterized them as shown in Figure 2-3.

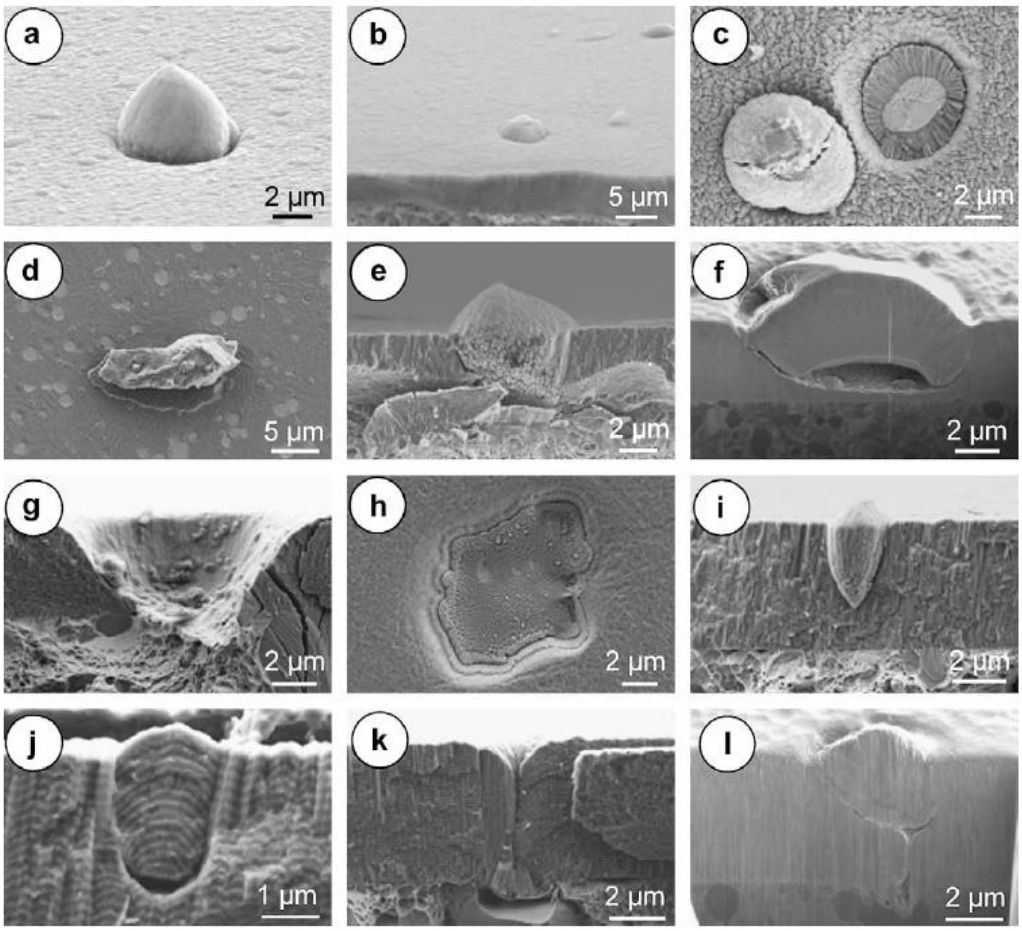


Figure 2-3 Plan view (a,b,c,d,h), cross-sectional SEM (e,g,i,j,k) and FIB images (f,l) of the following types of defects: (a) circular flat-topped morphological features at carbide inclusions in ASP30 tool steel (b) irregular flat-topped morphological features at carbide inclusions in D2 tool steel (c) nodular or flake defect (d) foreign particles preventing etching of the surface covered by them (e) cross-section of flake defect (f) FIB image of flake cross-section (g,h) through-voids or dish-like craters (i,j) cone-like defects (k) SEM image of pin-hole fracture cross-section (l) FIB image of pin-hole cross-section. (Panjan et al., 2009)

Defects originate from 'seeds', where a 'seed' is defined as a necessary condition for nodule formation. Their growth is then caused by the shadowing effect of PVD coatings. At the seed sites, the coating nucleates seperately to the bulk deposit causing nodular defects to form. The geometry of the defect is defined by the seed morphology (Panjan et al., 2013). Seeds originate from various sources. These include

substrate surface finish, substrate surface irregularities (such as pits), foreign particles like dust, debris or residues from grinding, blasting and polishing. Additionally, dust contamination on components in the chamber, such as the shields, rods, fixtures and heater can also remain in the system after the pre-treatment. Other defects include microdroplets from the deposition process itself; depending on the deposition conditions, these microdroplets (which can range from <1 μm up to around 7 μm in diameter) can form and fall on the surface. These microdroplets originate from the target due to non-conductive inclusions in the target material or from any contamination on the target surface (Čekada et al., 2007; Panjan et al., 2008). In the case of magnetron sputtering, seeds can be formed due to non-uniform erosion of the target material which results in material being redeposited on the perimeter and centre of the target. This build-up of material can then flake off or cause arcing. Seeds can also be generated during the heating stage as thermal expansion of coated surfaces within the vacuum chamber can generate flakes and particles. These can also be generated from wear particles due to the rotation of the substrates. The ion etch stage has also been known to create seeds (due to different etch rates) if the substrate is a non-homogenous material. Etching of coated parts in the chamber can also generate flakes and particles that can land on the substrate. During or after deposition, some growth defects can be pulled out due to high compressive stresses, or by wiping of the surface, leaving cavities in the coating. Cavities generated during deposition cannot be completely covered by the coating due to the shadowing effect of thin hard coatings. It is assumed that a lot of large defects are related to the cleaning and drying process and the cleanliness of the batching room (Altun and Sen, 2007; Durst et al., 2008; Panjan et al., 2009; Panjan et al., 2013).

Growth defects create pathways to the substrate, reducing the corrosion barrier performance of the coating. Nordin et al. (1999) carried out potentiodynamic tests to investigate the effect of multilayering and multilayer thickness of TiN/CrN coatings on the corrosion resistance of PVD coatings. Anodic polarisation curves were recorded up to 3 V with a scan rate of 1 mV s^{-1}. Coatings with two modulation periods (10 and

125 nm) were investigated in a 0.1 M H_2SO_4 solution. They found that the single layer TiN and CrN monolayer coatings showed a passive behaviour up to around 1.2 V and 0.9 V respectively. The CrN and TiN/CrN multilayer coating with a 125 nm bilayer period exhibited high current densities above 1.1 V (10 mA/cm^2); however, the TiN/CrN coating with a 10 nm bilayer period showed an anodic peak at 1.1 V and thereafter a decrease in current density. It was stated that, above 1.1 V, the current density of the coating with a 10 nm bilayer period exhibited a current density two orders of magnitude lower than the CrN and TiN/CrN multilayer with a bilayer period of 125 nm. This was attributed to the higher number of lamellae in the coating with a 10 nm bilayer period. It was said that, the oxidation process was by lateral dissolution of the CrN rather than vertical, therefore the oxidation rate was approximately inversely proportional to the number of lamellae. A higher number of lamellae was said to reduce the amount of pores running through the coating.

Liu et al. (2001) investigated the corrosion resistance of mild steel (polished to 14 μm) coated with single layered and multi-layered TiN and CrN coatings (2-2.5 μm thick) through potentiodynamic tests in 0.5 N NaCl solution against a saturated calomel reference electrode (SCE). The multiple layers were deposited by four sequential repetitions of the single-layer process. They found that the corrosion potential for the monolayer TiN and CrN coatings was 0.4 V and 0.45 V vs. SCE respectively. A slight increase in corrosion potential was seen for the four layer coatings giving a corrosion potential of 0.5 V vs. SCE, suggesting that the multilayered coating is more noble than the monolayer coatings. It was suggested that this improvement in corrosion resistance was due to a reduction in the number of pinholes; however, no evidence was given to explain the reason for the reduction in pinhole density.

As well as affecting corrosion performance, defects have been observed to affect the mechanical behaviour of PVD coatings. Aihua et al. (2012) investigated sliding wear on four coatings, TiN, TiAlN, AlTiN and CrAlN, deposited on a YG6 cemented carbide substrate. SiC was employed as the counterface and tests were run at 120 m/min. It

is interesting to note that the tests revealed that partial fracture of the coating occurred due to defects in the coating being pulled out during contact, leaving fractures in the coating which promoted further brittle fracture of the coating. Wear debris then formed micro-asperities in the sliding area, causing scratching. In order to improve the tribological properties of PVD coatings, it was argued that it is important to minimise the density of these defects.

Many attempts have been made to reduce these defects; however, not many investigations have been made into the effect of growth defects on the tribological and corrosion properties of coatings (Brandl and Gendig, 1996; Čekada et al., 2007; Panjan et al., 2008; Panjan et al., 2009; Panjan et al., 2012; Panjan et al., 2013). There are several ways which have been said to improve the corrosion resistance of PVD coatings such as: thicker coatings, dense coatings, elimination of droplets by modification of the deposition process, intermediate etching and the use of multilayers. The effect of multilayers and intermediate etching is discussed in section 2.2.4 and 2.2.5 respectively. Thicker coatings have been said to have a greater corrosion resistance due to fewer defects reaching the surface (defects may be covered over as the coating deposition process continues) (Jehn, 2000). Intermediate etching can remove dust, particles or defects from the surface part way through deposition (Jehn, 2000) which then disrupts the existing defects and reduces the chance of new defects being formed due to contaminants on the surface. (Brandl and Gendig, 1996; Jehn, 2000; Fenker et al., 2006). The idea of the multilayers is to block the path of the corrosion agents to the substrate by disrupting the structure of the coating and thus disrupting the defect growth through the coating. Research has shown (on various coating systems) that a thicker coating, or the use of interlayers, can reduce the number of pores and pinholes, therefore improving the corrosion resistance of PVD coatings (Jehn, 2000; Liu et al., 2001; Dobrzański et al., 2006; Bobzin et al., 2012; Bobzin et al., 2013).

2.2.3 Effect of deposition parameters on coating properties

The pressures and temperatures used during deposition can affect the microstructure of the coating. Thornton (1974) investigated the effect of deposition temperature and argon pressure during PVD deposition on the microstructure of the coatings. It was found that, as the substrate temperature was increased, coatings developed structures from an open columnar structure (Zone 1), to a dense columnar structure (Zone 2), to a dense equiaxed grain structure (Zone 3). A further region (Zone T) was discovered between Zone 1 and Zone 2 which consisted of densely packed fibrous grains as shown in Figure 2-4. In the case of a CFUBMSIP system, continuous ion bombardment of the coating during its growth occurs resulting in a dense film (Thornton, 1974; Thornton, 1977; PalDey and Deevi, 2003; Stallard, 2005).

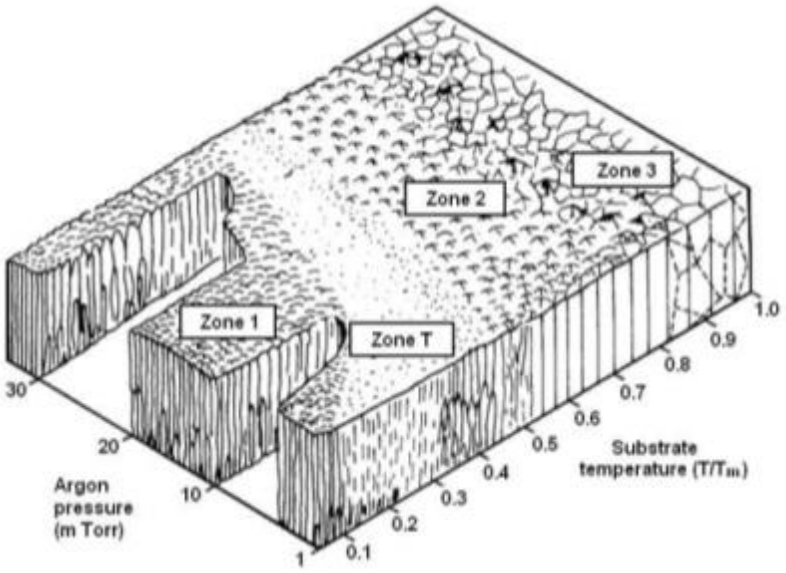


Figure 2-4 Schematic representation of the influence of substrate temperature and argon pressure on the microstructure of metal coatings deposited using cylindrical magnetron sputtering sources (Thornton, 1977)

The coating structure is also dependent upon the architecture and phase make-up of the coating. Research examining the microstructure of TiN and CrN PVD coatings demonstrated that TiN coatings have a compacted, columnar structure, whereas CrN

coatings have a compacted, submicrocrystalline structure and multilayer Ti/(TiAl)N coatings had a laminar structure. The authors noted these differences, but offered no explanation for the difference in structures (Dobrzański et al., 2005).

Research has also been carried out to observe the effect of varying the nitrogen flow rate when depositing CrN coatings by sputter deposition. Figure 2-5 shows the SEM micrographs of cross sections of four CrN_x coatings, (a)–(d), deposited by sputtering using varied N_2 flow rates of 0, 30, 50, and 70 standard cubic centimeters per minute (sccm) respectively (Liu et al., 2002).

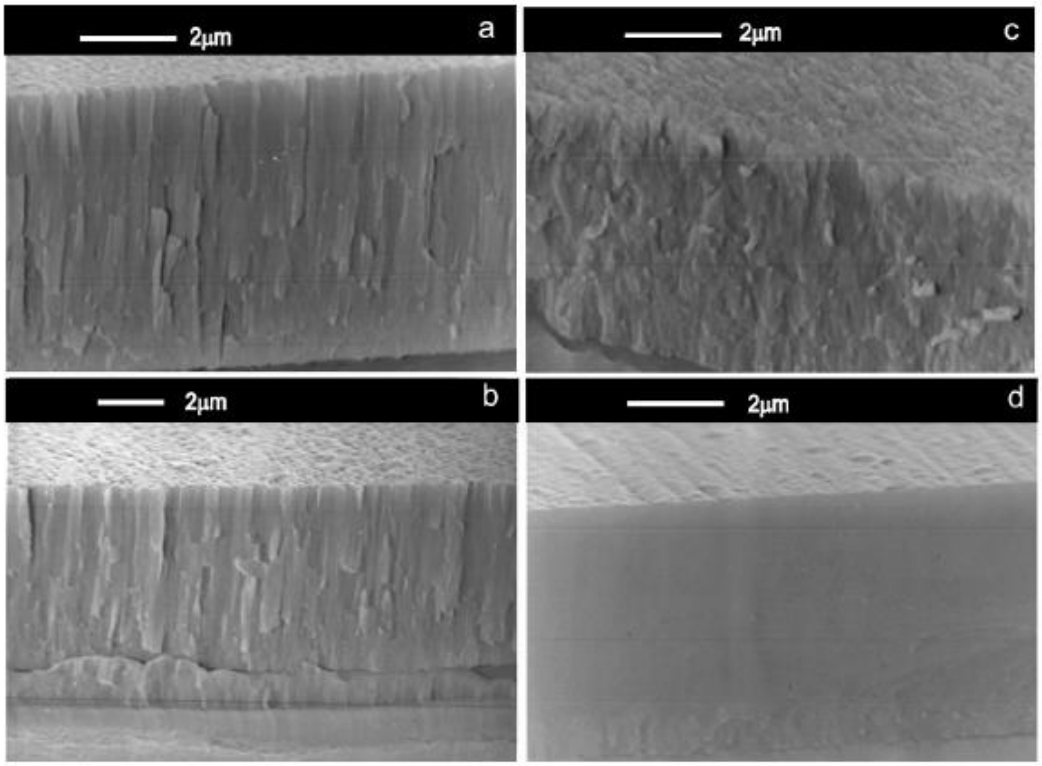


Figure 2-5 SEM micrographs of cross sections of CrN coatings deposited by sputtering using varied N_2 flow rates of (a) 0 sccm, (b) 30 sccm, (c) 50 sccm, and (d) 70 sccm (Liu et al., 2002)

It can be seen that variations in flow rates of nitrogen (which in this case is a reactive gas) can have a large effect on the microstructure of the coating due to changing nitrogen content in the film and an increase in lattice distortion (or microstrain) with increasing nitrogen content. Higher nitrogen flow rates of 70 sccm resulted in the tendency to form a structure with equiaxed, noncolumnar crystallites. Coatings

deposited with 0 and 30 sccm N_2 flow rates showed microcolumnar structures, whilst those deposited with N_2 flow rates of 50 sccm showed coarse semiequiaxed structures. XRD showed that an increased N_2 flow rate also resulted in reduced crystallite size and an increase in internal microstrain.

2.2.4 Multilayers

PVD can be used to produce single layer coatings or multilayered coatings. The thickness of a coating or its multiple layers can be controlled through different methods such as the rotational speed of the sample during deposition or, for multilayered coatings with individual layers greater than 50 nm, the layer thickness can be controlled by ramping the different targets (varying the power) up and down at appropriate intervals. Multilayers potentially offer a simple way of enhancing the tribological properties of a coating which cannot be achieved by simple monolayer coatings. The thickness of each individual layer can be controlled to give coatings that have a combination of properties to match the application of the coating such as high hardness, high corrosion resistance, low friction and high adhesion. Multilayers can also be employed to improve the resistance of a coating to crack propagation by deflecting cracks at layer interfaces (Holmberg et al., 1998; Mellor, 2006). Multilayer coatings have been shown to exhibit a higher hardness compared to monolayer films. Some explanations of this hardening are based on the Hall-Petch effect, on the variations of shear modulus or internal stresses (Holmberg et al., 1998; PalDey and Deevi, 2003; Mendibide et al., 2004; Cabrera et al., 2011; Sprute et al., 2014). Higher compressive residual stresses are desirable to an extent as they retard crack propagation and increase fracture toughness; however, if the compressive stresses are too high, then this can result in poor adhesion to the substrate and therefore, coating delamination. It is also suggested that the interfaces in a multi-layered structure disrupt defect growth across them and therefore increase the corrosion resistance of the coatings by reduction in the number of through-coating defects

(Holmberg et al., 1998; PalDey and Deevi, 2003; Mellor, 2006). It has also been said (Cabrera et al., 2011) that the interfaces between layers act as grain boundaries, so that dislocations pile up at the interfaces and harden the layer by strain.

PVD coatings can be designed using multilayers to create a coating which combines a high hardness with a low elastic modulus, through alternating layers of materials with high and low elastic modulus. This allows the harder, more brittle, layers to deflect relative to each other due to elastic shear which occurs in the softer layers. This means that the harder layers experience a lower bending stress than if the coating was a single thick layer (Matthews, 2003; Mendibide et al., 2006). It is known that thin hard coatings on a soft substrate generate lower stresses in the coating and at the coating/substrate interface compared to thicker coatings with the same deflection, as illustrated in Figure 2-6 (Holmberg et al., 1998).

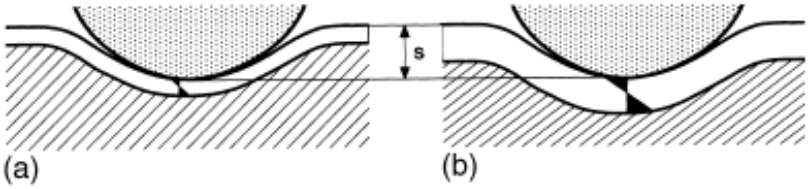


Figure 2-6 (a) Thin hard coatings on a soft substrate generate lower stresses in the coating and at the coating/substrate interface compared to (b) a thicker coating with the same deflection (Holmberg et al., 1998)

This theory may also apply for multilayered PVD coatings, depending upon the nature of the interface between the layers and the properties of the individual layers themselves. The strain in thin PVD coatings is affected by the substrate behaviour, resulting in a substrate-strain controlled deformation of the coating. Compliance in the deformation behaviour (either of the interfaces or of one of the multilayer materials) will facilitate motion (elastic or plastic) of layers with respect to each other, meaning that the multilayers of the coating will be less likely to be affected by cracking through substrate deformations. Therefore, these multilayer coatings may be able to withstand heavily loaded tribological applications better than single layer coatings which would undergo cracking when exposed to a high bending stress (Matthews et al., 2001).

Matthews et al (2001), modelled the deformation behaviour of a multilayer structure under load using lead and brass layers. It was observed that the shear occurred in the softer (lead) layers as shown in Figure 2-7. The score lines were initially straight before loading.

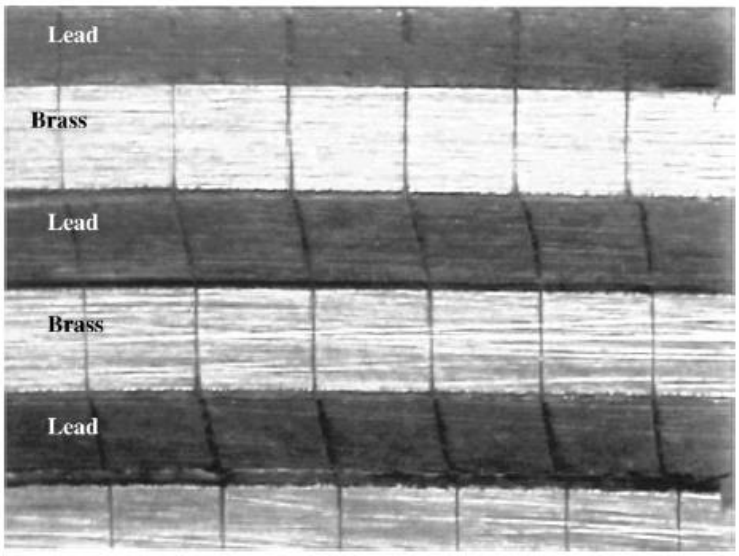


Figure 2-7 Optical microscope image of a multilayer lead/brass structure under load showing the shear occurring in the softer (lead) layers, the score lines were initially straight before loading (Matthews et al., 2001)

As well as the multilayer thicknesses and materials used, the interfaces between these multilayers play a large role in determining the properties of the coatings. It has been found that a graded interface (rather than a sharp interface) between layers can lead to an improvement in the corrosion resistance of multilayered coatings as the graded interface results in lower stress concentrations than a sharp interface. Higher stresses in a coating can result in delamination from the substrate or the ejection of material associated with growth defects, leaving pores, therefore, reducing the corrosion resistance of the coating (Ries et al., 1997).

Much research has been carried out on various different multilayer materials and it is clear that the effect of multilayering is strongly dependent on the materials used. Creus et al. (1998) investigated the corrosion resistance of a reactive cathodic arc deposited CrN coating with a TiN top layer compared to a CrN monolayer coating on AISI 4135 steel substrates. The corrosion resistance was measured through

electrochemical potential-current density measurements in 3% NaCl solution. The results showed that the CrN + TiN coating gave only a slight benefit in corrosion resistance (with a polarisation resistance (R_p) of 580 Ω cm^2 after 35 hours immersion) in comparison with the monolayer CrN coating (with a polarisation resistance of 560 Ω cm^2 after 35 hours immersion). The limited change in corrosion resistance was said to be attributed to local peeling off of the TiN layer during testing resulting in the resistance becoming similar to that of CrN.

Cabrera et al. (2011) examined the effect of varying the bilayer period on the properties of r.f magnetron sputtered multilayer CrN/AlN multilayer PVD coatings, on Si (100) and AISI D3 steel substrates. Bilayer periods of 1000, 300, 150, 75 and 60 nm were investigated. Hardness measurements (carried out by nanoindentation) showed that the coating with the thinnest bilayer period of 60 nm gave the highest hardness (29 GPa) which was 48% and 38% greater than the values obtained from monolayer AlN and CrN coatings respectively. It was suggested that this increase in hardness could be attributed to the Hall-Petch effect. This theory suggests that each interface in the multilayer system behaves as a grain boundary; dislocations pile up at the interfaces and harden the layer by strain.

The tribological properties of the coatings were measured through pin-on-disc tests using a Ø6 mm 100Cr6 steel ball at 0.5 N load for 1000 m. The friction coefficients ranged from 0.3 to 0.18, the lowest being reported for the coating with the lowest bilayer period of 60 nm, giving a decrease in friction coefficient of approximately 58% and 49% compared to monolayer AlN and CrN coatings. It was suggested that this behaviour was due to a higher hardness to elastic modulus ratio of 0.280 compared to that of the monolayer AlN and CrN coatings which showed a H/E ratios of 0.074 and 0.120 respectively. The H/E ratio was seen to increase with decreasing bilayer period. The multilayer coatings were said to show an increase in plastic deformation resistance compared to the monolayer coatings due to the increased coating density, hardness and elastic recovery. The adhesion was measured through scratch testing for a scratch length of 6 mm over a continually increasing load of 0-90 N. The failure load

was seen to increase with decreasing bilayer period and the coating with the thinnest bilayer period showed the highest critical load (adhesive failure) of around 42 N. The coating with a 60 nm bilayer period exhibited an increase of 38% and 42% in critical load compared to the monolayer CrN and AlN coatings respectively. The improvement in adhesion was said to be attributed to the increase in coating / substrate deformation resistance (Cabrera et al., 2011). The interfaces were also said to act as crack tip deflectors, further enhancing resistance to fracture.

2.2.5 Intermediate etching

One method that has been researched in order to reduce the porosity of PVD coatings is intermediate etching. When depositing a PVD coating, ion etching is carried out on the substrate before deposition. Intermediate etching involves an ion etch both prior to coating and part way through the coating process. It is argued that this process leads to a denser coating due to defect-induced renucleation and improved adatom mobility (Jehn, 2000; Fenker et al., 2002).

Fenker et al. (2002) investigated the effect of intermediate plasma etching on magnetron sputtered single layer CrN coatings deposited on polished high-speed steel substrates. The research investigated CrN with 4, 8 and 16 etching steps, and the results were compared to CrN without intermediate etching. Scratch tests were employed to assess the coating adhesion and Rockwell C indentation tests were used to measure coating hardness. Microhardness was shown to slightly increase from around 3650 N/mm^2 for CrN with no etching steps to around 3700 N/mm^2 for coatings with 4 etching steps. In contrast, a decrease in hardness was seen for coatings with more than 4 etching steps. A very significant decrease in hardness, to around 2500 N/mm^2, was seen when the number of etching steps was increased to 16. It was stated that three mechanisms could be responsible for this decrease in hardness, these being changes in texture, weakening of the coating integrity due to ion induced defects and stress relaxation due to ion generated thermal spikes. In the adhesion

tests, of all etched coatings showed a lower failure load (around 26, 27 and 28 N for coatings with 4,8 and 16 etching steps respectively) compared to the non-etched CrN coating which showed a failure load of around 33 N. Corrosion resistance was measured using potentiodynamic measurements in 0.8 M NaCl solution. The results showed that the corrosion resistance of the coatings increased with the number of etching steps. The E_{corr} of the CrN coating with 16 etch steps had moved approximately 80 mV in the positive direction showing that the etched system was more noble than the monolayer CrN coating. It was suggested that this improvement in corrosion resistance is due to the reduction of defect density. The corrosion resistance of multilayer coatings with intermediate etching steps was also investigated; however, the results showed that the corrosion behaviour of the different samples was almost identical and that the etching steps had provided no benefit to the corrosion resistance of multilayer coatings. It was suggested that there was no benefit of intermediate etching for multilayer coatings because any changes associated with the etching were insignificant in a system with a large number of multilayer interfaces already present.

Abusuilik and Inoue (2013) investigated the effect of intermediate etching on the corrosion resistance of cathodic arc PVD CrN coatings (8-9 μm thick) compared to a CrN coating with no intermediate treatments. The coating process was stopped at a coating thickness of around 4 μm and an Ar ion plasma etch was carried out for 15 minutes. The corrosion resistance was measured through immersion tests and anodic polarisation measurements in 10% sulphuric acid solution. The results showed that the coating deposited with an intermediate Ar etch gave an early increase in current density in the passive region, due to pitting as a result of local corrosion at the coating-substrate interface, and did not outperform the CrN coating with no intermediate treatments. The intermediate etch was not seen to reduce defect density. However, the authors of the paper did not provide an explanation for this observation.

2.2.6 Substrate surface roughness and the effect on coating properties

Due to the shadowing effect in thin PVD film deposition, the surface roughness of the substrate has an effect on the structure and therefore on the performance of the coating as it determines the coatings surface roughness. Substrate surface irregularities can also induce growth defects:

"as the peak to valley height on the substrate profile increases, there is an increasing tendency for coating defects to form" (Maeng et al., 2006).

Durst et al. (2008) investigated the effect of substrate surface finish on the corrosion resistance of magnetron sputtered graded ZrC, graded ZrC_g/Cr, and graded CrC_g coatings deposited on low alloy steel substrates with different surface finishes of Ra = 0.01, 0.3 and 1.2 µm. The corrosion resistance was measured through polarisation tests between approximately 100 mV below OCP up to 1200 mV in 2 mv steps with a change rate of 1000 mV per hour in artificial sea water at 30°C. The results showed that, in all tests, coatings deposited on a polished substrate (Ra = 0.01 µm) gave the lowest current densities (of around 0.0001 mA/cm^2 at around 200 mV potential); however, the current densities of the coatings deposited on rougher substrates were not actually presented. Microscopic evaluation revealed that for polished specimens, only a single void was highlighted in the corrosion area. The corrosion pits on the rougher (1.2 µm) substrate were said to obviously follow the peaks of the machining scratches. It was concluded that a higher surface roughness leads to a higher number of defects, thereby reducing the corrosion resistance of the coatings. No explanation was given for the physical mechanism behind the increase in defect density with increasing surface roughness.

Liu et al. (1995) investigated the effect of substrate surface roughness on the hardness and corrosion and scratch resistance of ion plated PVD CrN coatings on mild steel substrates which had been finished to different surface roughnesses with P240 SiC paper, polishing with M45 (45 µm) diamond paste and polishing with M6 (6 µm) diamond paste. Microhardness measurements were carried out with a Mitutoyo

MUK-G1 at a load of 25 gf and an indentation time of 10 s. The hardness was said to be similar for coatings deposited on substrates with different surface finishes. The adhesion of the coatings was measured through scratch testing at a loading rate of 100 N min^{-1} and a scratching velocity of 10 mm min^{-1} up to 100 N. The critical load (defined as the load at coating fracture) was said to double for coatings deposited on 45 μm polished substrates (15 N) compared to those deposited on substrates finished with P240 SiC paper (8 N). The critical load was then said to double again for coatings deposited on 6 μm finished substrates (30 N). It was noted that, coatings deposited on finer substrate surface finishes showed a reduction in coating defects, fractures and disbonded areas. The coating deposited on the P240-finished substrate exhibited fracture and separation from the substrate in the direction of the underlying grinding marks. The coating deposited on the M45-finished substrate showed similar behaviour, however, with less frequency and severity. Disbonded areas of 200 μm diameter were reported. The coating deposited on the M6-finished substrate showed significantly smaller disbonded areas of 20 to 50 μm diameter. The increase in coating scratch resistance could be attributed to the reduction in coating fractures and disbondment.

In addition, the corrosion resistance of the coatings was measured through A.C impedance measurements in 3% NaCl solution with a sinusoidal signal of 50 mV (r.m.s) amplitude over a bandwidth from 20 mHz to 10 kHz for around 500 hours. The corrosion potential was seen to increase for coatings deposited on substrates with finer surface finishes, indicating a more noble characteristic and therefore improved corrosion resistance. Coatings deposited on a substrate finished with P240 SiC paper exhibited a corrosion potential of -650 and -690 mV after a few hours, whereas, the coating on 45 μm polished substrates showed a more noble corrosion potential which then slowly decreased to -600 mV within two days of exposure and -650 mV after 12 days. The coating deposited on the 6 μm finished substrate showed a more noble initial corrosion potential of -550 mV after three days which dropped sharply to -650 mV on the fourth day. The increase in corrosion resistance was attributed to

the reduction in defect density for coatings deposited on polished samples compared to those deposited on a rougher surface finish. The increase in adhesion was also linked to the improved corrosion resistance; it was argued that a high adhesion makes it more difficult for corrosion product to undermine the coating and cause cracking in the vicinity of the corrosion site, therefore limiting the propagation of corrosion once initiated.

Munemasa and Kumakiri (1991) investigated magnetron sputtered TiN films (3 μm thick) and the effect of substrate surface roughness on the number of pinholes in a 400 mm^2 area. The surfaces of each substrate were finished by grinding to various roughnesses ranging from 0.2 R_{max} to 17 R_{max} μm. It was found that for R_{max} < 1 μm, the number of pinholes in a 400 mm^2 area was less than ten, whereas for R_{max} > 2 μm the number of pinholes significantly increased from 10 to 217 (the results are displayed in Figure 2-8). It was noted that the defect density never reached zero even at very low substrate surface roughnesses; however, no explanation was proposed relating to the reduction in defect density with decreasing surface finish.

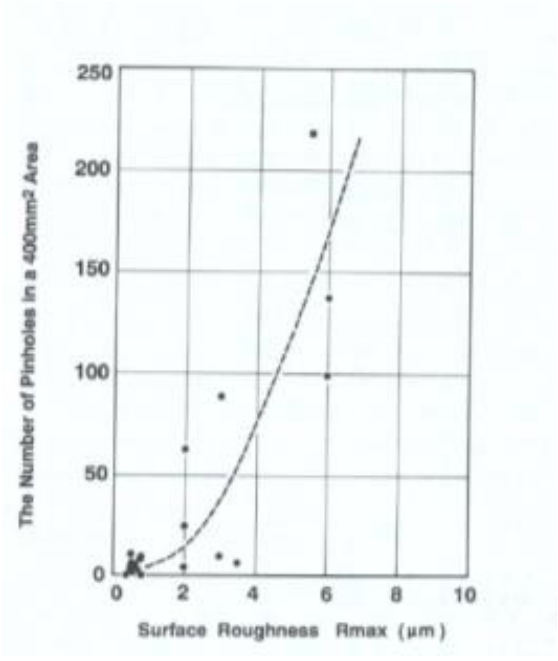


Figure 2-8 Variation in the number of pinholes with surface roughness R_{max} of substrates for titanium single-layer films of 3 μm total thickness (Munemasa and Kumakiri, 1991)

Lee et al. (1996) investigated the adhesion and corrosion resistance of cathodic arc PVD CrN coatings (2.36 μm thick) on AISI M2 high speed steel substrates with different surface finishes of Ra = 0.31, 0.2 and 0.1 μm. The corrosion resistance was measured through immersion tests in 5% NaCl solution at 25^{o}C from -1000 mV to 1000 mV at a sweep rate of 1 mV s^{-1}. After 10 days of immersion time, the samples were removed from the solution and weighed in order to calculate the corrosion rate; the results are displayed in Table 2-1.

Corrosion rate of specimens

Specimen	**Corrosion media/immersion time**	**surface roughness Ra (μm)**	**corrosion rate (mdd)***
Uncoated substrate	5% NaCl/10 days	0.10	58
CrN (A)		0.33	25
CrN (B)		0.22	19
CrN (B)		0.13	2

*mdd: mg per dm^2 per day.

Table 2-1 Rate of corrosion of CrN films for different substrate surface roughnesses (Lee et al., 1996)

It was found that the coating deposited on the substrate with the lowest surface roughness (Ra = 0.1 μm) exhibited the lowest corrosion rate, and this was attributed to the reduced number of pinholes in the CrN film.

The adhesion of the coatings was measured through scratch testing at an increasing load of ~ 8 N mm^{-1} against a diamond tipped hemispherical stylus with a 125 μm radius of curvature. Critical load was recorded as the load at which coating flaking or chipping occurred. It was found that a lower substrate surface roughness provided a coating with better adhesion as well as a lower friction coefficient; the scratch test results are shown in Figure 2-9. The increase in adhesion was said to be attributed to a decrease in frictional force at the indenter contact. The pile up of material ahead of the indenter causes bending of the coating and induces tension in the coating surface. The friction between the indenter and the coating causes the radial tensile stresses to

occur at the sides of the indenter. As the indenter scratches, the tangential friction add compressive stresses ahead of the indenter. This leads to deformation and coating cracking.

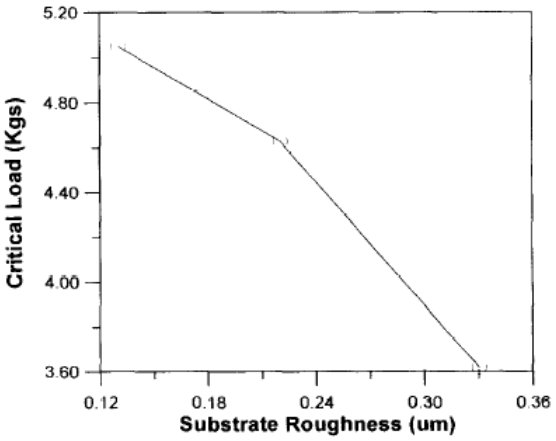


Figure 2-9 The effect of substrate surface roughness on the adhesion of CrN thin film (Lee et al., 1996)

2.3 Review of Friction, Wear and Contact Mechanisms

Wear is defined as the progressive removal of material from a surface that is under load whilst in relative motion (Ohring, 1992; Holmberg et al., 2007; Olofsson and Olander, 2013). Different modes of wear can occur, and normally wear involves a complex combination of wear modes associated with contact geometry, surface roughness, debris and changes in contact conditions. The main factors that determine the tribological behaviour of thin coatings are the intrinsic characteristics of the material, the coefficient of friction, the hardness and elastic modulus of the coating and substrate, the resistance of the coating and interface to cracking (or delamination), the coating thickness, the surface roughness of the coating and substrate and the size and hardness of any debris in the contact zone. This debris can be a result of the wear taking place, or can exist on the surface prior to wear taking place (Matthews et al., 1998).

2.3.1 Friction and contact mechanisms

The frictional behaviour of thin PVD coatings during sliding wear is complex and can be influenced by many factors, such as the coating microstructure, chemical composition, surface roughness and the ratio of coating to substrate stiffness and hardness. During sliding wear, the friction will vary as wear debris accumulates and becomes trapped between the coating surface and the counterface and as oxidation occurs. The frictional behaviour of PVD coatings during sliding wear is said to go through four stages (Olofsson et al., 2011).

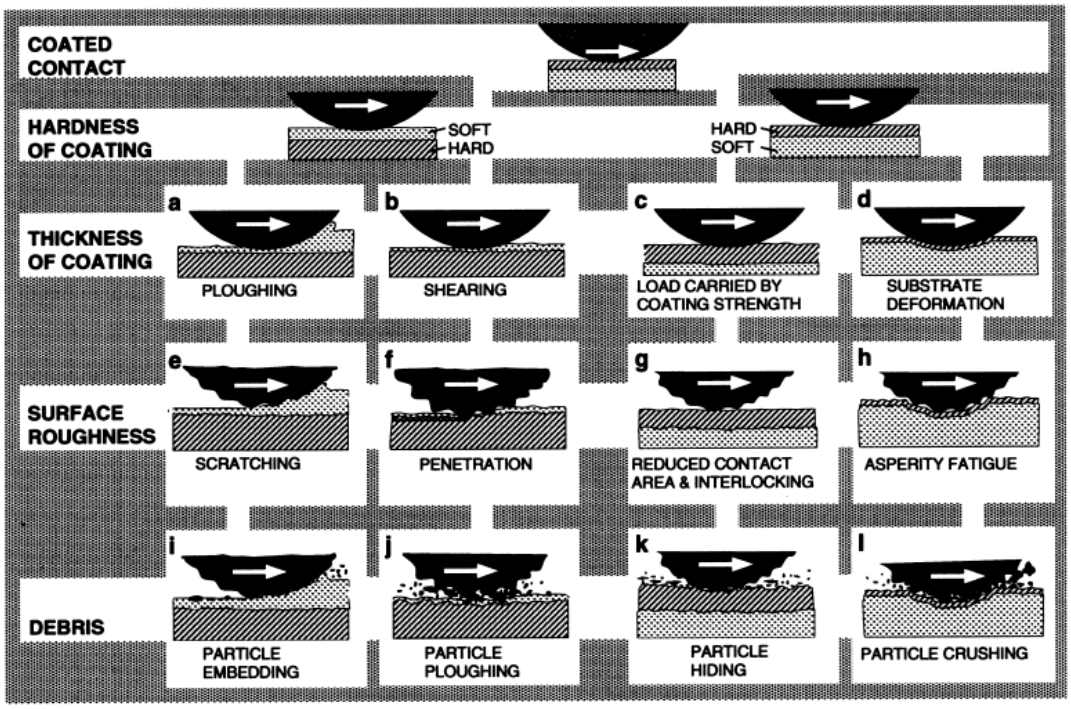


Figure 2-10 Macromechanical contact conditions for different mechanisms that influence friction when a hard spherical slider moves on a coated flat surface (Holmberg et al., 1998)

Four main parameters are said to control contact behaviour and therefore the friction behaviour: the ratio of coating to substrate hardness, thickness of the coating, the surface roughness and the size and hardness of any debris. Twelve contact types are shown in Figure 2-10 which seeks to characterize behaviour when a hard spherical slider moves across a coated surface. The relationship between coating and substrate hardness is an important factor. A hard coating on a softer substrate can reduce

ploughing and therefore the friction and wear. This can be reduced further by using a harder substrate. A thin hard coating on a softer substrate can result in substrate deformation and a strain induced failure of the coating (Figure 2-10 (d)); in contrast, a thick hard coating on a softer substrate reduces the contact area through assisting in carrying the load (Figure 2-10 (c)). For soft coatings on harder substrates, the thickness of the coating can influence ploughing behaviour (Figure 2-10 (a & b)), whereas the surface roughness affects the degree of asperity penetration through the coating and into the substrate (Figure 2-10 (e & f)). For hard coatings on softer substrates, the surface roughness reduces the contact area; however, asperities are subject to abrasive and fatigue wear (Figure 2-10 (g & h)). Wear debris, which can originate from the surrounding environment or due to different wear processes, greatly affects the friction and wear of coatings in sliding contact. For softer coatings on harder substrates, the wear debris can become embedded in the coating or in the case of thinner coatings, the debris undergoes ploughing (Figure 2-10 (i & j)). For harder coatings on softer substrates the wear debris can undergo crushing and particle hiding (Figure 2-10 (k & l)) (Holmberg et al., 1998; Stallard, 2005).

2.3.2 Wear mechanisms

Abrasive wear

Abrasive wear has long been recognized as one of the most significant types of wear. When it comes to material loss, it is said to cause 50% of wear in industry (Eyre, 1976). When a surface is in lateral motion with hard wear particles present (hard particles from the environment or asperities of another surface of higher hardness), abrasive wear can occur. Asperities from the harder surface can scratch the softer surface and remove material; in addition, cracking can also occur on surface with higher hardness. Abrasive wear can be reduced by reducing the surface roughness of the materials in contact, but as wear occurs, the material that has been removed can

interfere with the contacting surfaces in motion and increase abrasive wear. Abrasive wear is akin to scratching, and is therefore a wear mechanism which will need to be considered in the scratch tests performed in this research (Ohring, 1992; Matthews et al., 1998; Holmberg et al., 2007; Kamdi et al., 2011).

Fatigue wear

Fatigue wear can occur when surfaces in contact undergo repeated loading and unloading. Eventually, the material strength degrades below the point of being able to withstand the repeated loading resulting in cracking, fracture and wear debris being formed. Fatigue wear is known to occur in situations such as ball and roller bearings and in gears (Ohring, 1992; Matthews et al., 1998; Holmberg et al., 2007), and can be encountered as a failure mode in sliding wear if other wear modes do not dominate.

Sliding wear

Sliding wear is possibly one of the most complex as well as one of the most common types of wear and is the type of wear that will be encountered in the pin-on-disc tests carried out in this research. It can occur when two surfaces are loaded against each other and moved relative to one another tangentially to the point of contact (Matthews et al., 1998; Chokethawai, 2008).

Adhesive wear is a subset of sliding wear. When two contacting surfaces undergo tangential motion, asperities on the two surfaces will come in and out of contact and material and wear debris from one surface can be displaced and attached to the opposing surface. The two sliding surfaces can become bonded at asperities through material transfer. These bonds are then broken due to tangential motion, with the wear resulting from the detachment of fragments of material from the asperity junctions as they separate (Ohring, 1992; Lee, 2004; Holmberg et al., 2007).

For metals, contacting surfaces are said to undergo stages of wear during sliding. In the first stage, a contact surface is polished through a combination of abrasive and adhesive wear. In the second stage, plastic deformation is said to take place due to asperity interactions as micro-cracks are initiated and propagated. Finally, as the contacting surface nears the end of its service life, an acceleration in fatigue wear can be observed (Jisheng, 2002).

During sliding wear, abrasive wear can dominate if debris or loose particles (generated during early stages of sliding wear or from external contamination) become trapped between the two rubbing faces (Rigney, 1988). Contact stresses in the early stages of sliding wear are generally higher than those generated at later stages; as a result, the debris particles generated in early stages of sliding are large compared to those generated at later stages. Some of these large particles are removed from the rubbing interface, causing material loss; however, many of them remain within the rubbing interface where they are broken down to form a compact load-bearing debris layer (Jiang et al., 1998).

Sliding wear can be influenced significantly by heat, as elevated temperatures can facilitate oxidation of the metal asperities on the sliding surfaces in contact. This increase in temperature can be caused by friction or it can be associated with the conditions in the environment (Stott, 1998). The extent of oxidation is dependent on the temperatures developed at the asperities, the testing environment, the duration of contact and the oxidation characteristics of the material. The oxides formed can be completely removed producing oxide wear debris. These debris particles can be removed from the contacting surfaces, leaving exposed metal which then oxidises further, or can remain between the two rubbing faces as either freely-moving particles or non-moving particles. If the oxides remain as freely-moving particles, they can cause abrasive damage, whereas, if the oxides remain as non-moving particles on one of the interacting surfaces, they can lead to the development of a protective debris layer reducing the amount of wear damage. The sliding wear behaviour is also determined by the coating material. Solid lubricants, for example, are known to form

a transfer layer under sliding conditions, which help reduce or maintain a low friction coefficient between contacting surfaces. In addition to surface layers forming during sliding contact, other parameters can also change. Strain hardening takes place as well as softening of the surface due to a rise in local temperatures (Matthews et al., 1998; Stott, 2002).

Much research has also been carried out on the sliding wear of self-lubricating ceramics. The wear is affected by the tribochemical reaction which occurs at the contact surface. At the point of contact, a reaction of the ceramic with the environment (atmosphere or fluid) results in the formation of a thin protective film on the surface, consisting of fine wear particles. This thin film is known as the tribofilm, the formation of which can significantly reduce the amount of wear of the ceramic and also lowers the coefficient of friction (Suh et al., 2008; Gant and Gee, 2009). It is said that the wear behaviour of ceramics is highly dependent on the quantity of entrapped wear debris in the contact area as it is this debris which tends to form the tribofilm (Yang et al., 2004).

2.3.3 Sliding wear behaviour of PVD coatings

The sliding wear behaviour of PVD coatings is dependent on many things, such as the properties of the coating materials, the sliding speed, load applied, counterbody and testing environment. During the early stages of sliding wear on PVD coatings, flash temperatures (which can reach up to 800^{o}C at the point of contact in unlubricated sliding (Blok, 1963; Amiri and Khonsari, 2010)) can result in melting or an excessive softening of asperities. This softening of asperities can cause a transfer layer to form between the surface of the coating and the counterface which helps protect the coating from wear.

For hard PVD coatings, a strong adhesion between the transfer layer and the coating is often formed. Due to this strong adhesion, removal of the transfer layer can result

in removal of parts of the coating during sliding. In the case of self-lubricating coatings, this adhesion is not as strong. The lower adhesion between the transfer layer and the coating means that the removal of parts of the coating during sliding is less likely to occur. During testing, different wear mechanisms can operate alone; however, it is more likely that a combination of wear conditions will operate. In addition, during operation, the tribological conditions can change, and therefore, the wear modes can also change. As such, it is important to design a coating which can withstand a range of wear conditions (Matthews et al., 1998; Straffelini and Gariboldi, 2007; Mo and Zhu, 2008). For example, Jianxin et al. (2008) investigated the sliding wear of ZrN PVD coatings on a YG6 cemented carbide substrate using a high speed ring-block tribometer against a ring specimen of Ø50 mm x Ø35 mm x 15 mm. A load of 50 N was used for sliding distances of 100, 600 and 1000 m. It was found that in the early stages of friction, the wear mechanism was mild abrasive wear. After 600 m of sliding, brittle fracture and delamination of the coating was observed, as well as pits on the wear surface. After 1000 m of sliding the wear mechanism was severe abrasive wear as most of the coating was worn out and deep mechanical grooves and large scratches were observed on the substrate.

2.4 Review of Coating Materials and Diamond-Like Carbon (DLC)

The work presented in this thesis investigates coatings containing a combination of different materials, these being Cr, CrN, IN625 and a solid lubricant material Graphit-iC. CrN and Graphit-iC are commercially available coatings that are commonly used in industry. Other commonly used, commercially available coatings include variations of TiN, Ti(C,N), and (Ti,Al)N (Van Stappen et al., 1995; Holmberg et al., 2007); however, as this research is investigating materials for nuclear reactor primary circuit components (and titanium is not used in the manufacture of primary circuit components), it was requested that titanium-based materials would be avoided in this

research. Nickel based alloys are known for their excellent corrosion resistance, especially the 600 family; they have a broad range of applications across the aerospace, navy and marine industries as well as in nuclear reactor technology. Although much research has been carried out on the alloys themselves, little or no work has been carried out on PVD coatings of IN625. The paucity of research on PVD of Inconel relates to the fact that the majority of PVD research is aimed at enhancing tribological properties rather than corrosion resistance (Leroy et al., 2001; Czerwiec et al., 2003; Saker et al., 2008).

2.4.1 CrN

CrN is an industry-standard PVD coating which is known for its high hardness (around 2200 $HV_{0.05}$, depending on the deposition parameters (Nilsson and Olsson, 2011)), and good wear and corrosion resistance (Bayón et al., 2009). The coating is known to exhibit strong columnar structures (Han et al., 2000a). CrN is used in applications such as protection of cutting tools and dies. CrN is used as an alternative for TiN when the process involves elevated temperatures such as die casting under pressure (Navinšek et al., 1997).

The friction coefficient of cathodic arc deposited CrN (1.2 μm thick) and electroplated Cr (6 μm thick) coatings on 1200 grit surface finish AISI 4140 steel was measured against a Ø6.35 mm WC-6%Co ball at 10 N load and 300 rev/min sliding speed, for 1000 m, on a Ø25 mm wear track. The friction coefficient was measured to be around 0.47 for CrN compared to 0.73 for electroplated Cr (Han et al., 2000b).

Costa et al. (2010) compared the hardness and wear properties of cathodic arc deposited CrN coatings (4 μm thick) with WC-10 wt%Co-4 wt%Cr HVOF thermal spray coatings (150 μm thick). Coatings were deposited on a Ti-6Al-4V substrate with surface roughness Ra = 0.98 μm. Pin-on-disc tests were conducted against a Ø3 mm, aluminium-bronze 630, flat pin at 5 N load and 0.5 m/s sliding speed for 3000 m. The specific wear rate of CrN was measured to be 1.04×10^{-15} $m^3\,N^{-1}\,m^{-1}$, lower than that

of the thermally sprayed coating of $1.25x10^{-14}$ $m^3 N^{-1} m^{-1}$. The arc deposited CrN coating also resulted in a lower wear rate on the pin ($2.87x10^{-13}$ $m^3 N^{-1} m^{-1}$) compared to when the pin was slid against the thermally sprayed coating ($4.08x10^{-13}$ $m^3 N^{-1} m^{-1}$). The hardness of the CrN coating was measured to be 2000 HV compared to the thermal spray coating which showed a lower hardness of 1485±120 HV0.3.

2.4.2 IN625

Inconel 625 is a nickel based alloy which is known to possess good corrosion and oxidation resistance (Lim et al., 2003; Rai et al., 2004). The alloy is used in many applications in industry such as heat shields, furnace hardware, combustion liners and seawater applications (Lim et al., 2003; Rai et al., 2004). The chemical composition of Inconel 625 can be seen in Table 2-2.

Element	wt %
Nickel	58.0 min.
Chromium	20-23.0
Iron	5.0 max.
Molybdenum	8-10.0
Niobium (plus Tantalum)	3.15-4.15
Carbon	0.10 max.
Manganese	0.50 max.
Silicon	0.50 max.
Phosphorous	0.015 max.
Sulphur	0.015 max.
Aluminum	0.40 max.
Titanium	0.40 max.
Cobalt	1.0 max.
Copper	-

Table 2-2 IN625 chemical composition range (wt %) (Rasmussen et al., 2008; Vesel et al., 2014)

Although this alloy is widely used in industry, very little research has been carried out on the properties of IN625 when deposited as a thin film PVD coating. As iron and nickel-based alloys are used in the production of nuclear reactor primary circuit components, the IN625 alloy was an appropriate candidate for coating material.

2.4.3 Introduction to carbon and diamond-Like Carbon

Carbon has an outer shell arrangement $2s^2\ 2p^2$. Carbon forms a variety of crystalline and disordered structures because it can exist in three hybridisations sp^3, sp^2 and sp^1 as shown in Figure 2-11.

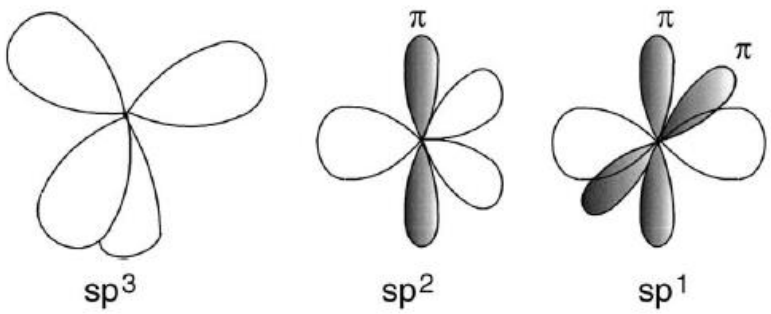


Figure 2-11 Hybrised orbitals in carbon (Robertson, 2002)

Diamond has an sp^3 configuration. In this configuration, each of the four electrons which can participate in the formation of chemical bonds are assigned to a tetrahedrally arranged sp^3 orbital. These make σ bonds, the strongest type of covalent bond, with an adjacent atom. In contrast, graphite has an sp^2 configuration where, for each carbon atom, three of the four electrons which can participate in the formation of chemical bonds are assigned to trigonally arranged sp^2 orbitals, which form σ bonds in a plane. The fourth electron lies in a p orbital perpendicular to the plane of the sp^2 orbitals. This orbital forms a ∏ bond, which is weaker than a σ bond, with another p orbital on one or more neighbouring atoms.

Properties of graphite and diamond

Diamond is the hardest naturally occurring material known, with its hardness being measured to be around 100 GPa. Diamond has the highest bulk modulus, the largest room temperature thermal conductivity and the smallest thermal expansion coefficient of any solid. The density of diamond is measured to be around 3.525 g cm^{-3}. Diamond derives its properties from its strong, directional σ bonds (Robertson, 2002).

Graphite has a density of around 2.267 g cm^{-3} and a melting point over 3600 ^{o}C. It is known for its low friction behaviour in sliding. Graphite has a lamellar structure composed of fine alternating layers of carbon atoms arranged in a hexagonal lattice. It has been suggested that the low friction of graphite is due to low interatomic forces between parallel planes of graphite carbon (Dobrzański et al., 2006). However, others suggest that it is due to the presence of absorbed gases and vapours (such as oxygen and water) saturating the forces on the surface of the crystallites, reducing the attractive forces between them, resulting in low friction (Hokao et al., 2000; Yang et al., 2001). In the absence of absorbed gases, the coefficient of friction of graphite is said to fluctuate due to the disintegration of graphite into a cloud of fine dust-like debris (Zhu et al., 2015).

Hokao et al. (2000) investigated the frictional properties of graphite against an alumina pin with a radius of 2.9 mm. Pin-on-disc tests were carried out at sliding speeds of 0.05, 0.1 and 0.5 m/s, with a normal load of 4.7 N and at a relative humidity of 25%-35% in ambient air. They found that friction coefficient of graphite ranged between 0.2 and 0.25.

Diamond-like carbon

Diamond-like carbon (DLC) is the name given to a variety of amorphous carbon materials which contain hydrogen in the range of less than 1 at.% hydrogen (a-C), up to around 50 at.% hydrogen (a-C:H). "*The a-C:H films typically contain sp^3 fractions*

smaller than 50%, while the a-C films can contain 85% or more sp^3 bonds" (Grill, 1999). Detailed tribological studies carried out on DLC have shown that the films exhibit attractive physical and mechanical properties, similar to those of diamond, such as low friction coefficient, self-lubrication, high wear resistance and high hardness. Because of their chemical inertness, they are also known to be resistant to corrosion and oxidation. These properties are due to significant fractions of sp^3 type carbon bonds.

The hydrogenated form of diamond-like carbon (a-C:H) is referred to by the term 'DLC', whereas, the non-hydrogenated form (a-C) is referred to by the term 'taC' (tetrahedral amorphous carbon), which contains high fractions of sp^3 hybridized carbon (Meletis et al., 1995; Liu et al., 1996; Erdemir, 2002; Robertson, 2002; Ohana et al., 2004).

The effect of hydrogen on DLC properties

The friction coefficients of a-C and a-C:H films strongly depend on the environmental conditions. The hydrogenated form of diamond-like carbon (a-C:H) is known to suffer from severe wear when tested in water-lubricated conditions, whereas, the non-hydrogenated form is known to perform much better under these conditions (Field et al., 2004; Stallard et al., 2004) The low friction of a-C:H coatings in dry environments is said to be attributed to a lubricious graphite-like layer which forms between the coating and the counterpart during sliding, known as the tribofilm. It is suggested that this tribofilm forms through the release of hydrogen from the coating surface during sliding due to friction induced annealing, caused by high local temperatures and pressures at the point of contact, which destabilise the sp^3 bonds and facilitate the formation of graphitic sp^2 bonds. The contact mechanism then becomes shear within sp^2 hybridised graphitic basal planes. The temperature required for sp^3 to sp^2 transformation depends on the density of hydrogen-terminated bonds on the surface on the environment. It is said to be in the range of 100-300^{o}C for DLC (Donnet and

Erdemir, 2008). The hydrogenated form of diamond-like carbon is the most widely used due to its low friction coefficient and high wear-resistance in dry conditions. (Field et al., 2004; Stallard et al., 2004; Stallard, 2005; Holmberg et al., 2007). The properties of hydrogenated DLC coatings make them ideal for use in applications where they will remain dry such as computer hard discs, microelectromechanical systems, cutting tools, mechanical seals, magnetic storage tape heads and drums, sunglasses and bar code readers (Bull and Hainsworth, 1999; Erdemir, 2002).

The high friction of a-C coatings during dry sliding is said to be caused by the removal of absorbed hydrogen on the film surface exposing strong adhesive dangling carbon bonds. These produce a high adhesion with the counterface atoms and therefore result in high friction (Stallard, 2005). In humid atmosphere or water conditions, hydrogen is absorbed by the film, followed by the formation of a graphitic sp^2 phase transfer layer (Stallard, 2005). The formation of this layer is known as graphitisation; the layer forms on the coating surface and is transferred onto the counterface which results in two graphitised layers in contact as shown in Figure 2-12, giving low friction (Holmberg et al., 2007). Graphitisation can be caused by friction-induced annealing, or through thermal and strain effects, which occur during sliding. The formation of the tribofilm can be affected by the load applied to the surface and the sliding speed of the counterface against the surface. It is said that when the DLC layer comes into sliding contact with another surface, wear particles are generated and accumulate in front of the contacting surface where they begin the formation of the graphitised transfer layer and tribofilm (Meletis et al., 1995; Grill, 1999; Holmberg et al., 2007; Olofsson et al., 2011).

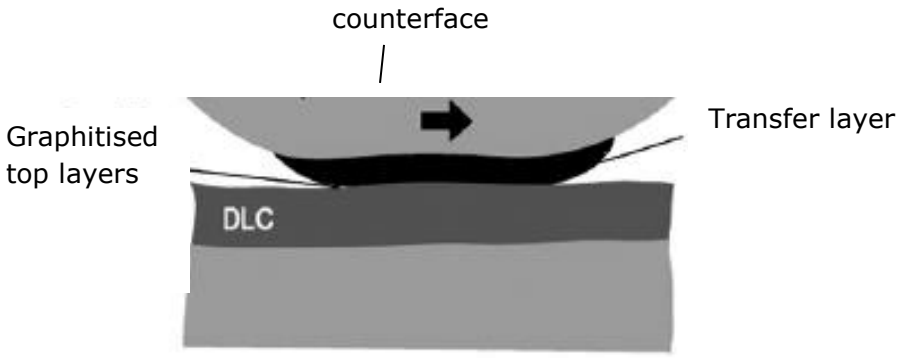


Figure 2-12 Graphitised transfer layer in sliding wear of DLC coatings (Holmberg et al., 2007).

Liu et al. (1996) investigated the effect of load and sliding speed on the friction and wear of 2 μm thick DLC films on SiC discs. Pin-on-disc tests were carried out against Ø 9.55 mm ZrO_2 balls at loads from <1 to 10 N and sliding speeds between 0.06 and 1.6 m s^{-1}. Tests were carried out at a relative humidity of ~35% and at room temperature. They found that at low load and velocity (1 N and 0.06 m s^{-1} respectively), steady state friction was not reached due to graphitisation not being able to occur. Therefore, the resulting friction coefficient of 0.18 was due to friction between the DLC and counterface, rather than graphite and the counterface. The wear rate of the disc was not measurable in these conditions; however the ZrO_2 ball exhibited the highest wear rate (10.1 x 10^{-9} mm^3 m^{-1} N^{-1}) out of all the tests. Tests carried out at the higher velocity (1.6 m s^{-1}) and 1 N load, showed a lower initial friction coefficient of 0.1 and an even lower steady state friction coefficient of 0.06. The wear rate of the disc and ball were measured to be 8.36 x 10^{-7} mm^3 m^{-1} N^{-1} and 3.56 x 10^{-9} mm^3 m^{-1} N^{-1} respectively. It was found that at lower loads and lower sliding speeds, the sliding distance required to reach steady state friction was increased, and therefore the wear rates of the discs and the ZrO_2 balls were increased. At 10 N load and 0.1 m s^{-1} sliding speed, steady state friction was reached after 9500 m, whereas, at the same load, with a 1.6 m s^{-1} sliding speed, steady state friction was reached after just 4300 m. The wear rates of the discs at 0.1 m s^{-1} and 1.6 m s^{-1} sliding speed, with 10 N load, were 2.48 and 1.99 x 10^{-7} mm^3 m^{-1} N^{-1}

respectively, and the ball wear rates were 1.82 and 0.56×10^{-9} mm^3 m^{-1} N^{-1} respectively. It was concluded that the decrease in wear rate and friction coefficient at increased load and velocity was due to the time taken for graphitisation to occur between the DLC coating and counterface.

2.4.4 Graphit-iC™ and Dymon-iC™ (Teer Coatings Ltd)

Since the development of diamond-like carbon (DLC), two hard carbon-based solid lubricant coatings, Graphit-iC and Dymon-iC, have been developed by Teer Coatings Ltd, the properties of which offer considerable benefits over traditional DLC coatings when it comes to low friction, high wear resistant applications (Field et al., 2004). Graphit-iC is a hydrogen-free amorphous carbon-chromium coating (a-C), whereas Dymon-iC is a hydrogenated amorphous carbon coating (a-C:H). Dymon-iC is deposited through a process called plasma enhanced chemical vapour deposition (PECVD) from a hydrocarbon precursor gas. The process also uses a closed field unbalanced magnetron sputter ion plating system (Stallard et al., 2004). The hardness of Dymon-iC can vary depending on the deposition parameters, but it is typically 12-18 GPa. The coating is an amorphous, metal free, hydrogenated carbon coating.

The wear rate and friction coefficient of Dymon-iC is increased severely when tested in water compared to testing in dry conditions due to its hydrogen content, whereas, Graphit-iC performs better when tested under water compared to being tested in dry conditions as explained in section 2.4.3. As this work investigates coatings for water lubricated conditions, Dymon-iC was not investigated in this research.

Graphit-iC coatings are deposited by closed field unbalanced magnetron sputter ion plating (CFUBMSIP) using carbon and chromium targets. A chromium layer is used to give good adhesion to the substrate, then a small amount of chromium (~5 at.%) is co-deposited with the carbon during the coating process. The wear rate of Graphit-iC depends on the counterface and testing environment. Field et al. (2004) investigated

the friction and wear properties of Graphit-iC deposited on an M42 substrate hardened to HRC 64±1 with a surface finish of Ra = 0.03 μm. Pin-on-disc tests were carried out in air and water lubricated conditions against a Ø 5 mm WC-6%Co ball. Graphit-iC exhibited wear rates between 4.3 and 2.1 x 10^{-17} m^3 N^{-1} m^{-1} for applied loads of 40 and 80 N respectively in dry conditions and 1.1 and 5.1 x 10^{-17} m^3 N^{-1} m^{-1} at loads of 10 and 40 N respectively in water lubricated conditions. The friction coefficient was said to be less than 0.1 in all tests. During pin-on-disc tests, it is also common to find a low initial friction; this is thought to be caused by the oxide layer on the surface of the coating. At the start of a pin-on-disc test, flash temperatures can occur resulting in softening of the surface oxides, with these softened surface oxides providing lubrication between the surface and the counterface. As the test continues, the contact area increases due to induced wear on the ball and disc; this lowers the flash temperatures and reduces the lubrication caused by of the oxide layer.

The hardness of Graphit-iC is dependent on the deposition parameters, but it can range from 15 GPa to over 40 GPa (Field et al., 2004). Graphit-iC has also been shown to have a high load-bearing capacity (>2.1 GPa). (The load bearing capacity of a material is its ability to maintain its integrity (without failure) under load (Wänstrand, 2000; Yang et al., 2000)). The structure of Graphit-iC is generally a dense amorphous structure with nano-crystalline graphitic regions within the amorphous carbon matrix (Field et al., 2004). Research has been carried out on the structure of Graphit-iC coatings and '*it can be stated that no significant amount of sp^3 bonding has been detected in the coatings and all the evidence indicates that the bonding is almost entirely sp^2*' (Field et al., 2004). Graphit-iC coatings are now used commercially to provide wear resistance and lubrication for systems such as fuel injection systems, gudgeon pins, cam followers, gears and bearings, tapping, cutting and machining systems (Field et al., 2004).

Other commercially available DLC coatings include a range of BALINIT® coatings by Oerlikon Balzers UK such as BALINIT® C (WC/C (a-C:H:W)). This is a hydrogenated DLC coating consisting of metal-carbon WC/C alternating layers (however, the

thickness of these layers is not specified) and an outermost W-containing hydrocarbon. BALINIT® C STAR (CrN + a-C:H:W) is a duplex coating consisting of alternating WC/C and CrN layers. Balzers also have a simple hydrogenated DLC coating BALINIT® DLC (a-C:H) and a hydrogenated DLC coating combining CrN BALINIT® DLC STAR (CrN + a-C:H) (Moorthy and Shaw, 2012a; Moorthy and Shaw, 2012b). The DLC coatings offered by Oerlikon Balzers UK are of hydrogenated form which in general perform less well than non-hydrogenated forms of DLC in water environments. As this research is investigating behaviour in water-wetted and corrosive environments, a decision was taken not to consider the BALINIT® range of coatings further (Stallard et al., 2004; Suresh Kannan and Ghosh, 2014).

2.4.5 DLC properties & surface roughness

It is known that DLC films closely mimic the original surface roughness of the substrate. Such coatings are said to have a surface roughness of around half that of the substrate onto which they are deposited (Singh et al., 2008), and therefore, when deposited on a rough substrate, the coating will have a rough surface finish.

Jiang and Arnell (2000) investigated the effect of substrate surface roughness on the friction and wear properties of DLC coatings deposited on M42 tool steel with surface finishes of: 0.01 μm Ra, 0.08 μm Ra, 0.24 μm Ra, 0.93 μm Ra and 1.15 μm Ra . Ball-on-disc tests were carried out in dry air against a Ø6.3 mm WC ball at sliding speeds of 50 mm s^{-1} at 20 and 40 N normal load. Due to the wear mechanisms of DLC coatings and the transfer layers that form during sliding wear (as explained in section 2.4.3), it was found that the frictional behaviour was not significantly affected by the roughness; however, the wear rate of the coatings was significantly increased as the substrate surface roughness increased. Above 0.93 μm Ra, the wear mechanism changed from adhesion to chip/flake formation and fragmentation of the coatings. This increase in wear rate was said to be attributed to an increase in contact pressure and an increase in lateral impact of the ball to the tops of the asperities.

Ohana et al. (2004) investigated the wear rate of pulsed-bias CVD DLC films against Ø4.76 mm AISI 304 steel and brass balls in water. Ball-on-disk tests were carried out at sliding speed 60 cycles min^{-1} (16 mm s^{-1}) with normal loads of 1.9, 9.4 and 15.1 N. Substrate surface roughnesses ranging from Ra = 1.4 to 740 nm were employed. The results showed that the friction coefficients of DLC coatings during sliding wear in water were not affected by the substrate surface roughness due to the tribolayer formed between the coating surface and the counterface as explained in section 2.4.3. However, an increase in specific wear rate on the counterface ball was seen with increasing substrate surface finish as shown in Figure 2-13; however, no specific explanation was offered for the increase in counterface wear rate with increasing substrate surface roughness.

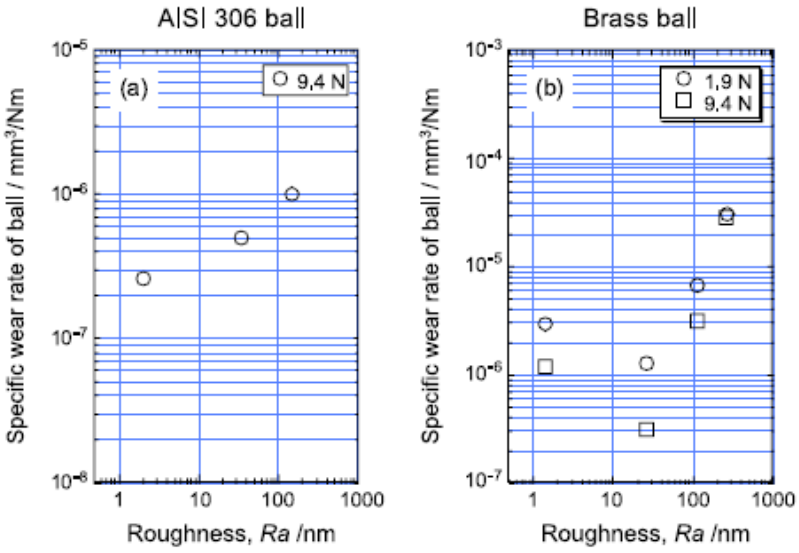


Figure 2-13 The specific wear rate of the counterface (a) AISI 306 ball (b) brass ball (Ohana et al., 2004)

2.4.6 Summary

Multilayering has been said to provide coatings with higher hardness, adhesion, wear resistance and corrosion resistance; however, conclusions about the efficacy of multilayering varies across the literature (Ries et al., 1997; Holmberg et al., 1998; Matthews, 2003; PalDey and Deevi, 2003; Mellor, 2006; Mendibide et al., 2006; Cabrera et al., 2011). Therefore, to investigate this effect, a multilayer system of IN625 and Cr was chosen with the intention of developing a coating with high scratch resistance and corrosion resistance (no previous research could be found for PVD of IN625).

Graphit-iC has been shown to have very low friction and high wear resistance in wet applications (Wiklund et al., 1999; Field et al., 2004) and CrN has been shown to have high hardness and wear resistance, but a higher coefficient of friction in most systems (Han et al., 2000a; Han et al., 2000b; Bayón et al., 2009; Costa et al., 2010). However, the field of research investigating the direct effect of multilayer architecture on coating properties is small and conclusions vary across the literature. Therefore, a multilayer system of CrN and Graphit-iC was chosen with the intention of developing a wear resistant coating with a low coefficient of friction. Dual layer coatings and coatings with different bilayer periods were selected to investigate the possible benefits of multilayering on the mechanical and corrosion properties of the selected coatings as suggested in the literature (Ries et al., 1997; Holmberg et al., 1998; Matthews, 2003; PalDey and Deevi, 2003; Mellor, 2006; Mendibide et al., 2006; Cabrera et al., 2011). Three substrates of different hardness were selected in order to investigate the effect of substrate hardness on the wear properties of coatings as well as multilayering and multilayer architecture.

Although studies exist investigating the effect of bilayer period on the properties of coatings (Creus et al., 1998; Cabrera et al., 2011), limited studies have been carried out regarding the effect of multilayer architecture on the mechanical properties of coatings when using a defined bilayer period. In light of this, a CrN/Graphit-iC

multilayer system was selected to investigate the effect of multilayer architecture on the mechanical properties of coatings when using different ratios of two materials in a multilayer system with a 100 nm bilayer period (termed λ100 nm). The study aims to investigate whether the possibility of tailoring coating properties through architectural design is feasible. λ100 nm was chosen as this was the thinnest bilayer period in which exact ratios of different material could be deposited with accuracy.

PVD coatings contain growth defects which limit the coatings corrosion resistance and mechanical properties (Liu et al., 2001; Liu et al., 2002; Merl et al., 2004). Limited studies have shown that multilayering, intermediate etching and using a finer surface finish substrate can result in and coating with a reduced defect density, an improved corrosion resistance and improved mechanical properties (Munemasa and Kumakiri, 1991; Liu et al., 1995; Jehn, 2000; Fenker et al., 2002; Maeng et al., 2006; Durst et al., 2008; Abusuilik and Inoue, 2013). However, conclusions vary across the literature and more research is needed in this field. In light of this, intermediate etching and an interrupted process were selected for investigation with the intention of developing a coating with high corrosion resistance as well as discovering whether the intermediate etching process or simply the interruption of the process, which occurs during an intermediate etch, disrupts growth defects. Substrates of three different surface roughnesses were selected to investigate the effect on the corrosion resistant properties of coatings.

3 Experimental Procedure

3.1 Introduction

This work aims to create coatings with a different range of properties for different applications. Those properties include wear, scratch and corrosion resistance. Table 3-1 illustrates the expected properties of the chosen coatings and architectures, therefore the choice of materials used throughout this work.

Coating	Expected properties
CrN	Durable
IN625	Corrosion resistant
IN625 + Cr	Corrosion & scratch resistant
CrN + Graphit-iC	Durable & low friction
IN625/Cr multilayers	Corrosion & scratch resistant
CrN/Graphit-iC multilayers	Durable & low friction

Table 3-1 Expected and intended properties of coatings deposited in this work

The IN625 and IN625/Cr multilayer coatings are intended to be corrosion and scratch resistant, the CrN/Graphit-iC multilayer coatings are intended to be durable and have low coefficient of friction. The effect of substrate hardness on the properties of the coatings is investigated as well as the coating materials, substrate surface roughness, deposition conditions and coating architecture (from here onwards the bilayer period of multilayer coatings will be referred to as lambda (λ)). It is known that PVD coatings contain growth defects which limit the performance of the coating, especially in corrosive environments. Interrupted deposition conditions and intermediate etching were investigated. The aim of interrupted deposition conditions and multilayering was to create coatings with tailored properties, as well as to block the corrosive agents' path to the substrate by disrupting defect growth.

3.2 Coating deposition

Coatings were deposited in three batches. In batch one, ten coatings were deposited: CrN, IN625, IN625 + Cr, CrN + Graphit-iC, CrN/Graphit-iC multilayers (λ20 nm, λ100 nm and λ600 nm) and IN625/Cr multilayers (λ20 nm, λ100 nm and λ600 nm). Each coating was deposited onto four substrates of different hardness, 304L (HV = 190 ± 5 kg f mm^{-2}), 440C (HV = 476 ± 7 kg f mm^{-2}), M42 (HV = 946 ± 12 kg f mm^{-2}) and mild steel (HV = 98 kg ± 10 kg f mm^{-2}).

In batch two, three coatings were deposited: IN625 and two IN625/Cr multilayers (λ100 nm and λ600 nm). The coatings were deposited on M42 substrates with a 1200 grit surface roughness and 440C substrates of varying surface roughnesses. The coatings deposited on a 1200 grit finish, 440C substrate, were also subjected to three different deposition conditions. These conditions included, standard conditions, in which the coating process was carried out in one stage. Interrupted process conditions, in which deposition was paused half way, then continued. Finally, intermediate etch conditions, in which the coating process was stopped half way through and an argon etch was carried out on the coating surface before deposition was continued.

In batch three, three multilayer coatings were deposited with the same bilayer period, however, different architectures were used: CrN/Graphit-iC λ100 nm (1:1, 1:3 and 3:1) as shown by the schematic in Figure 3-1.

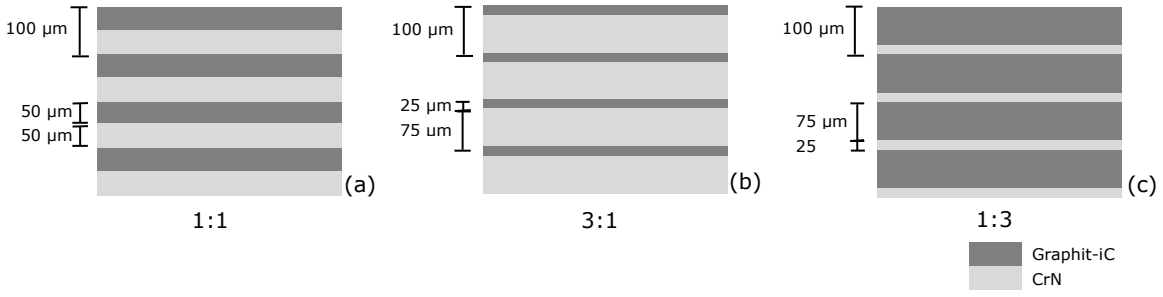


Figure 3-1 Schematic of CrN/Graphit-iC multilayer coatings with λ100 nm and multilayer ratios of (a) 1:1 (b) 3:1 and (c) 1:3

These coatings were used to investigate the effect of multilayer architecture on the friction and wear properties of coatings. Coatings were deposited on M42 and 440C substrates with a 1200 grit surface finish. Table 3-2 shows all PVD coatings deposited in this research.

Coating	Adhesion layer	Coating architecture	Investigation into substrate surface finish and deposition conditions
CrN	Cr	CrN	-
IN625	none	IN625	-
	Cr	IN625	varying surface finish
			Interrupted process
			Intermediate etch
IN625 + Cr	Cr	IN625 + Cr	-
CrN + Graphit-iC	Cr	CrN + Graphit-iC	-
IN625/Cr multilayers	Cr	IN625/Cr 20 nm bilayer period	varying surface finish
			Interrupted process
			Intermediate etch
	Cr	IN625/Cr 100 nm bilayer period	varying surface finish
			Interrupted process
			Intermediate etch
	Cr	IN625/Cr 600 nm bilayer period	-
CrN/Graphit-iC multilayers	Cr	CrN/Graphit-iC (Final layer Graphit-iC) 20 nm bilayer period	-
	Cr	CrN/Graphit-iC (Final layer Graphit-iC) 100 nm bilayer period (1:1, 1:3 & 3:1 architecture ratios)	-
	Cr	CrN/Graphit-iC (Final layer Graphit-iC) 600 nm bilayer period	-

Table 3-2 All PVD coatings and conditions requested

3.3 Substrate preparation

Prior to being surface finished; the, Ø35 mm, 440C substrates (from Unicorn Metals) were hardened to around 544 HV. This process involves pre-heating 3.2 mm thick discs at 775 ^{o}C for 25 minutes; the material is then heated to the austenitic region at 1030 ^{o}C for 25 minutes. After austenitization the discs were quenched in oil. The measured sample hardness after quenching was an average of 800 HV (61.5 HRC).

The discs were tempered at 555 °C for 1 hour resulting in a measured average hardness of HV = 476 ± 7 kg f mm^{-2} (49 HRC). After heat treatment the oxide layer was ground away by removing 0.1 mm from either side of the disc, the 440C discs were then ground to a rough workshop grind (343 ± 40 nm Ra), 1200 grit (78 ± 12 nm Ra) and 6µm polish (12 ± 4 nm Ra). The mild steel and 304L substrates were ground to 343 ± 40 nm Ra, the M42 was polished to 44 ± 4 nm Ra.

3.3.1 Optical emission spectroscopy

Optical emission spectroscopy is a method of chemical analysis. The process uses the intensity of light emitted from a spark. The spark heats up the sample and excites the atoms within the vapour produced. The excited atoms emit light at specific wavelengths depending on the atom. These frequencies are dispersed with a monochromator and the atoms are identified. Optical emission spectroscopy was used to determine the composition of the 304L, 440C and M42 steel substrates, shown in Table 3-3.

	wt %		
Element	**304L**	**440C**	**M42**
Fe	68.1 ± 0.30	80.0 ± 0.20	80.2 ± 0.80
C	0.10 ± 0.05	1.06 ± 0.01	0.82 ± 0.02
Si	0.55 ± 0.05	0.45 ± 0.02	0.32 ± 0.02
Mn	1.74 ± 0.06	0.33 ± 0.01	0.33 ± 0.01
P	<0.02	0.02 ± 0.01	<0.03
S	0.03 ± 0.01	0.01 ± 0.00	<0.02
Cr	18.9 ± 0.10	17.10 ± 0.10	5.10 ± 0.57
Mo	0.48 ± 0.02	0.44± 0.00	4.58 ± 0.19
Ni	9.25 ± 0.25	0.20 ± 0.01	0.49 ± 0.33
Al	<0.02	0.03 ± 0.08	<0.03
Co	0.11 ± 0.05	0.02 ± 0.00	<0.08
Cu	0.44 ± 0.03	0.04 ± 0.01	<0.10
Nb	<0.05	0.01 ± 0.00	0.04 ± 0.02
Ti	<0.01	<0.01	<0.01
V	<0.07	0.09 ± 0.01	1.85 ± 0.01
W	0.07 ± 0.01	<0.03	6.06 ± 0.11
Pb	<0.05	<0.05	<0.05

Table 3-3 Average chemical compositions of 304L, 440C and M42 steel substrates (wt %)

Measurements were carried out using an Oxford Instruments FOUNDRY-MASTER, a minimum of three measurements were taken for each material and an average was calculated.

3.3.2 Coating methods and parameters

Coatings were deposited at Teer Coatings Ltd. Prior to coating the samples are cleaned in acetone for 15 minutes in an ultrasonic bath then dried before being loaded into the coating system. Once in place, the parts are given a final wipe with a cleanroom cloth soaked in methanol to remove possible dust particles.

The system was pumped down for a minimum of an hour to 3 x 10^{-15} Torr to remove possible contaminants, then it is back filled with argon at 25 sccm; the deposition pressure used was around 2 x 10^{-3} Torr.

An ion clean of the surface was carried out for 20 minutes in which a negative voltage of 400 V was applied to the samples while a low current of around 0.2 A was applied to the targets with a voltage of around 250 V using a pulsed DC power supply set at a frequency of 250 kHz and pulse width of 500 ns. After cleaning, a chromium layer (typically 100 nm) is often deposited to improve the adhesion of the coating to the substrate, however for some coatings IN625 was used as an adhesion layer. The two different material targets were mounted opposite each other in the chamber to try to produce distinct multilayers using a target to substrate distance of around 150 mm. The rotation speed was varied to produce layer thicknesses of 10 nm and λ100 nm so that a Cr layer followed by an Inconel 625 layer can be deposited in a single rotation. Coatings with λ600 nm layers were deposited by ramping the targets (alternating the power) up and down at appropriate intervals. The substrate bias temperature is expected to be around 150^{0}C. Throughout this work, this deposition process will be referred to as 'standard deposition conditions'. Images of the sample holder and deposition chamber can be seen in Figure 3-2 and Figure 3-3 respectively.

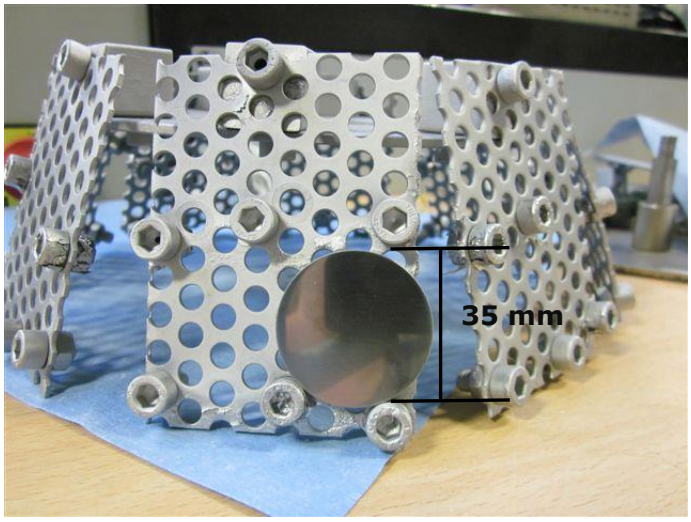


Figure 3-2 Sample and sample holder outside the deposition chamber

The interrupted process involved stopping the coating process half way through and allowing the coating to grow in the chamber before the coating process is completed. During this process the system is vented and the temperature dropped to around 50^0C.

For coatings produced with an intermediate etch stage, the coating process was stopped half way and an ion clean of the newly coated surface is carried out, for 5 minutes, before the coating process is continued. This process did not require venting of the system therefore, no drop in temperature occurred.

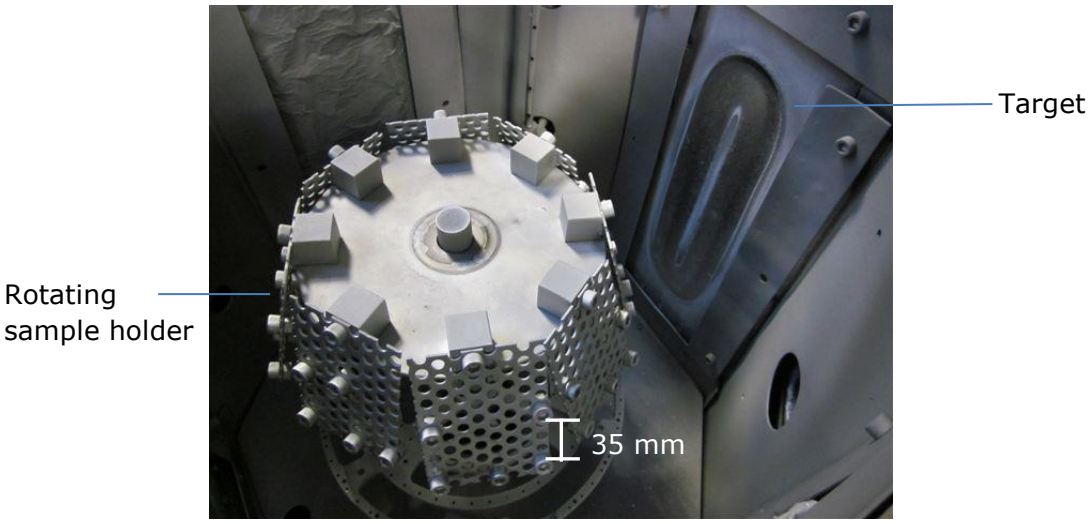


Figure 3-3 Inside the coating chamber

3.4 Sample preparation for characterisation

Samples were sectioned using a fluid lubricated Struers Accutom-5 and an Acu-Thin abrasive cut-off wheel which is designed to cause minimal structural damage to the specimens. The cutting wheel rotated at 3000 rpm with a specimen feed speed of between 0.008 and 0.01 mm s^{-1} and all cuts were made in the direction of the lay of the coating.

Samples were hot mounted in Conducto-Mount conductive phenolic mounting resin using a Metaserv automatic mounting press. Mounted samples were ground in water using increasing grades of Hermes waterproof SiC grit paper (240, 400, 800, and 1600). After grinding, the samples were polished in Struers DP-Lubricant blue using 6 µm then 1 µm diamond polishing paste. Finally the samples were finished with a Microcloth polishing cloth and amorphous colloidal silica polishing suspension from MasterMet™ 2.

Samples were washed using methanol between every grinding and polishing stage to reduce the possibility of large solid particles being transferred from the sample to the grit paper or polishing cloth, they were then dried using hot air to reduce the possibility of sample corrosion.

3.5 Characterisation of Materials

3.5.1 Scanning electron microscopy (SEM)

Microstructural analysis of the mounted cross-sectioned samples was carried out using a Phillips XL-30 FEG-ESEM. Images were taken using a 20 kV beam, 30 µm Hivac aperture position, 10 mm working distance and a spot size setting of 4. Images were taken using both secondary electron (SE) and back scattered electron (BSE) modes. When using secondary electron mode, steep surfaces and edges appear brighter than

flat surfaces due to the number of electrons reaching the detector; this gives images with a three-dimensional appearance.

When using back scattered electron mode, elements with a high atomic number backscatter electrons more than elements with a low atomic number, the former therefore appearing brighter and the latter appearing darker; this allows for materials with different chemical compositions to be differentiated from one another. The SEM was also used for energy dispersive x-ray spectroscopy (EDX) analysis, which is used to determine the chemical composition (excluding carbon) of selected areas of samples.

Focussed ion beam milling was carried out on coatings in order to view growth defect cross sections clearly without the risk of causing damage to the coating through cutting and polishing, it also allowed for a three dimensional view into the growth defect giving more details of the depth and shape of the defects. The machine used was a Zeiss Nvision40 Crossbeam equipped with an Everhart-Thornley secondary-electron detector; a Gemini column with in-lens and energy selective BSE detectors was utilised.

3.5.2 Energy Dispersive X-ray Spectroscopy (EDX)

Energy dispersive x-ray spectroscopy (EDX) is used to determine the composition of a selected area when using the SEM. When carrying out EDX a spot size setting of 3 and a process time of 5 seconds was used, the image setup was selected at a resolution of 1024 x 832 pixels.

3.5.3 X-ray Diffraction (XRD)

X-ray diffraction is a technique used to determine the atomic and molecular structure of a crystal. The sample is irradiated by a monochromatic X-ray beam which is then diffracted by crystalline atoms within the material. The angles and intensities of the

diffracted x-rays is related to the crystal structure via Bragg's law (Jafarian et al., 2015).

$n \lambda = 2 d \sin \theta$ **Eq.3.1**

where n is the order of diffraction, λ is the wavelength of the x-ray signal, d is the distance between atomic planes (d-spacing) of crystalline atoms and θ is the angle between the incident x-ray and the scattered x-ray.

X-ray diffraction (XRD) was carried out using a Bruker D8 Advance, using monochromatic Cu-Kα radiation with a wavelength (λ) of 1.5418 nm, emitted through a 0.6 mm slit. A glancing angle was used with a 2θ step size of 0.02°, and a two second dwell. The machine was operated at 40 kV and 35 mA using 2θ diffraction angles that varied between 10° and 100°.

Residual stress of coatings was measured using XRD. In crystalline materials, residual stress causes a change in interplanar spacing. XRD can be used to measure this by measuring the d-spacing using the $\sin^2\psi$ technique. In this technique a diffraction peak is chosen at the high range of 2θ angles. The workpiece is tilted at different angles and the d-spacing of crystal planes is measured at each different position. The residual stress can then be calculated using Eq 3.2 (Fitzpatrick et al., 2005; Jafarian et al., 2015).

$$\sigma = \frac{\mathrm{E}}{(1+\upsilon)\sin^2\psi}\left[\frac{d_\Psi - d_n}{d_n}\right] \qquad \textbf{Eq.3.2}$$

where σ is the residual stress, E is Young's modulus, υ is Poisson's ratio, d_n is the d-spacing of crystal planes reflecting at normal incidence under stress and d_ψ is the d-spacing of stressed crystal planes in the ψ direction (Cullity, 1956; Fitzpatrick et al., 2005; Jafarian et al., 2015). Using the $\sin^2\psi$ method, a number of measurements were taken at different ψ tilts. The inter-planar spacing (d) was measured for each tilt

angle and plotted against $\sin^2\psi$. Equation 3.2 can then be simplified to equation 3.3 (Prevéy, 1986).

$$\sigma = \left(\frac{\mathrm{E}}{(1+\upsilon)} \right) \frac{m}{d_{\mathrm{n}}} \quad \textbf{Eq.3.3}$$

Where m is the gradient of the d vs. $\sin^2\psi$ plot. This method does not require the unstressed plane spacing d_0 and therefore, is non-destructive as it does not require cutting of the sample to gain a stress-free sample (Cullity, 1956).

Residual stress measurements were carried out with XRD using a Bruker D8 Discover. Before residual stress measurements were carried out, a phase analyses was performed on the coating to determine which phases are present and to determine the 2θ angles at which the analysis can be carried out. A monochromatic Cu-Kα radiation with a wavelength (λ) of 1.5418 nm through a 0.6 mm slit was used. Measurements were taken from 0° to 60° (2θ) in 7 steps and at rotation angles of 0° and 90° from parallel to the coating surface. A step time of 45 s was used and a 2θ step size of 0.1°.

3.5.4 Transmission electron microscopy (TEM)

Transmission electron microscopy (TEM) is used to examine samples at a very high resolution. An electron beam is passed through a thin (typically 100 nm) sample. Direct transmitted or scattered electrons can be used for imaging. When using transmitted electrons for imaging, the portion of the beam that is transmitted through the sample is used. A portion of the beam is scattered due to the crystal structure of the sample which results in a contrast from the crystal structure. This method forms what is known as a bright field image. When using scattered electrons for imaging a dark field image is formed. This method can be used to produce selected area electron diffraction (SAED) patterns, which provides information about the crystal structure of

the sample. The angle of diffraction (θ) in SAED is very small due to the very small wavelength of high energy electrons in comparison with the wavelength of X-rays. Since the angle θ is very small, an approximation of sin θ ≈ θ can be made, therefore the Bragg equation can be simplified to:

$n\lambda = 2d\theta$ **Eq.3.4**

The geometry of the TEM setup dictates that:

$\tan 2\theta = \frac{R_{hkl}}{L}$ **Eq.3.5**

where L is the effective distance between the sample and the recording plane, known as the camera length. Given that tan θ ≈ θ, the resulting equation can be derived:

$n\lambda L = R_{hkl}d$ **Eq.3.6**

where λL is known as the camera constant and is obtained using a reference aluminium sample of known lattice parameters under the same electron-optic conditions and R_{hkl} is the radius of the diffraction ring. Once the camera constant is calculated using the reference sample, the crystal plane spacings of an unknown material can be calculated and associated diffraction spots can be indexed (Wen et al., 2000; Fry, 2013).

TEM analysis was performed using a JEOL 2100F transmission electron microscope at 200 kV. A section was milled out of the samples using a focussed ion beam, FEI Quanta 3D, operated at 15 kV. FIB milling was operated at 30 kV with a milling current between 5 nA to around 0.1 nA. A final mill was carried out at 10 kV with a milling current of around 16 pA.

The ion beam was then used to thin the sample, to around 200 nm in areas, however, regions of varying thickness were produced to gain different images of the coatings.

The lift-outs were then mounted onto Omnniprobe copper lift out grids, in order to allow TEM imaging of the cross-section of the coatings. A Gatan Orious camera was used for conventional and high resolution imaging, the Gatan scanning transmission electron microscopy (STEM) detector was used for bright field and dark field imaging. High angle annular dark field (HAADF) images were taken using the JEOL STEM detector which provide elemental (Z-) contrast.

3.6 Tribological Behaviour

3.6.1 Wear testing

The wear tests carried out in this work were pin-on-disc tests. Tests were run in de-ionised water. Details of the pin-on-disc rig and its dimensions can be seen in Figure 3-4 and Figure 3-5 respectively. The main load arm is mounted on a bearing (pivot), horizontal restraints are provided by the load post where the LVDT is positioned. The arm is balanced using the counterweight to ensure that the applied downward force is only contributed to by the load applied to the load arm by the hanging weights.

Pin-on-disc tests were carried out on the Ø35 mm stainless steel (304L and 440C) and Ø 30mm M42 coated discs at The University of Nottingham. Tests were performed at a sliding speed of 0.05 m s^{-1} for 5700 revolutions, using a Ø3/8" WC-6%Co ball (HV = 1700 ± 10 kg f mm^{-2}), from Spheric-Trafalgar Ltd. This ball was chosen to investigate how the coatings behave in aggressive wear conditions. A set of tests were also carried out on coatings deposited on 440C substrates against a Ø3/8" Stellite 20 balls (HV = 740 ± 10 kg f mm^{-2}), from Dejay Distribution.

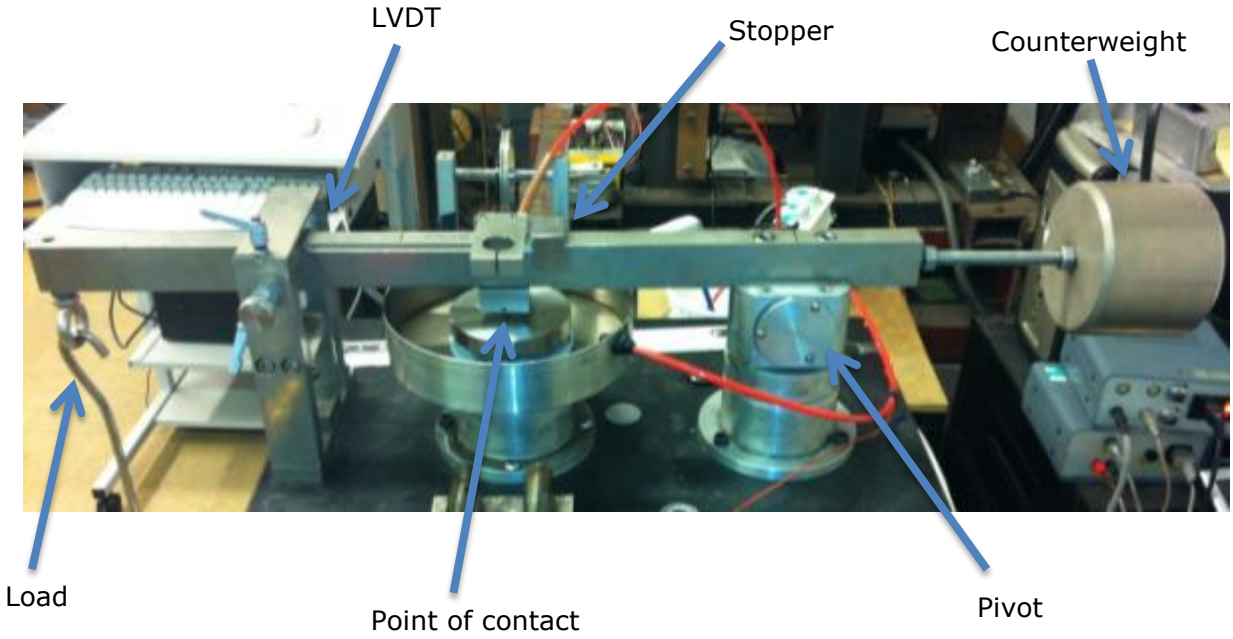


Figure 3-4 Photograph of the wear rig

The Stellite 20 balls were chosen with the aim of creating a less aggressive wear environment compared to the WC-6%Co balls which, in turn, would allow a more detailed investigation into the frictional behaviour of the coatings. The composition of the Stellite 20 balls can be seen in Table 3-4.

Element	wt %
Co	Balance
Ni	2.50 max.
Fe	2.50 max.
C	2.45
Cr	33.00
Mn	1.00
Si	1.00
W	17.50

Table 3-4 Chemical composition of Stellite 20 balls (wt %)

The tests were run in de-ionised water with a constant stream flowing onto the point of contact throughout the test. Prior to testing, the samples were washed using methanol to remove any debris or surface contamination that could affect the results

of the wear test and profilometry was used to measure the surface roughness of the coated samples by measuring the average Ra value across the surface.

By changing the position of the ball, multiple wear tests can be carried out on the same sample using different track diameters on the discs. When using a different track diameter, the rotational velocity of the disc was changed to preserve the sliding velocity at the contact. The number of revolutions determined the number of passes the counterbody ball made across any point on the wear track and this was maintained at 5700 revolutions. As each point along the wear track underwent the same number of passes, regardless of track diameter, the measurements of wear depth on the coatings can be compared across different loads and track diameters, however, the ball is subject to different sliding distances at different track diameters, therefore, the specific wear rate was used to compare the wear of the balls.

Track diameters of 10 mm and 14 mm were generally utilised for loads of 40 and 10 N respectively. When using a Ø10 mm wear track, the tests were run for one hour in order to achieve 5700 revolutions; when using a Ø14 mm wear track, the tests were run for one hour and twenty four minutes in order to achieve 5700 revolutions. A schematic of the wear rig is presented in Figure 3-5.

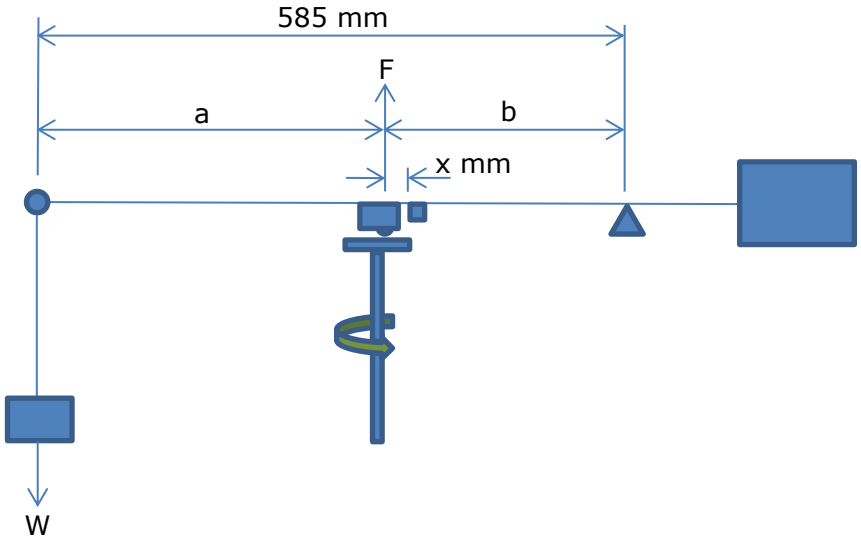


Figure 3-5 Dimensions of the wear rig

To ensure that the counterface ball is positioned reproducibly, the ball is held in a holder which is positioned at variable distances from a fixed plane on the rig (the stopper) using machined steel blocks to fix the distances. Using equilibrium of forces the load (W) is calculated in order to produce the required force (F) at the point of contact using the following equations:

Moment = Force x Distance **Eq.3.7**

⇨ W x (a+b) = F x (b) **Eq.3.8**

$$W = \frac{F \times (b)}{(a+b)} \quad \textbf{Eq.3.9}$$

For a Ø14 mm wear track: a = 347 mm, b = 238 mm. The chosen force at the point of contact for this diameter wear track is 10 N (1.02 kg) therefore the load that needs to be applied is $W = \frac{1.02 \times 238}{585}$ = 0.41 kg.

For a Ø10 mm wear track: a = 350 mm, b = 235 mm. The chosen force at the point of contact for this diameter wear track is 40N (4.08 kg) therefore the load that needs to be applied is $W = \frac{4.08 \times 235}{585}$ = 1.64 kg.

A wear test is run on each sample at 10 mm diameter with a rotational speed of 95 rpm and an applied load of 40 N and at 14 mm diameter with a rotational speed of 68 rpm and an applied load of 10 N. During the test, the friction is measured using an LVDT connected to LabView software (from Cyber-Sol); this is used to measure and record the readings from the LVDT, these results are then converted from voltage into a lateral force and then into friction coefficient.

Prior to testing, for each diameter position, the LVDT and rig was calibrated, a load was applied perpendicular to the arm in stages. Four approximately 1 kg weights A, B, C and D were weighed to measure their exact mass. Starting with no load on the arm, with the arm balanced using the counterweight, the output voltage from the LVDT was

continually recorded, and then the weights A, B, C and D were added, in order, one after another and then removed in order D, C, B then A. This is done twice; a plot of applied load versus measured voltage is made, the gradient of which is employed as the system response, *k*. In a test, the voltage measured when the disc is stationary (V_o) is subtracted from the measured voltage at any point during the test (V); this is converted to a friction coefficient (μ) using equation 3.10.

$$\mu = \frac{(V - V_o)}{(k\,W)} \qquad \textbf{Eq. 3.10}$$

where W is the applied load.

3.6.2 Scratch testing

Scratch testing was carried out on samples with an M42 substrate at Teer Coatings using an ST3001 scratch tester with a Rockwell Diamond indenter tip radius 0.2 mm, the scratch test was used to determine the coating adhesion. During tests the computer control facility records the friction force, the applied load and the acoustic emission intensity.

Tests were carried out at a linear velocity of 10 mm min^{-1}, a loading rate of 100 N min^{-1} is used with a starting load of 10 and final load of 100 N, or until maximum friction of 30 N is reached, if the coating reaches total failure, defined by total delamination from the substrate, before the final load or maximum friction force of 30 N is reached, then the test was stopped.

The load at which failure occurs was calculated using optical microscopy by noting the distance along the track at which the event has occurred and relating that to the proportion of load that had been applied at that position along the track. As tests were run at a linear velocity of 10 mm min^{-1} and a loading rate of 100 N min^{-1}, the load of failure along the wear track was calculated using the failure position and conversion of 1 mm = 10 N.

3.6.3 Hardness testing

Rockwell Hardness testing was carried out using a HR-523 Series 810-Rockwell Type Hardness Testing Machine. This machine uses real time electronic test force control for accurate loading; this eliminates the possibility of overshooting the load force. This hardness testing machine was used to measure the hardness of the heat treated 440C stainless steel after quenching and after tempering as it allowed quick and accurate hardness measurements to be taken between heat treatment processes, an average of 4 measurements were taken for each reading.

Micro-hardness testing was carried out using a Leco M-400 microindentation hardness tester with a diamond tipped Vickers indenter. Microindentation was carried out on the mounted and polished cross-section of 440C stainless steel after heat treatment; indentations were made at 200 g load and were measured optically using a viewfinder with a sliding gauge. An average of 10 measurements was taken starting at 40 μm from the edge of the surface to be coated. The distance between measurements was increased as the centre of the sample was neared starting at 100 μm then increasing to 200 μm then 400 μm.

The hardness and indentation modulus of the coatings was measured at Teer Coatings using a Fischerscope HM2000C hardness tester equipped with a Vickers indenter. An applied load of 50 mN load was used and a minimum of three measurements were carried out on the top surface of coatings. To establish the Vickers hardness of coatings, the indentation hardness is measured using equation 3.11 (Oliver and Pharr, 2004).

$$H_{IT} = \frac{F_{max}}{A_p} \qquad \textbf{Eq. 3.11}$$

Where F_{max} is the maximum applied load and A_p is the projected area of contact. From this the Vickers hardness can be calculated using the relation $H_v = 0.0945\ H_{it}$.

The indentation modulus of the coatings was determined using the load-penetration curves obtained with a Vickers indenter. When determining the indentation modulus

from indentation experiments, the elasticity of the indenter must also be accounted for. This is done by determining a reduced elastic modulus (E_r) as shown in equation 3.12 (Oliver and Pharr, 2004).

$$E_r = \frac{\sqrt{\pi}}{2\beta}\frac{S}{\sqrt{A_P}} \quad \textbf{Eq. 3.12}$$

Where β is a constant that depends on the geometry of the indenter and S is the stiffness of the sample. The indentation modulus (E_{IT}) can then be calculated using equation 3.13 (Oliver and Pharr, 2004).

$$\frac{1}{E_r} = \frac{(1-\nu^2)}{E_{IT}} + \frac{(1-\nu_i^2)}{E_i} \quad \textbf{Eq. 3.13}$$

Where ν is the Poisson's ratio of the test material and E_i and ν_I are the elastic modulus and Poisson's ratio of the indenter respectively.

3.6.4 Corrosion testing

3.6.4.1 Salt spray testing

Salt spray tests were used to assess the porosity and corrosion barrier performance of the coatings. Tests were carried out using a salt spray cabinet, model SF/450 from CW Specialist Equipment Ltd. Initial tests were carried out on 25 x 25 mm square, 2 mm thick coated mild steel samples ground to around 0.2 Ra, later tests were carried out on quarter sections of Ø35 mm, 3 mm thick coated 440C stainless steel. Prior to testing, the coated samples were washed using methanol to remove any large particles or surface contamination.

The backs and sides of the samples were masked using a waterproof red stopping off lacquer (from MacDermid) to prevent direct attack of the mild steel substrates and ensure that the salt solution only came into contact with the coated surface.

A 5 wt% salt solution was made by dissolving 250 g of NaCl in 4750 g of de-ionised water. The salt solution was maintained at a temperature of 35 °C during the test. Each test was run for 18 to 20 hours in 1 hour intervals. After every hour the samples

were washed of any excess salt or corrosion product, dried then photographed. Image analysis of the exposed surface was carried out using imageJ software.

3.6.4.2 Potentiodynamic testing

The corrosion behaviour of uncoated and PVD coated 440C was studied using potentiodynamic testing. Samples were cut to 10 x 10 mm and mounted in Dap Mount Blue hot mounting resin from MetPrep Ltd. Using a 2.5 mm drill followed by M3 tap, a hole was created in the back of the mount reaching the back of the sample. The sample was then cleaned and a copper rod was inserted into the back until it made connection with the back of the sample, the connection was tested using a voltmeter. Following this the copper rod and sample were coated in lacquer, coating only the edges of the sample face, leaving as much of the face exposed as possible. The exposed area was then measured for use in calculating current density. A schematic of the potentiodynamic equipment is shown in Figure 3-6.

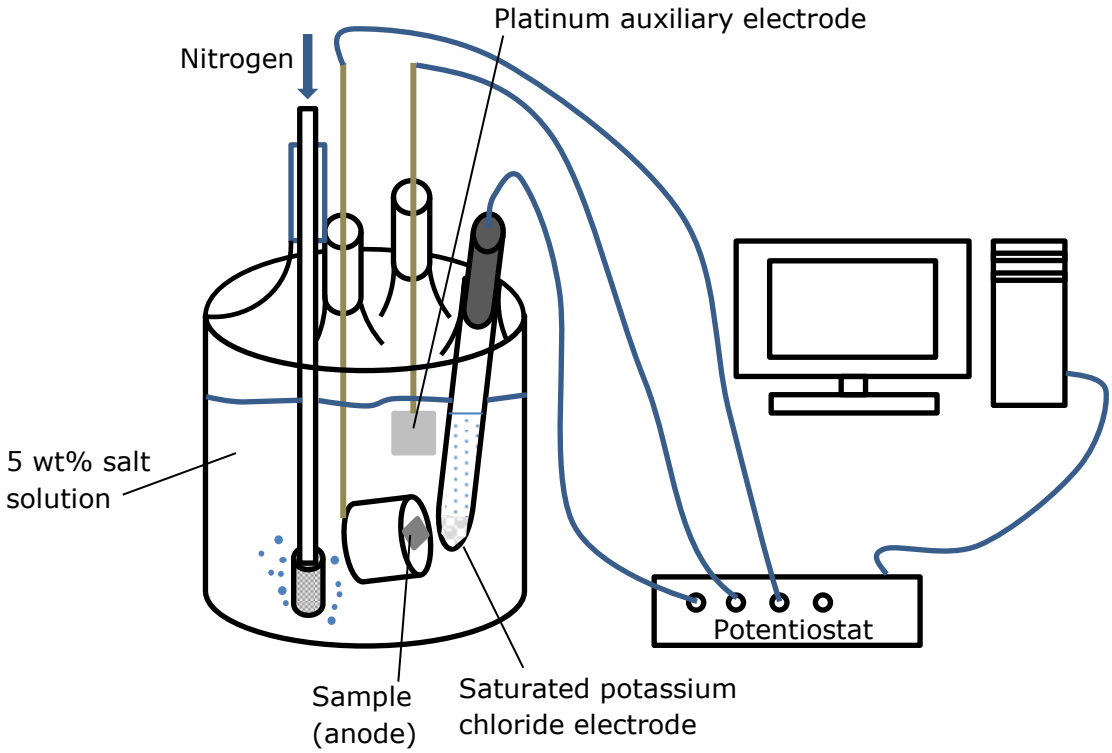


Figure 3-6 Potentiodynamic testing setup

Tests were carried out using a VoltaLab PGZ 100 Potentiostat and Voltamaster 4 software. A platinum auxiliary electrode was used and a saturated potassium chloride electrode was used as a reference. The test was carried out in 5 wt% salt solution made by dissolving 52.6 g of NaCl in 1000 g of de-ionised water. All equipment was cleaned and rinsed in deionised water before testing.

The system was deoxygenated by pumping nitrogen for 1 hour. After an hour the nitrogen was turned off, the temperature of the solution was measured and an open circuit potential scan was run. A potential linear voltage scan was then run between -250 mV below OCP and 1500 mV at a scan rate of 0.5 mV s^{-1} and a sampling rate of 1 measurement per second.

The corrosion current (I_{corr}) was calculated from the Tafel plot, as shown in Figure 3-7, using the Tafel method according to the 1st Stern equation (Stern and Geary, 1957).

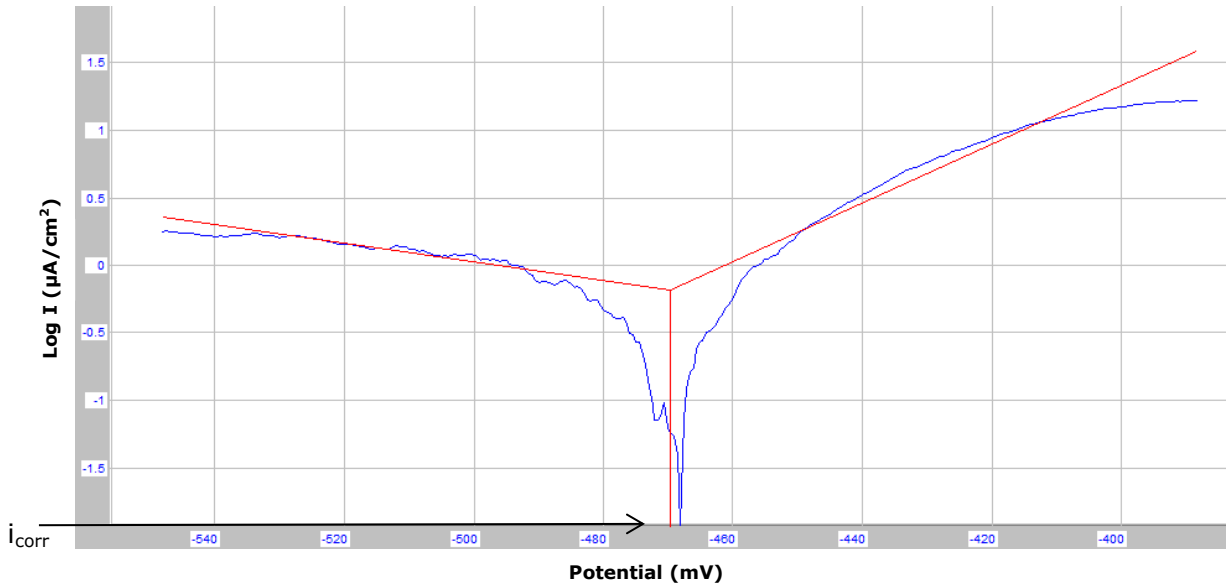


Figure 3-7 Tafel plot of IN625/Cr multilayer (λ100 nm) coating on a 1200 grit substrate

Calculations of i_{corr} were carried out using Voltamaster 4 software. The parameters of smoothing, calculation zone and segment were varied until a line of best fit was

reached. Corrosion potential (E_{corr}) and polarisation resistance (R_P) were measured by plotting potential Vs current density and drawing a line of best fit as shown in Figure 3-8.

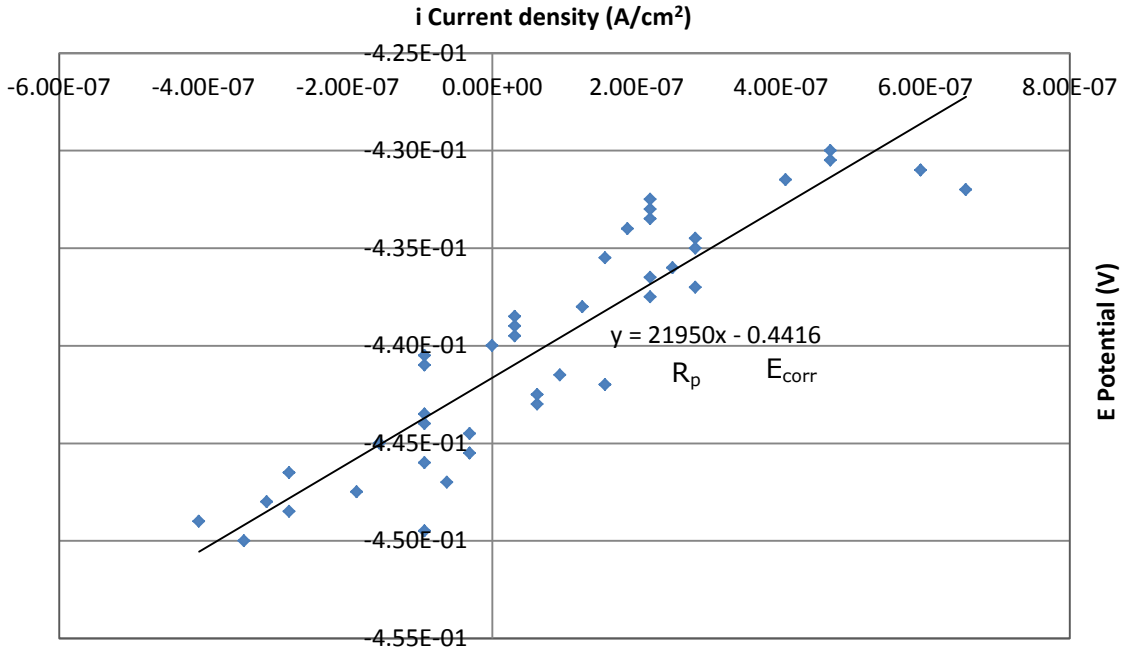


Figure 3-8 Potential Vs current density plot for IN625/Cr multilayer (λ100 nm) coating on a polished substrate

E_{corr} was calculated at the point of zero current density (i=0) and the polarisation resistance was measured by the gradient of the line $\left(\frac{\Delta E}{\Delta i}\right)$.

3.7 Analysis of Tested Samples

3.7.1 Profilometry

The wear scar dimensions on the disc specimens were measured using a Mitutoyo Surftest SV-600 profilometer, with a resolution of 0.001 µm. The profilometry was carried out over a length of 5 mm and the areas of the wear scars were calculated using 'Area Under A Curve' software (from Cyber-Sol). Four measurements were taken, 90° apart, for each wear scar as shown in Figure 3-9.

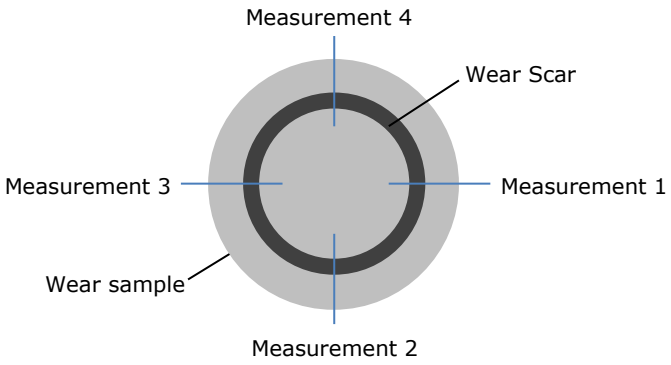


Figure 3-9 Schematic of profilometry measurements on samples after sliding wear tests

To measure the surface roughness the μm Ra value was measured, this is the average distance between the surface and the mean line looking at all the points along the profile.

3D profilometry was carried out using a Bruker ContourGT-I 3D Optical Microscope, with a resolution of 0.001 nm, and Vision64 software. Ra values were measured using a 20x magnification. Three measurements were taken at different positions on the surface and an average was taken.

3.7.2 Wear scar measurements

The four sets of profilometry results are loaded into 'Area Under a Curve' software and the wear scar area is selected as shown in Figure 3-10.

An average was taken of the 4 readings to give an average area of the wear scar, this was multiplied by the circumference of the wear scar to give the volume (V), the specific wear rate is calculated by dividing the volume of the wear scar by the load (L) multiplied by the sliding distance (d).

$$Specific\ Wear\ Rate = \frac{V}{L \times d} \qquad \textbf{Eq. 3.14}$$

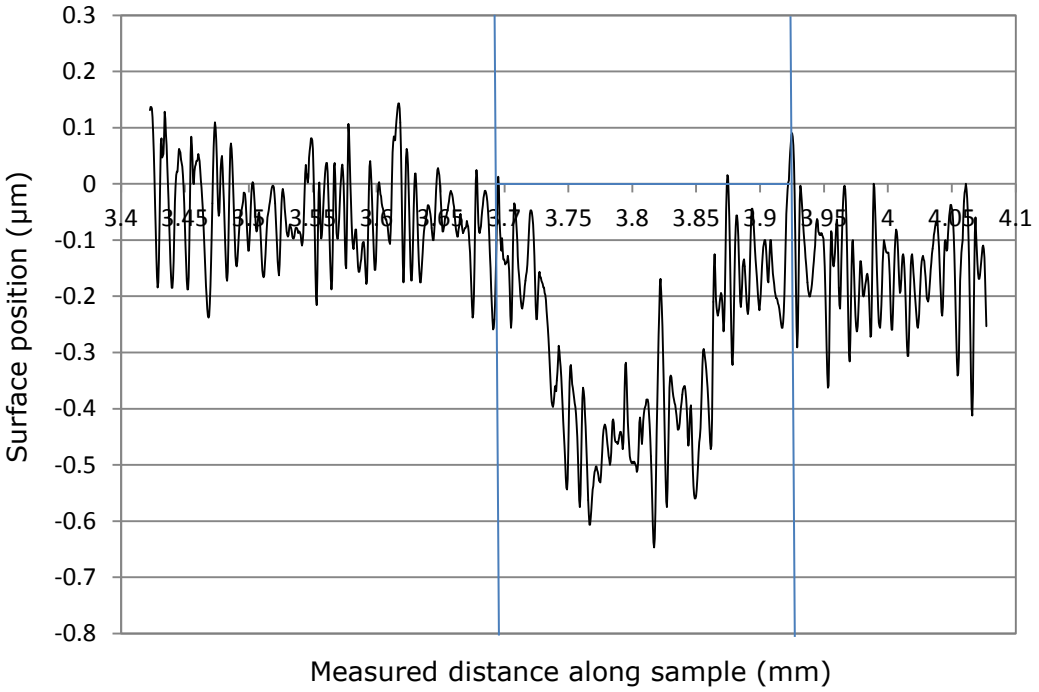
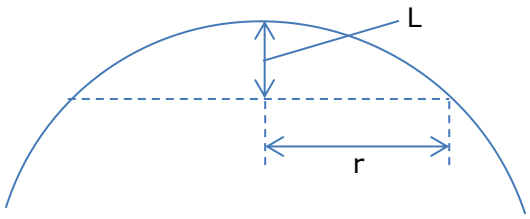


Figure 3-10 Profilometry curve of a wear scar

3.7.3 Ball wear scar measurements

The wear tests were carried out against a Ø3/8" WC-6%Co ball; this undergoes wear during the test which needs to be measured. The ball wear scars were observed using a Nikon FX-35 optical microscope with an attached Microflex UFX-II camera. The diameters of the wear scars on the balls were measured and then used to calculate the wear volumes of the balls (assuming that the wear scar is a pure spherical cap), this is then used to calculate the specific wear rate of the ball using the following equations.



R = the radius of the ball

r = the radius of the wear scar on the ball

L = R - $\sqrt{R^2 - r^2}$ **Eq.3.15**

Cap volume (V_c) = $\pi L^2(R - \frac{L}{3})$ **Eq.3.16**

Sliding distance (d) = Circumference x number of revolutions

$$Specific\ Wear\ Rate\ \left(\frac{m^3}{Nm}\right) = \frac{V_c}{L \times d}$$ **Eq. 3.17**

Where L is the applied load.

3.7.4 Image analysis

Image analysis was carried out on samples after salt spray corrosion testing. A clear, well focussed image, with no shadows, was taken with a digital camera of the corroded sample face which was then loaded in to ImageJ software and the area of the face that is exposed was selected by cropping the image. The image threshold was adjusted by changing the hue, contrast and brightness until only the corroded areas are selected. The adjustments depend on the coating colour and the brightness of the photo, these particles were then analysed giving the percentage of corroded area on the exposed face.

4 Results

4.1 Introduction

Throughout this work, three batches of coatings were produced by an industrial supplier. A description of all coatings and thicknesses can be seen in Table 4-1 along with their relevant batch numbers; the thicknesses were measured from cross-sections using SEM.

Coating	Adhesion layer	Coating architecture	Conditions	Coating thickness (µm)
CrN	0.3 µm Cr	CrN	-	3.0 ± 0.1
IN625	none	IN625	-	4.0 ± 0.1
	0.3 µmCr	IN625	varying surface finish	4.0 ± 0.1
			Interrupted process	5.0 ± 0.1
			Intermediate etch	5.5 ± 0.1
IN625 + Cr	0.3 µm Cr	3.7 µm IN625 + 3.0 µm Cr	-	7.0 ± 0.1
CrN + Graphit-iC	0.3 µm Cr	2.3 µm CrN + 2.4 µm Graphit-iC	-	5.0 ± 0.1
IN625/Cr multilayers	0.3 µm Cr	IN625/Cr 20 nm bilayer period	varying surface finish	4.0 ± 0.5
			Interrupted process	5.0 ± 0.1
			Intermediate etch	4.5 ± 0.1
	0.3 µm Cr	IN625/Cr 100 nm bilayer period	varying surface finish	4.0 ± 0.5
			Interrupted process	5.0 ± 0.1
			Intermediate etch	4.5 ± 0.1
	0.3 µm Cr	IN625/Cr 600 nm bilayer period	-	4.0 ± 0.1
CrN/Graphit-iC multilayers	0.3 µm Cr	CrN/Graphit-iC (Final layer Graphit-iC) 20 nm bilayer period	-	4.0 ± 0.1
	0.3 µm Cr	CrN/Graphit-iC (Final layer Graphit-iC) 100 nm bilayer period (1:1, 1:3 & 3:1 architecture ratios)	-	4.5 ± 0.1
			1:1	4.0 ± 0.1
			1:3	3.7 ± 0.1
			3:1	5.0 ± 0.1
	0.3 µm Cr	CrN/Graphit-iC (Final layer Graphit-iC) 600 nm bilayer period	-	4.0 ± 0.1

Table 4-1 All PVD coatings deposited in this research and their measured thicknesses

In batch 1, 10 coatings were produced, including two separate groups of multilayers aimed at producing coatings with different target properties. These are separated into (i) durable and low friction coatings (CrN/Graphit-iC); (ii) corrosion and scratch resistant coatings (IN625/Cr). Following this, a 2nd batch of coatings aimed at being corrosion and scratch resistant were produced (IN625/Cr) in order to investigate the effects of substrate surface roughness and deposition conditions on the coating properties. A 3rd batch of coatings was later deposited to allow investigation of the

effect of multilayer architecture on the wear and friction properties of coatings intended to be durable and low friction (CrN/Graphit-iC). Coatings deposited in different batches were manufactured under nominally identical conditions; however, some variation was seen in the mechanical properties of coatings (see appendix). Therefore, care was taken in assessing the validity of any comparisons of results from coatings deposited in different batches.

4.2 Mechanical and Tribological Properties of Single and Multilayered PVD Coatings

This section presents the structural characterization, mechanical and tribological properties of CrN, CrN + Graphit-iC and CrN/Graphit-iC multilayer PVD coatings. This section of the research aims to investigate whether the tribological and mechanical properties of coatings can be tailored through coating design as well as other factors that could affect coating behaviour such as multilayering, substrate hardness, multilayer architecture and counterface ball type.

4.2.1 Coating microstructure

Scanning electron microscopy and X-ray diffraction were employed to characterise the structure of the coatings. Figure 4-1 shows a cross-section of a CrN/Graphit-iC multilayer (λ600 nm) coating on a mild steel substrate. The cross section (Figure 4-1) shows a chromium adhesion layer and the coating multilayers, clearly identified in backscattered imaging due to their differences in mean atomic number. The Graphit-iC layers were visibly much darker than the CrN layers and the chromium adhesion layer. Not all coatings in this work were deposited with an adhesion layer; a summary of all coatings deposited and their adhesion layers can be seen in Table 4-1. Cross sections of the CrN, CrN + Graphit-iC and CrN/Graphit-iC multilayer (λ100 nm & λ20 nm) coatings are shown in Figure 4-2.

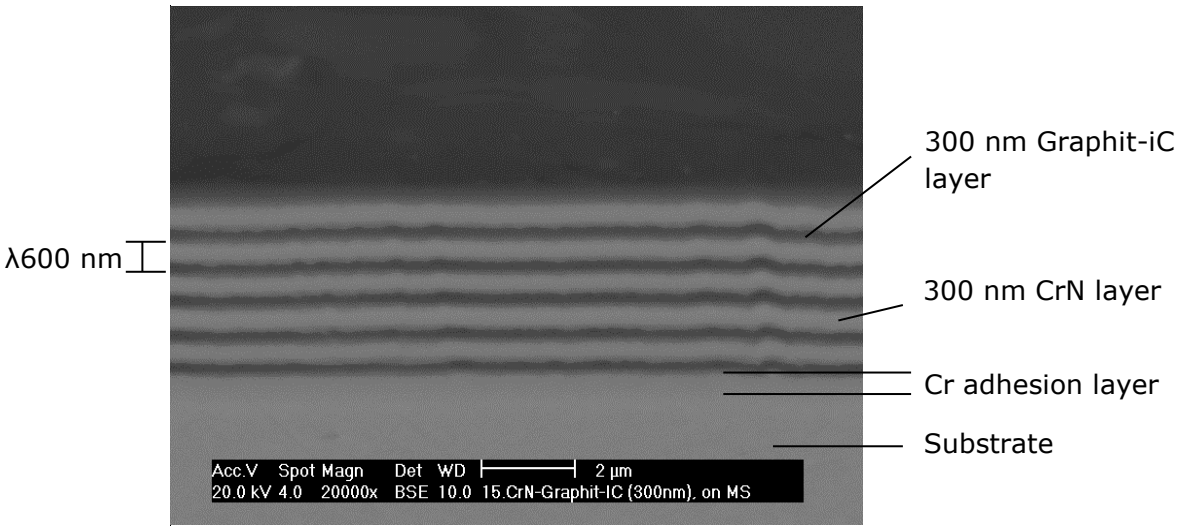


Figure 4-1 SEM micrograph of a CrN/Graphit-iC (λ600 nm) coating cross-section on a mild steel substrate

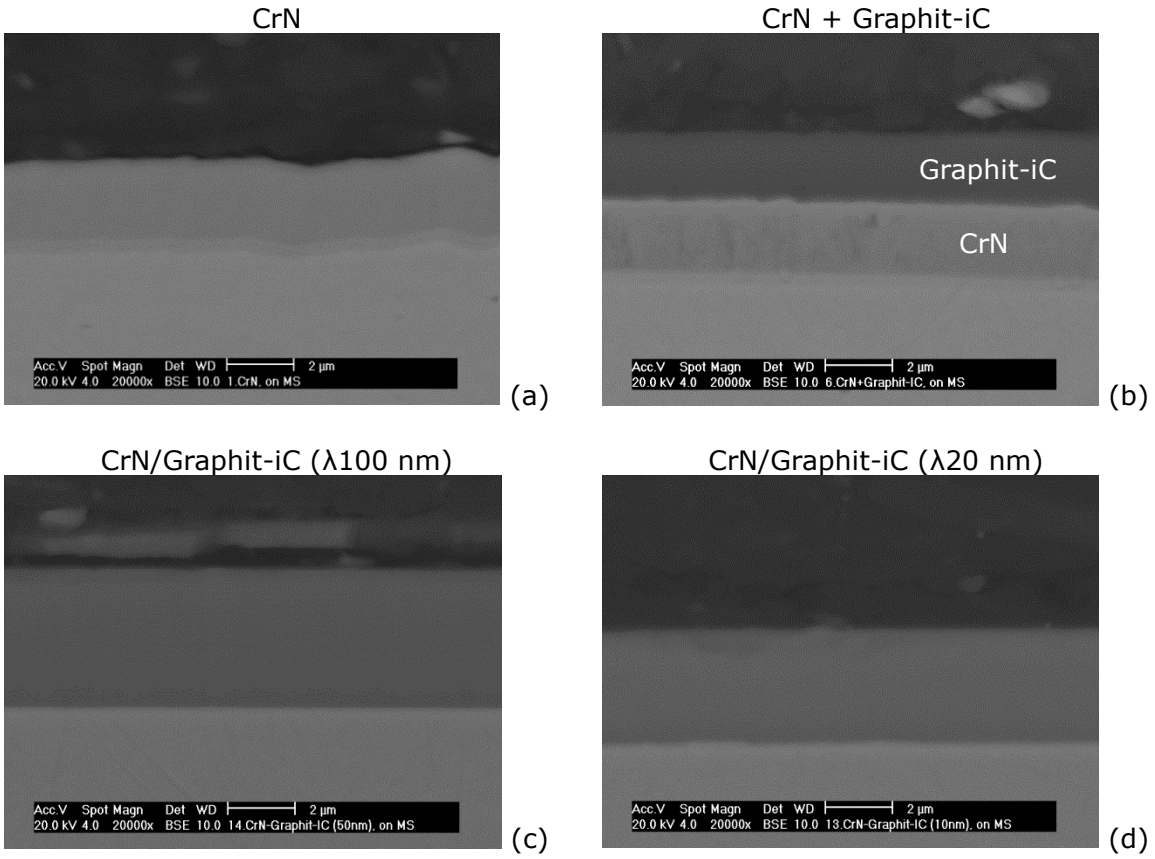


Figure 4-2 Cross-sectional SEM micrographs of (a) CrN (b) CrN + Graphit-iC (c) CrN/Graphit-iC multilayer (λ100 nm) (d) CrN/Graphit-iC multilayer (λ20 nm) on mild steel substrates

For the CrN coating (Figure 4-2 (a)), the chromium adhesion layer was clearly visible.

Cross sectional images of the CrN/Graphit-iC multilayer (λ100 nm & λ20 nm) coatings

(Figure 4-2 (c & d)), the individual layers are not visible in the images presented due to the magnification. The two layers in the CrN + Graphit-iC coating were clearly visible (Figure 4-2 (b)). Diffraction patterns of the coatings can be seen in Figure 4-3.

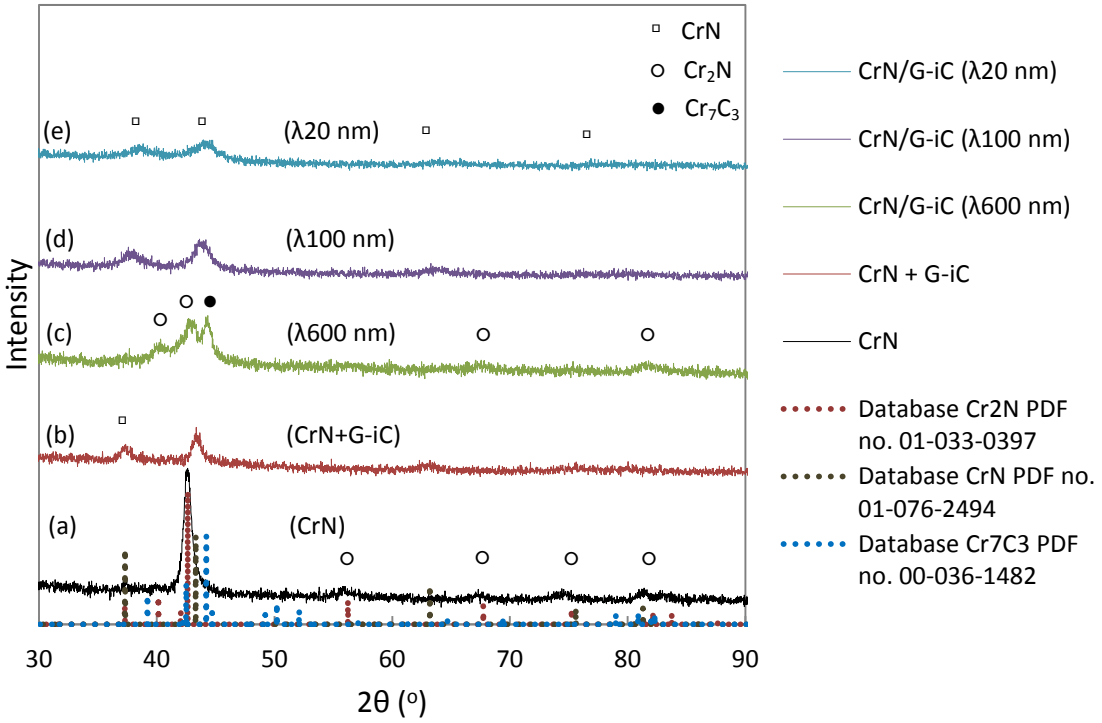


Figure 4-3 XRD patterns of (a) CrN, (b) CrN + Graphit-iC, (C) CrN/Graphit-iC multilayer (λ600 nm) (d) CrN/Graphit-iC multilayer (λ100 nm) (e) CrN/Graphit-iC multilayer (λ20 nm) coatings on 440C substrates

The CrN and CrN/Graphit-iC multilayer (λ600 nm) coatings (Figure 4-3 (a & c)) showed a preferred orientation of diffraction peaks in the {-1-1 1} plane of the Cr_2N phase at 42.6° 2θ. Peaks were also observed in the {0 0 2}, {-1-1 2}, {3 0 0}, {1 1 3} and {3 0 2} planes of the Cr_2N phase at 40.1°, 55.7°, 66.8°, 74.5° and 81.3° 2θ respectively. It should be noted, throughout this thesis, the coatings identified as CrN and CrN/Graphit-iC multilayer (λ600 nm) coatings are Cr_2N and Cr_2N/Graphit-iC multilayer (λ600 nm).

The CrN/Graphit-iC multilayer (λ600 nm) coating also exhibited diffraction peaks in the {1 5 1} plane of the chromium carbide phase at 44.2° 2θ. The CrN + Graphit-iC and CrN/Graphit-iC multilayer (λ100 nm & λ20 nm) coatings (Figure 4-3 (b, d & e)) exhibited diffraction peaks from the {2 0 0} plane of the CrN phase at 43.3° 2θ, also

the {1 1 1}, {2 2 0} and {2 2 2} planes at 37.3°, 63.2° and 81.3° 2θ respectively. Peak broadening was observed for the multilayered coatings, with the broadening increasing as the bilayer period decreased.

A cross section of the electroplated chromium coating (which was used as a reference in this research) can be seen in Figure 4-4.

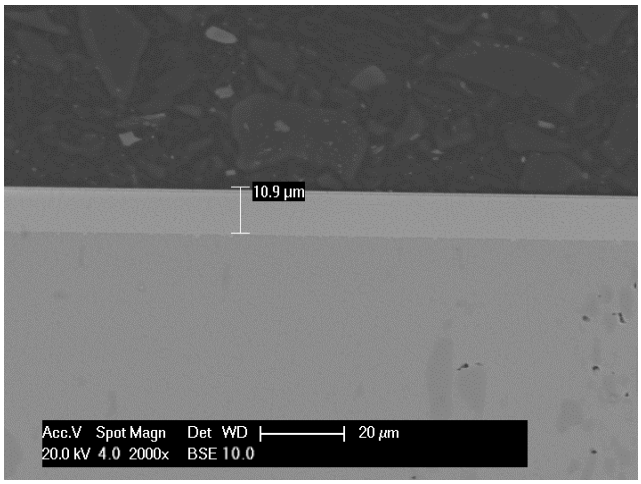


Figure 4-4 SEM micrograph of chromium plate coating cross-section on a 440C substrate

The coating was measured to be around 10.9 ± 0.1 µm thick and had a hardness of around HV = 508 ± 70 kg f mm^{-2}.

4.2.2 Effect of multilayering on the mechanical and tribological properties of coatings

4.2.2.1 Effect of multilayering on the mechanical properties of coatings

The hardness and scratch resistance of the coatings was measured to examine the effect of multilayering on the mechanical properties of coatings compared to mono and dual layered coatings. The results are shown in Figure 4-5. Hardness measurements were carried out on the top surface of coatings using an applied load of 50 mN.

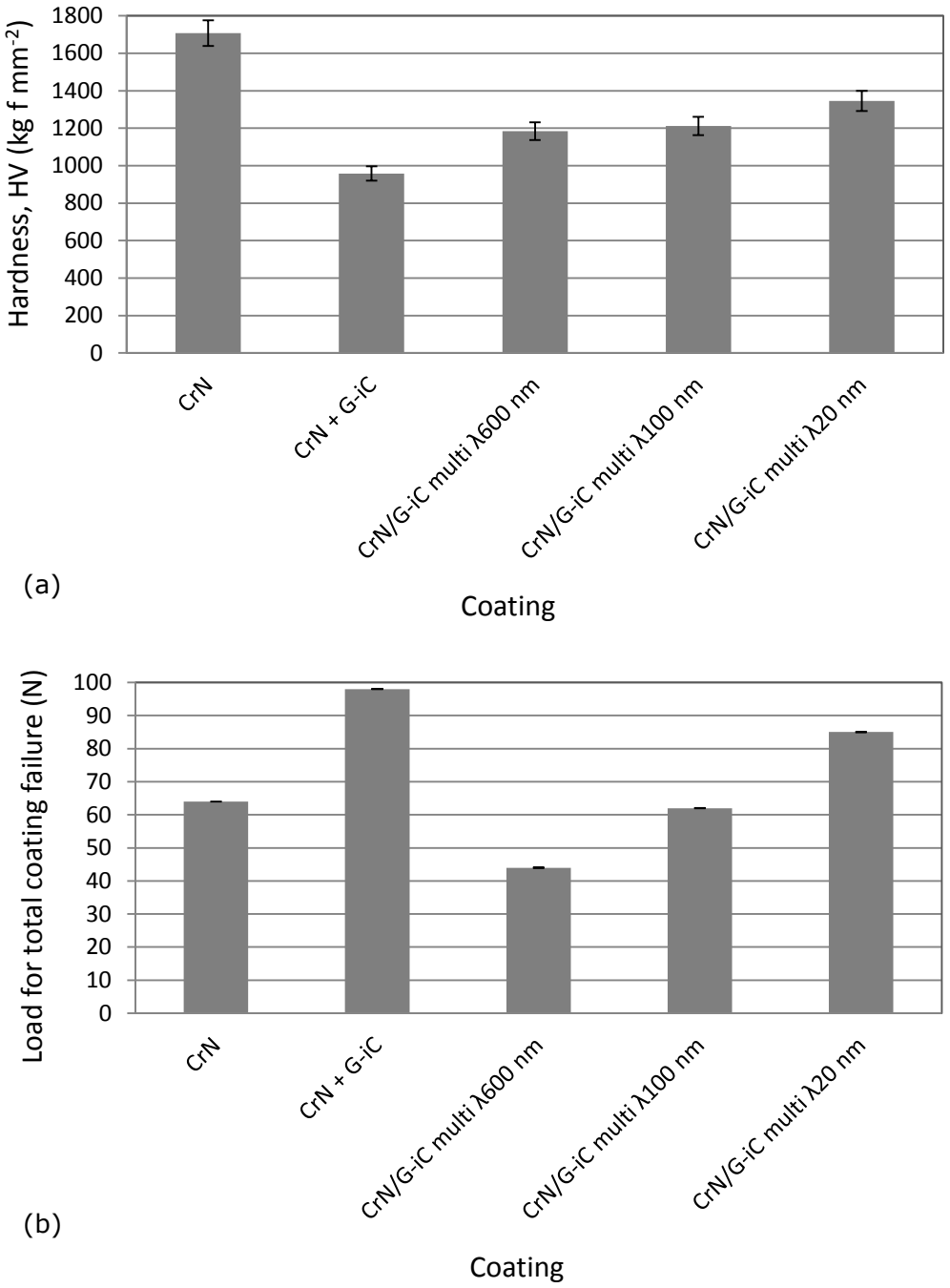


Figure 4-5 Effect of multilayering on the (a) hardness and (b) scratch resistance of coatings deposited on M42 substrates (HV = 946 ± 2 kg f mm^{-2}) in batch 1, error bars represent the equipment errors

From the hardness results (Figure 4-5 (a)), it can be seen that CrN was the hardest coating at HV = 1707 kg f mm^{-2}, followed by the CrN/Graphit-iC multilayered (λ20 nm) coating at HV = 1346 kg f mm^{-2}. The CrN/Graphit-iC coating with the smallest bilayer period exhibited the highest hardness out of the CrN/Graphit-iC multilayered and dual layered coatings. All multilayer coatings exhibited a higher

hardness than the dual layered CrN + Graphit-iC coating. The indentation depth for the CrN + Graphit-iC coating was 0.582 μm; therefore the measured hardness was predominantly contributed to by the Graphit-iC top layer.

Scratch testing on the multilayered systems (Figure 4-5 (b)) exhibited a clear trend that the coating scratch resistance increased with decreasing bilayer period. The CrN/Graphit-iC multilayered (λ20 nm) and CrN + Graphit-iC coatings both exhibited a higher scratch resistance than CrN. However, the CrN/Graphit-iC multilayered coatings all exhibited a lower scratch resistance than the dual layered CrN + Graphit-iC coating which could be a result of the much thicker low friction Graphit-iC top layer compared to the multilayer coatings.

Images of scratch scars on CrN, CrN + Graphit-iC and CrN/Graphit-iC multilayer coatings, deposited in batch 1 on M42 substrates, can be seen in Figure 4-6. The CrN monolayer coating exhibited a ribbed scratch scar with some chipping at the edges of the scar (Figure 4-6 (a)). The CrN + Graphit-iC coating did not show any serious delamination until the final stages of the test, where cracks and delamination could be seen in the wear track (Figure 4-6 (b)). The CrN/Graphit-iC multilayer coatings exhibited periodic delamination on the edge of the wear tracks (Figure 4-6 (c-e)). It could be seen that this was more severe on the coating with a thicker bilayer period (Figure 4-6 (e)).

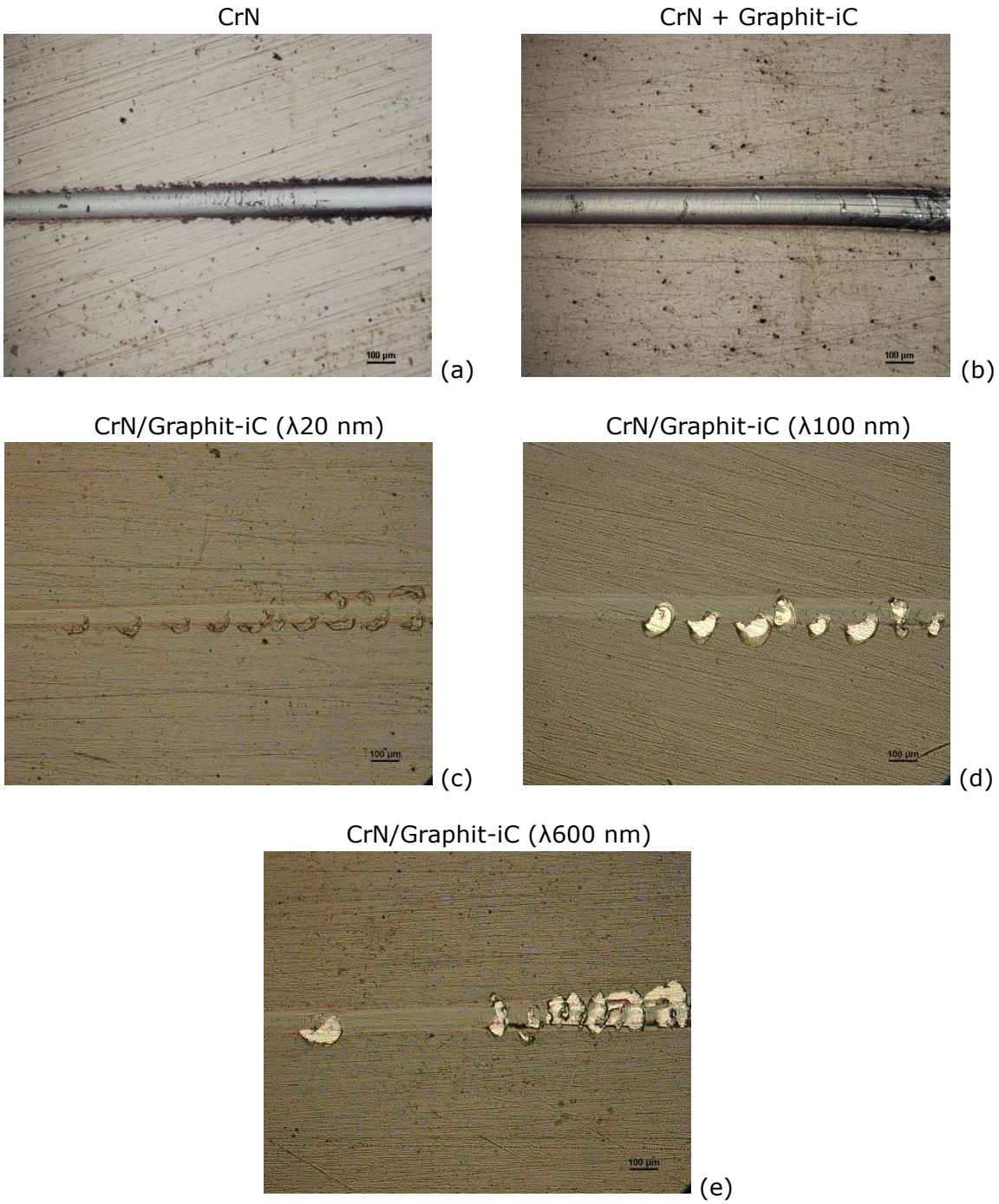


Figure 4-6 Scratch scar images of coatings on M42 substrates (a) CrN (b) CrN + Graphit-iC (c, d & e) CrN/Graphit-iC multilayer (c) λ20 nm & (d) λ100 nm & (e) λ600 nm

Some authors suggest that the key parameter for a high coating wear resistance is a high ratio of hardness to elastic modulus (Mendibide et al., 2004; Zhang et al., 2009). The values of indenter depth, hardness, indentation modulus and H/E values from hardness tests are presented in Table 4-2.

Coating	Coating Thickness (µm)	$Depth_{(max.)}$ (µm)	HV (kg f mm^{-2})	$E_{IT}/(1-v_s^2)$ (GPa)	Ratio H/E
CrN	3.0 ± 0.1	0.44 ± 0.02	1707 ± 68	248 ± 9	6.85 ± 0.05
CrN + G-iC	5.0 ± 0.1	0.58 ± 0.02	958 ± 38	123 ± 4	7.78 ± 0.06
CrN/G-iC multi λ600 nm	4.5 ± 0.1	0.54 ± 0.02	1184 ± 47	142 ± 5	8.33 ± 0.03
CrN/G-iC multi λ100 nm	4.5 ± 0.1	0.54 ± 0.02	1212 ± 48	136 ± 5	8.92 ± 0.02
CrN/G-iC multi λ20 nm	4.0 ± 0.1	0.51 ± 0.02	1346 ± 53	155 ± 6	8.68 ± 0.01

Table 4-2 Effect of multilayering on the indentation depth, hardness, indentation modulus and H/E ratio of coatings

Multilayer coatings showed higher H/E ratios compared to the monolayer and dual layer coatings. All indentation depths were between $1/7^{th}$ and $1/8^{th}$ of the coating thicknesses. Multilayering was seen to increase the H/E ratio compared to mono and dual layered coatings, however, the λ20 nm coating showed a lower H/E value than the λ100 nm coating. No patterns were observed between the H/E ratios and scratch results of the coatings (Figure 4-5 (b)).

4.2.2.2 Effect of multilayering and substrate hardness on the tribological properties of coatings

In this section, the effect of substrate material on the friction and wear properties of coatings is investigated. Coatings were deposited onto 3 different substrates, namely 304L stainless steel, M42 tool steel and heat treated 440C stainless steel. The hardness of the 304L, 440C and M42 substrates were measured to be HV = 190 ± 5 kg f mm^{-2}, 476 ± 7 kg f mm^{-2} and 946 ± 2 kg f mm^{-2} respectively.

The M42 tool steel was ground to 1200 grit giving a surface roughness of 44 ± 4 nm Ra. The 304L and 440C substrates were ground to an average surface roughness of 343 ± 40 nm Ra. Pin-on-disc tests were carried out at the University of Nottingham against Ø3/8" WC-6%Co balls at a sliding speed of 0.05 m s^{-1} for 5700 revolutions, at 10 and 40 N normal loads on wear track diameters of 14 mm and

10 mm respectively. Tests were carried out in de-ionised water. Cr plate on a 1200 grit 440C substrate was used as a reference system for the wear tests.

The average wear depths of coatings after sliding wear tests at 10 N & 40 N normal loads are presented in Figure 4-7. At 10 N load (Figure 4-7 (a)), the wear scars were unmeasurably small (< 0.02 μm) for all coatings deposited on M42 substrates. In almost all cases, at 10 N and 40 N normal load (Figure 4-7 (a & b)), the wear depths were lowest for coatings deposited on M42 substrates. At 10 N load (Figure 4-7 (a)), the wear depths of coatings on 304L and 440C substrates were similar. However, at 40 N normal load (Figure 4-7 (b)), coatings deposited on 304L substrates exhibited the highest wear depths in most cases as expected due to increased substrate deformation of softer substrates under load. At both loads, all coatings exhibited an improvement in wear resistance compared to the Cr plate (Figure 4-7 (a & b)). Multilayering conferred no improvement in wear resistance. No patterns were observed between the H/E ratios and wear results of coatings (Table 4-2 & Figure 4-7 respectively).

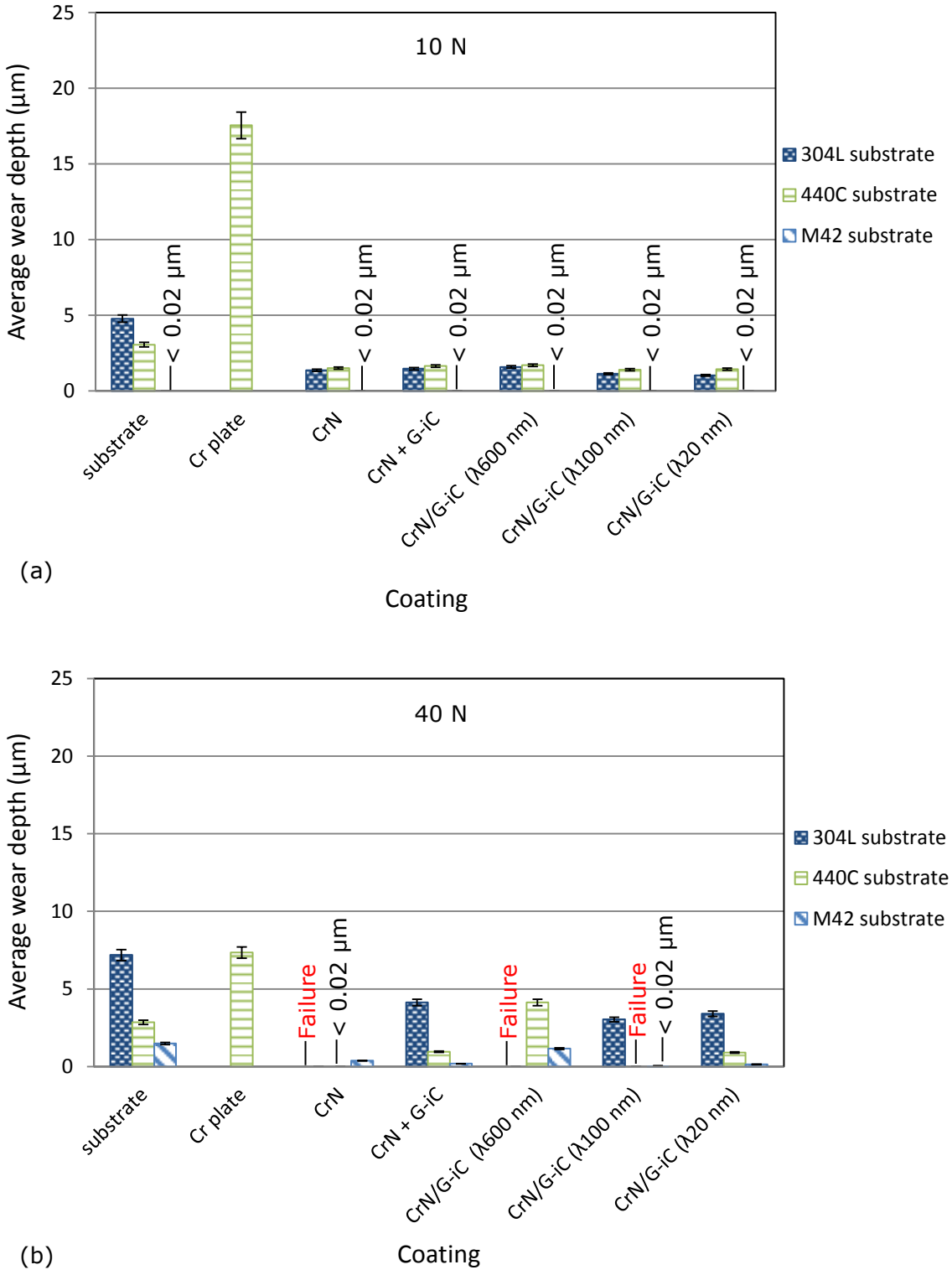


Figure 4-7 Average wear depths on coatings on different substrates, deposited in batch 1, after sliding wear tests at (a) 10 N & (b) 40N normal load against a Ø3/8" WC-6%Co ball, error bars represent the standard deviation

The wear rates of the counterface balls were also measured and are presented in Figure 4-8.

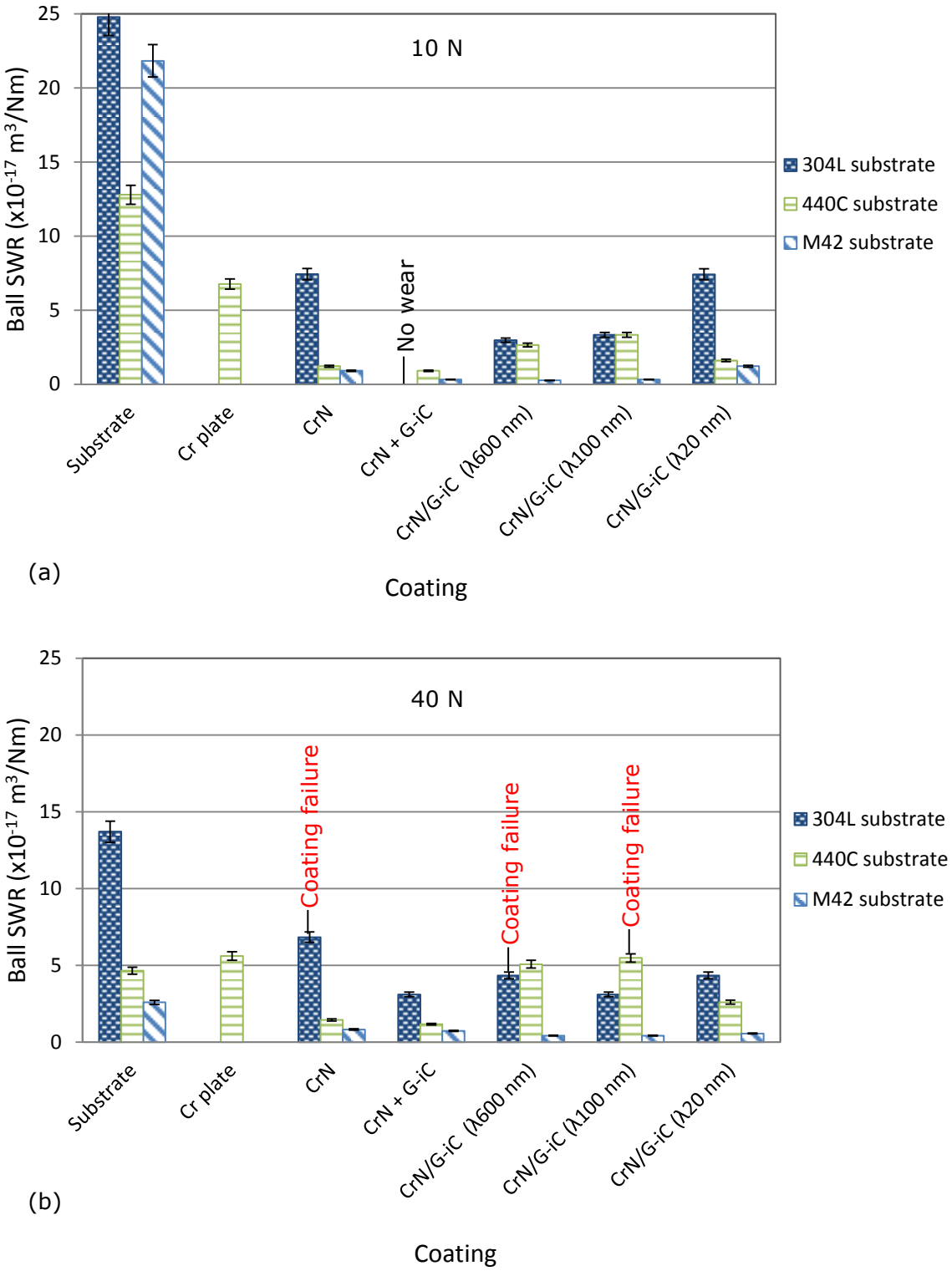


Figure 4-8 Specific wear rate of WC-6%Co counterface balls at (a) 10 N & (b) 40 N normal load against batch 1 coatings on different substrates, error bars represent the standard deviation

At 10 N load (Figure 4-8 (a)), all coatings resulted in a lower wear rate on the counterface ball compared to that observed following sliding against the appropriate

uncoated substrate. For tests carried out on the CrN + Graphit-iC coating, deposited on a 304L substrate, a transfer layer was deposited onto the ball surface; however, no wear was observed on the ball itself.

At 40 N load (Figure 4-8 (b)), for coatings deposited on 440C substrates, only the CrN, CrN + Graphit-iC and CrN/Graphit-iC (λ20 nm) coatings exhibited lower ball wear rates than those achieved against the uncoated substrate. On the 304L and M42 substrates, all PVD coatings resulted in lower ball wear rates than the uncoated substrates. When comparing the wear depths of the coatings (Figure 4-7 (b)) and the wear rates of the counterface balls (Figure 4-8 (b)) at 40 N load, the wear of the coating and ball appear to follow the same trend of the lowest wear being observed for coatings deposited on M42 substrates. Multilayering resulted in little improvement in the wear resistance of coatings (Figure 4-7) and little change in the wear observed on the counterface balls (Figure 4-8). Images of some typically observed ball wear scars are displayed in Figure 4-9.

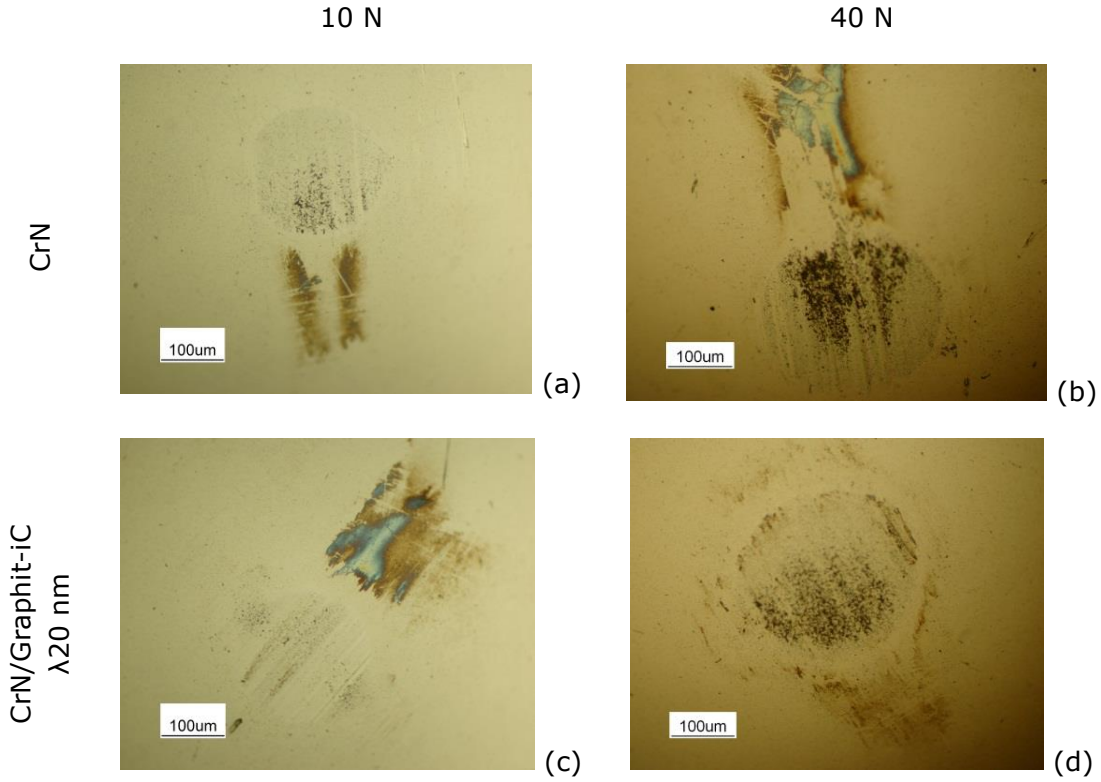


Figure 4-9 Optical microscope images of WC-6%Co ball wear scars after sliding wear tests against batch 1 coatings on M42 substrates (a & b) CrN at (a) 10 N and (b) 40 N normal load (c & d) CrN/Graphit-iC multilayer λ20 nm at (c) 10 N and (d) 40 N normal load

The balls tested against the CrN + Graphit-iC coatings showed almost no wear scars (Figure 4-10), however, transfer layers were observed on the balls tested against coatings on softer substrates (Figure 4-10 (c & d)). It was also observed that, after testing against multilayer coatings, the counterface balls often showed smaller transfer layers (Figure 4-9 (c & d)) compared to those tested against dual layer CrN + Graphit-iC coatings (Figure 4-10 (c & d)).

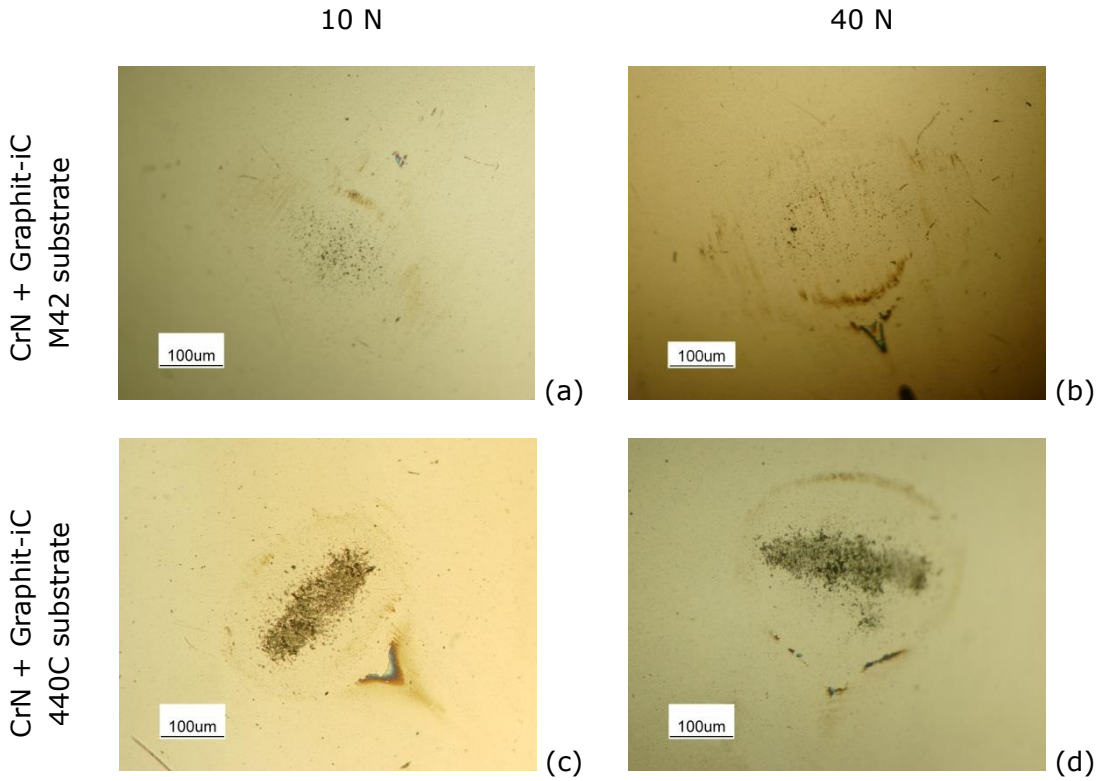


Figure 4-10 Optical microscope images of WC-6%Co ball wear scars after sliding wear tests against CrN + Graphit-iC coatings (a & b) on M42 substrates at (a) 10 N and (b) 40 N normal load and on 440C substrates (c & d) at (c) 10 N and (d) 40 N normal load

Top surface SEM images were taken of the wear scars after pin-on-disc tests to help understand the wear mechanisms that had occurred and the differences in wear behaviour for coatings deposited on different substrates (Figure 4-11 & Figure 4-12). Top surface images of the CrN + Graphit-iC coatings are presented in Figure 4-11.

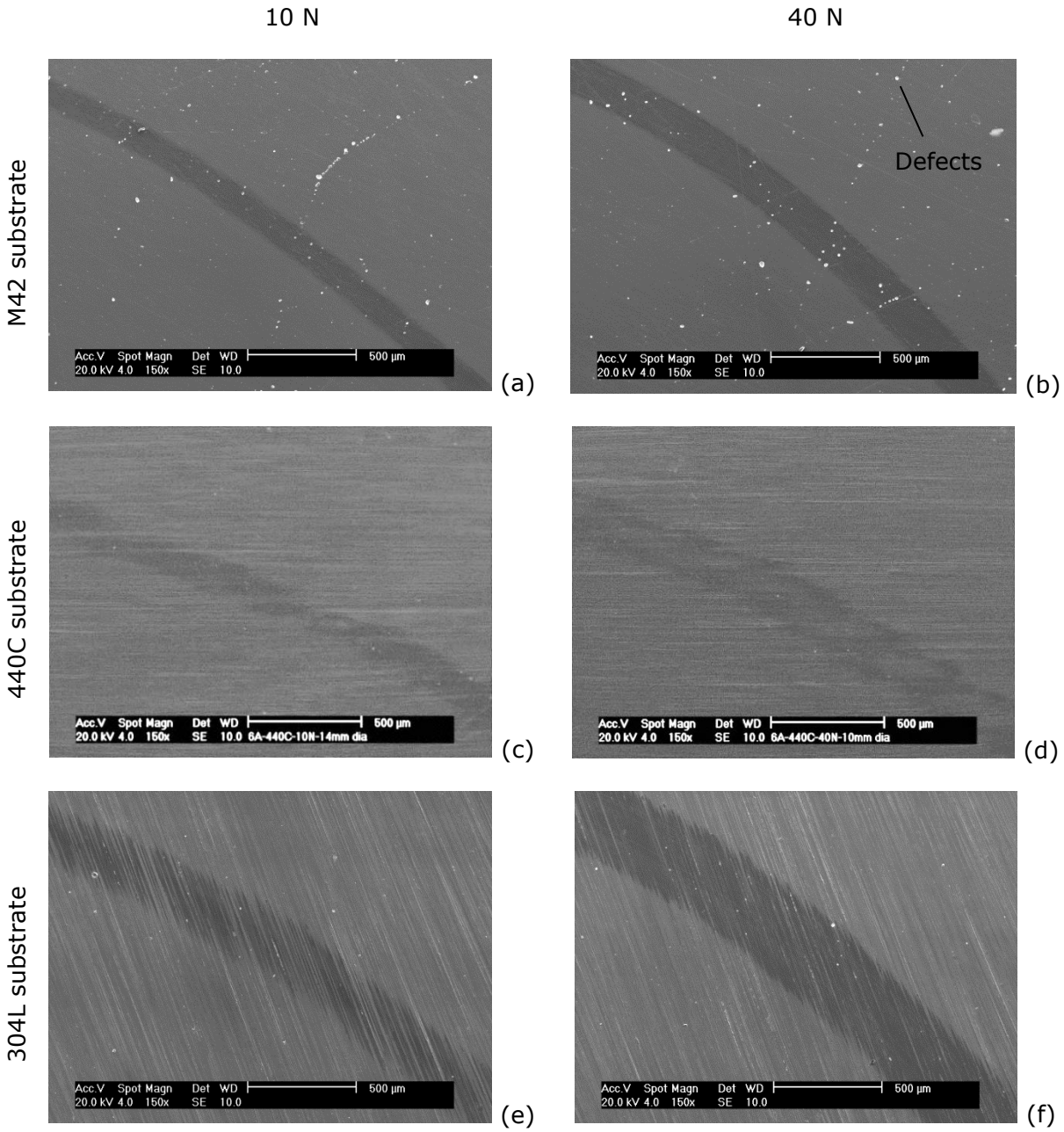


Figure 4-11 Top surface SEM micrographs of the wear scars on the CrN + Graphit-iC coatings, deposited in batch 1, (a & b) on M42 substrates after sliding wear tests at (a) 10 N and (b) 40 N normal load (c & d) on a 440C substrate after sliding wear tests at (a) 10 N and (b) 40 N normal load (e & f) on a 304L substrate after sliding wear tests at (e) 10 N and (f) 40 N normal load against WC-6%Co balls

Top surface SEM images of the wear scars on CrN/Graphit-iC (λ20 nm) multilayer coatings are presented in Figure 4-12.

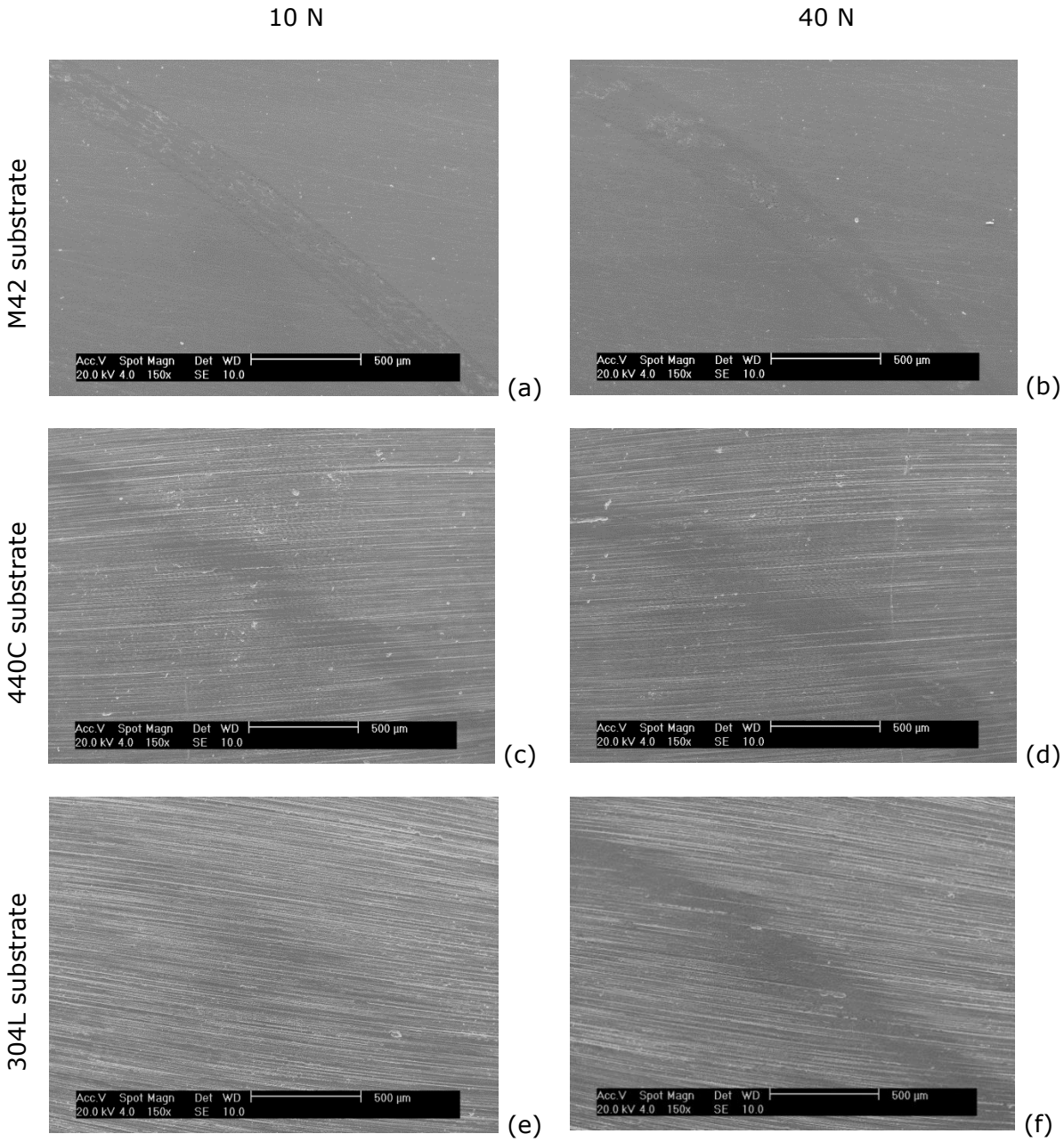


Figure 4-12 Top surface SEM micrographs of wear scars on the CrN/Graphit-iC multilayer (λ20 nm) coatings, deposited in batch 1, on (a & b) M42 substrates after sliding wear tests at (a) 10 N & (b) 40 N (c & d) 440C substrates after sliding wear tests at (c) 10 N & (d) 40 N (e & f) 304L substrates after sliding wear tests at (e) 10 N & (f) 40 N normal load against WC-6%Co balls

For the CrN + Graphit-iC coating deposited on an M42 substrate (Figure 4-11 (a & b)), a large quantity of surface defects were present; however, no delamination was seen along the wear track. For the CrN + Graphit-iC coatings, on all three substrates (Figure 4-11), no delamination had occurred, with only wear and smoothing of the top layer of Graphit-iC being observed, as shown by the example profile in Figure 4-13.

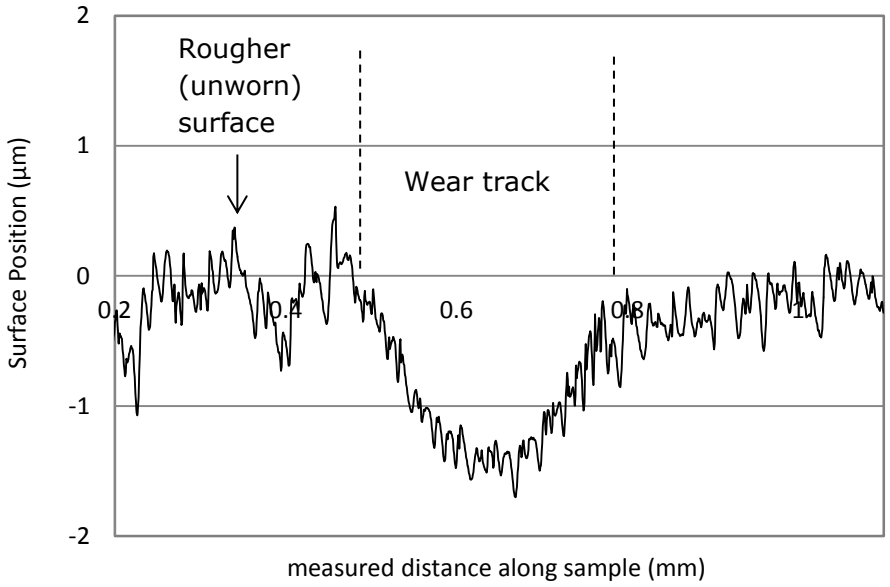


Figure 4-13 Example wear track profile showing smoothing on the CrN + Graphit-iC coating after sliding wear tests at 40 N normal load against a WC-6%Co ball on a 440C substrate, top surface images of the wear track can be seen in Figure 4-11 (d)

For the CrN/Graphit-iC (λ20 nm) multilayer coatings (Figure 4-12), the coatings exhibited very little wear at both 10 N and 40 N, on all substrates. In all cases, smoothing of the top surface was observed. The coating with λ20 nm layers exhibited the least wear of the CrN/Graphit-iC multilayers. It was observed that the coatings with λ600 nm and λ100 nm layers exhibited more severe delamination on the 304L and 440C substrates at 10 N and 40 N loads.

The friction coefficient for most coatings was relatively steady over the duration of the tests as shown in Figure 4-14. A gradual increase was seen at the start of the test as the system was reaching steady state friction. Other systems exhibited a gradual increase in friction throughout the entire duration of the test as shown in Figure 4-14 (b & c). The systems that exhibited a gradual increase in friction throughout the tests were the CrN/Graphit-iC multilayer (λ20 nm & λ100 nm) coatings on 304L substrates (Figure 4-14 (b & c)).

For systems where a steady state friction was reached, the friction coefficient is measured from the region where the coefficient of friction had reached steady state. For coatings deposited on 304L substrates, multilayering with λ20 nm

(Figure 4-14 (b)) appeared to result in no reduction in friction coefficient compared to the monolayer CrN coating at 10 N (Figure 4-14 (a)). All CrN/Graphit-iC coatings exhibited high friction coefficients around 0.2 at 10 N load, whereas, a very low friction coefficient was exhibited by the dual layered CrN + Graphit-iC coating (Figure 4-14 (d)).

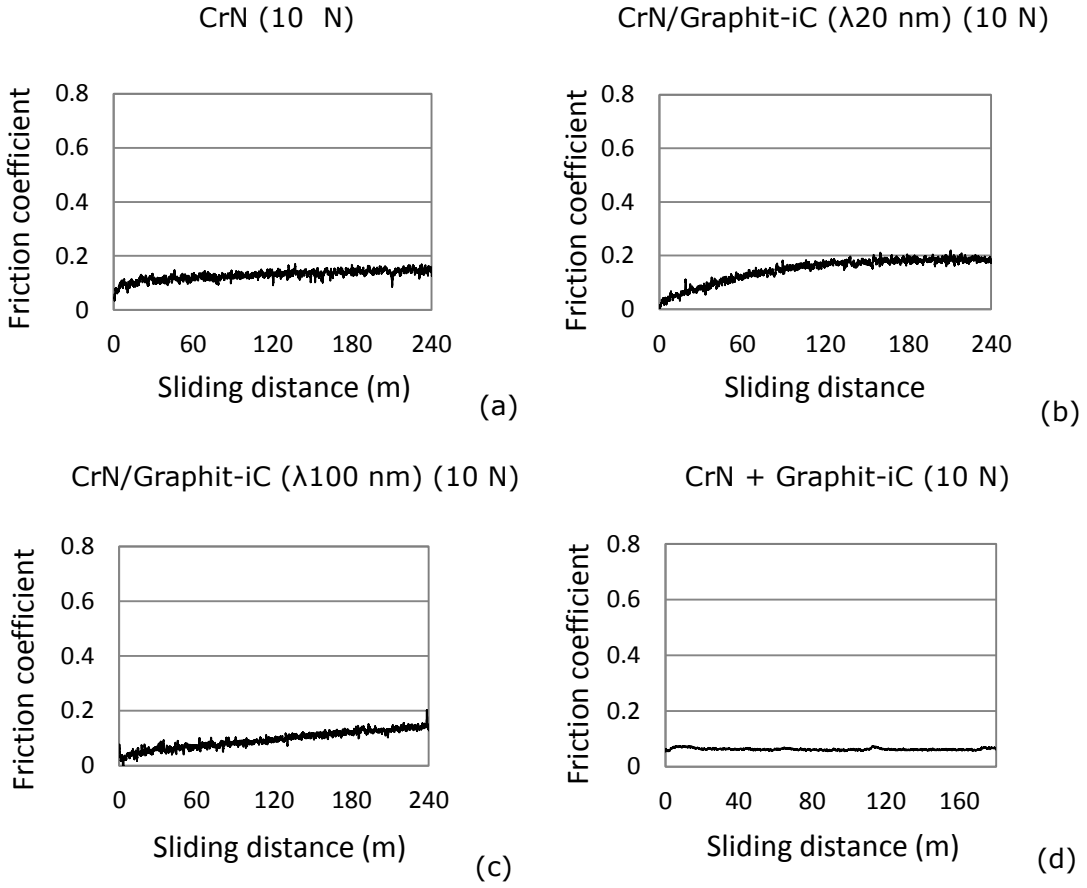


Figure 4-14 Friction coefficients of coatings, deposited in batch 1, on 304L substrates (a) CrN (b) CrN/Graphit-iC (λ20 nm) (c) CrN/Graphit-iC (λ100 nm) (d) CrN + Graphit-iC at 10 N load against WC-6%Co balls

The friction coefficients during 10 N and 40 N tests across all coatings are shown in Figure 4-15. In the tests carried out with a 10 N normal load (Figure 4-15 (a)), all coatings resulted in a lower friction coefficient than the relevant substrate. The friction coefficients of CrN/Graphit-iC multilayer coatings were similar across the different coating architectures. In general, the friction coefficients of multilayer coatings were higher than that of CrN at 10 N load. At both 10 N and 40 N loads, it can be seen that,

by applying a top layer of Graphit-iC to CrN, a clear reduction in friction coefficient can be achieved; this was observed on all substrates. The dual layer CrN + Graphit-iC coating exhibited a very low friction coefficient due to the thick Graphit-iC top layer providing a smooth transfer layer between the coating and the counterface. The CrN + Graphit-iC coating resulted in lower friction coefficients than CrN on all substrates. In most cases, this coating gave the lowest friction coefficient out of all the coatings. In the 40 N sliding wear tests (Figure 4-15 (b)), the CrN/Graphit-iC multilayer coatings exhibited very low friction coefficients, similar to or lower than CrN. For all coatings, friction was generally lower for those deposited on the harder, and lower surface roughness, M42 substrates compared to those deposited on 440C and 304L substrates. This could be attributed to greater substrate deformation for coatings on softer substrates resulting in coating cracking, fracture and a larger contact area. Multilayering generally resulted in a coating with a friction coefficient similar to or higher than that of CrN. At both loads (Figure 4-15 (a & b)), all coatings resulted in a lower friction coefficient than the reference Cr plate on a 440C substrate.

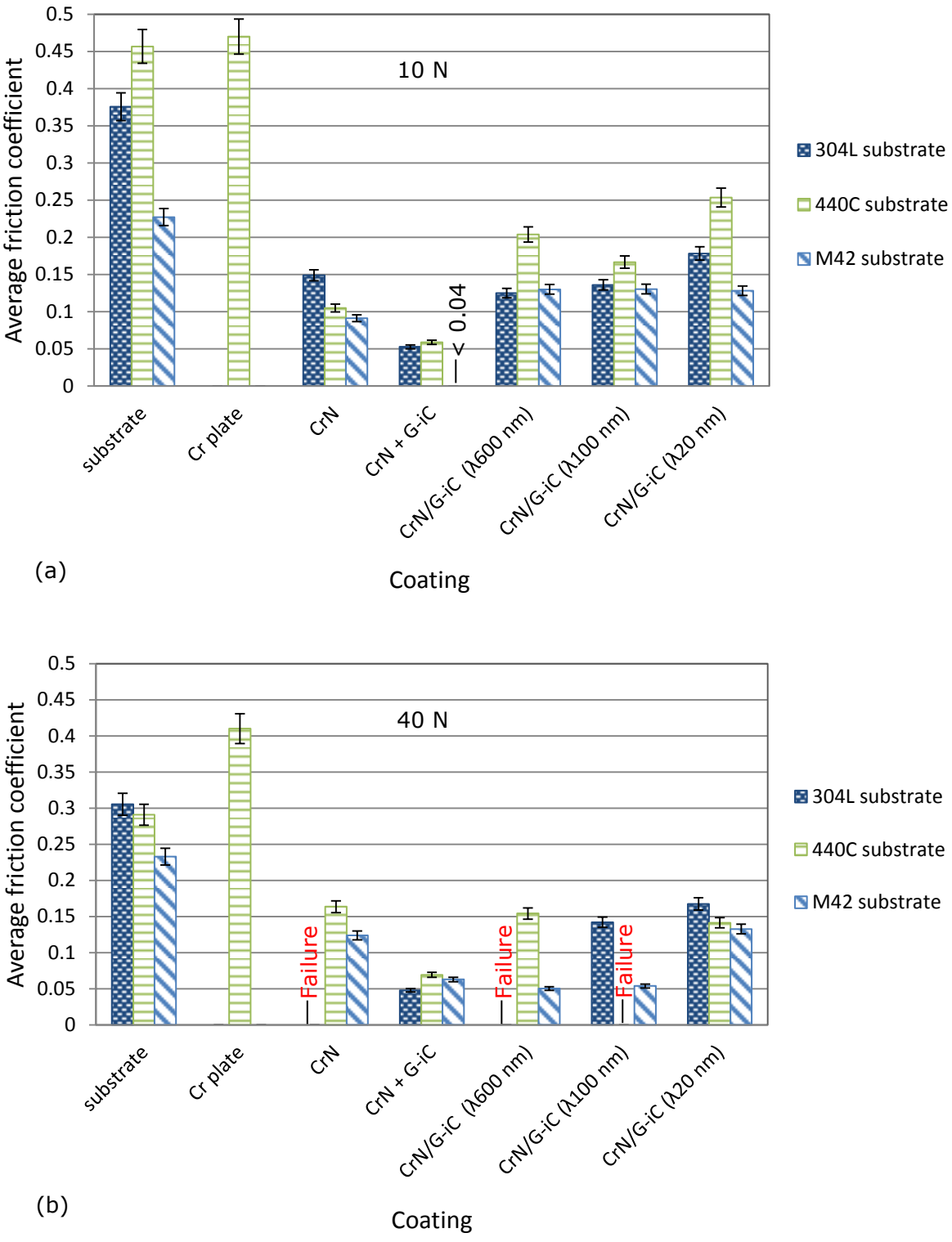


Figure 4-15 Friction coefficients of coatings on different substrates, deposited in batch 1, during sliding wear tests at (a) 10 N & (b) 40 N normal load against a Ø3/8" WC-6%Co ball, error bars represent the standard deviation

4.2.3 Effect of multilayer architecture on the mechanical and tribological properties of coatings

The effect of multilayer architecture on the tribological properties of CrN/Graphit-iC multilayer coatings was investigated using an overall bilayer period of 100 nm (λ100 nm) and three different multilayer architectures with material ratios of 1:1, 1:3 and 3:1, i.e. the same number of interfaces in each coating. Coatings were deposited on 440C substrates with 1200 grit surface finishes (Ra =78 ± 12 nm) and tests were run against WC-6wt%Co balls at a sliding speed of 0.05 m s^{-1} for 5700 revolutions. A Cr plate coating on a 440C substrate was used as a reference.

4.2.3.1 Effect of multilayer architecture and substrate hardness on the mechanical properties of coatings

The hardness and scratch resistance of CrN/Graphit-iC coatings, deposited in batch 3, was measured on 440C and M42 substrates (Figure 4-16). Coatings deposited on the softer 440C substrates exhibited slightly lower values of hardness and scratch resistance compared to those deposited on M42 substrates (Figure 4-16 (a & b)). It was seen that the multilayer architecture can also have an effect on the coating properties. A larger amount of CrN can result in a higher hardness and vice versa. This is partially expected as the CrN coating deposited in batch 1 exhibited the highest hardness out of all coatings (Figure 4-5).

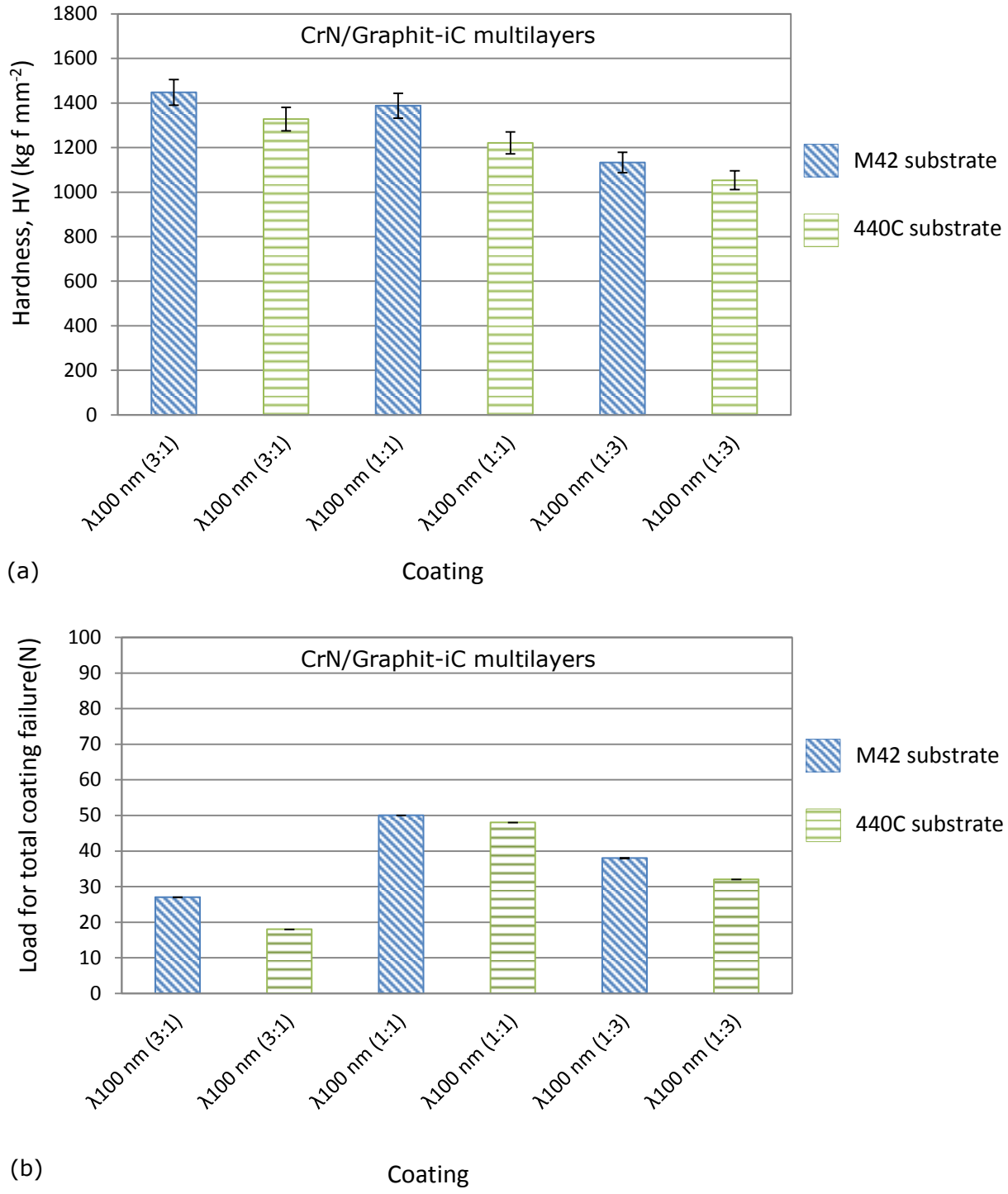


Figure 4-16 Effect of substrate hardness and multilayer architecture on the (a) hardness & (b) scratch resistance of CrN/Graphit-iC λ100 nm multilayer coatings deposited in batch 3, error bars represent the equipment errors

For the CrN/Graphit-iC multilayers (Figure 4-16 (a)), coatings deposited on the softer 440C substrates tended to exhibit hardness values around HV = 80 kg f mm^{-2} to HV = 167 kg f mm^{-2} lower than those deposited on M42 substrates despite the

indentation depth being no more than 20% of the coating thickness. The change in architecture from CrN/Graphit-iC λ100 nm (3:1) to (1:1) resulted in a reduction in hardness of HV = 60 kg f mm^{-2} for coatings on M42 substrates and HV = 107 kg f mm^{-2} for coatings deposited on 440C substrates. Another reduction in hardness was seen from the CrN/Graphit-iC (λ100 nm (1:3)) coatings compared to CrN/Graphit-iC (λ100 nm (1:1)) (of HV = 255 kg f mm^{-2} for coatings on M42 substrates and HV = 168 kg f mm^{-2} for coatings deposited on 440C substrates). The multilayer coating with equal layer thicknesses (CrN/Graphit-iC (λ100 nm (1:1)) exhibited the highest scratch resistance on both substrates and the CrN/Graphit-iC (λ100 nm (3:1)) coating exhibited the lowest (Figure 4-16 (b)).

The H/E ratios of coatings were investigated, with the results being presented in Table 4-3.

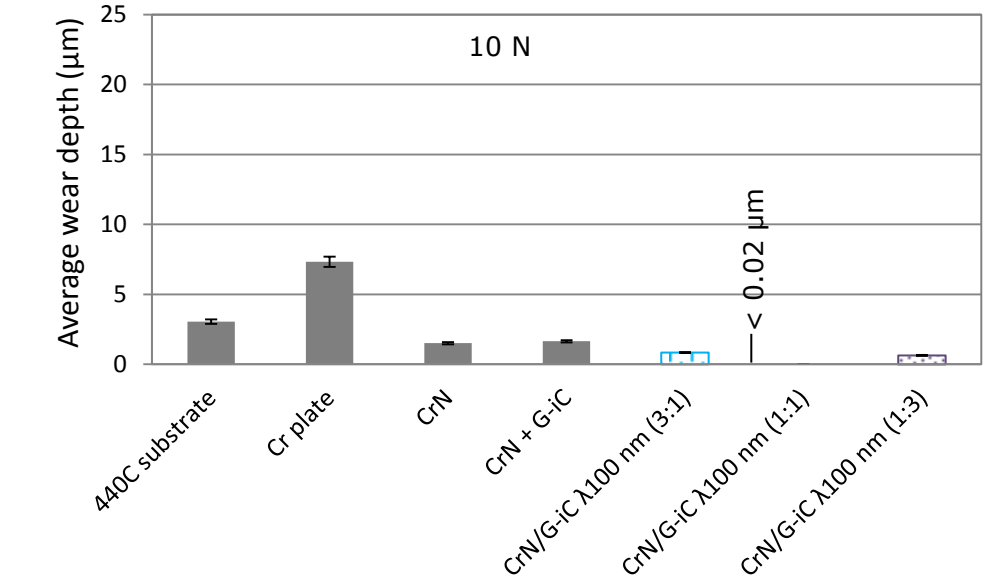
	Coating	Coating Thickness (µm)	$Depth_{(max.)}$ (µm)	HV (kg f mm^{-2})	$E_{IT}/(1-v_s^2)$ (GPa)	Ratio H/E
M42 substrate	CrN/G-iC multi λ100 nm (3:1)	5.0 ± 0.1	0.48 ± 0.02	1448 ± 59	191 ± 7	7.58 ± 0.03
	CrN/G-iC multi λ100 nm (1:1)	4.0 ± 0.1	0.49 ± 0.02	1388 ± 55	167 ± 7	8.31 ± 0.02
	CrN/G-iC multi λ100 nm (1:3)	3.7 ± 0.1	0.54 ± 0.02	1133 ± 45	143 ± 6	7.92 ± 0.02
440C substrate	CrN/G-iC multi λ100 nm (3:1) 440C	5.0 ± 0.1	0.49 ± 0.02	1328 ± 53	182 ± 7	7.30 ± 0.01
	CrN/G-iC multi λ100 nm (1:1) 440C	4 ± 0.1	0.52 ± 0.02	1221 ± 48	162 ± 6	7.53 ± 0.02
	CrN/G-iC multi λ100 nm (1:3) 440C	3.7 ± 0.1	0.56 ± 0.02	1053 ± 42	136 ± 5	7.75 ± 0.03

Table 4-3 Effect of multilayer architecture and substrate hardness on the indentation depth, hardness, indentation modulus and H/E ratio of coatings

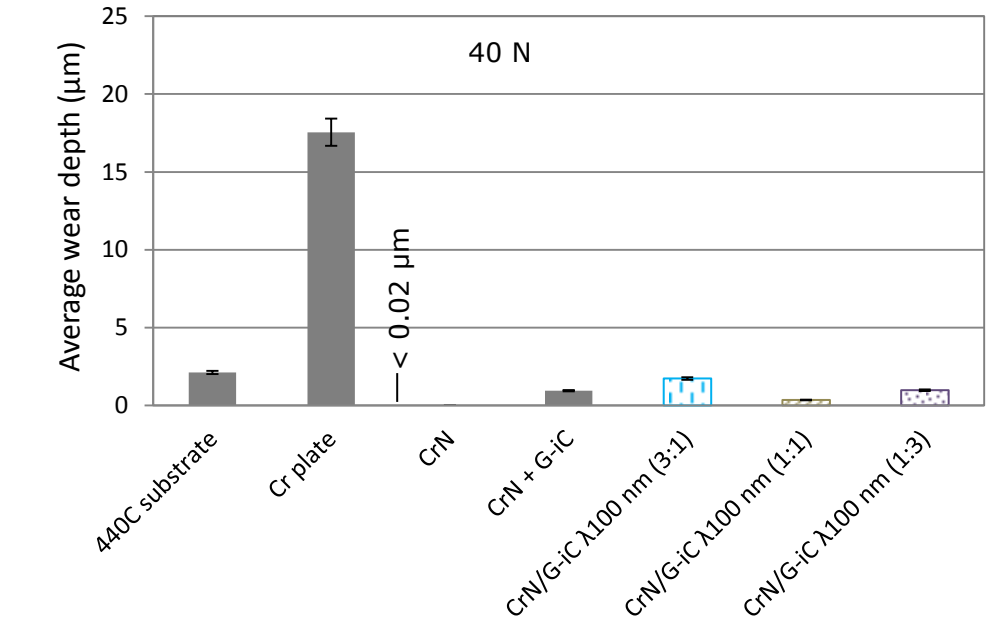
For all coatings, the hardness, indentation modulus and H/E ratio results were lower for coatings deposited on the softer 440C substrates (Table 4-3). All indentation depths were between 1/7^{th} and 1/11^{th} of the coating thicknesses.

4.2.3.2 Effect of multilayer architecture on the tribological properties of coatings

In the wear tests at both 10 N and 40 N normal load (Figure 4-17), a clear trend was seen showing that the CrN/Graphit-iC multilayer (λ100 nm (1:1)) coating exhibited the lowest wear depths (< 0.02 μm and 0.35 μm for 10 N and 40 N tests respectively) and the CrN/Graphit-iC multilayer (λ100 nm (3:1)) coating gave the highest wear depths (0.84 μm and 1.7 μm for 10 N and 40 N tests respectively) out of the multilayer coatings. After tests at 10 N, all multilayer coatings exhibited lower wear depths than the single layer and dual layered coatings (Figure 4-17 (a)). In both 10 N and 40 N tests (Figure 4-17 (a & b)), all PVD coatings exhibited lower wear depths than both the Cr plate and the uncoated substrate. The Cr plate exhibited significantly larger wear depths than all the PVD coatings in both tests. In tests carried out at 40 N normal load (Figure 4-17 (b)), the wear scar was unmeasurably small on the CrN coating (< 0.02 μm). Some authors suggest that, for multilayer coatings, a high H/E ratio is key for developing a coating with high wear resistance (Matthews, 2003; Mendibide et al., 2004; Mendibide et al., 2006; Zhang et al., 2009); however, no relation was observed between the measured H/E ratios (Table 4-3) and wear resistances of the coatings (Figure 4-17).



(a)



(b)

Figure 4-17 Average wear depths on coatings, deposited in batch 3, on 440C substrates after sliding wear tests at (a) 10 N & (b) 40N normal loads against Ø3/8" WC-6%Co balls, error bars represent the standard deviation

The specific wear rates of the counterface balls were measured and are presented in Figure 4-18.

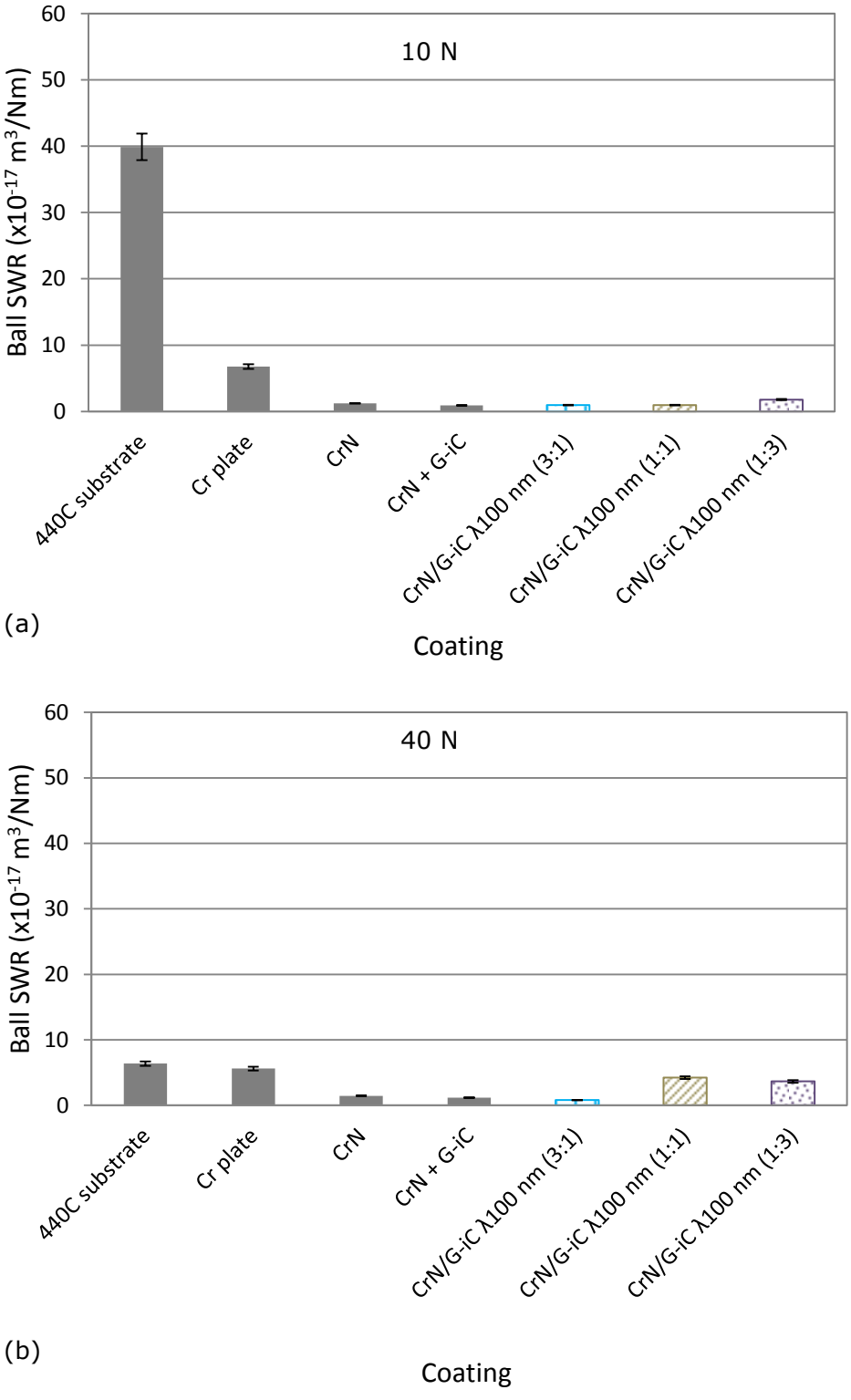


Figure 4-18 Specific wear rate of WC-6%Co counterface balls at (a) 10 N & (b) 40 N normal load against batch 3 coatings on 440C substrates, error bars represent the standard deviation

At 10 N normal load, the specific wear rates of the counterface balls were low for all PVD coatings (less than 1.7 x 10^{-17} m^3 N^{-1} m^{-1}) (Figure 4-18 (a)). The effect of

multilayer architecture appears to have little effect on the specific wear rate of the counterface balls at 10 N normal load. All PVD coatings showed a clear reduction in specific wear rate on the counterface balls compared to the Cr plate and uncoated 440C in both 10 N and 40 N tests (Figure 4-18 (a & b)).

In wear tests carried out at 40 N normal load (Figure 4-18 (b)), the CrN/Graphit-iC (λ100 nm (1:1)) multilayer coating resulted in the highest ball wear rate out of the PVD coatings; however, the coating itself exhibited the lowest wear depth (Figure 4-17 (b)). There was a clear trend for the multilayer coatings at 40 N normal load showing that coatings which gave the lowest wear depths (Figure 4-17 (b)) resulted in the highest wear rates on the counterface balls (Figure 4-18 (b)) and vice versa.

It was observed that the CrN coating deposited on a 440C substrate exhibited less wear at 40 N compared to at 10 N (Figure 4-17), however a wider wear scar was observed on the ball (Figure 4-19). This larger contact area could have resulted in a lower contact pressure and therefore less wear on the coating.

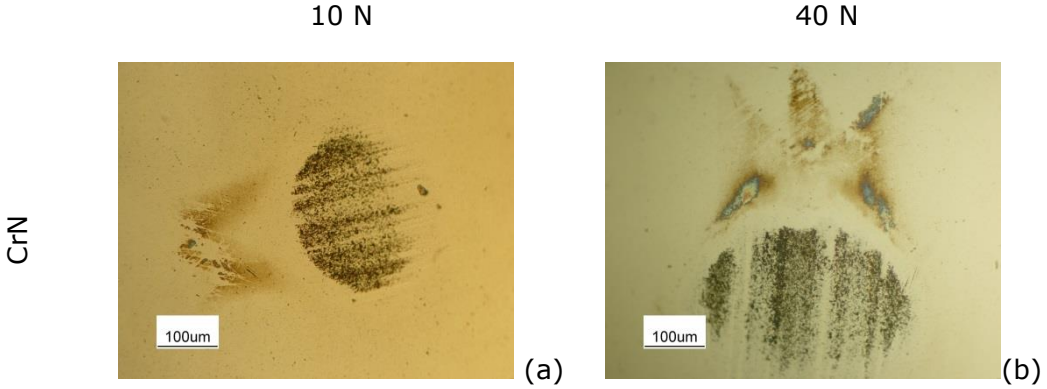


Figure 4-19 Optical microscope images of WC-6%Co ball wear scars after sliding wear tests against CrN coatings on 440C substrates at (a) 10 N and (b) 40 N

Optical microscopy images of the wear scars on the WC-6wt%Co counterface balls are shown in Figure 4-20. The smallest transfer layer was observed on the ball tested at 40 N against the CrN/Graphit-iC (λ100 nm (1:1)) coating (Figure 4-20 (f)). For the balls tested against the uncoated 440C substrate, a lower magnification was used due to the size of the wear scars (Figure 4-20 (a & b)).

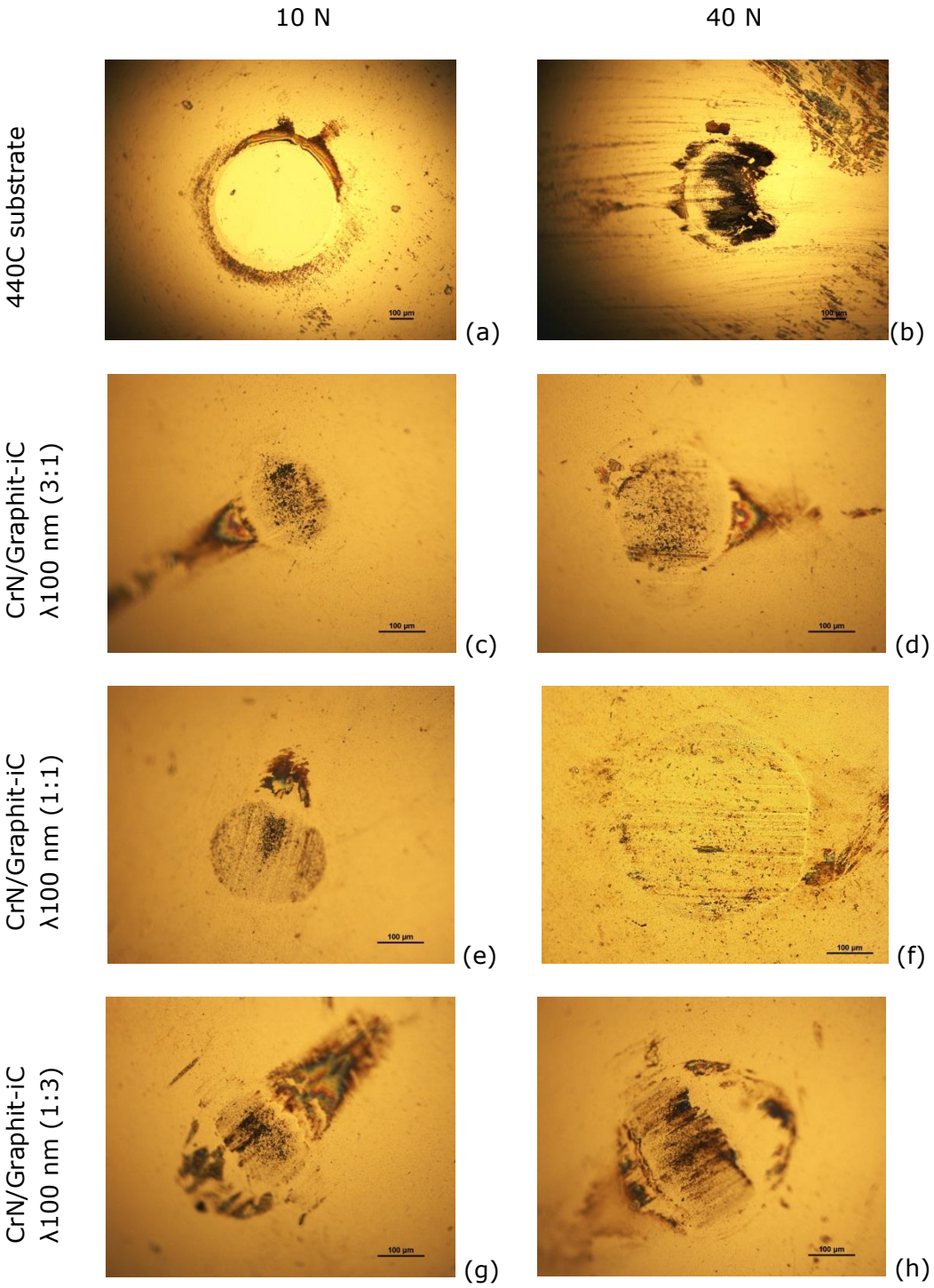


Figure 4-20 Optical microscope images of WC-6%Co ball wear scars after sliding wear tests against batch 3 coatings on 440C substrates (a & b) 440C substrate at (a) 10 N and (b) 40 N (c & d) CrN/Graphit-iC multilayer (λ100 nm (3:1)) at (c) 10 N and (d) 40 N normal load (e & f) CrN/Graphit-iC multilayer (λ100 nm (1:1)) at (e) 10 N and (f) 40 N normal load (g & h) CrN/Graphit-iC multilayer (λ100 nm (1:3)) at (g) 10 N and (h) 40 N normal load

The ball tested against the uncoated 440C substrate showed a significantly larger amount of wear when tested at 10 N (Figure 4-20 (a)) compared to when tested at

40 N (Figure 4-20 (b)), however, a dark debris layer was present on the ball tested at 40 N, this debris could have acted as a protective layer resulting in less ball wear.

Top surface SEM images of the wear scars on the multilayer coatings are presented in Figure 4-21.

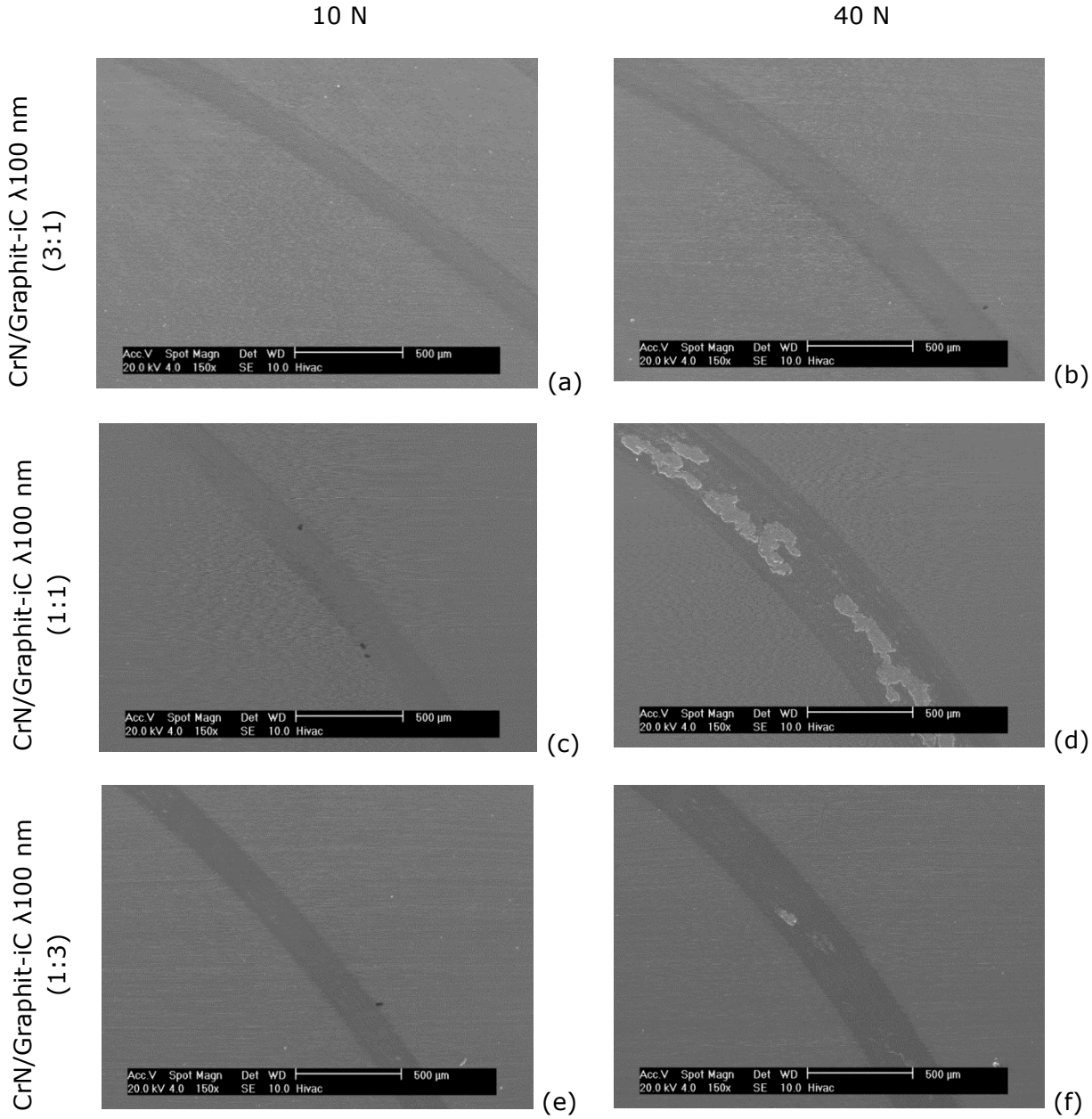


Figure 4-21 Top surface SEM micrographs of the wear scars on the CrN/Graphit-iC λ100 nm multilayer coatings, deposited in batch 3, on 440C substrates after sliding wear tests (a & b) CrN/Graphit-iC multilayer (λ100 nm (3:1)) coating at (a) 10 N and (b) 40 N normal load (c & d) CrN/Graphit-iC multilayer (λ100 nm (1:1)) coating at (c) 10 N and (d) 40 N normal load (e & f) CrN/Graphit-iC multilayer (λ100 nm (1:3)) coating at (e) 10 N and (f) 40 N normal load against Ø3/8" WC-6%Co balls

All CrN/Graphit-iC coatings with 100 nm bilayer periods, with different architectures, showed similar wear modes (Figure 4-21 (a-f)). Smoothing of the top surface was seen in most cases. The CrN/Graphit-iC λ100 nm (1:1) and λ100 nm (1:3) coatings showed some delamination of the Graphit-iC top layers at 40 N normal load (Figure 4-21 (d & f)).

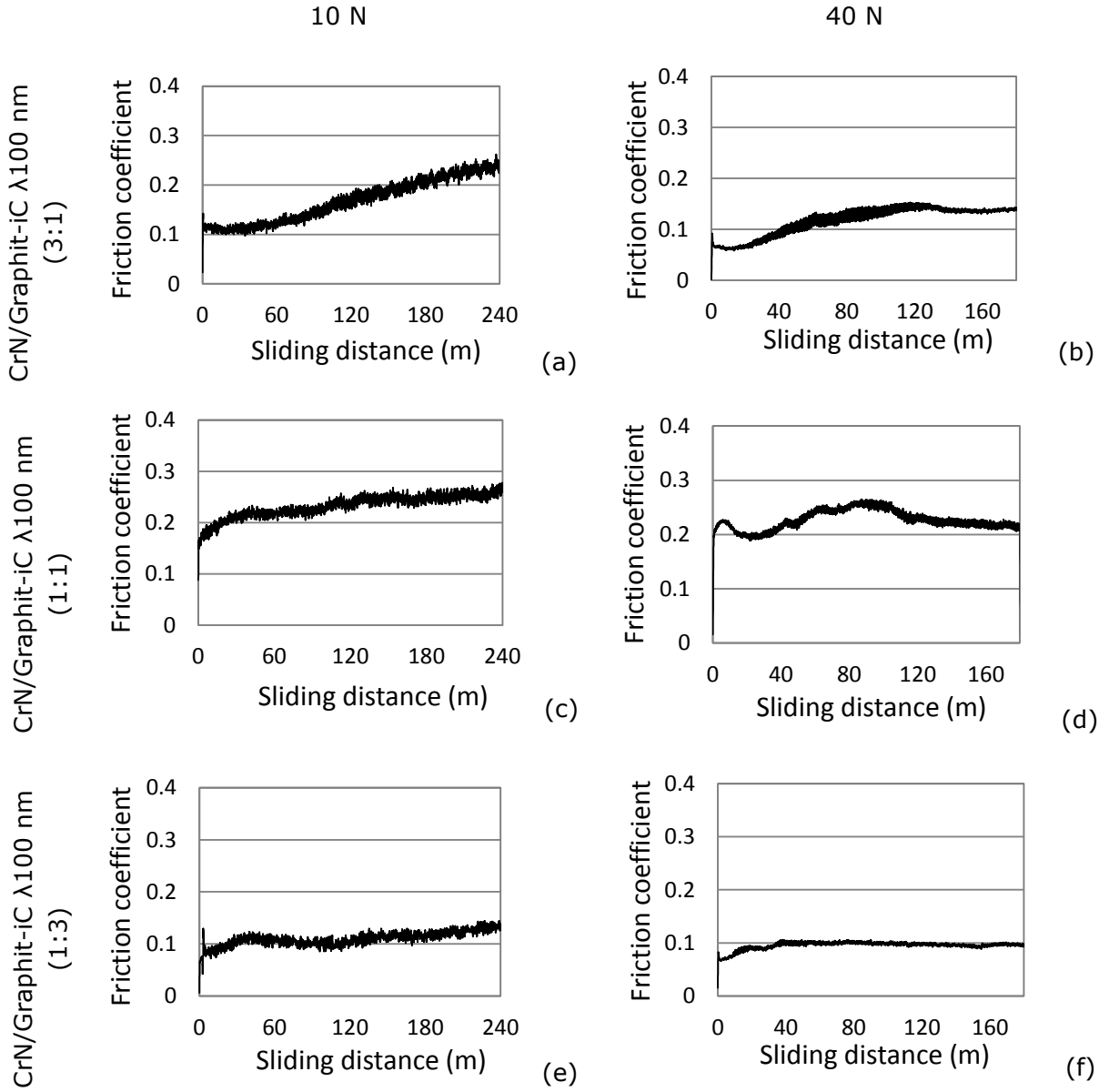


Figure 4-22 Friction coefficients of coatings, deposited in batch 3, on 440C substrates (a & b) CrN/Graphit-iC multilayer (λ100 nm (3:1)) at (a) 10 N and (b) 40 N normal load (c & d) CrN/Graphit-iC multilayer (λ100 nm (1:1)) at (c) 10 N and (d) 40 N normal load (e & f) CrN/Graphit-iC multilayer (λ100 nm (1:3)) at (e) 10 N and (f) 40 N normal load against Ø3/8" WC-6%Co balls

Friction coefficients of the multilayer coatings are presented in Figure 4-22. For the CrN/Graphit-iC λ100 nm (3:1) multilayer coating (Figure 4-22 (a & b)), the initial

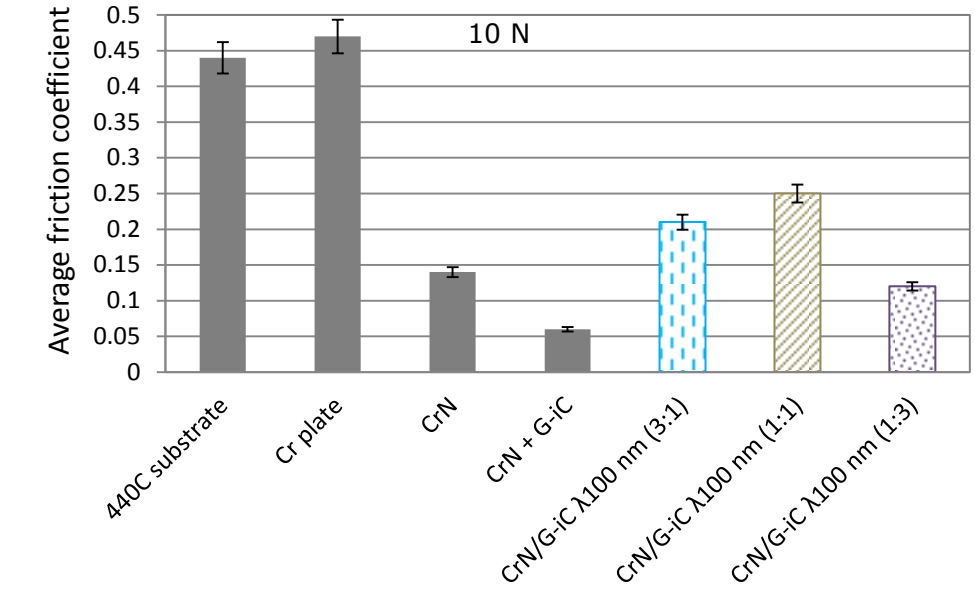
friction coefficient was lower than that of the 1:1 coating. At 10 N normal load (Figure 4-22 (a)) the friction coefficient was seen to increase throughout the duration of the test to around 0.24. At 40 N normal load (Figure 4-22 (b)) the friction coefficient remained lower than that observed under a 10 N normal load. A gradual increase was observed to around 0.15 at 120 m sliding distance, where steady state friction was reached.

The friction coefficients of the CrN/Graphit-iC λ100 nm (1:1) multilayer coatings (Figure 4-22 (c & d)) showed an initial friction coefficient of around 0.2 which then gradually increased throughout the test. In the 10 N tests (Figure 4-22 (c)), the friction gradually increased the entire way through the test; however, at 40 N (Figure 4-22 (d)), the friction was seen to increase initially and then decrease after a sliding distance of around 100 m. The friction coefficients of the CrN/Graphit-iC λ100 nm (1:3) multilayer coating (Figure 4-22 (e & f)) exhibited a lower initial friction than the 1:1 coating and a more steady friction coefficient throughout the test. At 10 N normal load (Figure 4-22 (e)), the friction coefficient gradually increased by around 0.05 throughout the duration of the test; however, at 40 N normal load (Figure 4-22 (f)) the friction reached steady state of 0.1 at around 40 m sliding distance and remained constant thereafter.

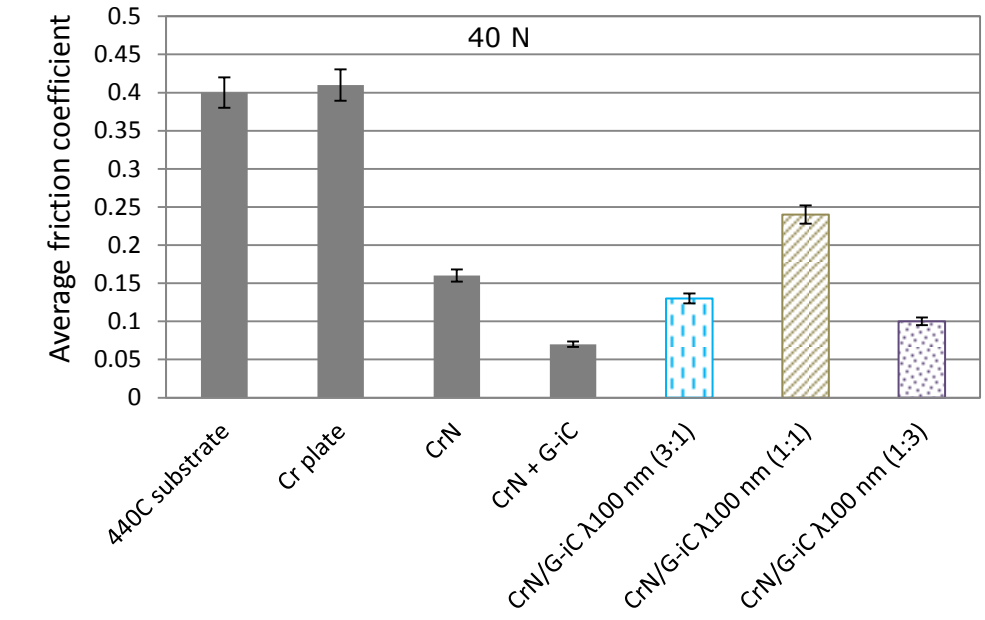
Figure 4-23 shows the average friction coefficients of all systems at both 10 N and 40 N loads. For systems where a steady state friction was reached, the friction coefficient was measured from the coefficient of steady state friction. For systems where the friction coefficient gradually increased throughout the test, an average coefficient was taken for the friction coefficient of the system.

As can be seen from Figure 4-23, all coatings resulted in a lower friction coefficient than the uncoated 440C substrate and Cr plate. All coatings exhibited similar trends at both 10 N and 40 N normal load. The CrN + Graphit-iC coating provided the lowest friction coefficient in both tests. Looking at the multilayer coatings with different architectures, in both tests, the CrN/Graphit-iC λ100 nm (1:1) coating gave the

highest friction coefficient and the CrN/Graphit-iC λ100 nm (1:3) coating gave the lowest.



(a)



(b)

Figure 4-23 Friction coefficients of coatings on 440C substrates, deposited in batch 3, at (a) 10 N & (b) 40 N normal load against Ø3/8" WC-6%Co balls, error bars represent the standard deviation

The CrN/Graphit-iC λ100 nm (1:3) coating resulted in a lower friction coefficient than CrN in both 10 N and 40 N tests; however, the CrN/Graphit-iC λ100 nm (3:1) coating only exhibited a lower friction coefficient than CrN at 40 N normal load (Figure 4-23 (b)), indicating that, in some cases the friction coefficients of the multilayer coatings were higher than those of the monolayer CrN and dual layer CrN + Graphit-iC.

4.2.4 Effect of ball type on the tribological properties of coatings

In this section, the counterface ball type is investigated and its effect on the friction and wear of coatings investigated in the previous section. For these investigations a 440C substrate was selected with a 1200 grit surface finish. A Ø3/8" Stellite 20 ball (HV = 740 ± 10 kg f mm^{-2}) was used as the counterface and the results were compared to those obtained with a Ø3/8" WC-6%Co ball (HV = 1700 ± 10 kg f mm^{-2}). The aim of this work was to investigate the friction of coatings in a situation where it was intended that less wear would be inflicted on the coating. This was attempted using Stellite 20 balls, a less aggressive ball compared to the WC-6%Co balls due to its lower hardness.

The average wear depths on coatings after wear tests at 10 N and 40 N load are presented in Figure 4-24. At 10 N normal load (Figure 4-24 (a)), all CrN/Graphit-iC multilayer coatings showed higher wear depths when tested against a Stellite 20 ball compared to those tested against a WC-6%Co ball; however, the wear scars on single and dual layer coatings (Cr plate, CrN and CrN + Graphit-iC) were not measurable (< 0.02 μm) when tested against a Stellite 20 ball, with loads of both 10 and 40 N (Figure 4-24 (a & b)). The wear depth on the CrN/Graphit-iC λ100 nm (1:1) coating at 10 N load was also not measurable (< 0.02 μm) against the WC-6%Co ball. At 40 N normal load (Figure 4-24 (b)), tests carried out against a Stellite 20 ball, except for the CrN/Graphit-iC λ100 nm (1:1) and λ100 nm (1:3) multilayer coatings, showed lower wear depths than those obtained in tests against a WC-6%Co ball. When tested

against a Stellite 20 ball, all PVD coatings provided a lower wear depth than the uncoated 440C substrate.

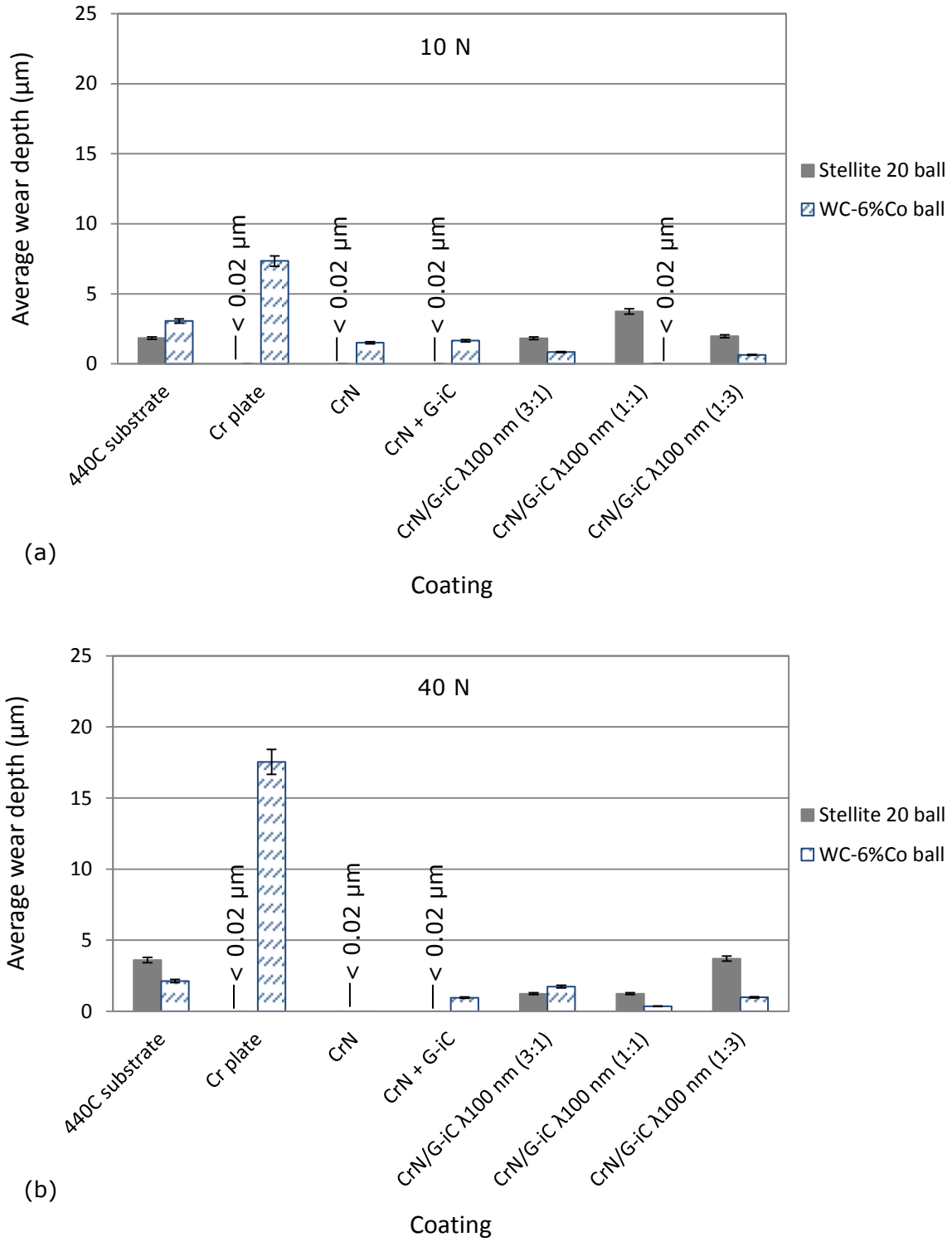


Figure 4-24 Average wear depths on coatings, deposited in batch 3, on 440C substrates after sliding wear tests at (a) 10 N & (b) 40N normal load against Ø3/8" Stellite 20 and WC-6%Co balls, error bars represent the standard deviation

The wear rates of the counterface balls are presented in Figure 4-25.

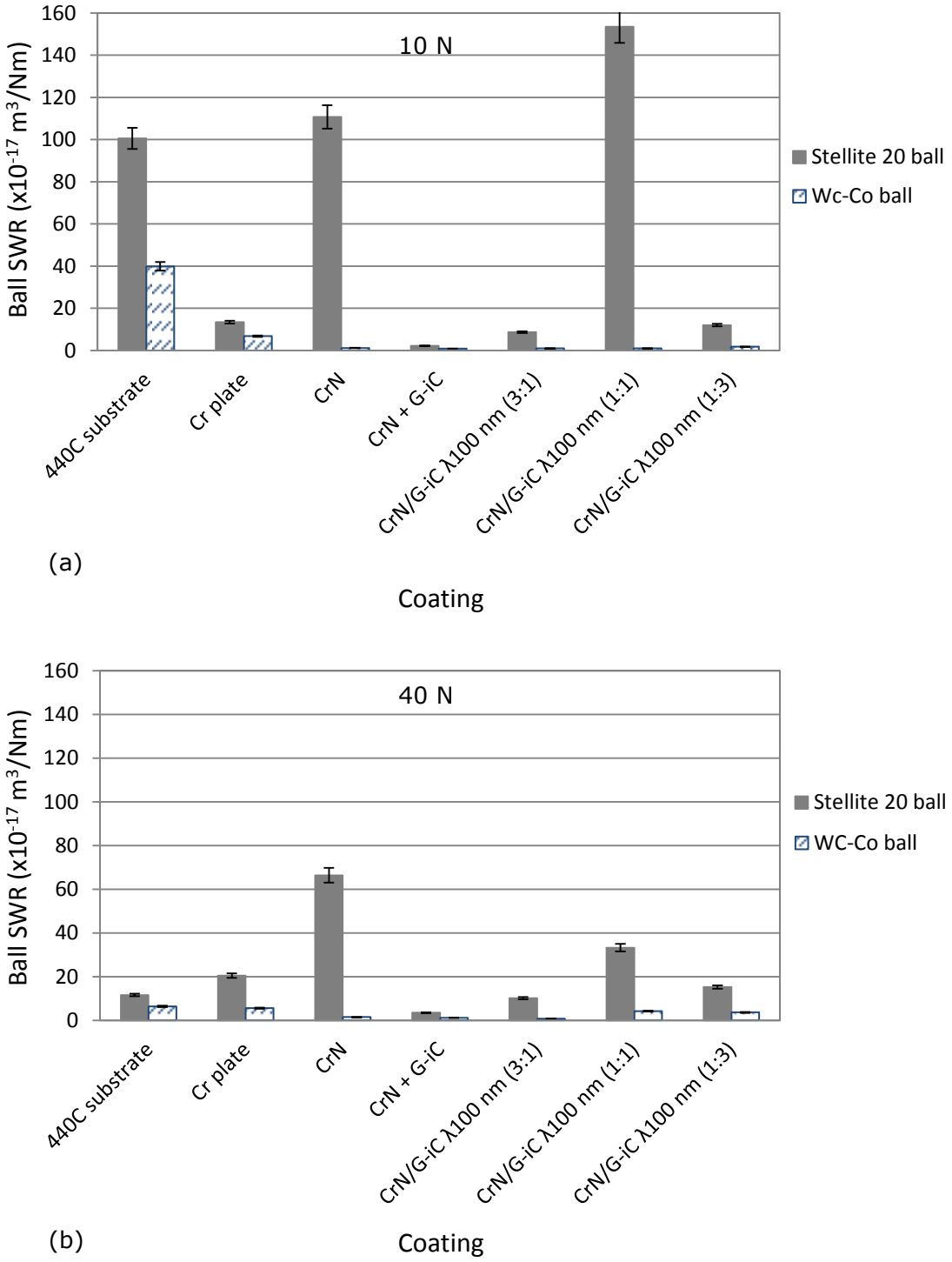


Figure 4-25 Specific wear rate of Stellite 20 and WC-Co counterface balls at (a) 10 N & (b) 40 N normal load against batch 3 coatings on 440C substrates, error bars represent the standard deviation

It was observed that the wear of the Cr plate was high when tested against a WC-6%Co ball, however, the wear was not measurable when tested against a Stellite 20 ball (Figure 4-24) as expected due to the harder and more aggressive nature of the WC-6%Co ball. In turn, the Stellite 20 ball suffered more wear than the WC-6%Co ball (Figure 4-25). This highlights the importance of testing coatings using a counterface material that represents the service conditions of the coating.

The wear rates of the counterface balls were higher for the Stellite 20 balls, against all coating types, at both 10 and 40 N normal load (Figure 4-25 (a & b)), compared to those resulting from tests carried out with the WC-6%Co balls. The CrN + Graphit-iC coating resulted in the lowest counterface wear rate at both 10 and 40 N normal load. At both loads, a trend was seen across the multilayer coatings, showing that the CrN/Graphit-iC λ100 nm (1:1) coating caused the highest counterface ball wear rate and the CrN/Graphit-iC λ100 nm (3:1) coating caused the lowest. In tests carried out at 40 N normal load (Figure 4-25 (b)), only the CrN + Graphit-iC and CrN/Graphit-iC λ100 nm (3:1) coatings resulted in lower ball wear rates than the uncoated substrate. Optical microscope images of typical wear scars observed on the Stellite 20 balls are shown in Figure 4-26. Tests against the CrN/Graphit-iC (1:1) coating revealed a smaller ball wear scar at 40 N (Figure 4-26 (d)), however a wider and more uniform wear tack was observed on the coating (Figure 4-28 (d)) which could have resulted in a lower contact pressure and therefore lower wear on the ball.

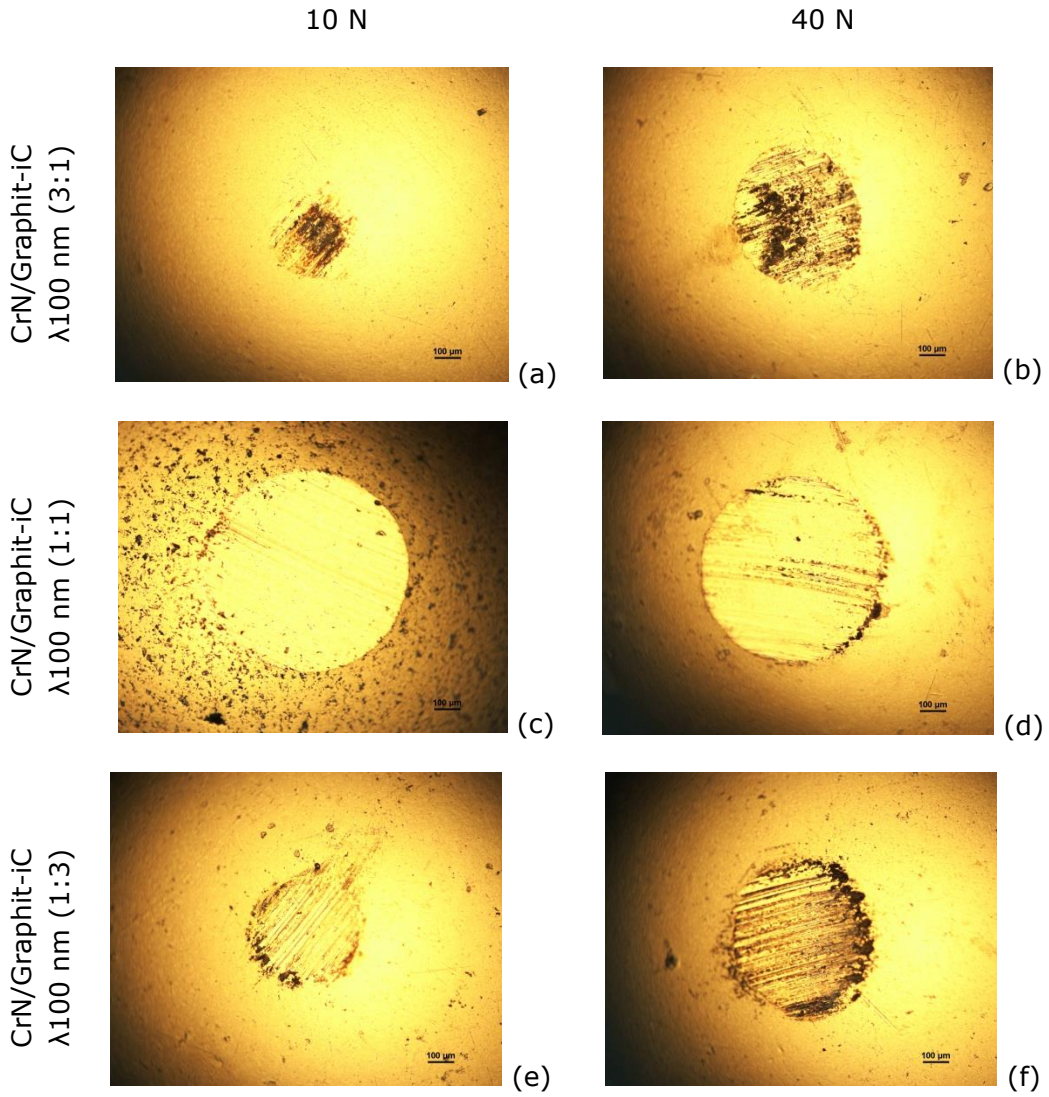


Figure 4-26 Optical microscope images of Stellite 20 ball wear scars after sliding wear tests against batch 3 coatings on 440C substrates (a & b) CrN/Graphit-iC (λ100 nm (1:3)) at (a) 10 N and (b) 40 N normal load (c & d) CrN/Graphit-iC (λ100 nm (1:1)) at (c) 10 N and (d) 40 N normal load (e & f) CrN/Graphit-iC (λ100 nm (3:1)) at (e) 10 N and (f) 40 N normal load

The largest transfer layer was observed on the balls tested against the CrN/Graphit-iC λ100 nm (3:1) coating and almost no transfer layer was observed on the balls tested against the CrN/Graphit-iC λ100 nm (1:1) coating (Figure 4-26 (c & d)).

Optical microscope images of the wear scars observed on the Stellite 20 balls after testing against the uncoated 440C substrates are shown in Figure 4-27. A smaller wear scar was observed on the ball tested at 40 N load compared to that tested at 10 N, however, at 40 N a larger dark debris layer was present which could have helped protect the ball from wear.

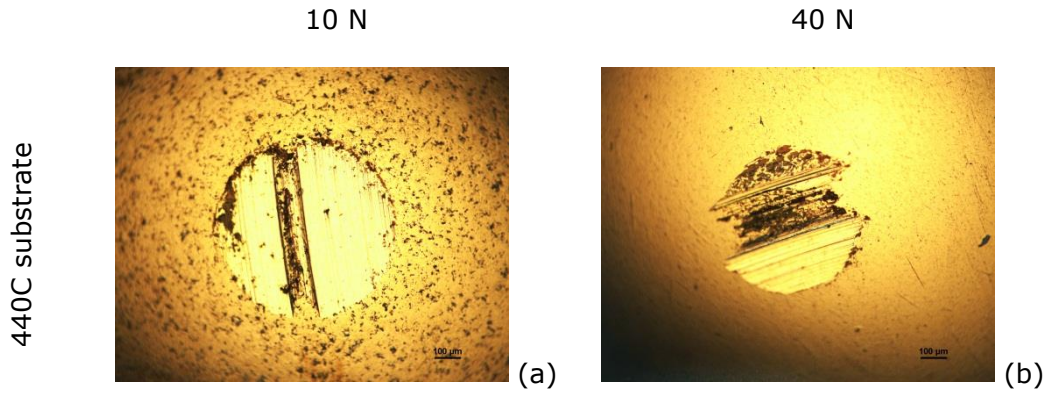


Figure 4-27 Optical microscope images of Stellite 20 ball wear scars after sliding wear tests against uncoated 440C substrates at (a) 10 N and (b) 40 N normal load

A much larger specific wear rate is observed for balls tested against the CrN, CrN/Graphit-iC λ100 nm (1:1) coatings and the uncoated 440C substrate (Figure 4-25) at 10 N load & compared to 40 N as seen by the larger ball wear scars observed in optical microscope images (Figure 4-26 (c & d) & Figure 4-27). The large increase in specific wear rate value is related to the calculation used to derive the specific wear rate and the different loads utilised (10 N and 40 N) and different sliding distances of 252 m and 180 m respectively:

$$Specific\ Wear\ Rate\ \left(\frac{m^3}{Nm}\right) = \frac{V_c}{L \times d} \qquad \textbf{Eq. 3.14}$$

For coatings tested at 10 N, the specific wear rate is calculated by $\frac{V_c}{10 \times 252} = \frac{V_c}{2520}$

Whereas, for coatings tested at 40 N, the specific wear rate is calculated by $\frac{V_c}{40 \times 180} = \frac{V_c}{7200}$, which could explain the large difference in wear rates.

Top surface SEM images of the wear scars on coatings deposited on 440C substrates are presented in Figure 4-28 and Figure 4-29.

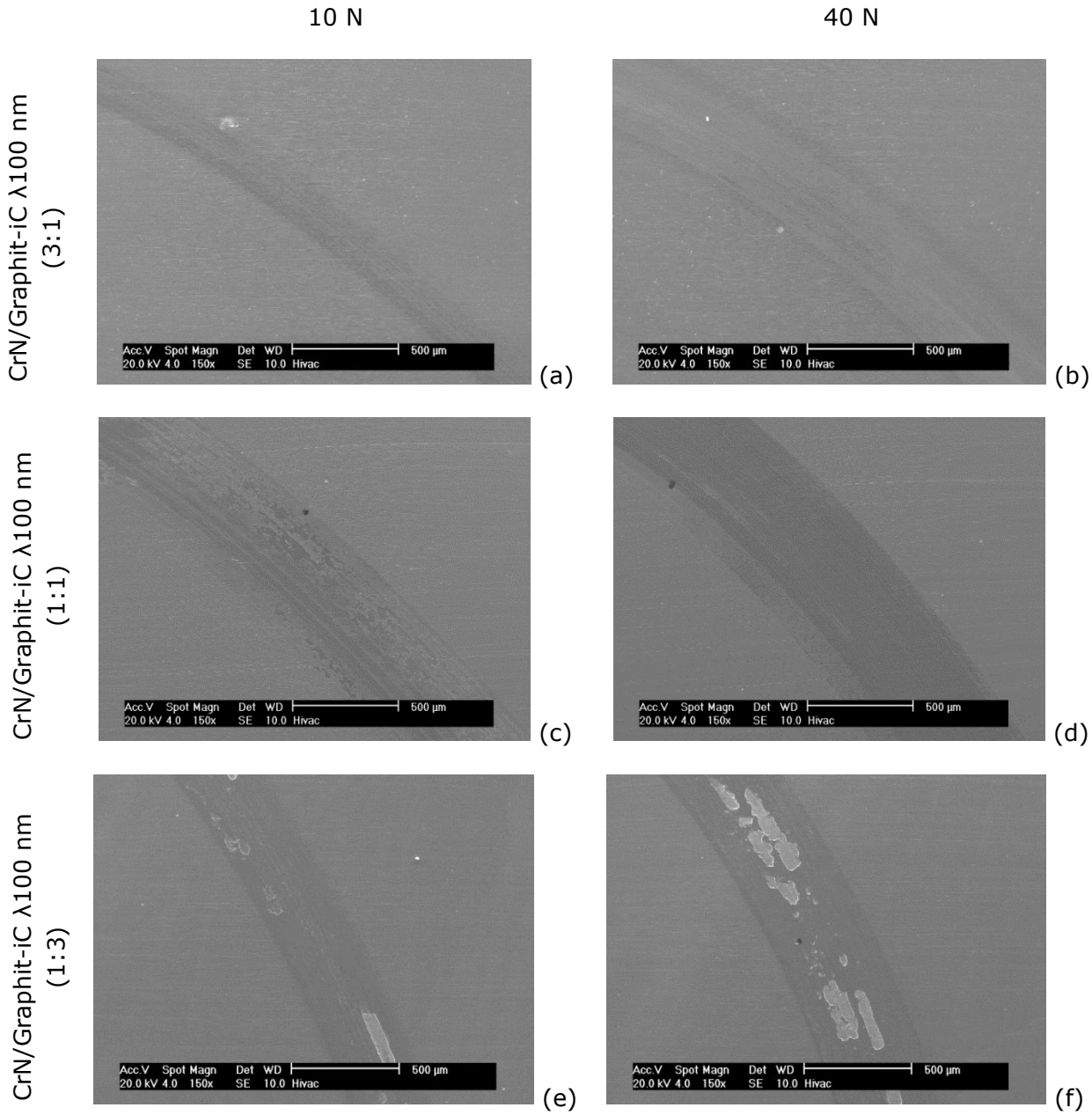


Figure 4-28 Top surface SEM micrographs of the wear scars on the CrN/Graphit-iC λ100 nm multilayer coatings, deposited in batch 3, on 440C substrates after sliding wear tests (a & b) CrN/Graphit-iC multilayer (λ100 nm (3:1)) coating at (a) 10 N and (b) 40 N normal load (c & d) CrN/Graphit-iC multilayer (λ100 nm (1:1)) coating at (c) 10 N and (d) 40 N normal load (e & f) CrN/Graphit-iC multilayer (λ100 nm (1:3)) coating at (e) 10 N and (f) 40 N normal load against Ø3/8" Stellite 20 balls

All CrN/Graphit-iC coatings with 100 nm bilayer periods, with different architectures, showed similar wear modes when tested against Stellite 20 balls (Figure 4-28 (a-f)). Smoothing of the top surface was seen on all coatings. Delamination of multilayers was seen on the CrN/Graphit-iC multilayered (λ100 nm (1:3)) coating at both 10 N and 40 N (Figure 4-28 (e & f)); however, the substrate was not exposed.

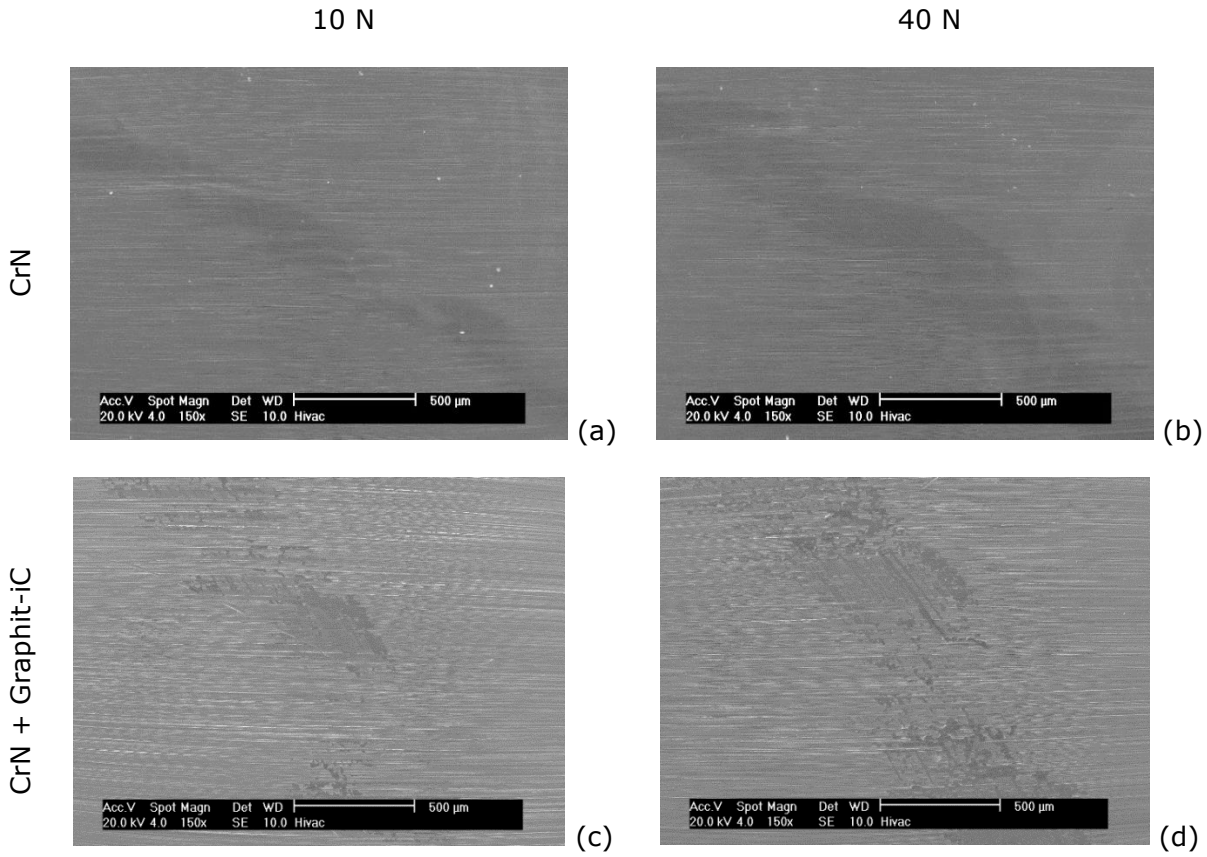


Figure 4-29 Top surface SEM micrographs of the wear scars on the CrN and CrN + Graphit-iC coatings, deposited in batch 3, on 440C substrates after sliding wear tests (a & b) CrN coating at (a) 10 N and (b) 40 N normal load (c & d) CrN + Graphit-iC coating at (c) 10 N and (d) 40 N normal load against Ø3/8" Stellite 20 balls

The wear scars on the CrN and CrN + Graphit-iC coatings (Figure 4-29 (a-d)) were not measurable by profilometry. It can be seen from the SEM images of the wear scars that some smoothing of the top surface of the coatings has occurred; however, little wear had taken place on the coatings. Friction coefficients recorded for the CrN/Graphit-iC multilayer coatings when tested against Stellite 20 balls are presented in Figure 4-30.

The friction coefficients from tests using Stellite 20 balls (Figure 4-30) showed similar patterns to those using a WC-6%Co ball (Figure 4-22). The friction during tests on the CrN/Graphit-iC λ100 nm (3:1) (Figure 4-30 (a & b)) and λ100 nm (1:1) coatings (Figure 4-30 (c & d)) showed an increase in coefficient throughout the duration of the test.

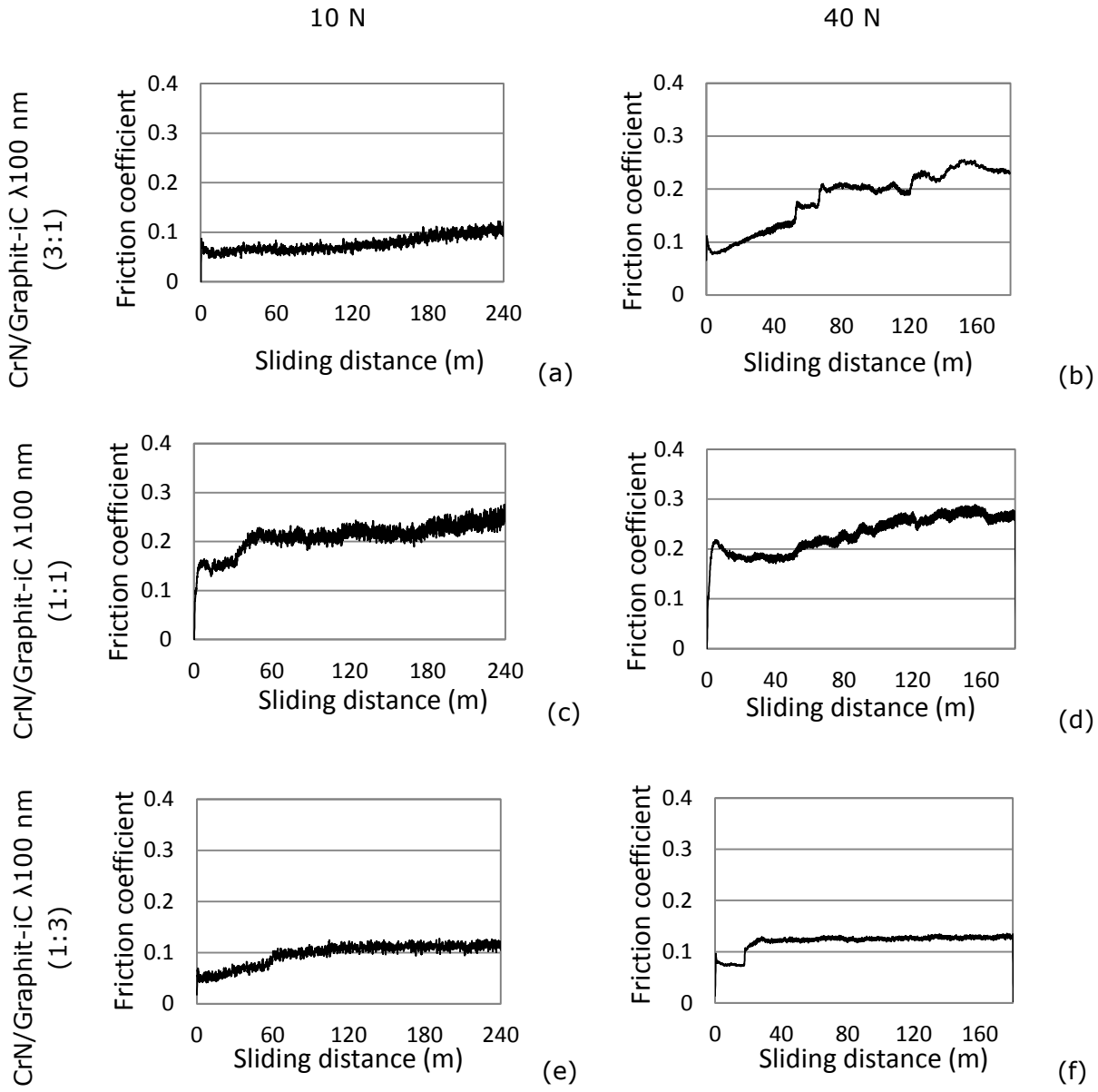


Figure 4-30 Friction coefficients of coatings, deposited in batch 3, on 440C substrates (a & b) CrN/Graphit-iC multilayer (λ100 nm (3:1)) at (a) 10 N and (b) 40 N normal load (c & d) CrN/Graphit-iC multilayer (λ100 nm (1:1)) at (c) 10 N and (d) 40 N normal load (e & f) CrN/Graphit-iC multilayer (λ100 nm (1:3)) at (e) 10 N and (f) 40 N normal load against Ø3/8" Stellite 20 balls

Tests on the CrN/Graphit-iC λ100 nm (3:1) coating at 40 N (Figure 4-30 (b)) showed a steep increase in friction coefficient compared to other tests as the friction coefficient increased from around 0.1 to 0.25 throughout the test.

The CrN/Graphit-iC λ100 nm (1:3) coating (Figure 4-30 (e & f)) showed the most stable friction coefficient. A steady state friction coefficient of around 0.1 was reached

after around 60 m of sliding at 10 N normal load (Figure 4-30 (e)), and after around 20 m of sliding at 40 N normal load (Figure 4-30 (f)).

Friction coefficients of all systems are presented in Figure 4-31. For systems where a steady state friction was reached, the friction coefficient is measured from the coefficient of steady state friction. For systems where the friction coefficient gradually increased throughout the test, an average coefficient was taken for the friction coefficient of the system. The friction coefficients, at both 10 and 40 N normal load (Figure 4-31 (a & b)), followed similar trends regardless of the counterface ball type. In tests carried out at 10 N normal load (Figure 4-31 (a)), the friction coefficients against Stellite 20 balls were generally lower than, or equal to, those acquired using WC-6%Co balls. However, tests against the uncoated 440C substrate and CrN coating showed higher friction coefficients when tested against Stellite 20 balls. All coatings resulted in a reduction in friction coefficient compared to the uncoated 440C substrate and chromium plate. The CrN/Graphit-iC λ100 nm (1:3) and λ100 nm (3:1) multilayer coatings, tested against a Stellite 20 ball, exhibited lower friction coefficients than the CrN coating; however, all multilayer coatings showed higher friction coefficients than the dual layered CrN + Graphit-iC coating against both balls, at both 10 N and 40 N (Figure 4-31 (a & b)).

At 40 N normal load (Figure 4-31 (b)), tests on the CrN +Graphit-iC coating and Cr plate resulted in a lower friction coefficient when tested against a Stellite 20 ball compared to when tested against a WC-6%Co ball. However, the friction coefficients acquired with Stellite 20 balls were generally higher than those acquired using WC-6%Co balls, as opposed to the opposite trend seen under testing with a 10 N normal load (Figure 4-31 (a)). As was seen in tests at 10 N normal load, the CrN/Graphit-iC λ100 nm (1:1) coating resulted in the highest friction coefficient and the CrN/Graphit-iC λ100 nm (1:3) coating resulted in the lowest friction coefficient out of the multilayer coatings (Figure 4-31 (b)).

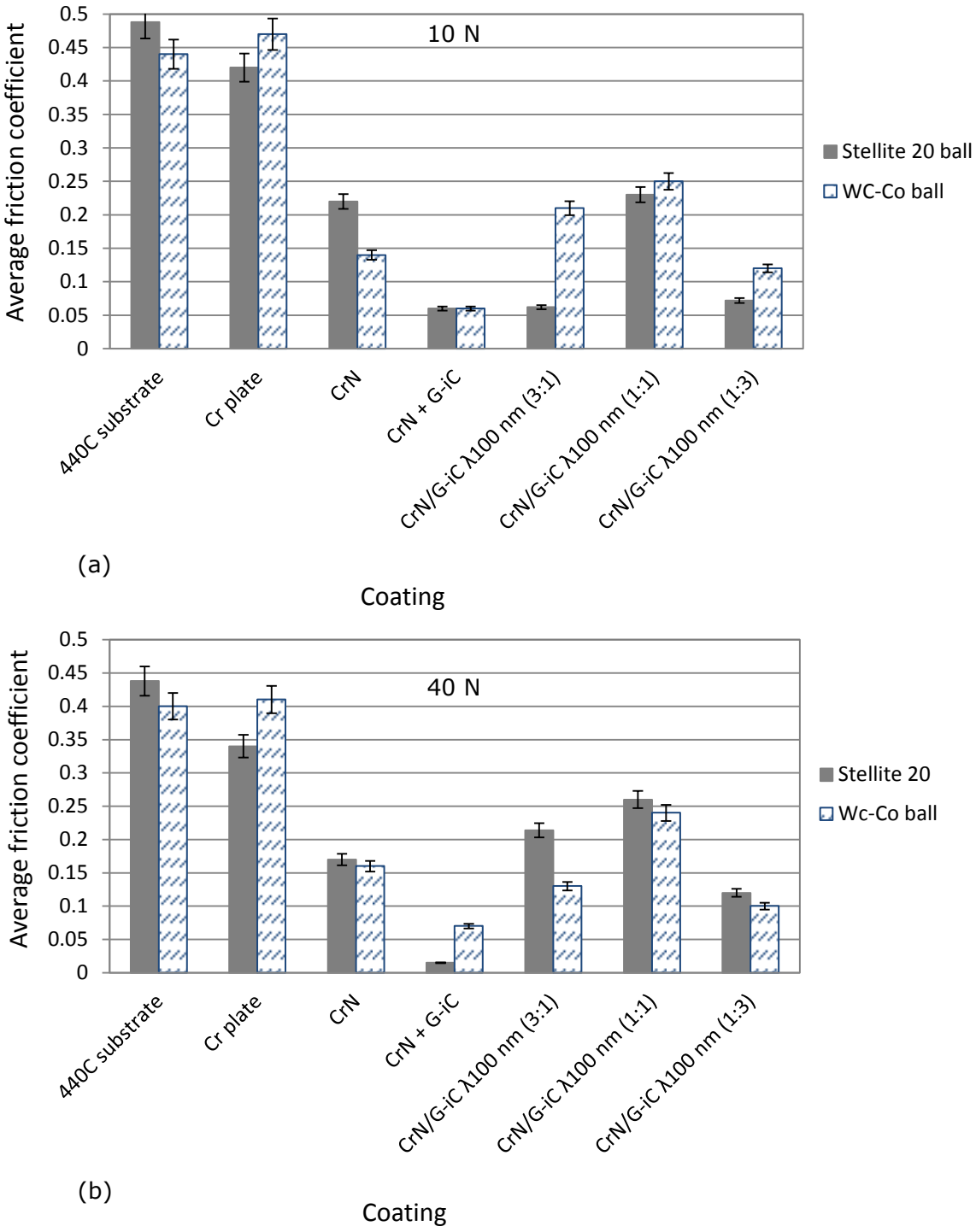


Figure 4-31 Friction coefficient of coatings on 440C substrates, deposited in batch 3, against Ø3/8" WC-6%Co and Stellite 20 balls at (a) 10 N & (b) 40 N normal load, error bars represent the standard deviation

The CrN + Graphit-iC coating exhibited the lowest ball wear rates (Figure 4-25), friction coefficients (Figure 4-31) and a low coating wear (Figure 4-29), outperforming all coatings.

4.2.5 Summary

Multilayering was seen to increase coating hardness and scratch resistance with a trend of the thinner the bilayer period the higher the scratch resistance and hardness of the coatings. All multilayer coatings gave higher hardnesses than the dual layered CrN + Graphit-iC coating. However, the dual layered CrN + Graphit-iC coating showed the highest scratch resistance out of all coatings. Multilayering generally resulted in no improvement in coating wear resistance and often resulted in an increase in friction coefficient. It was observed that, for multilayer systems, the friction coefficient is generally determined by the material with the highest friction coefficient in that system (rather than by that with the lowest) as, once the coating is worn, the counterface ball is generally in contact with both materials (multiple layers) from the multilayer system at one time. The dual layer CrN + Graphit-iC coatings generally resulted in the lowest friction coefficients, wear depths and counterface ball wear rates. The hardness of the substrates appeared to affect the wear properties of coatings. A general trend was seen indicating that the lower the substrate hardness, the higher the wear rate of the coating and the higher the friction. Coatings deposited on hard M42 substrates generally exhibited the least wear and lowest friction coefficients. Multilayering resulted in peak broadening of X-ray diffraction scans which could be attributed to smaller grain sizes or residual stresses in coatings.

The multilayer architecture was seen to have a clear effect on the hardness, scratch, wear and frictional properties of coatings. It was seen that both the CrN/Graphit-iC λ100 nm (3:1) and λ100 nm (1:3) coatings exhibited lower friction coefficients than the λ100 nm (1:1) coating however, the λ100 nm (1:1) coating resulted in the lowest wear depths out of the multilayer coatings as the λ100 nm (1:3) coating exhibited heavy delamination. The dual layered CrN + Graphit-iC coatings still showed the lowest wear rates and friction coefficients. Tests against the Stellite ball generally showed higher friction coefficients and higher counterface ball wear rates than those when tested against a WC-6%Co ball.

4.3 Mechanical and Corrosion Resistant Properties of Single and Multilayered PVD Coatings

This section presents the data regarding structural characterization, mechanical and corrosion resistant properties of IN625, IN625 + Cr and IN625/Cr multilayer PVD coatings which were being investigated for their potential to be both corrosion and scratch resistant. This section of the research aims to investigate growth defects within the coatings and their relation to the corrosion resistance of the coatings. Through the results, this research also aims to provide a step forward in the progress towards the development of PVD coatings with enhanced corrosion resistance and mechanical properties (particularly the ability to resist scratching).

4.3.1 Coating microstructure

Scanning electron microscopy and X-ray diffraction were employed to characterise the structure of the coatings. Growth defects were observed in the coatings which were later demonstrated to create a pathway for corrosive media to the substrate. Typical defects found in PVD coatings can be seen in cross-sectional micrographs shown in Figure 4-32 (a-d).

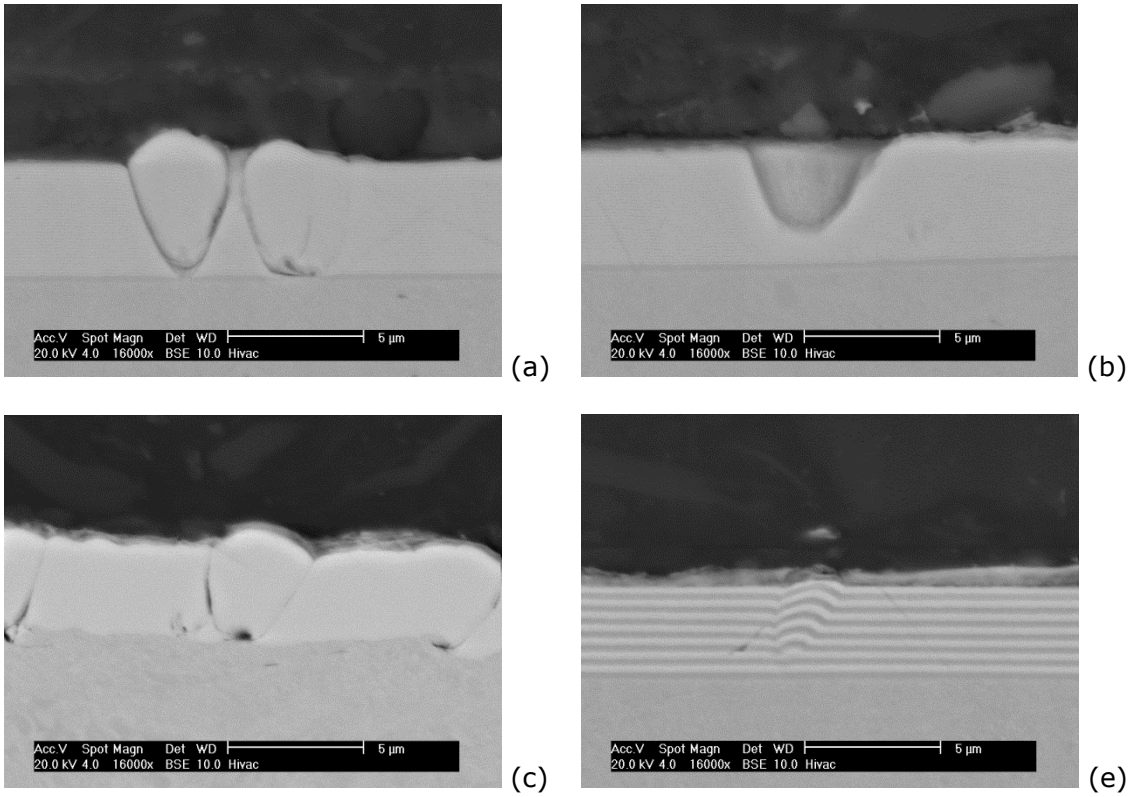


Figure 4-32 Typical defects found in PVD coatings (a & b) IN625/Cr multilayer (λ100 nm) (c) IN625/Cr multilayer (λ20 nm) (d) IN625/Cr multilayer (λ600 nm) deposited on mild steel substrates

Under standard deposition conditions, it was found that there are generally around 100 to 200 of these defects in a 4300 μm^2 area as discussed later in section 4.3.5.4. These defects have a deleterious effect on the mechanical and corrosion properties of the coatings (Brandl and Gendig, 1996; Ries et al., 1997; Cunha and Andritschky, 1999; Jehn, 2000; Lewis et al., 2006; Altun and Sen, 2007; Čekada et al., 2007; Panjan et al., 2009; Hoche et al., 2011; Panjan et al., 2012; Panjan et al., 2013) and it is an aim of this work to tailor the processing of the coatings to reduce their defect density. Further investigation into these defects and their origin is presented in section 4.3.4.

X-ray diffraction patterns from the coatings are presented in Figure 4-33. The IN625, IN625 + Cr and IN625/Cr multilayer coatings showed a preferred orientation of diffraction peaks in the {1 1 1} plane of the nickel matrix phase at 43.4° 2θ. Peaks were also observed in the {2 2 0} and {3 1 1} planes for the nickel matrix phase at

74.3° and 90.2° 2θ. The IN625 + Cr and IN625/Cr multilayer coatings also showed strong diffraction peaks in the {1 1 0} plane for the chromium phase at 44.4° 2θ. Peaks were also observed in the {2 0 0}, {2 1 1} and {2 2 0} planes for the chromium phase at 64.6°, 81.7° and 98.1° 2θ respectively. Peak broadening was observed for the multilayered coatings indicating that the thinner the bilayer period the greater the broadening.

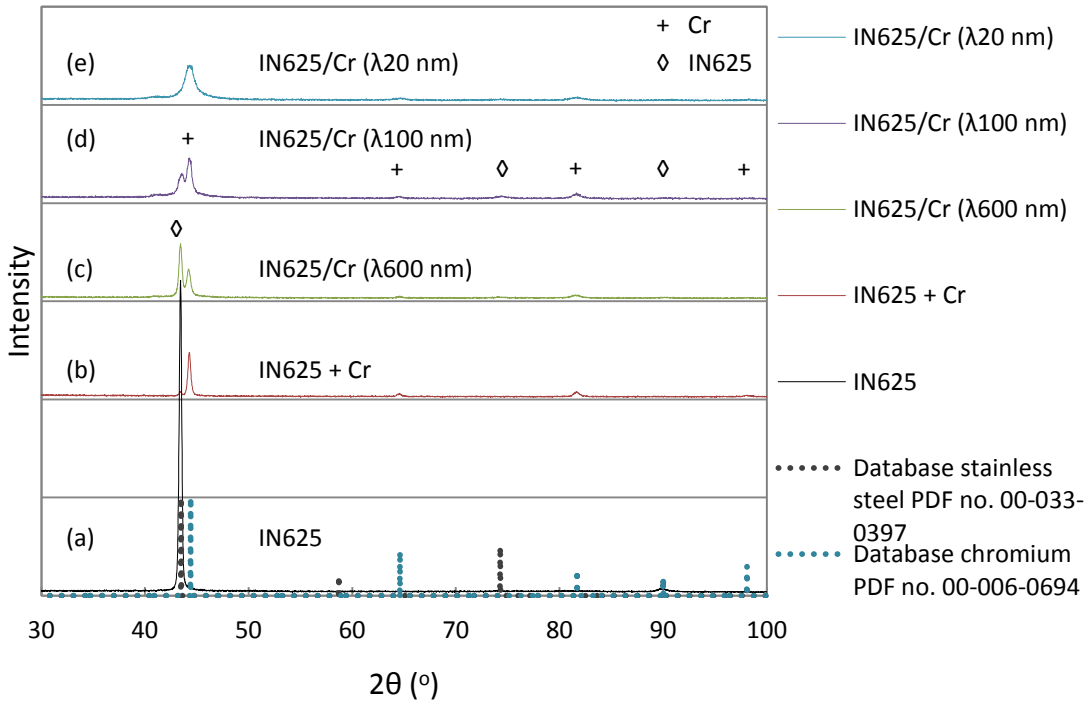


Figure 4-33 XRD patterns of (a) IN625 (b) IN625 + Cr, (c) IN625/Cr multilayer (λ600 nm) (d) IN625/Cr multilayer (λ100 nm) (e) IN625/Cr multilayer (λ20 nm) coatings on 440C substrates

A nickel plate coating was used as a reference material in this research, a cross--section of the coating can be seen in Figure 4-34.

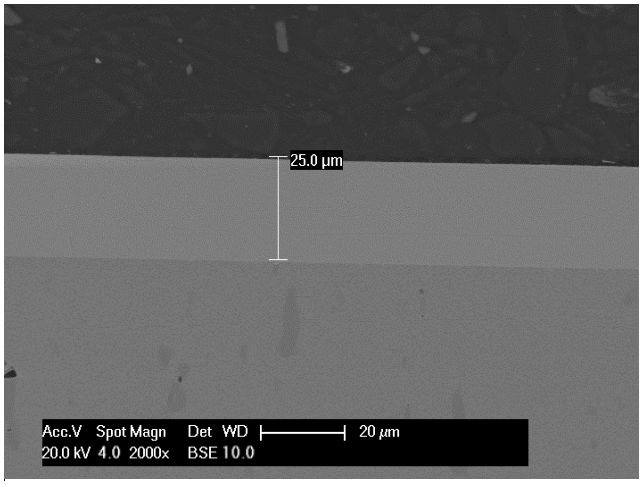
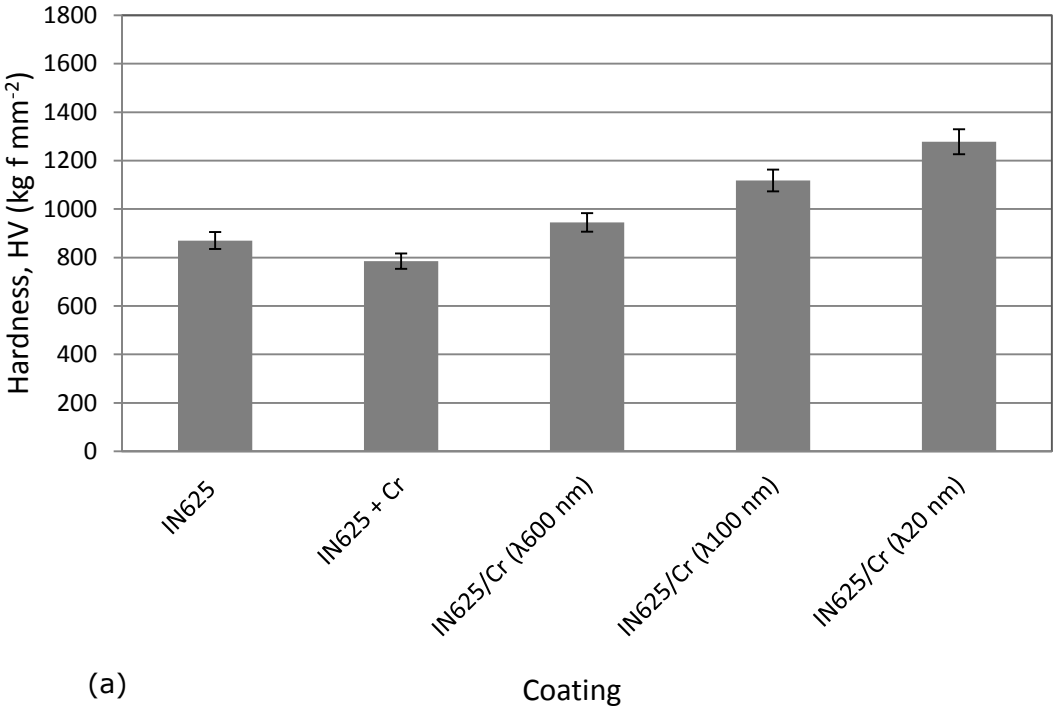


Figure 4-34 SEM micrograph of nickel plate coating cross-section on a 440C substrate

The coating thickness was measured, using SEM, to be 25 ± 0.1 µm (much thicker than any of the PVD coatings). The hardness of the coating was measured using a Buehler 1600-6400 microhardness tester at 25 gf. The hardness was measured to be around HV = 614 ± 42 kg f mm^{-2}.

4.3.2 Effect of multilayering on the mechanical properties of coatings

The hardness and scratch resistance of coatings was measured; the results are presented in Figure 4-35. The microhardnesses of coatings (Figure 4-35 (a)) showed that adding a chromium top layer to the IN625 did not increase the coating hardness compared to monolayer IN625; however, multilayering of the IN625/chromium did result in a substantial hardness increase. There was also a clear trend that the smaller the bilayer period, the higher the hardness of the coating. The IN625/Cr (λ20 nm) multilayer coating showed a hardness of HV = 1278 kg f mm^{-2} compared to the monolayer IN625 coating which showed a hardness of HV = 870 kg f mm^{-2}. All indentation depths were between $1/7^{th}$ and $1/12^{th}$ of the coating thicknesses.



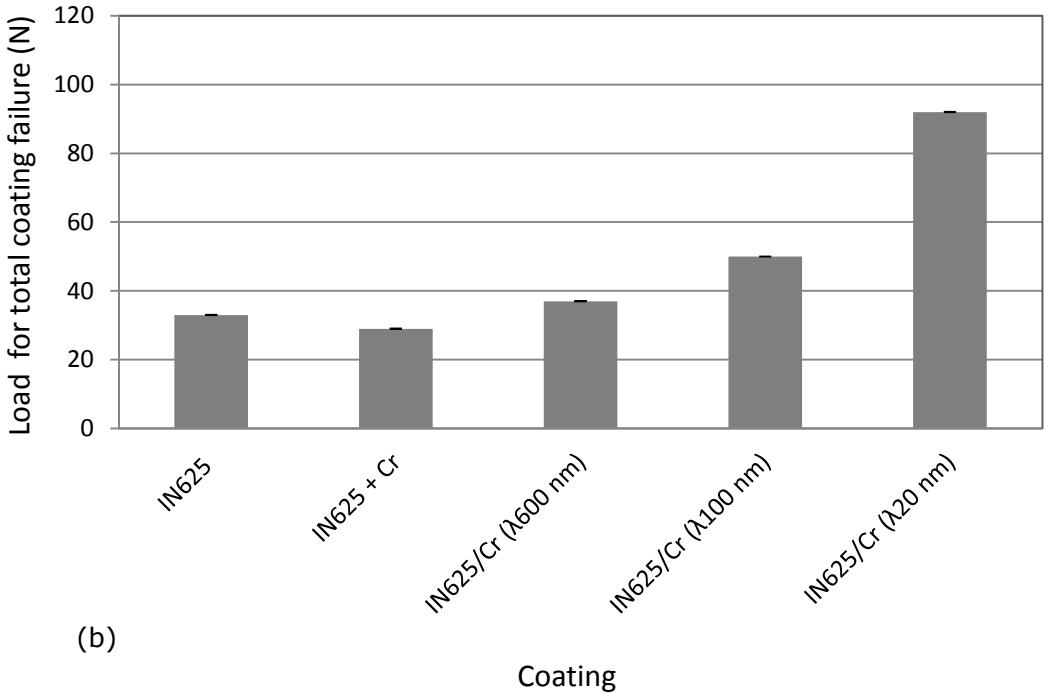


Figure 4-35 Effect of multilayering on the (a) hardness and (b) scratch resistance of coatings deposited on an M42 substrate (HV = 946 ± 2 kg f mm^{-2}) in batch 1, error bars represent the equipment errors

Scratch testing on the multilayered also showed a clear trend that, the smaller the bilayer period, the higher the adhesion of the coating (Figure 4-35 (b)). All IN625/Cr

multilayered systems showed higher scratch resistances than the dual layered IN625 + Cr and the monolayer IN625. The IN625/Cr (λ20 nm) multilayer system experienced total failure at 92 N compared to the dual layered IN625 + Cr coating which failed at just 29 N. Images of typical scratch scars at the point of failure are presented in Figure 4-36.

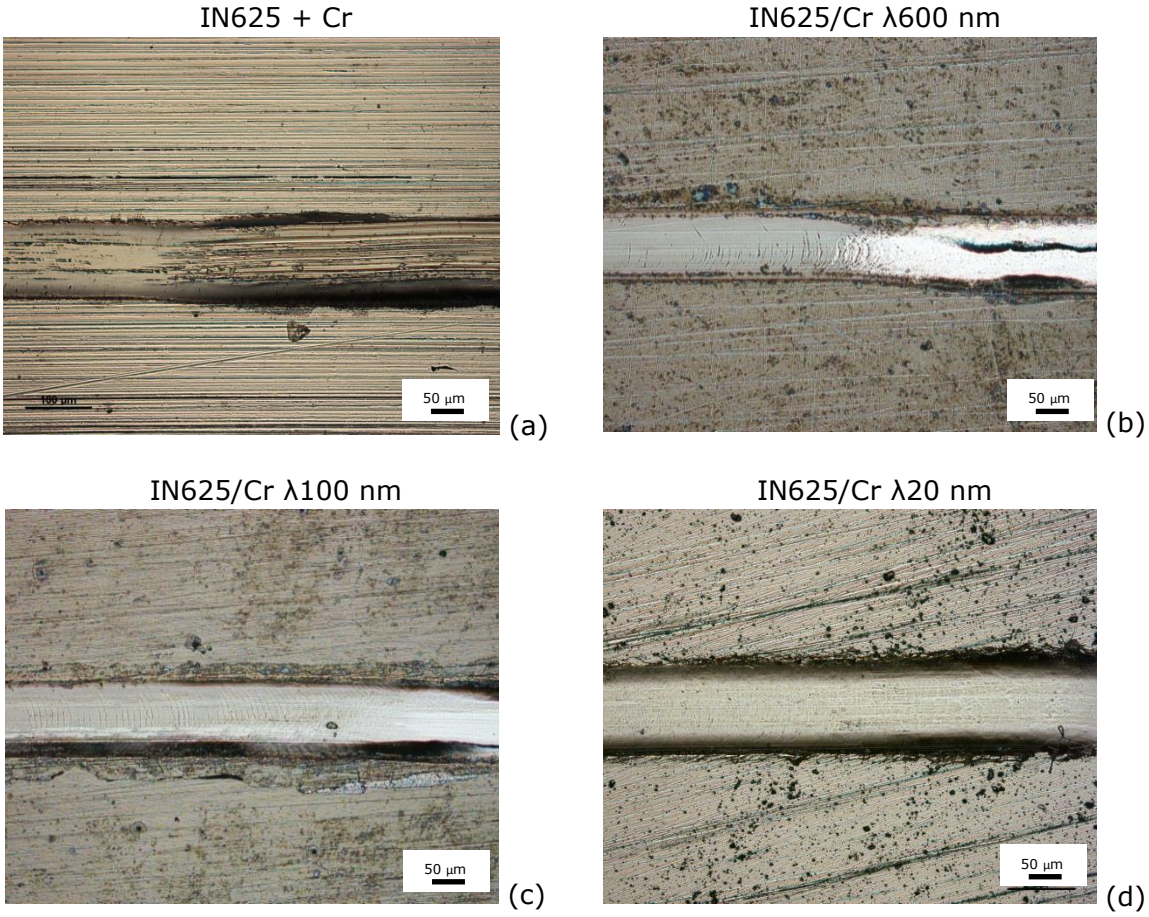


Figure 4-36 Scratch scar images of coatings on M42 substrates (a) CrN (b) IN625/Cr λ600 nm (c) IN625/Cr λ100 nm (d) IN625/Cr λ20 nm

Coating failure is defined by total delamination from the substrate, before the final load or maximum friction force of 30 N is reached. The IN625 + Cr coating showed a lot of delamination throughout the track (Figure 4-36 (a)) compared to the multilayer coatings (Figure 4-36 (b, c & d)). The IN625/Cr λ600 nm coating (Figure 4-36 (b)) showed a ribbed scratch scar until complete delamination occurred at the point of failure. In comparison, the λ100 nm and λ20 nm coatings (Figure 4-36 (c & d))

showed partial delamination prior to failure, which then, for the λ100 nm coating, resulting in total delamination and for the λ20 nm coating, resulted in further partial delamination. FIB milling was carried out on the scratch scar on the IN625/Cr λ100 nm coating to investigate the presence of crack deflection caused by multilayers and the possibility of interfacial debonding. SEM was carried out on the scratch scar near the point of coating failure, a cross section of the coating is shown in Figure 4-37.

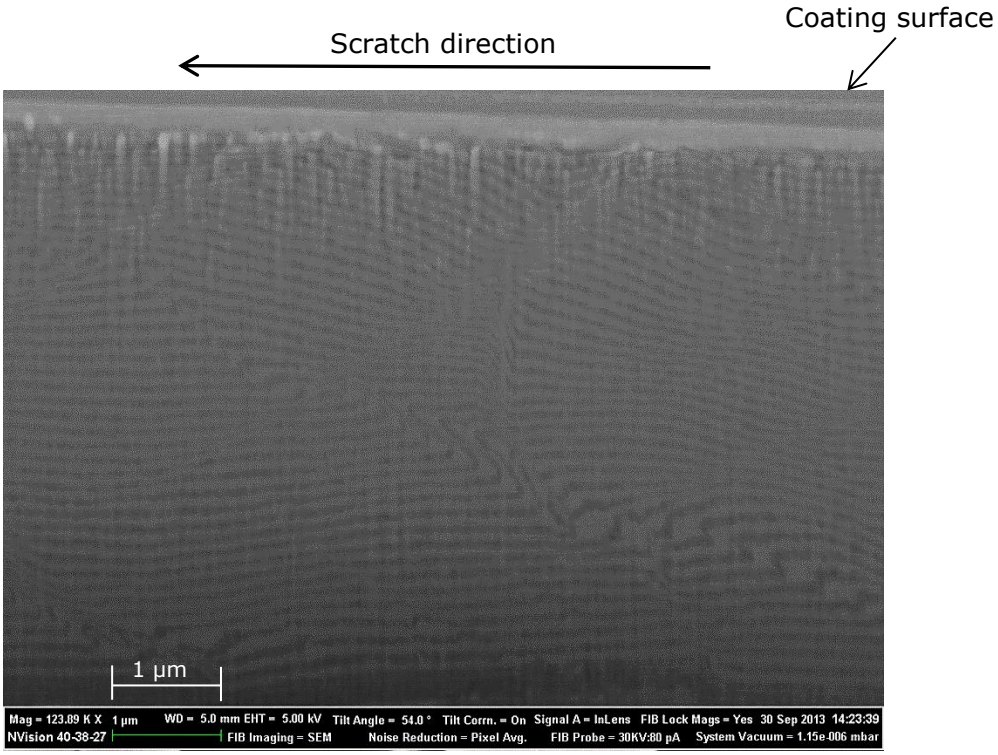


Figure 4-37 FIB SEM cross-section of the scratch scar on the IN625/Cr λ100 nm coating on an M42 substrate

Disruption of the multilayers was observed along the scratch scar. No cracks were clearly identified; however, features running through the coating were observed to be disrupted in direction by the multilayers suggesting the occurrence of plastic flow within the coating. It is not known if these features are related to cracks, interfacial debonding of the multilayers or shear through the coating.

4.3.3 Effect of coating architecture on the corrosion barrier performance of coatings

In this section, the coatings investigated are IN625, IN625 + Cr and IN625/Cr multilayered systems (intended to be corrosion and scratch resistant). As nickel plate is a commonly used coating for corrosion resistance in industry, it was used as a reference. Samples were masked using a waterproof red stopping off lacquer leaving only the coating face exposed as seen in Figure 4-39. Salt spray tests were carried out in 5 wt% salt solution.

The first set of results presented here investigates if multilayering has a beneficial effect on the corrosion behaviour of the coatings. The results of salt spray tests are displayed in Figure 4-38.

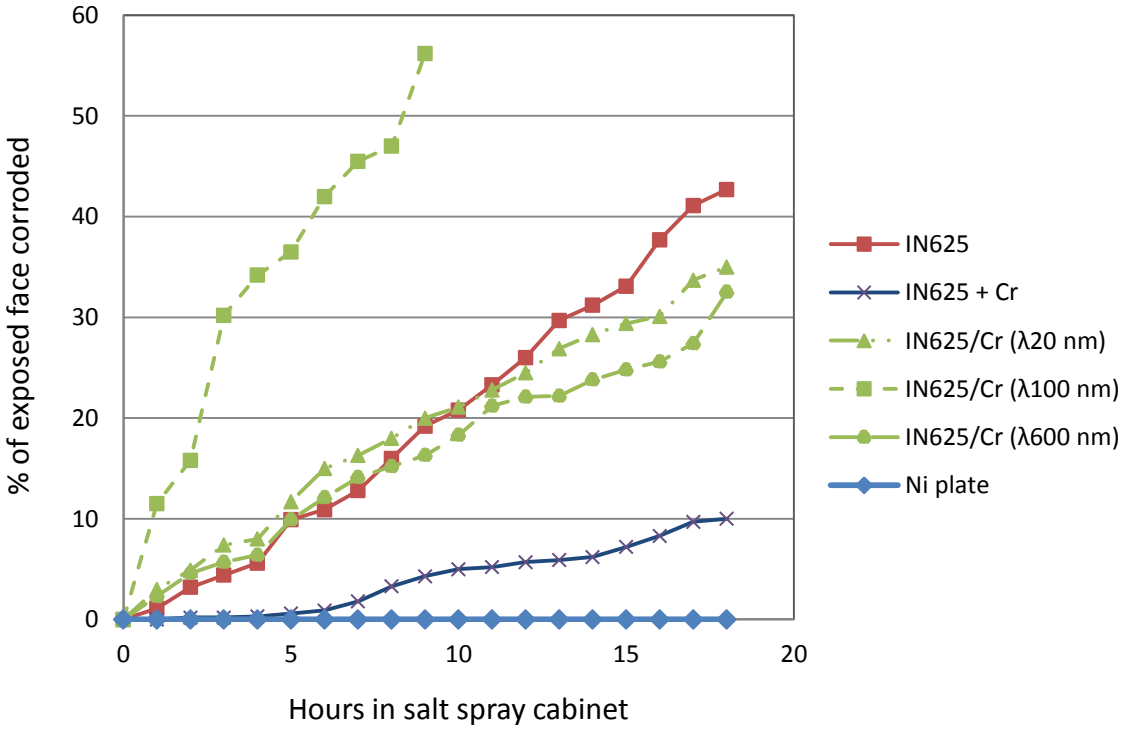


Figure 4-38 Corrosion rate of coatings, deposited in batch 1, with different materials and architectures on mild steel substrates

It can be seen from Figure 4-38, that most coatings exhibited poor corrosion resistance. The dual layered IN625 + Cr coating showed the lowest corrosion rate and the IN625/Cr multilayered (λ100 nm) coating showed the highest corrosion rate.

The multilayers did not provide the improvement to the corrosion resistance of the coatings that had been suggested in the literature (Brandl and Gendig, 1996; Jehn, 2000; Fenker et al., 2006). In comparison, the nickel plate reference sample showed no corrosion for over 200 hours; indicating that none of the PVD coatings were at all competitive in this regard.

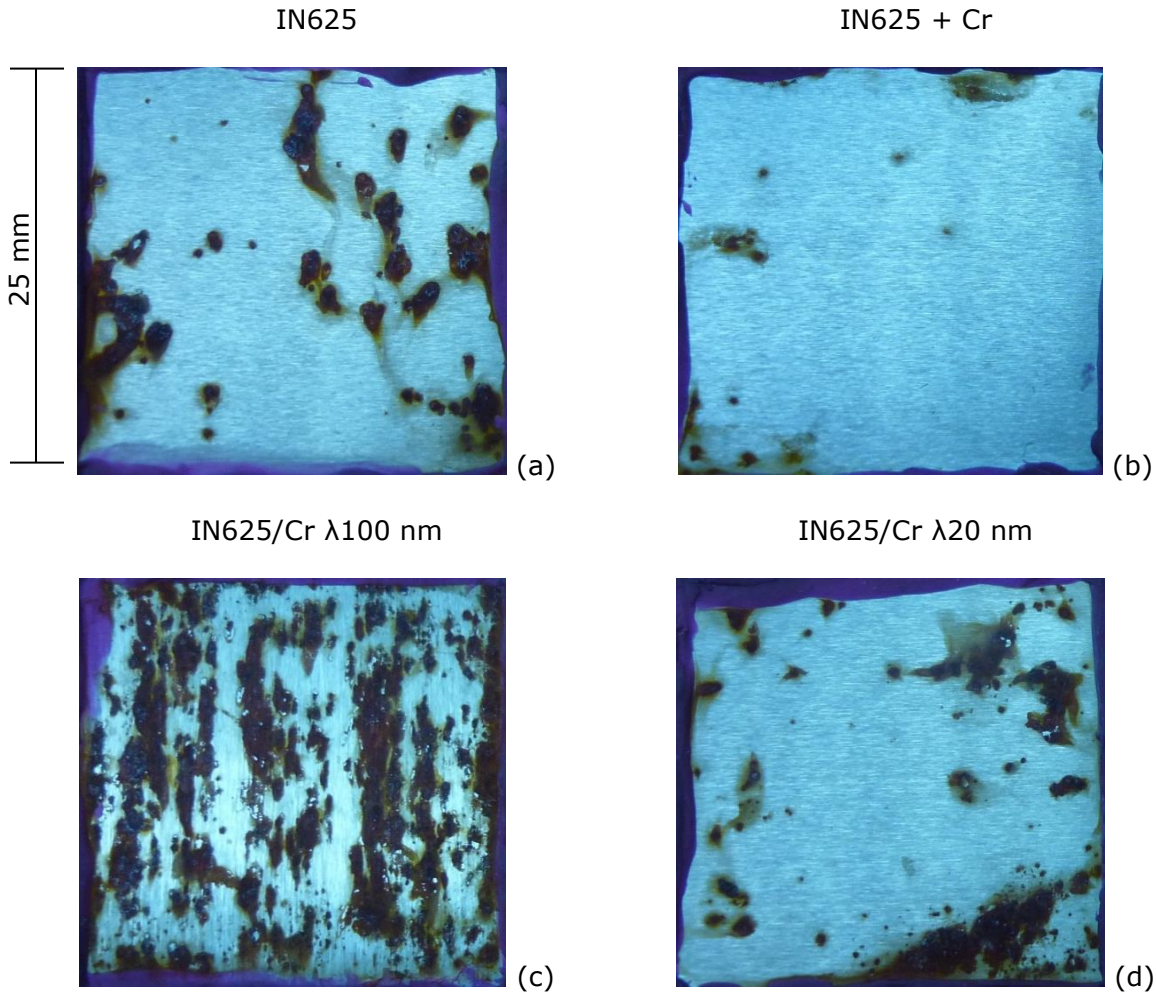


Figure 4-39 Top surface images of corroded batch 1 samples on mild steel substrates after 8 hours of salt spray testing (a) IN625 (b) IN625 + Cr (c) IN625/Cr multilayer (λ100 nm) (d) IN625/Cr multilayer (λ20 nm)

The top surface images of corroded samples (Figure 4-39 (a-d)), show that the corrosion is very localised. This was seen across all coatings. This suggests the corrosive media is reaching the substrate through localised defects such as pores and pinholes within the coatings. Cross sectional SEM was carried out on the corroded

samples to understand how the coatings were failing to act as an effective corrosion barrier.

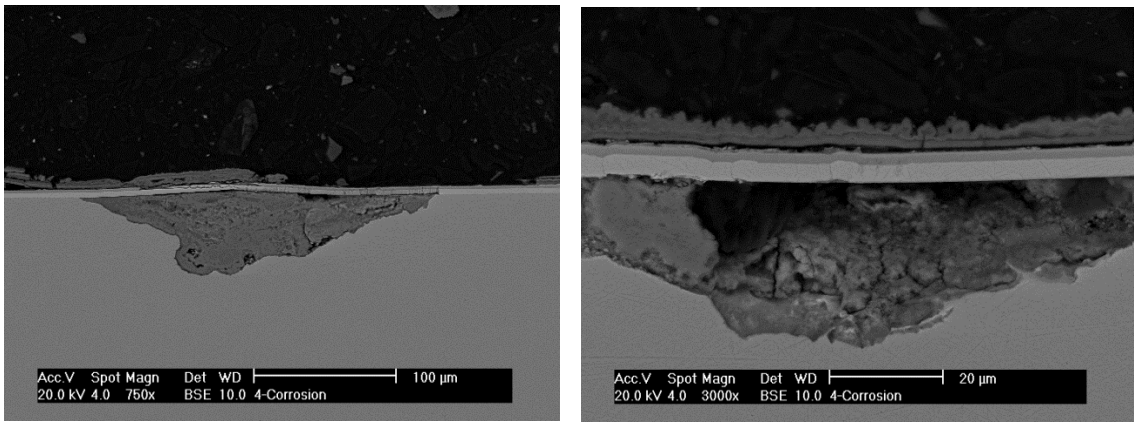


Figure 4-40 Cross sectional SEM micrographs of IN625 + Cr coating, deposited in batch 1 on a mild steel substrate, after 18 hours of salt spray testing

From example cross sectional images of the IN625 + Cr coating (Figure 4-40), it can be seen that the substrate is heavily corroded; however, the coating itself remains intact. This suggests that the corrosive media is reaching the substrate through pores and defects in the coating; the corrosion products then travel from the substrate, through coating pores, and are deposited on the coating surface.

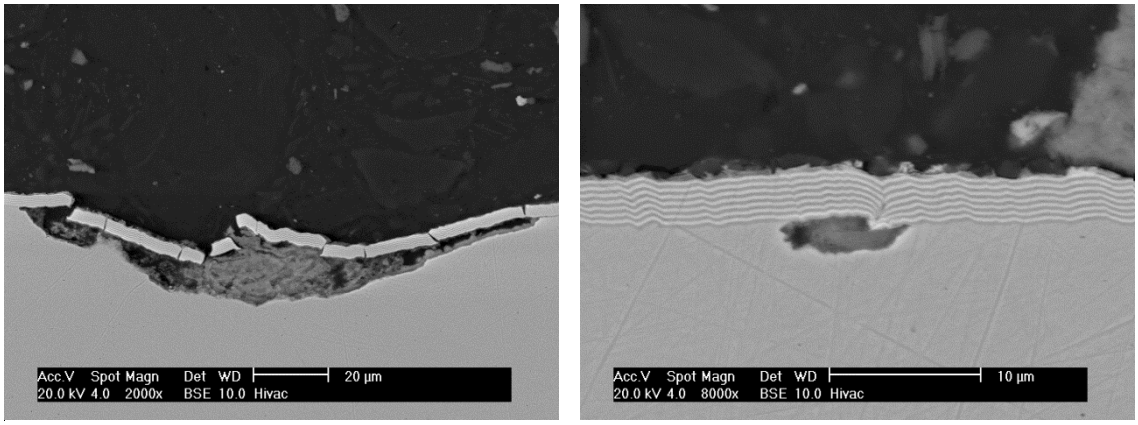


Figure 4-41 Cross sectional SEM micrographs of IN625/Cr multilayered (λ600 nm) coating, deposited in batch 1 on a mild steel substrate, after 18 hours of salt spray testing

From Figure 4-41 it can be seen, where the substrate is heavily corroded and can no longer support the coating, the coating fractures and delaminates. Corrosion can also be seen on the substrate beneath a defect in the coating. The multilayered structure aids in identifying locations of defects within the coatings and has thus assisted in the clear identification of the link between corrosion and the presence of defects as seen in Figure 4-41.

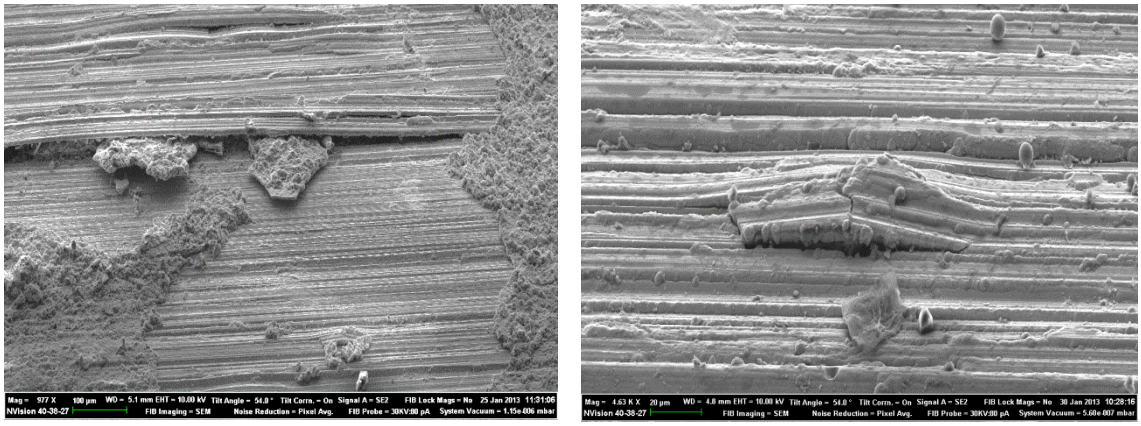
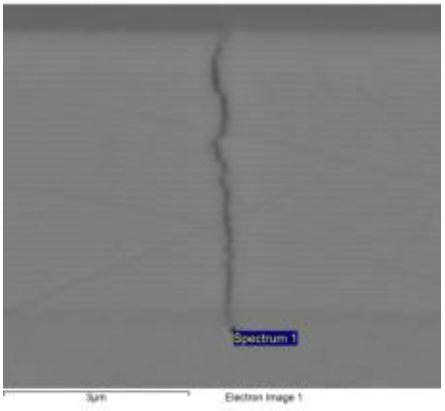


Figure 4-42 Top surface SEM micrographs of the IN625/Cr multilayered (λ100 nm) coating, deposited in batch 1 on a mild steel substrate, after 18 hours of salt spray testing

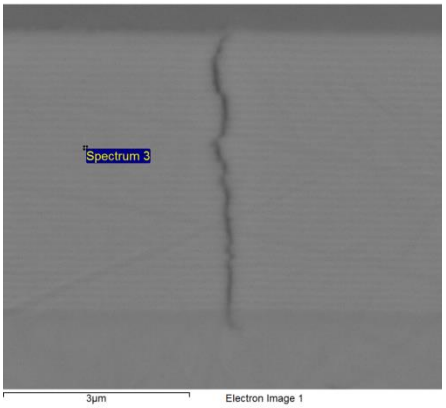
Top surface SEM images were taken of the corroded IN625/Cr (λ100 nm) sample (Figure 4-42). Corrosion products were observed to be pushing up from below the surface of the coating and therefore, delaminating the coating. EDX analysis was carried out on a heavily corroded section underneath the IN625/Cr λ100 nm coating. The analysis indicated the material was an oxide of iron. This was consistent with the rust coloured surface deposits observed in Figure 4-39. A crack was found (Figure 4-43) in the IN625/Cr multilayered (λ100 nm) coating, where slight corrosion could be observed on the substrate at the bottom of the crack.

Element	Weight %	Atomic %
C K	14	42
O K	2	5
Cr K	16	11
Fe K	64	40
Ni K	4	2
Totals	100	



(a)

Element	Weight %	Atomic %
C K	16	47
Cr K	47	32
Fe K	3	2
Ni K	29	17
Mo K	5	2
Totals	100	



(b)

Figure 4-43 EDX results taken on the corroded IN625/Cr multilayered (λ100 nm) coating, deposited in batch 1 on a mild steel substrate, after 18 hours of salt spray testing (a) at the coating substrate interface below the crack (b) at the coating away from the crack

EDX analysis was carried out on the corroded section (Figure 4-43). Below the crack in the IN625/Cr multilayered (λ100 nm) coating, a small amount of suspected corrosion was seen on the substrate (Figure 4-43 (a)). EDX analysis detected a small amount of oxygen suggesting some substrate corrosion at the bottom of the crack. The detected carbon is assumed to be from the conductomount resin, in which the sample is secured, or surface contamination. An EDX scan was carried out in the centre of the coating (Figure 4-43 (b)) to confirm that the oxygen seen in Figure 4-43 (a) was a result of the crack.

4.3.4 Effect of growth defects on the structure of coatings

As the IN625/Cr multilayer coatings all showed similar corrosion resistances, and no benefits were seen to the corrosion resistance through multilayering, further investigation was carried out on the growth defects, defect types, their origins and how they affect corrosion resistance. This section investigates and documents defects that are present in as deposited coatings, prior to and after salt spray testing.

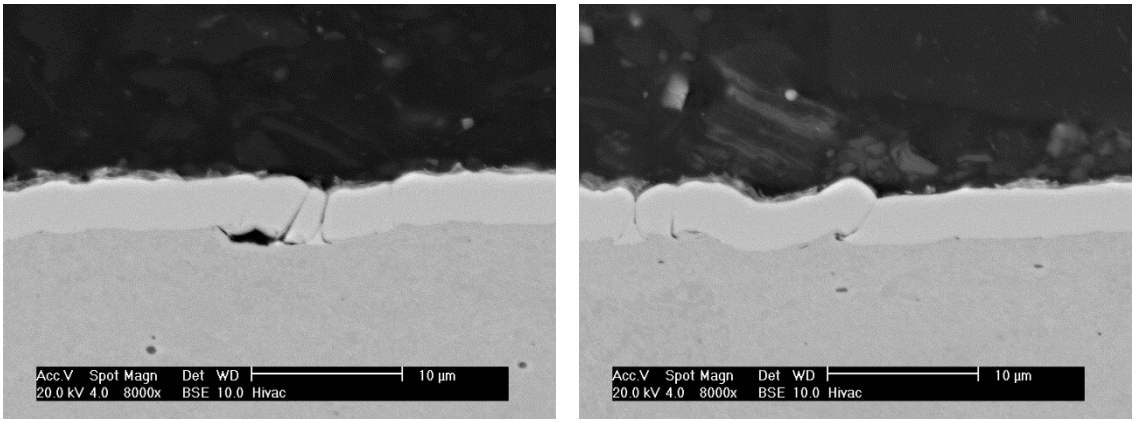


Figure 4-44 Cross sectional SEM micrographs of the as deposited IN625/Cr multilayer (λ20 nm) coating, deposited in batch 1 on a mild steel substrate

In Figure 4-44, clear voids can be seen between the coating and the substrate as well as paths from the substrate to the surface of the coating. It has been argued that the voids are most likely to be caused by dust or particles on the substrate surface prior to deposition, or through pits and asperities on the substrate surface prior to coating deposition (Panjan et al., 2009; Depner et al., 2011; Panjan et al., 2013).

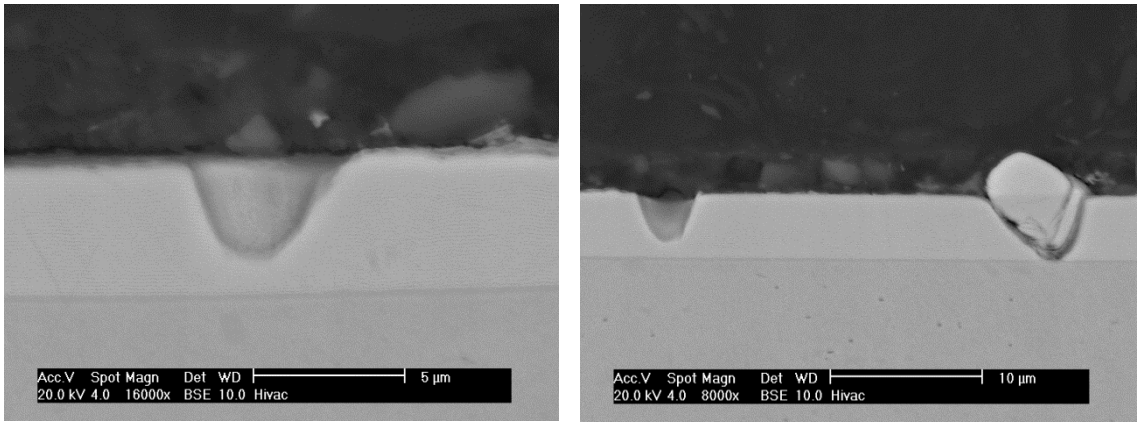


Figure 4-45 Cross sectional SEM micrographs of the as deposited IN625/Cr multilayer (λ100 nm) coating, deposited in batch 1 on a mild steel substrate

Figure 4-45 shows cone like defects in the IN625/Cr multilayered (λ100 nm) coating. It has been argued that these defects are caused by dust or particles on the substrate or coating surface, prior to or during deposition. The coating forms around the foreign particle, this forms a defect which then nucleates separately form the coating resulting in a cone shape (Čekada et al., 2007; Panjan et al., 2008; Panjan et al., 2009). The void is assumed to be a cone like defect which has detached from the coating.

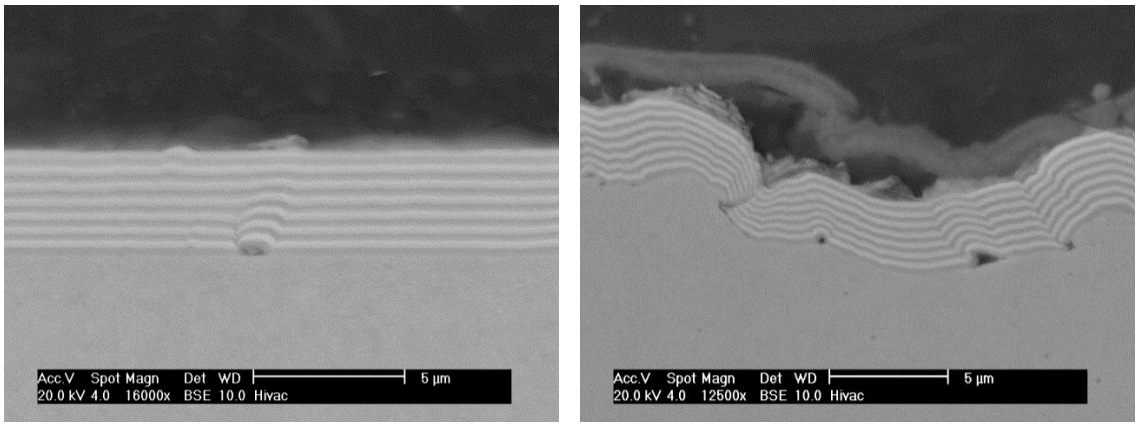


Figure 4-46 Cross sectional SEM micrographs of the as deposited IN625/Cr multilayer (λ600 nm) coating, deposited in batch 1 on a mild steel substrate

Figure 4-46 shows defects which have occurred at the substrate surface; these could be due to dust or particles on the surface as well as defects caused by the substrate surface roughness (Panjan et al., 2009; Depner et al., 2011; Panjan et al., 2013). The

defect shown in the left image appears to have been healed during deposition of subsequent multilayers, and therefore, a defect penetrating from the surface to the substrate has not been generated. However, as this is a two-dimensional image of a three-dimensional object, it cannot be said for certain that the defect does not expose the substrate in a different plane.

Further cross sectional SEM images of cone-like defects in the IN625/Cr multilayered (λ100 nm) coating can be seen in Figure 4-47; however, it can be seen that these defects did not result in corrosion of the substrate, despite penetrating very deeply through the coating.

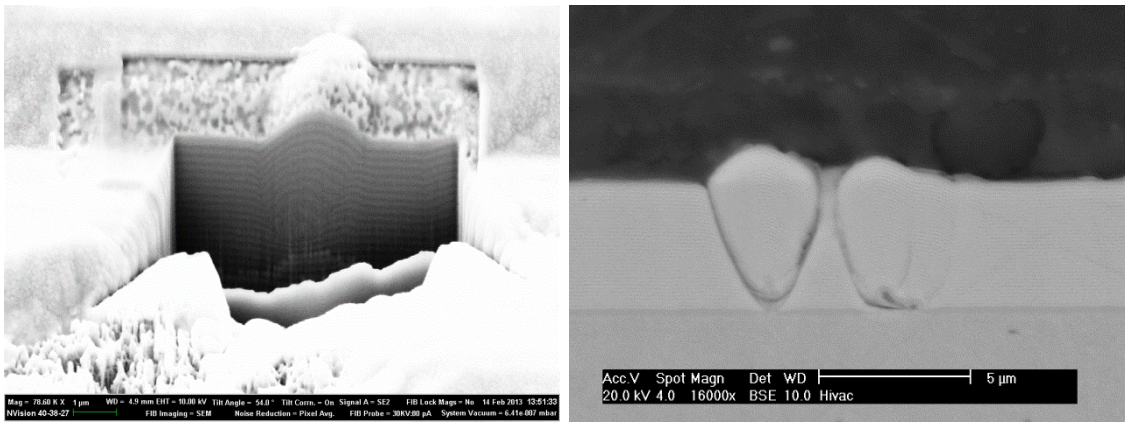


Figure 4-47 Cross sectional SEM micrographs of cone like defects in the IN625/Cr multilayered (λ100 nm) coating, deposited in batch 1 on a mild steel substrate, after 18 hours of salt spray testing

To ensure that the defects were not being affected, or even generated, by the grinding and polishing process carried out to prepare SEM cross sections, FIB cross sections were carried out. A cross-sectional FIB image of the IN625/Cr multilayered (λ100 nm) coating can be seen in Figure 4-48. The cross section is taken parallel to grinding marks on the substrate, visible due to the shadowing effect of PVD coatings. A clear void can be seen between the substrate and the base of the coating. This develops into a crack which reaches the surface of the coating, therefore exposing the substrate to corrosive media. The multilayers were seen to follow the cracks suggesting the defects are produced during deposition, not afterwards.

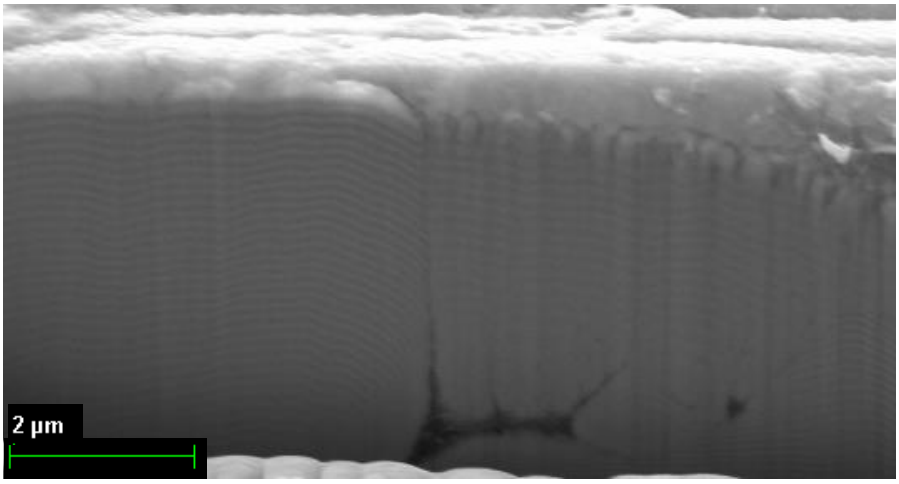


Figure 4-48 Cross sectional FIB micrograph of a defect within the IN625/Cr multilayered (λ100 nm) coating, deposited in batch 1 on a mild steel substrate, after 18 hours of salt spray testing

SEM was carried out on the top surface of an as deposited IN625/Cr (λ100 nm) coating. From the secondary electron, images (Figure 4-49), the coating surface appeared damaged with deep pits and cracks travelling along the direction of the lay; this is evidence of the shadowing effect of PVD coatings (Panjan et al., 2013) i.e. how the substrate surface roughness can affect the surface roughness and the microstructure of the coating.

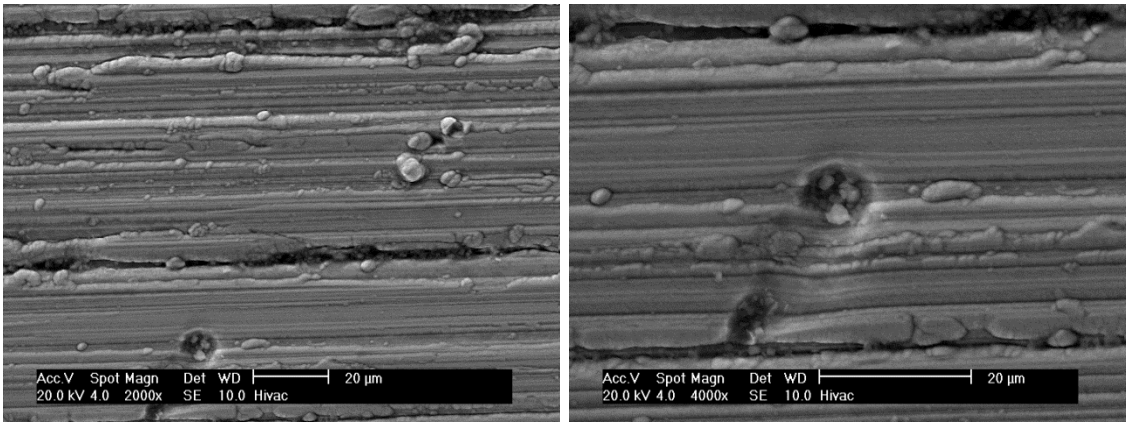


Figure 4-49 Top surface SEM micrograph of as deposited IN625/Cr multilayered (λ100 nm) coating, deposited in batch 1 on a mild steel substrate

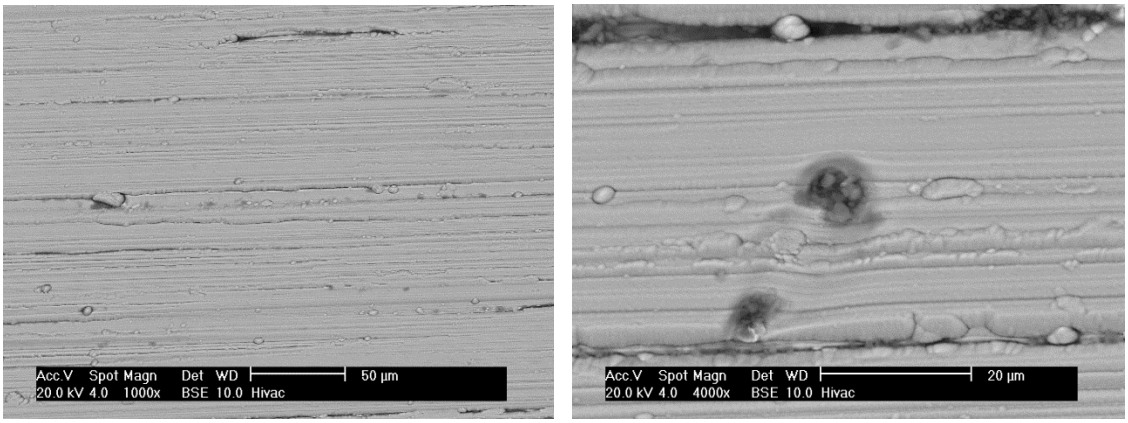


Figure 4-50 Top surface BSE SEM micrographs of as deposited IN625/Cr multilayered (λ100 nm) coating, deposited in batch 1 on a mild steel substrate

The backscattered electron images in Figure 4-50 show darker areas in the cracks and pits due to lack of signal due to topography.

4.3.5 Effect of substrate surface roughness and deposition conditions on the structure of coatings

To investigate the effect of substrate surface roughness and deposition conditions on defect generation and corrosion resistance further, a batch of coatings was produced on substrates with different surface roughnesses. Two different interrupted process conditions were also investigated, intermediate etch and interrupted conditions. Both require the coating process to be stopped mid-way. For the intermediate etch process, an ion etch was carried out for 5 minutes on the coating surface during an interruption in the deposition. For the interrupted conditions, the coating process was stopped mid-way through deposition and the system is vented; however, no ion etch was carried out. The system was then pumped down for a minimum of an hour to 3×10^{-15} Torr to remove possible contaminants.

For this investigation, three coatings were selected, IN625 and IN625/Cr multilayered (λ20 nm & λ100 nm). Coatings were deposited on 440C substrates of three different surface roughnesses: a rough workshop grind (126 ± 8 nm Ra), 1200 grit (78 ± 12 nm Ra) and 6µm polish (12 ± 4 nm Ra). The coatings, deposition processes

and substrate surface roughnesses used are presented in Table 4-4. The coating thicknesses were measured from coating cross-sections using SEM.

	Coating	Adhesion layer	Coating architecture			Total coating thickness (µm)
Batch 2	IN625	0.3 µm Cr	IN625	Standard process	WG (Ra =126 ±8 nm)	4.0 ± 0.1 µm
					1200 grit (Ra = 78 ± 12 nm)	4.0 ± 0.1 µm
					6 µm polish (Ra = 12 ± 4 nm)	4.0 ± 0.1 µm
				Interrupted process		5.0 ± 0.1 µm
				Intermediate etch		5.5 ± 0.1 µm
	IN625/Cr multilayers	0.3 µm Cr	10 nm IN625/10 nm Cr	Standard process	WG (Ra =126 ±8 nm)	4.0 ± 0.1 µm
					1200 grit (Ra = 78 ± 12 nm)	4.0 ± 0.1 µm
					6 µm polish (Ra = 12 ± 4 nm)	4.0 ± 0.1 µm
				Interrupted process		5.0 ± 0.1 µm
				Intermediate etch		4.5 ± 0.1 µm
			50 nm IN625/50 nm Cr	Standard process	WG (Ra =126 ±8 nm)	4.0 ± 0.1 µm
					1200 grit (Ra = 78 ± 12 nm)	4.0 ± 0.1 µm
					6 µm polish (Ra = 12 ± 4 nm)	4.0 ± 0.1 µm
				Interrupted process		5.0 ± 0.1 µm
				Intermediate etch		4.5 ± 0.1 µm

Table 4-4 Batch 2 coatings deposited, different substrate surface roughnesses and deposition conditions used

3D profilometry of the different substrate surface roughnesses prior to deposition of the coatings can be seen in Figure 4-51.

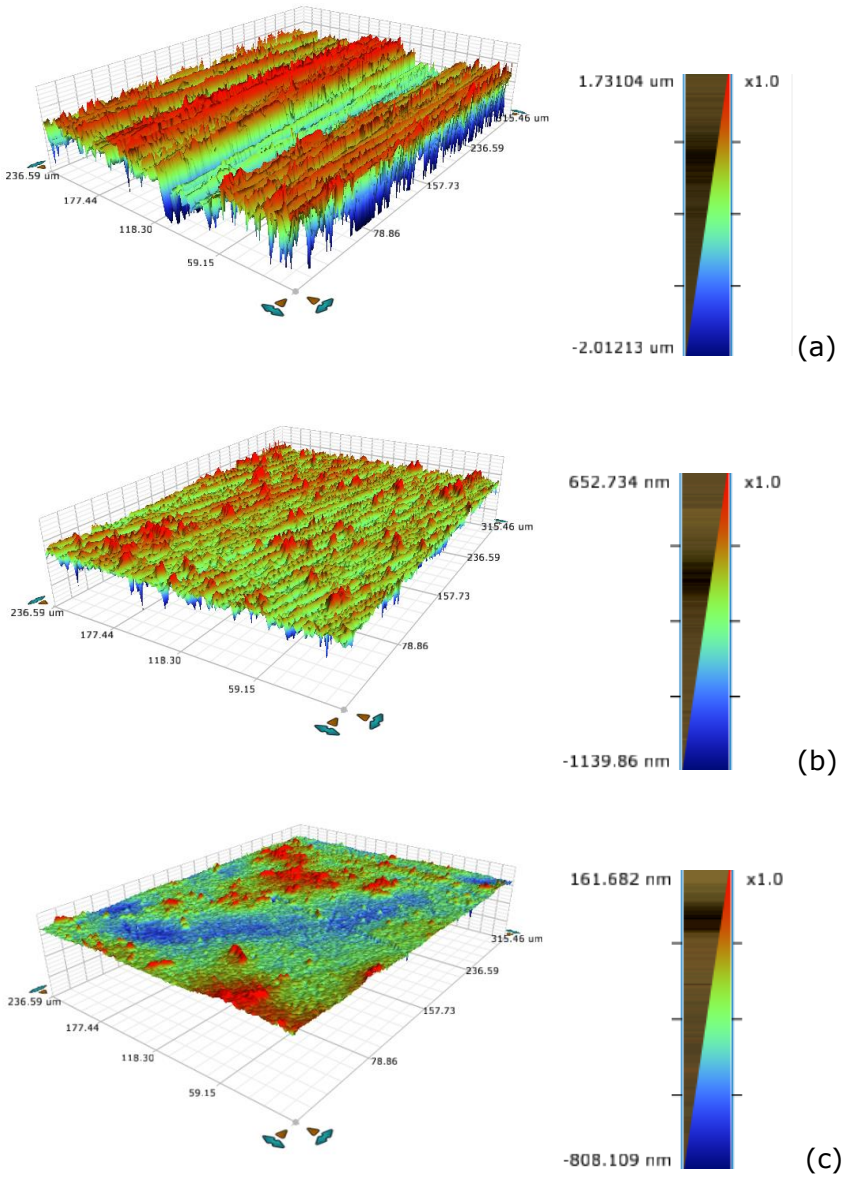


Figure 4-51 3D profilometry of 440C substrates with different surface roughnesses (a) workshop grind (b) 1200 grit (c) 6 µm polish

The interrupted and intermediate etch processes were carried out on coatings deposited on substrates with a 1200 grit finish as this is the standard substrate surface finish used for coatings by our manufacturer.

4.3.5.1 Effect of substrate surface finish and deposition conditions on the microstructure of coatings

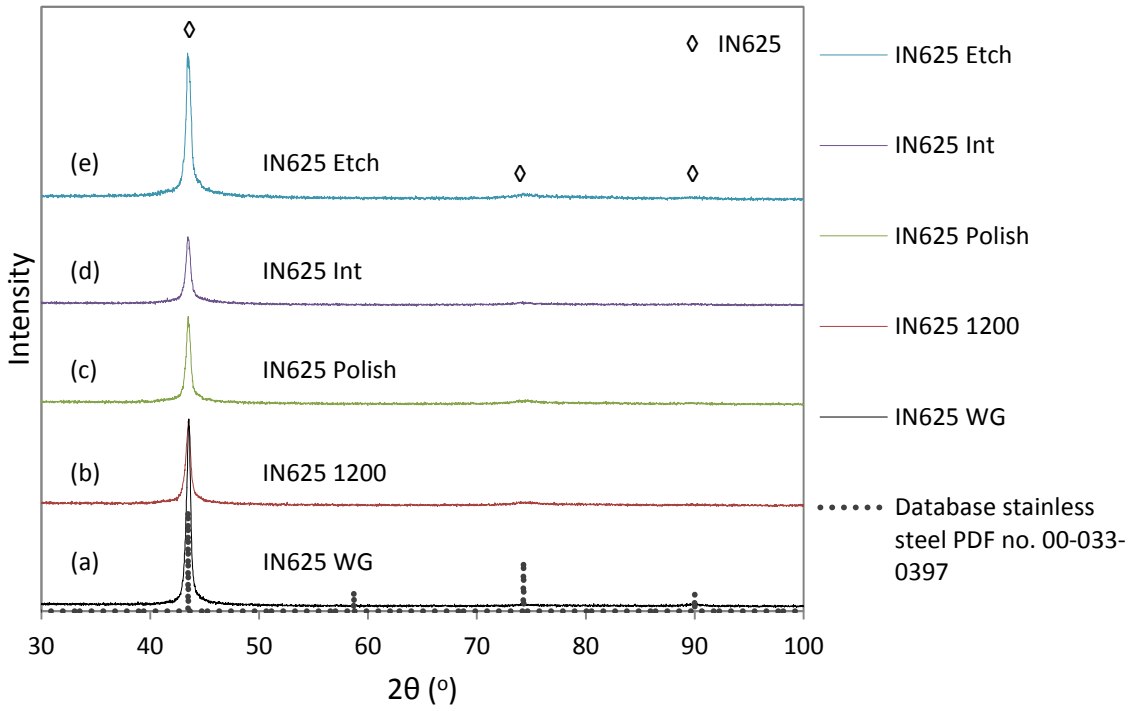


Figure 4-52 XRD patterns of IN625 coatings on different surface finish substrates and under different deposition conditions (a) deposited on a workshop ground substrate (b) deposited on a 1200 grit substrate (c) deposited on a polished substrate (d) deposited under interrupted conditions (e) deposited under intermediate etch conditions, on 440C substrates

The IN625 coatings (Figure 4-52) showed a preferred orientation of diffraction peaks in the {1 1 1} plane of the nickel matrix phase at 43.4° 2θ. Small peaks were also observed in the {2 2 0} and {3 1 1} planes of the nickel matrix phase at 74.3° and 90.2° 2θ respectively. No difference in diffraction peaks was observed for coatings deposited on different surface finish substrates and under different deposition conditions. However, some peak broadening was observed for coatings deposited on a 1200 grit substrate, on a polished substrate and under interrupted deposition conditions.

The IN625/Cr multilayer (λ100 nm) coatings (Figure 4-53) showed a preferred orientation of diffraction peaks in the {1 1 1} plane of the nickel matrix phase at 43.4° 2θ and the {1 1 0} plane for the chromium phase at 44.4° 2θ. Small peaks were

also observed in the {2 0 0}, {2 1 1} and {2 2 0} planes for the chromium phase at 64.6°, 81.7° and 98.1° 2θ respectively, and the {2 2 0} and {3 1 1} planes for the nickel matrix phase at 74.3° and 90.2° 2θ respectively. Peak broadening was again observed for coatings deposited on a 1200 grit substrate, polished substrate and under interrupted deposition conditions.

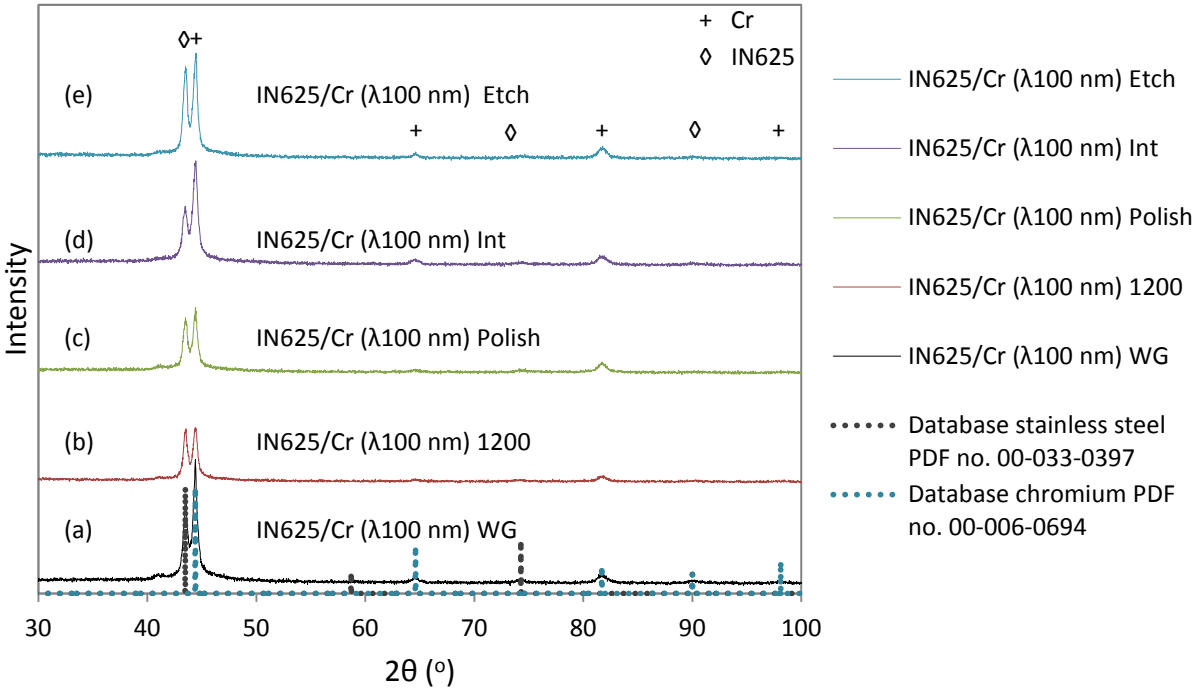


Figure 4-53 XRD patterns of IN625/Cr multilayer (λ100 nm) coatings on different surface finish substrates and under different deposition conditions (a) deposited on a workshop grind substrate (b) deposited on a 1200 grit substrate (c) deposited on a polished substrate (d) deposited under interrupted conditions (e) deposited under intermediate etch conditions, on 440C substrates

Large peak broadening was observed for the IN625/Cr multilayer (λ20 nm) coatings (Figure 4-54). The coatings showed a preferred orientation of diffraction peaks in the {1 1 1} plane of the nickel matrix phase at 43.4° 2θ and the {1 1 0} plane for the chromium phase at 44.4° 2θ. However, the nickel matrix and chromium peaks had showed as one due to peak broadening. Small peaks were also observed in the {2 0 0}, {2 1 1} and {2 2 0} planes for the chromium phase at 64.6°, 81.7° and 98.1° 2θ respectively, and the {2 2 0} and {3 1 1} planes for the nickel matrix phase at 74.3° and 90.2° 2θ respectively.

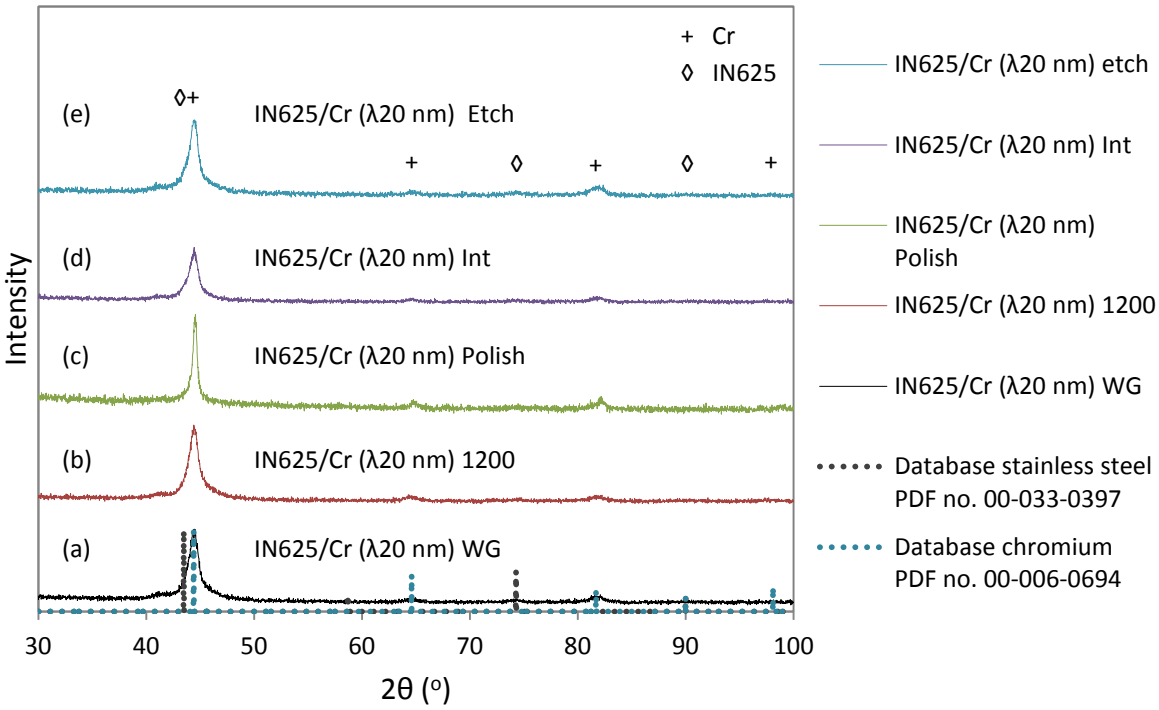


Figure 4-54 XRD patterns of IN625/Cr multilayer (λ20 nm) coatings on different surface finish substrates and under different deposition conditions (a) deposited on a workshop grind substrate (b) deposited on a 1200 grit substrate (c) deposited on a polished substrate (d) deposited under interrupted conditions (e) deposited under intermediate etch conditions, on 440C substrates

The residual stresses in coatings deposited on different surface finish substrates and under different deposition conditions were investigated using XRD. A diffraction peak was chosen at the high range of around 115° 2θ. Using the $\sin^2\psi$ method, a number of measurements were taken at different psi (ψ) tilts (0°,20.7°, 30°, 37.76°, 45°, 52.24° and 60°) and two different phi (ϕ) tilts (0° and -90°). The measured peak shifts for the IN625/Cr λ100 nm coating deposited on a 1200 grit substrate are presented in Figure 4-55.

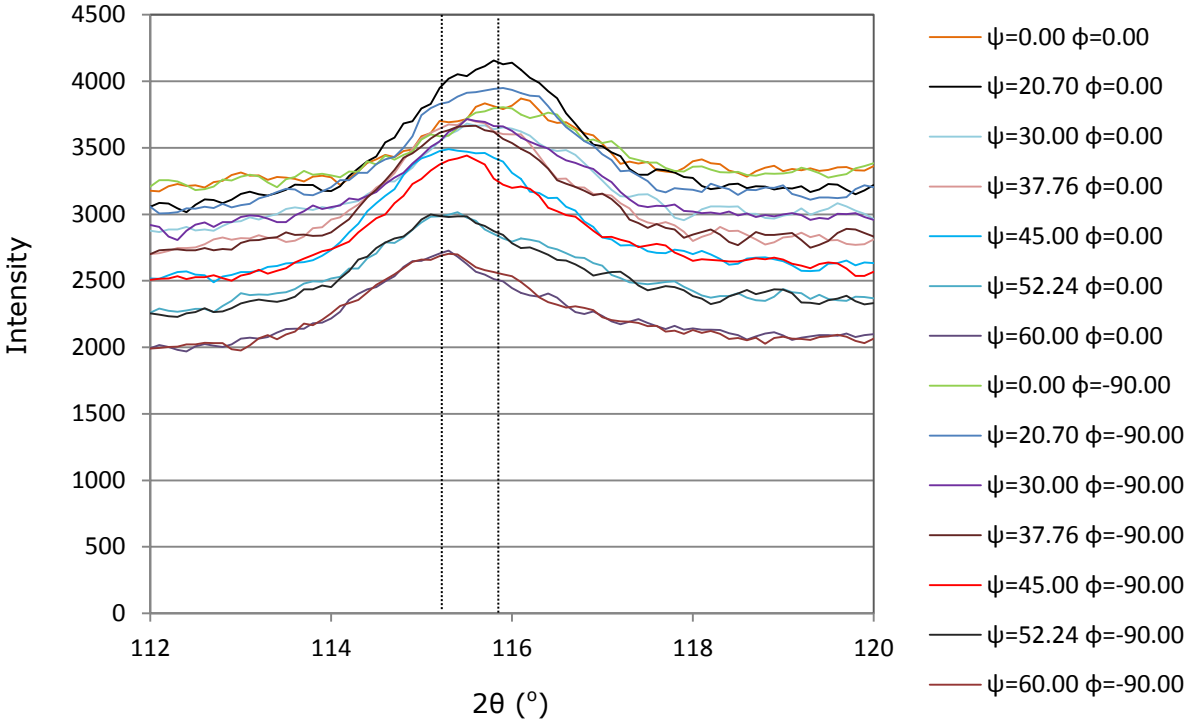


Figure 4-55 Peak shift measurements at different ψ and ϕ tilts for IN625/Cr λ100 nm coating deposited on a 1200 grit substrate

The inter-planar spacing (d) was measured for each tilt angle and plotted against $\sin^2\psi$ as shown in Figure 4-56.

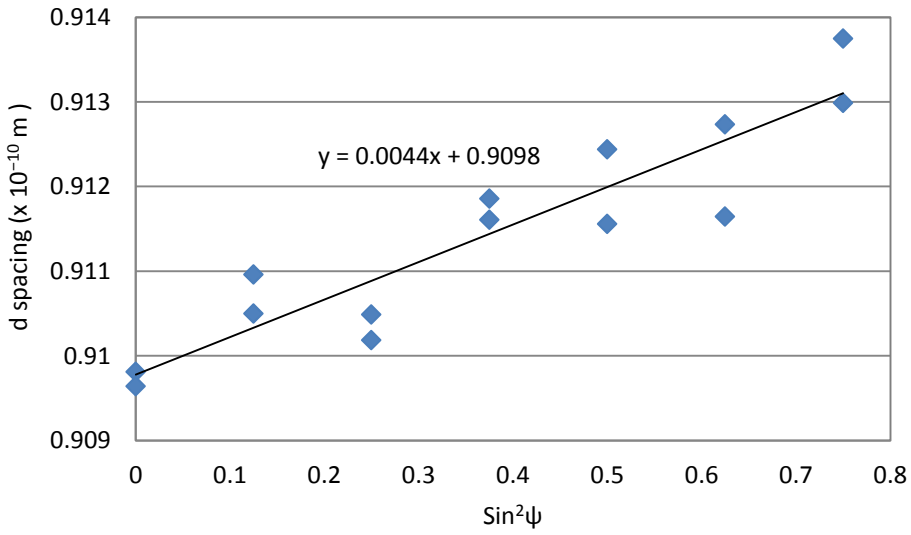


Figure 4-56 d-spacing vs. $\sin^2\psi$ for IN625/Cr λ100 nm coating deposited on a 1200 grit surface finish 440C substrate

The stress can then be calculated using equation 3.3, where m is the gradient of the d vs. $\sin^2\psi$ plot.

$$\sigma = \left(\frac{\mathrm{E}}{(1+\upsilon)}\right)\frac{m}{d_{\mathrm{n}}}$$ **Eq.3.3** (Prevéy, 1986)

The results are displayed in Figure 4-57. The values of Young's modulus (E) and Poisson's ratio (ν) were taken as those documented for PVD chrome (Material Property Database (1990)), giving E = 240 GPa and ν = 0.2. All coatings showed compressive residual stresses (Figure 4-57). A significantly higher residual stress was recorded for the IN625/Cr λ100 nm coating deposited on a 1200 grit substrate in comparison to the IN625/Cr λ20 nm coating. An increase in residual stress was also seen as the substrate surface roughness decreased, however, due to errors, a definite trend could not be concluded relating lower substrate surface finish to higher residual stress. The highest stress recorded was for the IN625/Cr λ100 nm coating deposited under intermediate etch conditions.

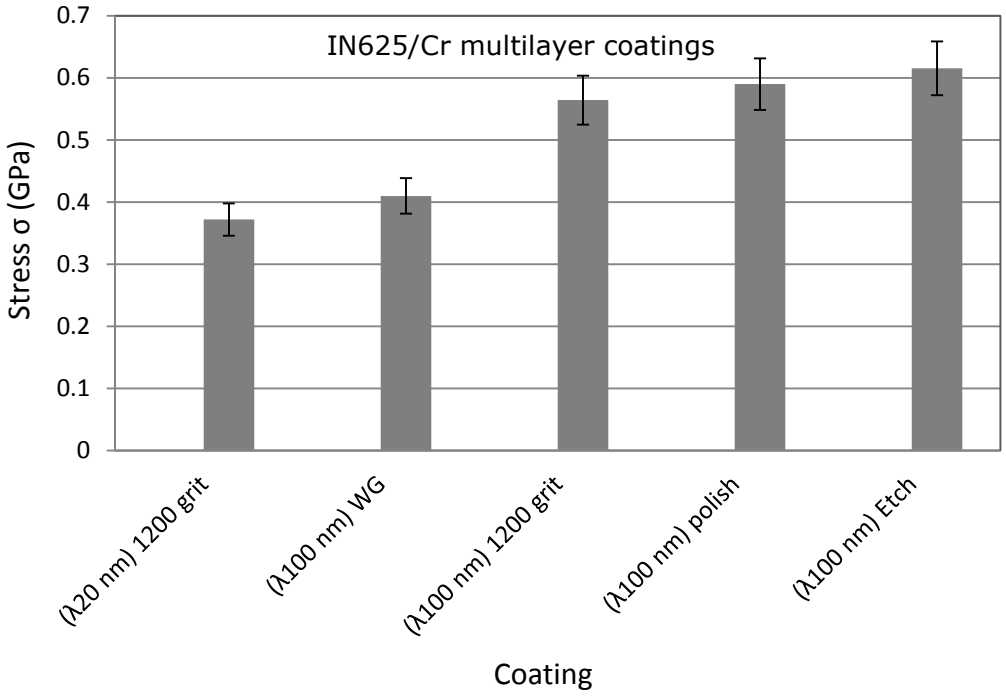


Figure 4-57 Compressive residual stresses in coatings deposited on different surface finish substrates and under different deposition conditions, error bars represent the standard deviation

Transmission electron microscopy was employed to investigate the structure of the IN625/Cr λ100 nm coating deposited on a 1200 grit substrate under intermediate etch conditions.

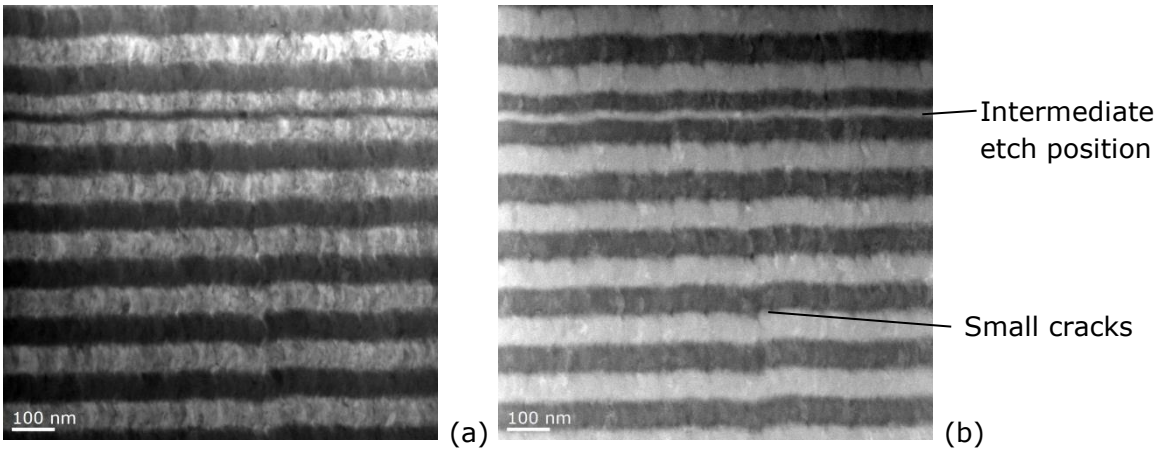


Figure 4-58 Cross-sectional (a) bright field (b) dark field transmission electron microscopy images of the IN625/Cr λ100 nm coating deposited on a 1200 grit, 440C substrate under intermediate etch conditions

From the TEM images (Figure 4-58), no change in coating structure was observed either side of the intermediate etch. Small crack-like features were observed in the dark field image (Figure 4-58 (b)). The sample was observed at different tilts in high angle annular dark field STEM (HAADF-STEM) mode to confirm whether the dark features were cracks rather than diffraction effects. The results suggested that the features were cracks. TEM analysis also revealed larger defects which appeared to disrupt the multilayer structure (Figure 4-59).

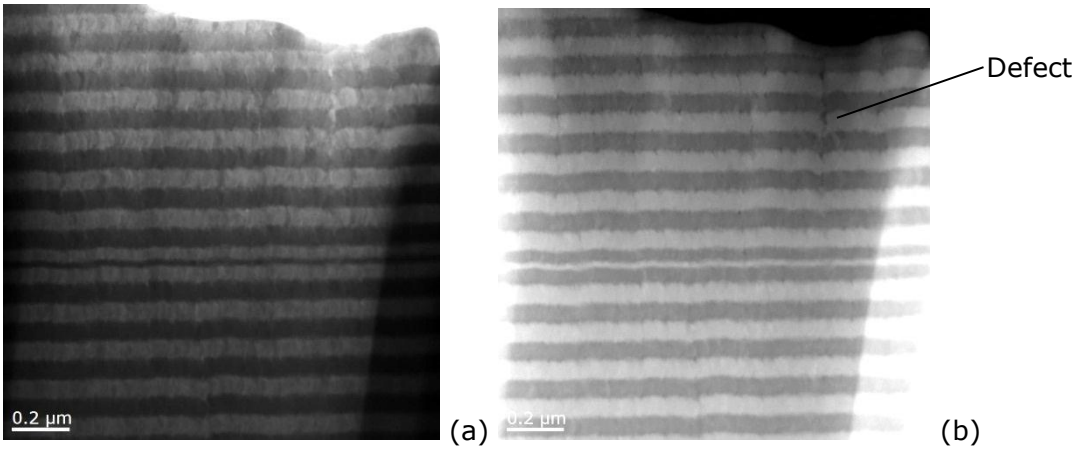


Figure 4-59 Cross-sectional (a) bright field (b) dark field transmission electron microscopy images of a crack within the IN625/Cr λ100 nm coating deposited on a 1200 grit, 440C substrate under intermediate etch conditions

From the high-resolution TEM images of the coating (Figure 4-60), it was observed that the coating layers were polycrystalline; however, each area shows multiple overlapping crystals.

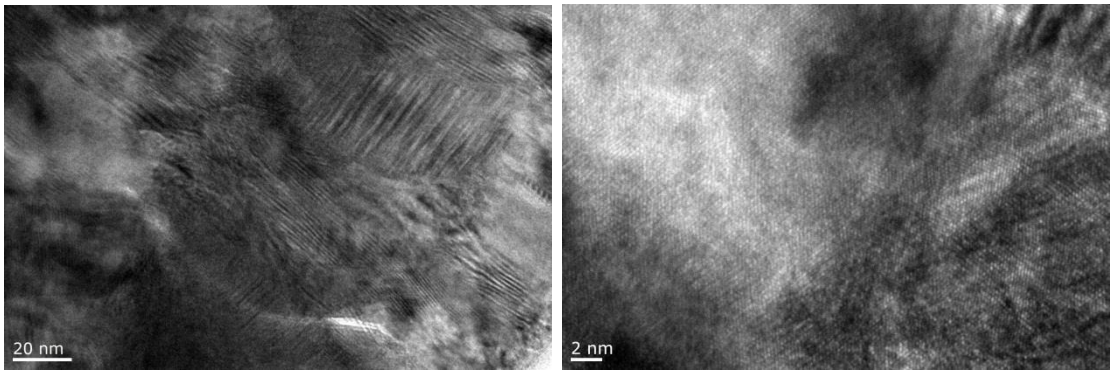
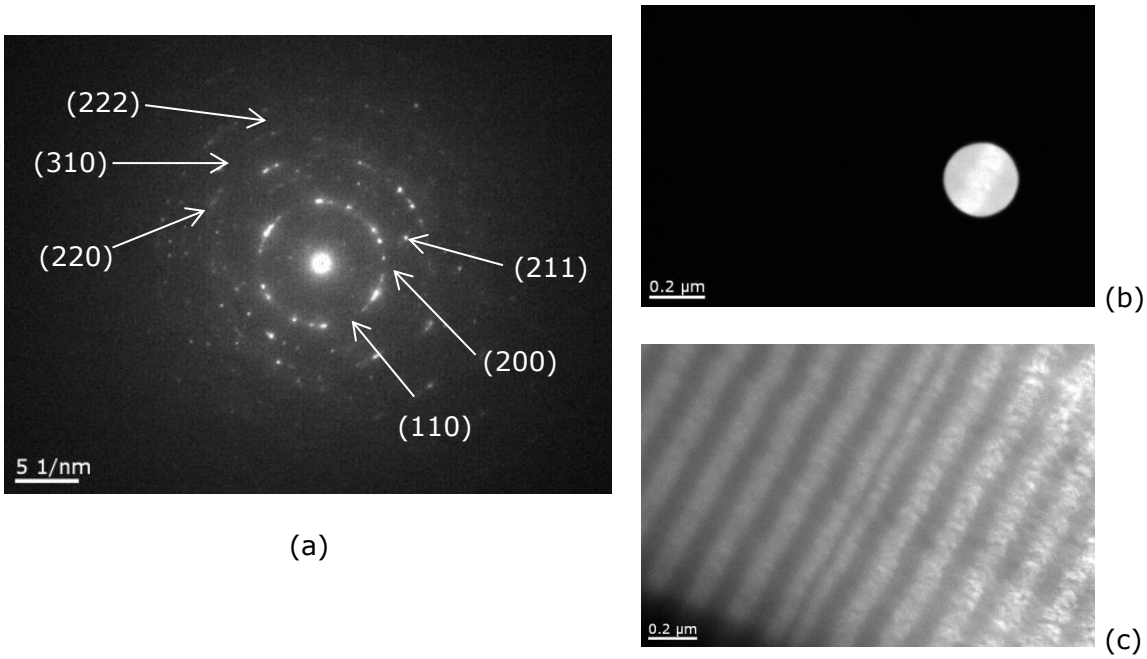


Figure 4-60 Cross-sectional high-resolution transmission electron microscopy micrographs of the IN625/Cr λ100 nm coating deposited on a 1200 grit, 440C substrate under intermediate etch conditions

Selected area electron diffraction patterns were obtained from the cross section of the multilayer structure as shown in Figure 4-61.



(a) (b) (c)

Figure 4-61 Cross-sectional TEM images of a FIB-SEM lift-out of the as deposited IN625/Cr λ100 nm multilayer coating with an intermediate etch (a) selected area electron diffraction pattern from the area highlighted in (b) located in the upper region of the multilayers (c) a high-angle annular dark field image of the multilayers and intermediate etch position

The electron diffraction pattern (Figure 4-61 (a)) was taken from the area highlighted in Figure 4-61 (b & c). A clear series of diffraction rings were obtained which corresponded to the diffraction pattern of chromium, however, no rings were identified from the selected area to correspond with the diffraction pattern of the IN625. The SAED patterns suggest the coating has a variation in crystal orientation.

4.3.5.2 Effect of substrate surface finish and deposition conditions on the mechanical properties of coatings

The effect of substrate surface roughness on the hardness and scratch resistance was investigated on IN625 and IN625/Cr λ100 nm multilayer coatings (Figure 4-62). The IN625/Cr λ20 nm coating was not investigated as it delaminated from the substrate after deposition which could be due to higher residual stresses for coatings deposited on polished substrates. It was expected that a lower surface roughness would result in a higher hardness and scratch resistance due to a reduction in growth defects which can act as stress raisers and result in higher friction and localised loss of adhesion (Brandl and Gendig, 1996; Ries et al., 1997; Cunha and Andritschky, 1999; Jehn, 2000; Lewis et al., 2006; Altun and Sen, 2007; Čekada et al., 2007; Panjan et al., 2009; Hoche et al., 2011; Panjan et al., 2012; Panjan et al., 2013).

For the monolayer IN625 (Figure 4-62 (a)), it was seen that the polished substrate surface finish resulted in no significant change in hardness. A slight increase in hardness was seen on the IN625/Cr λ100 nm coating deposited on a polished substrate compared to that deposited on a 1200 grit substrate, showing an increase from HV = 868 kg f mm^{-2} to HV = 954 kg f mm^{-2}. It was seen that the scratch resistance of the IN625 coating (Figure 4-62 (b)) deposited on a polished substrate exhibited little difference compared to that deposited on a 1200 grit substrate (74 N and 72 N total failure respectfully). However the IN625/Cr λ100 nm coating showed a lower scratch resistance when deposited on a polished substrate (58 N) compared to that deposited on a 1200 grit substrate (71 N).

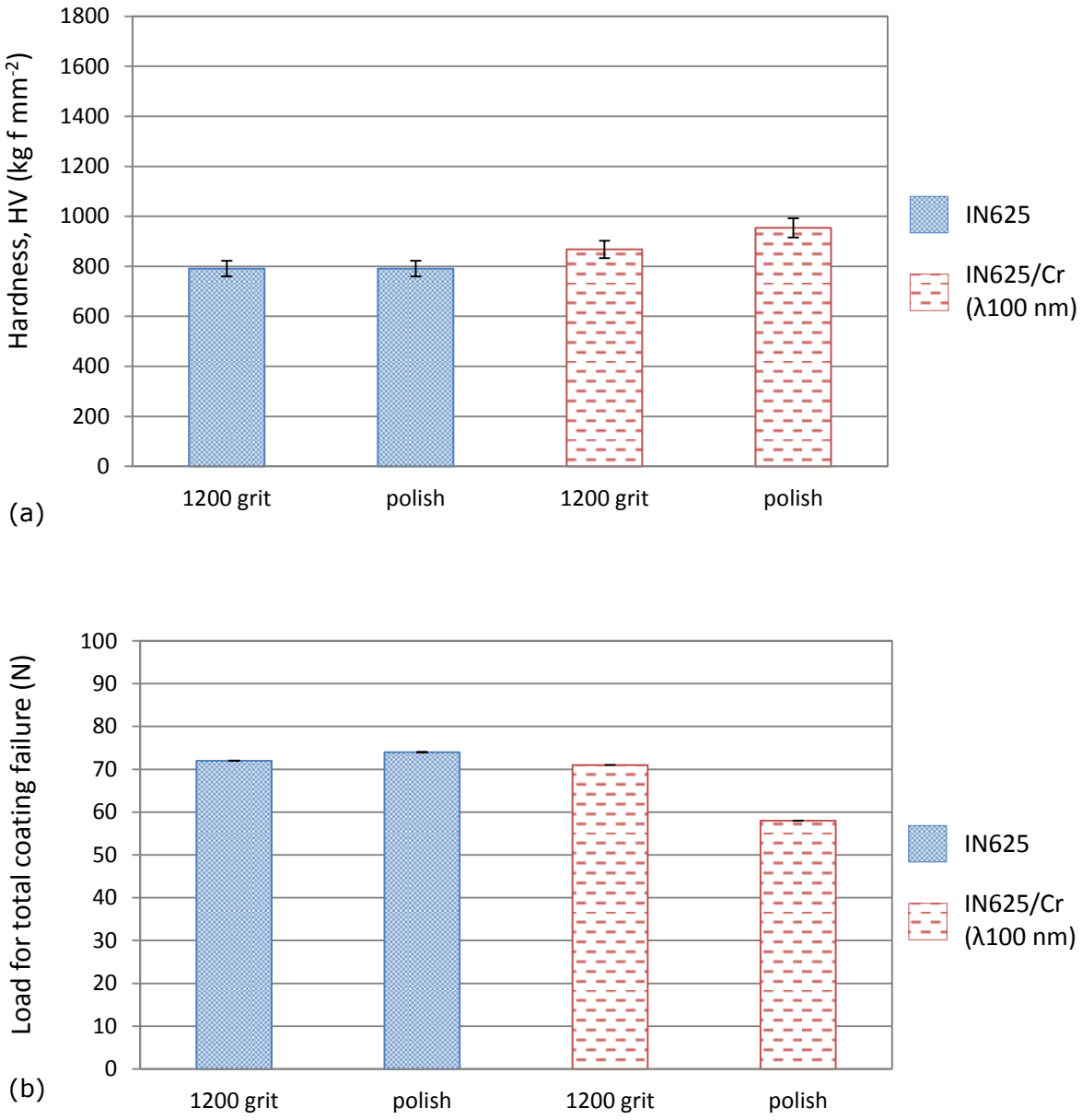


Figure 4-62 Effect of substrate surface roughness on the (a) hardness (b) scratch resistance of IN625 and IN625/Cr λ100 nm multilayer coatings, deposited in batch 2 on 440C substrates, error bars represent the equipment errors

Figure 4-63 shows the effect of process conditions on the hardness and scratch resistance of coatings. It was observed that that the process conditions had little effect on the hardnesses and scratch resistances of coatings (Figure 4-63 (a & b)). In most cases, a trend was seen across the multilayer coatings showing that the smaller the bilayer period, the higher the hardness (Figure 4-63 (a)). The scratch results (Figure 4-63 (b)) showed an opposite trend of decreasing scratch resistance with

decreasing bilayer period for coatings deposited on a 440C substrate. However, tests on coatings deposited on M42 substrates indicated that most coatings did not fail in tests up to the maximum load of 100 N.

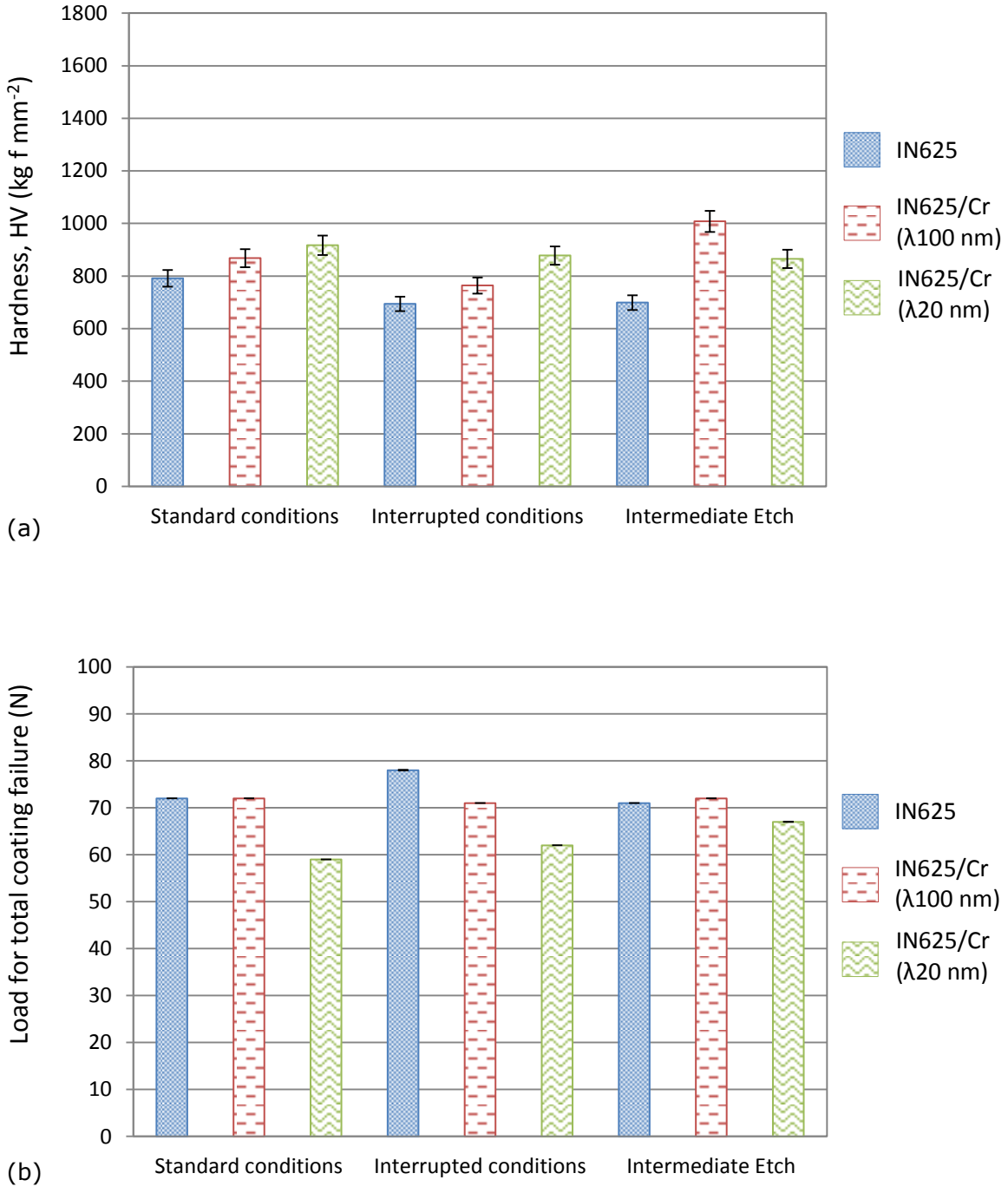


Figure 4-63 Effect of process conditions on the (a) hardness (b) scratch resistance of IN625 and IN625/Cr multilayered coatings deposited in batch 2, on 440C substrates, error bars represent the equipment errors

4.3.5.3 Effect of substrate surface finish and deposition conditions on the corrosion barrier performance of coatings

Salt spray tests on the monolayer IN625 coatings (Figure 4-64), showed that coatings deposited on a 1200 grit substrate provided the lowest corrosion rate.

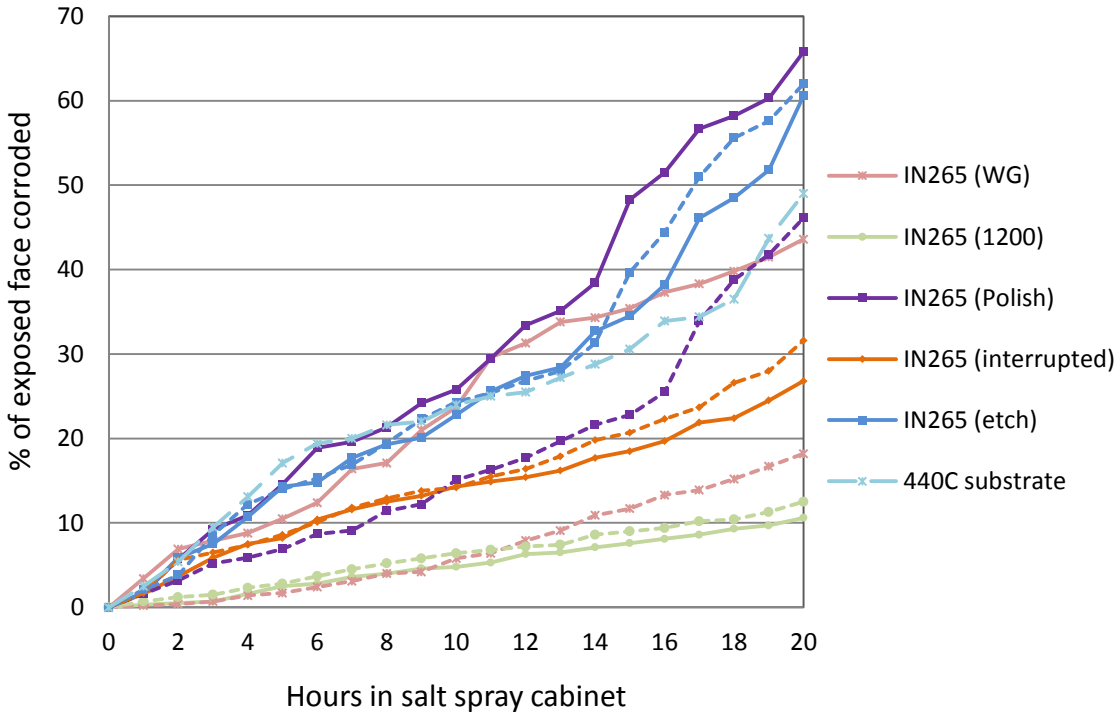


Figure 4-64 Salt spray results of IN625 coatings, dotted lines show repeat tests

There is a large variation in corrosion rates between initial and repeat tests for the coating deposited on a workshop grind substrate. The coating deposited with an interrupted process showed some improvement in corrosion resistance compared to the corrosion rate of the substrate.

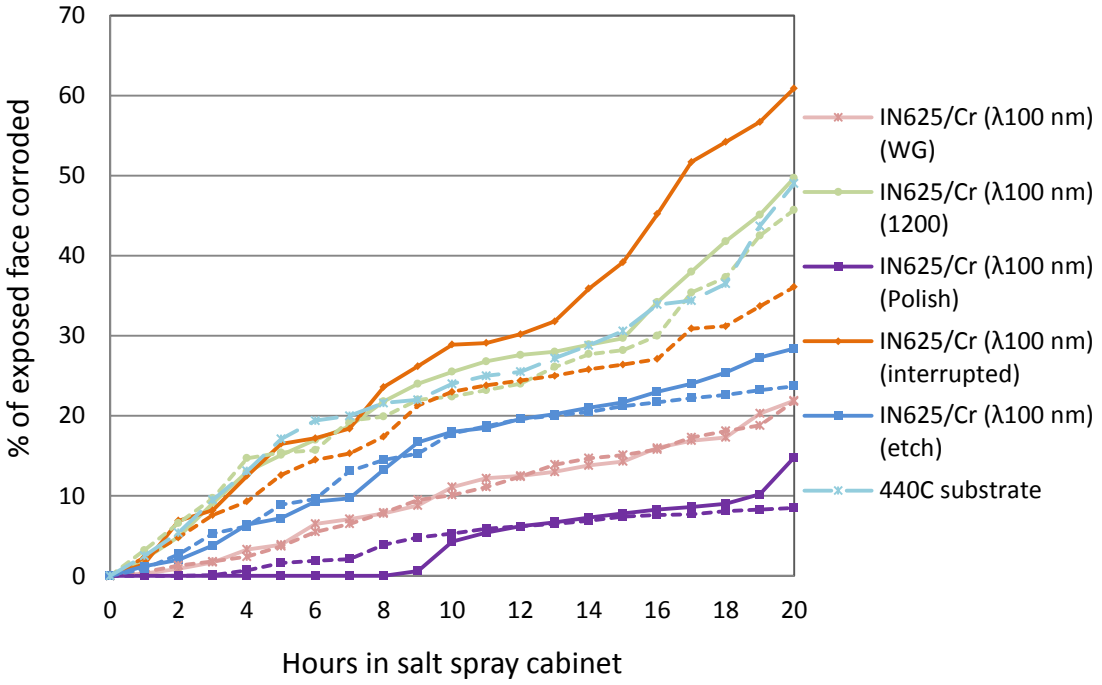


Figure 4-65 Salt spray results of IN625/Cr multilayered (λ100 nm) coatings on 440C substrates, dotted lines show repeat tests

Salt spray tests on the IN625/Cr multilayered (λ100 nm) coating (Figure 4-65), showed that coatings deposited on a polished surface finish substrate exhibited a significantly lower corrosion rate compared to the rest of the coatings, with one sample showing no corrosion for the first eight hours. Coatings deposited with an intermediate etch and on a rough workshop grind (WG) substrate showed some improvement in corrosion resistance compared to the corrosion rate of the uncoated 440C substrate, however, coatings deposited on a 1200 grit substrate and under interrupted conditions appeared to exhibit no improvement in the corrosion resistance.

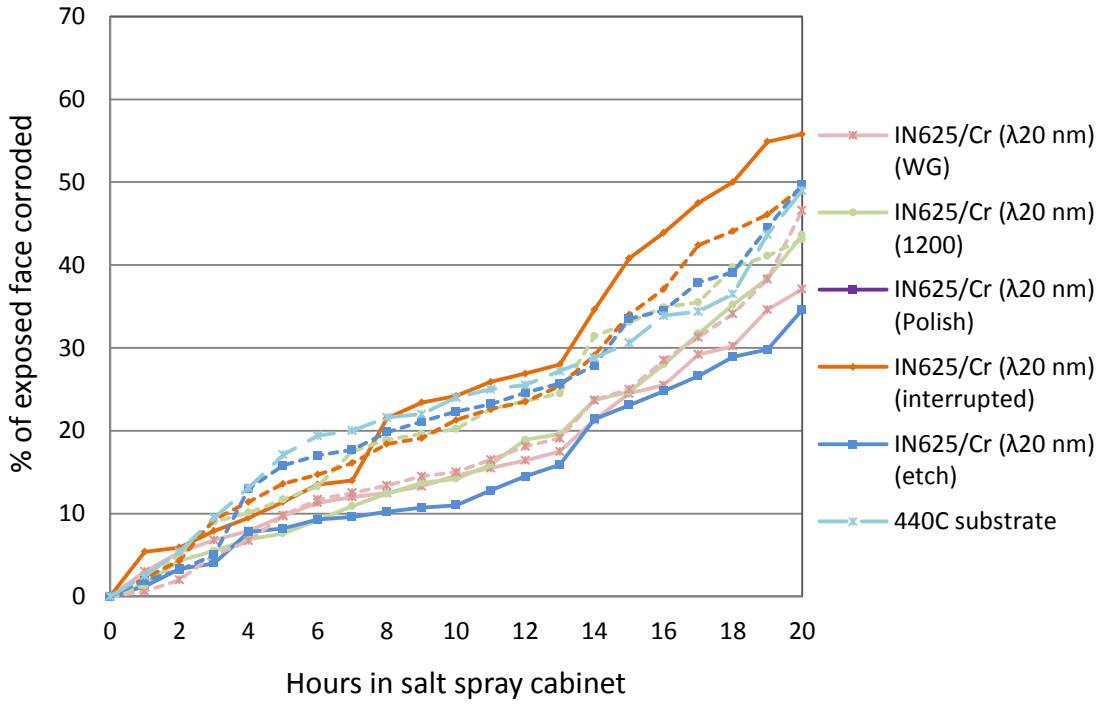


Figure 4-66 Salt spray results of IN625/Cr multilayered (λ20 nm) coatings on 440C substrates, dotted lines show repeat tests

Salt spray tests on IN625/Cr multilayered (λ20 nm) coatings (Figure 4-66), showed little difference in corrosion rates for coatings deposited on different substrate surface roughnesses and under different deposition conditions. The coating deposited on a polished substrate is not displayed as the coating delaminated from the substrate after deposition.

4.3.5.4 Effect of substrate surface finish and deposition conditions on the density of defects

Top surface SEM was carried out to determine the number and size of defects in the coatings over a 4300 μm^2 area. Images were taken at 4000x magnification and two images were taken of areas representing the defect density across the whole coating. Defects were categorised by size and shape, including pits, linear defects, cracks and circular defects. Circular defects were separated into three groups: larger than 3 μm,

between 1 and 3 μm and smaller than 1 μm. Images of the categorised defects can be seen in Figure 4-67.

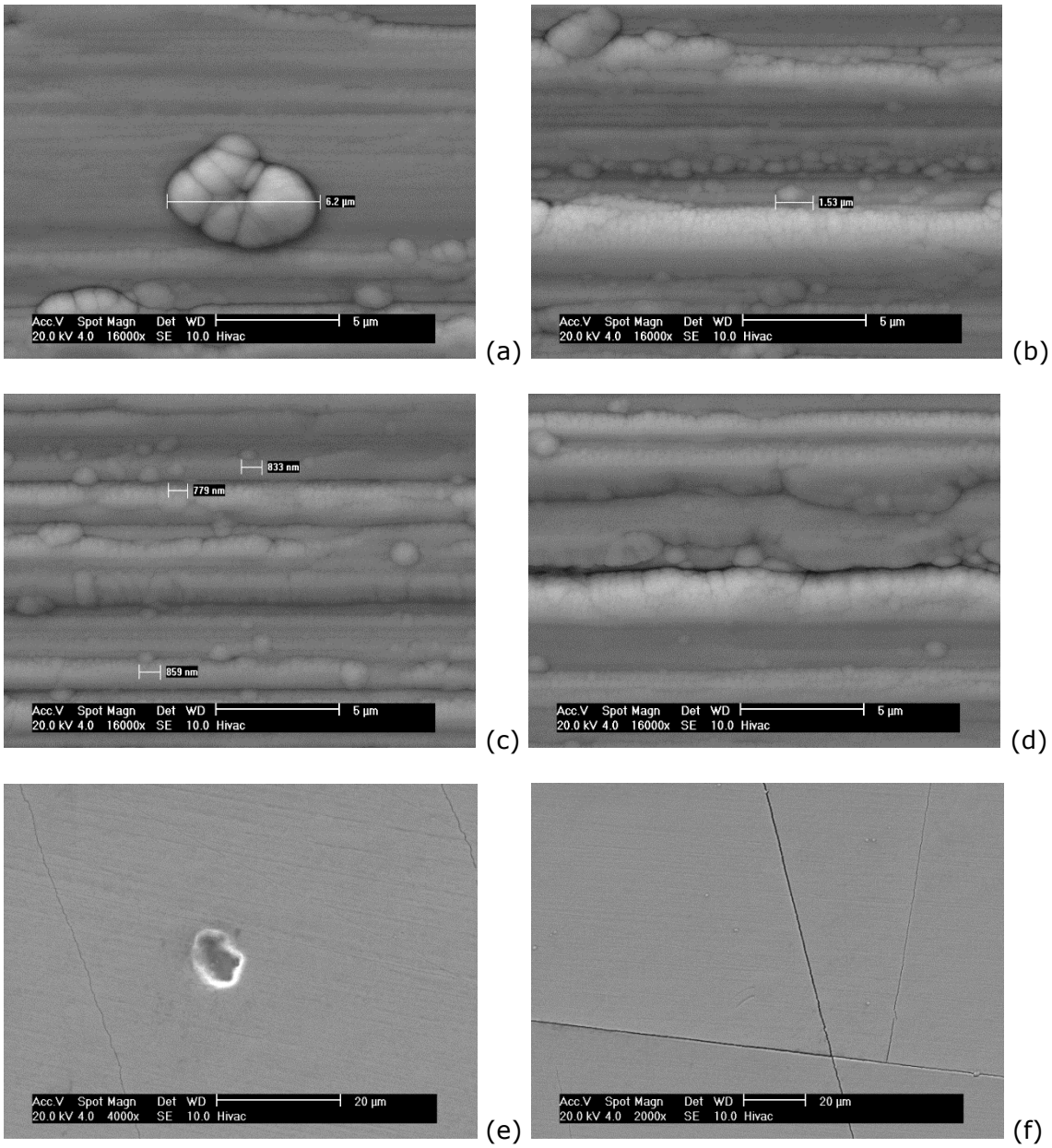


Figure 4-67 Categories of defects on IN625/Cr multilayer (λ100 nm) and IN625 coatings, deposited in batch 2, on different substrate surface roughnesses (a) a >3 μm defect on an IN625/Cr multilayer (λ100 nm) coating on a WG substrate (b) a 1-3 μm defect on an IN625/Cr multilayer (λ100 nm) coating on a WG substrate (c) <1 μm defects on an IN625/Cr multilayer (λ100 nm) coating on a WG substrate (d) linear defects on an IN625/Cr multilayer (λ100 nm) coating on a WG substrate (e) a pit defect on an IN625 coating on a 6 μm polish substrate (f) cracks on an IN625 coating on a 6 μm polish substrate

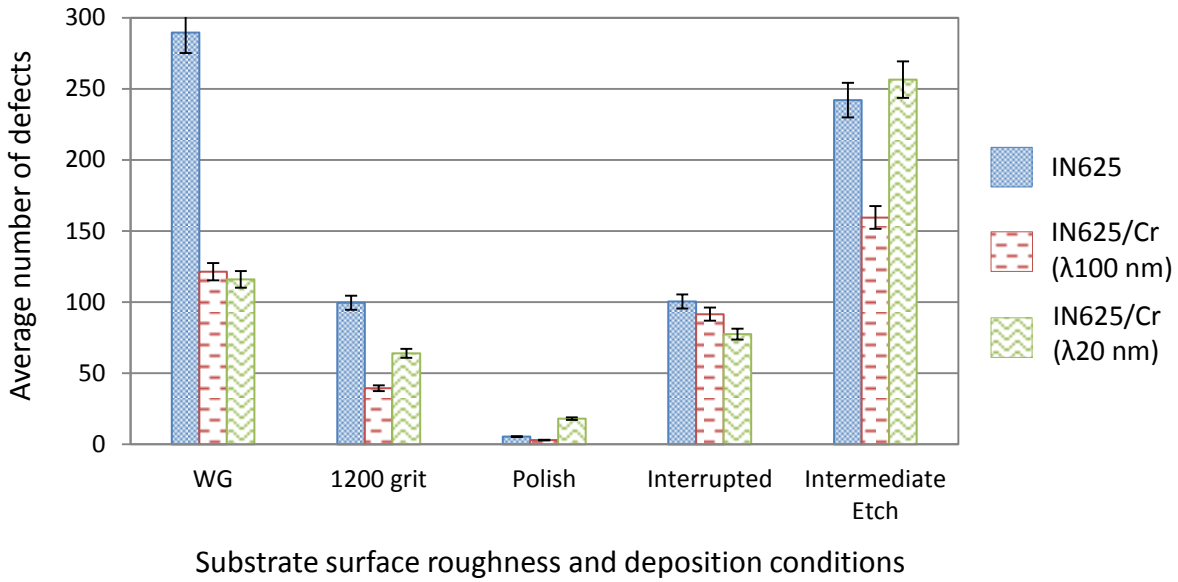


Figure 4-68 Average number of defects in a 4300 μm^2 area on IN625 and IN625/Cr multilayer coatings, deposited in batch 2, on different surface roughness 440C substrates and under interrupted and intermediate etch conditions, error bars represent the standard deviation

All coatings deposited on a polished substrate clearly showed the lowest defect densities (Figure 4-68). Coatings deposited on 1200 grit substrates showed lower defect densities than those deposited on rough workshop grind substrates. Coatings deposited under interrupted process conditions (1200 grit substrate surface finish) showed no reduction in defect density compared to coatings deposited on 1200 grit substrate surface finish with no intermediate process. Coatings deposited under intermediate etch conditions generally showed a higher defect density than all other conditions, except for the IN625 on a rough workshop grind surface finish substrate which showed the highest defect density out of all coatings and conditions.

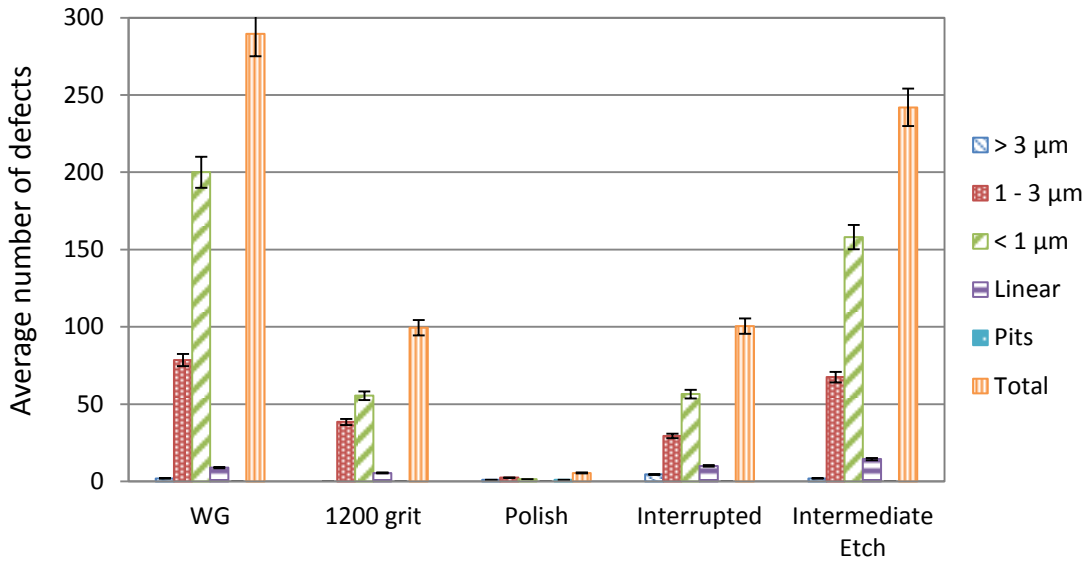


Figure 4-69 Average number of defects in a 4300 µm^2 area on IN625 coatings, deposited in batch 2, on different surface roughness substrates and under different deposition conditions, error bars represent the standard deviation

The defect density in IN625 monolayer coating (Figure 4-69) was clearly highest for that deposited on the rough workshop grind substrate. There is a clear reduction in defect density for all types of defects when the substrate surface roughness is reduced to 1200 grit, and a further reduction in defect density for coatings deposited on a 6 µm polished substrate. However, monolayer IN625 coating on a polished substrate also showed cracks throughout the coating. As seen from the stress results (Figure 4-57), coatings deposited on polished substrates had higher residual stresses. For the monolayer IN625 coating this resulted in cracks; however, the stress of the coating was not measured as it was expected that the cracks would result in stress relief, giving uncertain results. The interrupted and intermediate etch processes were carried out on coatings on 1200 grit substrate surface finishes. There was no reduction in defect density from the interrupted process and the intermediate etch resulted in a coating with a higher defect density than the coating deposited on a 1200 grit surface finish substrate under non-interrupted conditions.

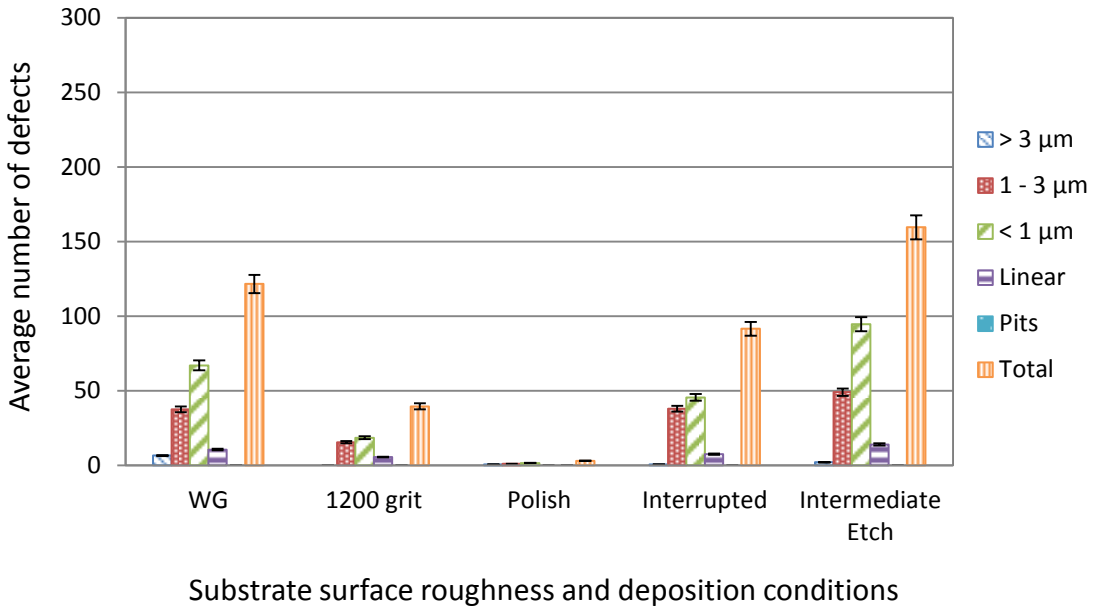


Figure 4-70 Average number of defects in a 4300 µm^2 area on IN625/Cr multilayer (λ100 nm) coatings, deposited in batch 2, on different surface roughness substrates and under different deposition conditions, error bars represent the standard deviation

The IN625/Cr multilayer (λ100 nm) and (λ20 nm) coatings (Figure 4-70 and Figure 4-71 respectively) generally showed a lower defect density than the IN625 coatings (Figure 4-69). For the λ100 nm multilayered coating (Figure 4-70), a clear reduction in defect density was again seen with decreasing substrate surface roughness. Coatings deposited on a 1200 grit substrate surface finish showed a lower defect density than those deposited on a rough workshop grind substrate, and coatings deposited on the 6 µm polished substrate showed the lowest defect density. For IN625/Cr multilayer (λ100 nm) coatings deposited with interrupted and intermediate etch conditions, both showed higher defect densities than coatings deposited on the 1200 grit surface finish substrate under non-interrupted conditions. The coating deposited under intermediate etch conditions exhibited the highest number of defects out all conditions.

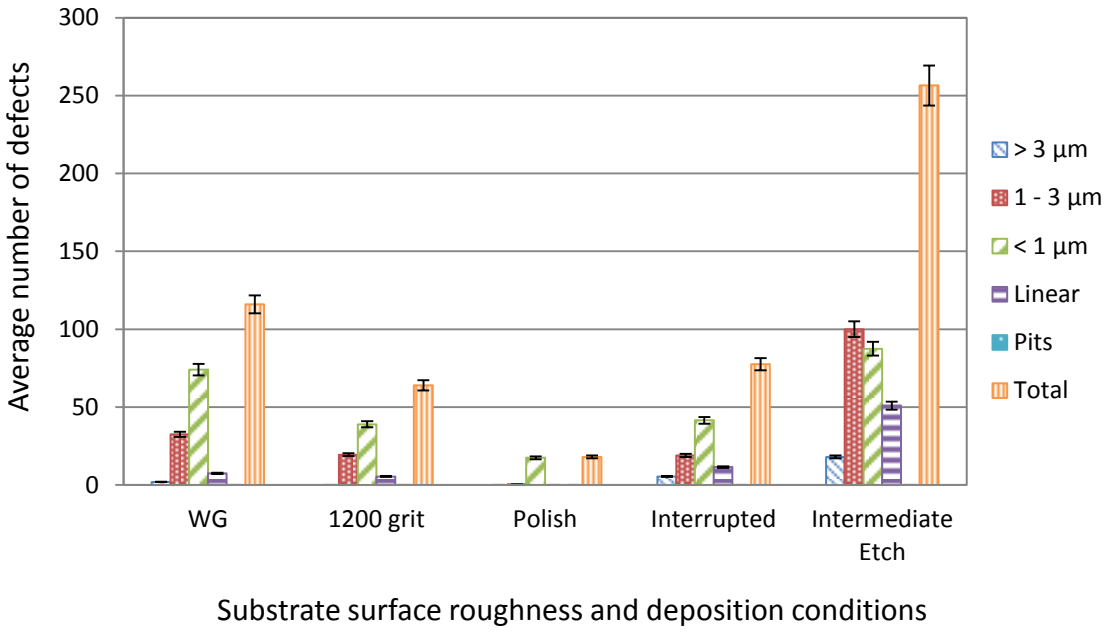


Figure 4-71 Average number of defects in a 4300 µm^2 area on IN625/Cr multilayer (λ20 nm) coatings, deposited in batch 2, on different surface roughness substrates and under different deposition conditions, error bars represent the standard deviation

The defect density on the IN625/Cr multilayer (λ20 nm) coatings (Figure 4-71) again showed that a reduction in substrate surface roughness resulted in a reduction of defects. However, the multilayer λ20 nm coating deposited on a 6 µm polished substrate almost entirely delaminated from the substrate after deposition, suggesting poor adhesion to the substrate due to high stresses as high stresses were recorded for the λ100 nm coating deposited on polished substrate (Figure 4-57). The IN625/Cr multilayer (λ20 nm) coatings deposited under interrupted and intermediate etch conditions showed higher defect densities than the coating deposited on a 1200 grit substrate surface finish under non-interrupted conditions. Interrupted etch conditions resulted in a large increase in defects greater than 1 µm, as well as total defect density, which could be a result of dust or particle contamination on the surface during the venting or pumping stages, generating seeds for growth defects. The IN625/Cr multilayered (λ100 nm) coatings (Figure 4-70) generally showed higher defect densities than the IN625/Cr multilayered (λ20 nm) coatings (Figure 4-71). However, both multilayer coatings generally show lower defect densities than the

monolayer IN625 coatings (Figure 4-69). Reducing the substrate surface roughness appears to reduce the defect density of all types of defects. Some example top surface SEM images of the coatings are shown in Figure 4-72 (a-f).

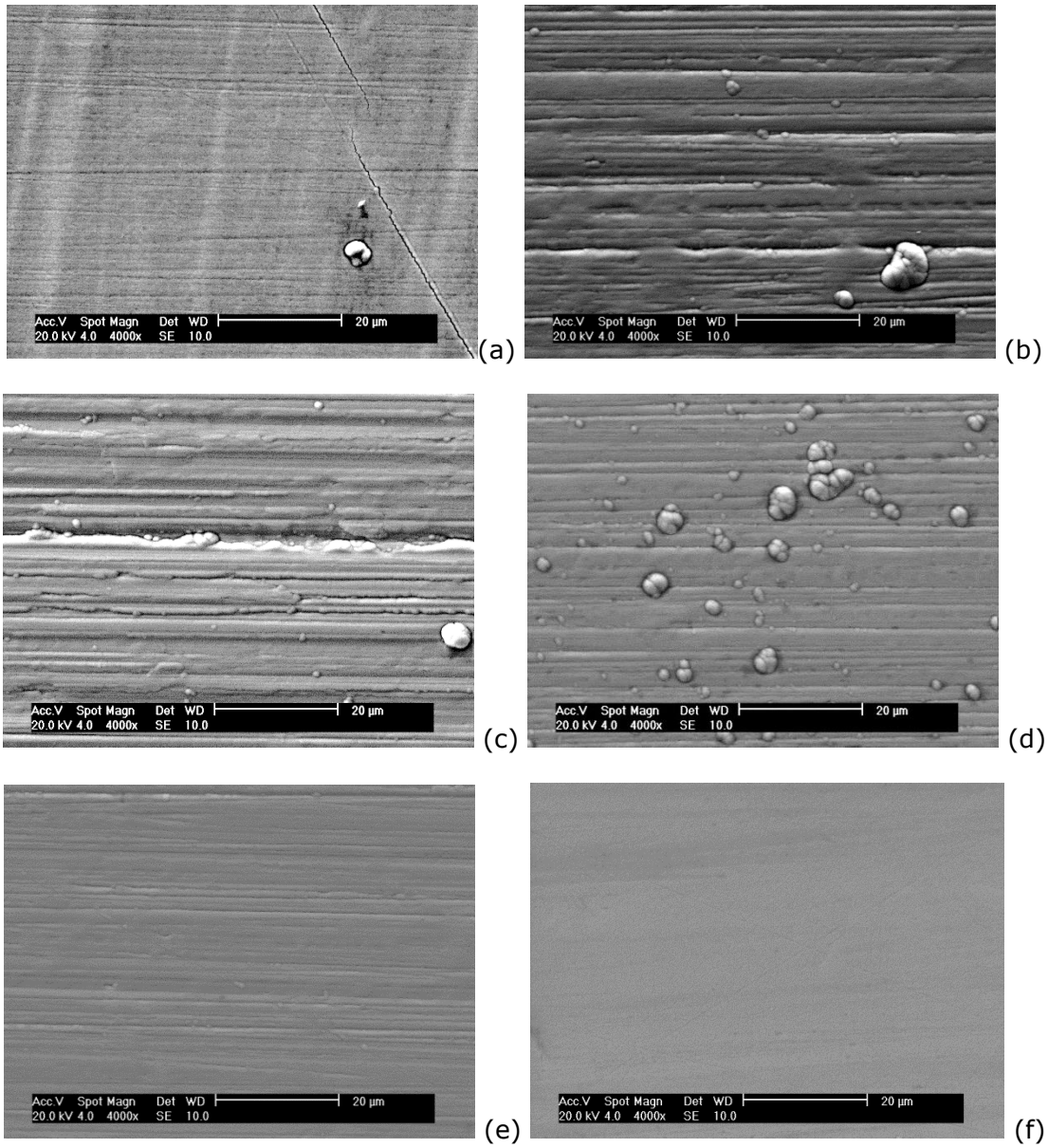


Figure 4-72 Top surface SEM micrographs of (a & b) (a) IN625 on a polished substrate (b) with an interrupted process (c & d) (c) IN625/Cr multilayer (λ20 nm) on a workshop grind substrate (d) with an intermediate etch (e & f) (e) IN625/Cr multilayer (λ100 nm) on a 1200 grit substrate (f) on a polish substrate

There is a clear reduction in defects for coatings deposited on a polished surface finish. Coatings deposited on substrates finished to 1200 grit exhibit lower numbers of

defects than coatings deposited on substrates with rougher workshop ground surface finishes. The IN625 coating deposited on a polished substrate (Figure 4-72 (a) & Figure 4-73) shows few defects; however, the coating is cracked.

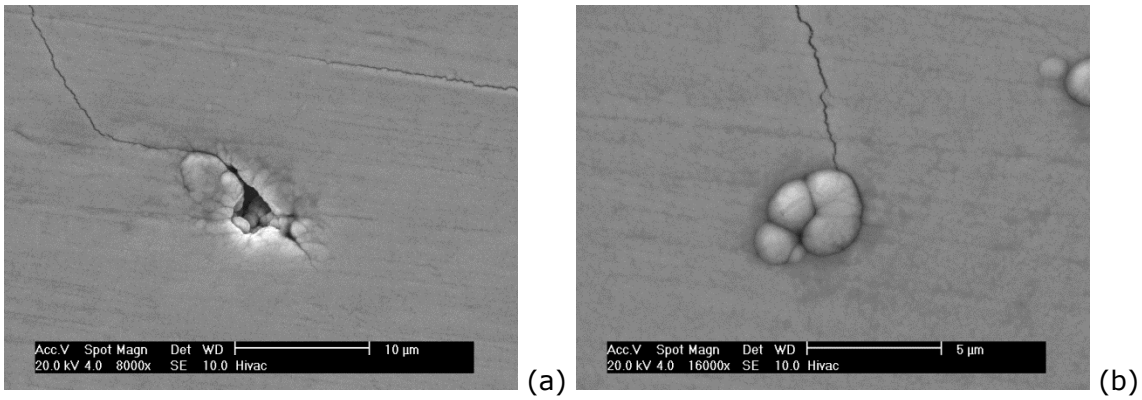


Figure 4-73 Cracks generated by defects on an IN625 coating, deposited in batch 2, on a 6 µm polish substrate

Defects have been said to act as stress raisers within coatings (Brandl and Gendig, 1996; Ries et al., 1997; Cunha and Andritschky, 1999; Jehn, 2000; Lewis et al., 2006; Altun and Sen, 2007; Čekada et al., 2007; Panjan et al., 2009; Hoche et al., 2011; Panjan et al., 2012; Panjan et al., 2013); Figure 4-73 shows cracks which appear to have been generated by defects. This suggests that defects do act as stress raisers and can therefore form cracks which limit the coatings ability to perform as a corrosion barrier for the substrate.

4.3.5.5 Potentiodynamic testing

Potentiodynamic testing was carried out to further explore the corrosion behaviour of coatings deposited on different substrate surface finishes and under different deposition conditions. As the IN625/Cr multilayered (λ100 nm) coating was the only coating which could be deposited without delamination or cracking for all conditions explored, this coating was selected for potentiodynamic testing.

Tests were carried out in the same solution used for salt spray testing (5 wt% NaCl solution) from -250 mv below OCP up to 1500 mv at a scan rate of 0.5 mV s^{-1} and a sampling rate of 1 sample per second. The potential-current density curves as well as values of corrosion potential (E_{corr}), corrosion current (i_{corr}) and polarisation resistance (R_P) were measured. The results are shown in Figure 4-74, Figure 4-75 and Table 4-5 respectively.

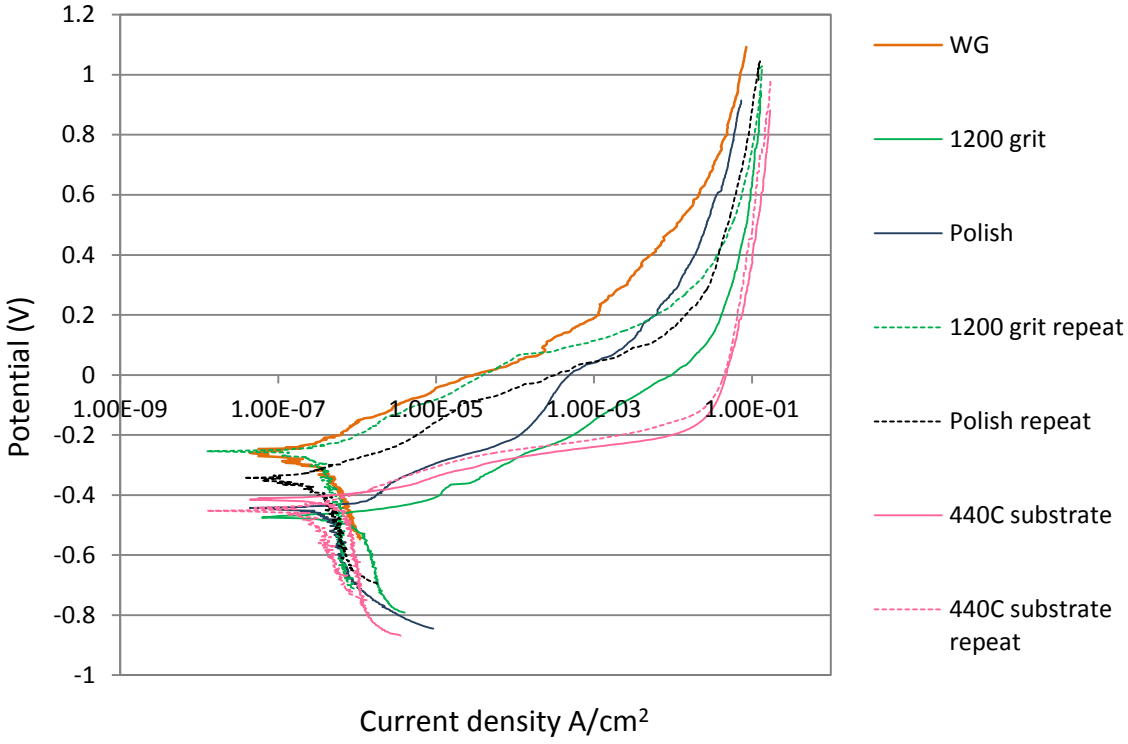


Figure 4-74 Potential-current density curves of IN625/Cr multilayer (λ100 nm) coatings deposited on different surface finishes, in 5 wt% NaCl solution

For coatings deposited on different surface roughness substrates (Figure 4-74), all coatings exhibited a large variation in potential-current curves between initial and repeat tests, however, little variation was observed in tests carried out on the uncoated 440C substrate. For coatings deposited under different deposition conditions (Figure 4-75), little variation was seen between repeat and initial tests and for different deposition conditions except for the coating deposited under standard conditions (1200 grit).

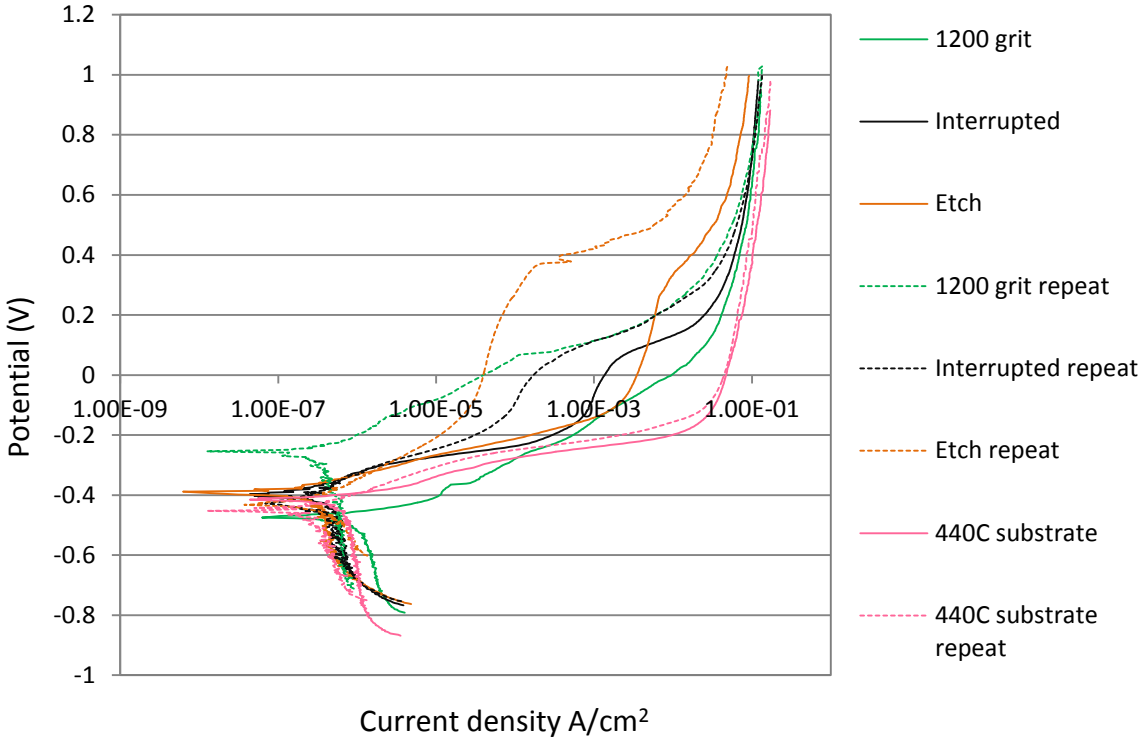


Figure 4-75 Potential-current density curves of IN625/Cr multilayer (λ100 nm) coatings deposited under different deposition conditions, in 5 wt% NaCl solution

	Initial tests			Repeat tests		
Coating	R_P (ohm.cm²)	i_{corr} (μA/cm²)	E_{corr} (V)	R_P (ohm.cm²)	i_{corr} (μA/cm²)	E_{corr} (V)
440C	26728	0.580	-0.411	25907	0.212	-0.445
λ100 nm WG	48704	0.397	-0.259	-	-	-
λ100 nm 1200	23617	0.654	-0.469	24176	0.421	-0.264
λ100 nm Polish	21950	0.318	-0.442	29821	0.163	-0.346
λ100 nm interrupted	38315	0.186	-0.393	42223	0.197	-0.417
λ100 nm etch	40218	0.114	-0.386	28933	0.339	-0.422

Table 4-5 Polarisation resistance (R_P), i_{corr} and E_{corr} values from potentiodynamic tests on IN625/Cr multilayer (λ100 nm) coatings deposited on different surface finishes and under different deposition conditions, in 5 wt% NaCl solution

The coating deposited on a workshop ground substrate exhibited the highest polarisation resistance. The interrupted process and intermediate etching process appeared to have little effect on the corrosion potential of coatings (Table 4-5). However, an increase in polarisation resistance was seen as well as some passivation on the potential-current density curves (Figure 4-75). Variations were seen in values of corrosion current, corrosion potential and polarisation resistance for two different

sections taken from the same piece of material; this suggests that defect density can vary across a coating, confirming that the defects are randomly distributed across the sample. In all tests, the coatings did not appear corroded. However, heavy delamination from the substrate was seen (Figure 4-76). Although the coating deposited on a polished substrate showed low values of corrosion potential and polarisation resistance, it was the coating that showed the least delamination.

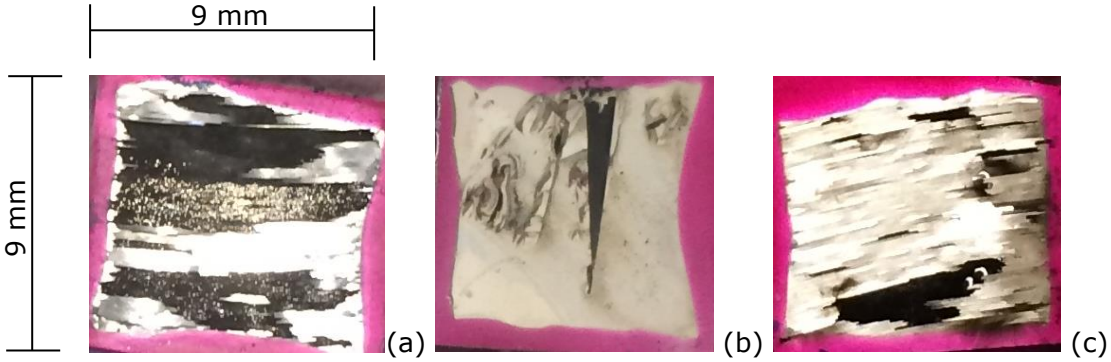


Figure 4-76 Top surface photographs of IN625/Cr multilayer (λ100 nm) coatings after potentiodynamic testing (a) deposited on a 1200 grit substrate, (b) deposited on a polished substrate (c) deposited with an interrupted process

4.3.6 Summary

Multilayering appeared to show no benefit to the corrosion barrier performance of coatings. Coatings contained large amounts of defects which created a pathway to the substrate for corrosive agents; defects were not disrupted by the multiple layers. The majority of defects were in the range of <1 μm and 1-3 μm. The substrate surface finish had a great impact on defect density. Defect density decreased with decreasing surface finish and therefore the corrosion barrier performance of coatings increased with decreasing substrate surface finish. However, stress related cracks caused delamination of the IN625/Cr λ20 nm multilayer coating from the polished substrate and resulted in cracks in the IN625 monolayer coating on a polished substrate. XRD and TEM images showed that the coatings had a polycrystalline structure in the {1 1 1} plane of the nickel matrix phase and the {1 1 0} plane for the chromium

phase. Potentiodynamic testing showed a large variation in results for different sections of a single sample suggesting growth defects are sporadic and vary in density across a coating.

5 Discussion

5.1 Coatings Intended to be Durable and Low Friction

5.1.1 Effect of multilayering, multilayer architecture and substrate hardness on the hardness of coatings

It was expected that multilayering would result in coatings with a higher hardness compared to related monolayer coatings. Different explanations exist regarding the hardening of multilayer PVD films. Some say the hardening is attributed to the Hall-Petch effect, relating the increase in coating hardness with the decrease in grain size for multilayer coatings (Holmberg et al., 1998; PalDey and Deevi, 2003; Mendibide et al., 2004; Cabrera et al., 2011; Sprute et al., 2014). Multilayering was seen to be an effective tool in creating a coating with high hardness, with the general trend showing that the smaller the bilayer period the higher the coating hardness. It was seen that the hardness of Graphit-iC coatings can be increased by multilayering with a harder material, in this case CrN.

It was expected that coatings deposited on a substrate with lower hardness would exhibit a lower hardness themselves due to increased substrate deformation. Bull and Korsunsky (1998) investigated the effect of substrate hardness on the hardness of DLC coatings, relating to the indentation depth and coating thickness, on aluminium substrates. Figure 5-1 shows the comparison between the coating hardness and the ratio of indenter penetration, δ, to the coating thickness, t, for coatings of three different thicknesses.

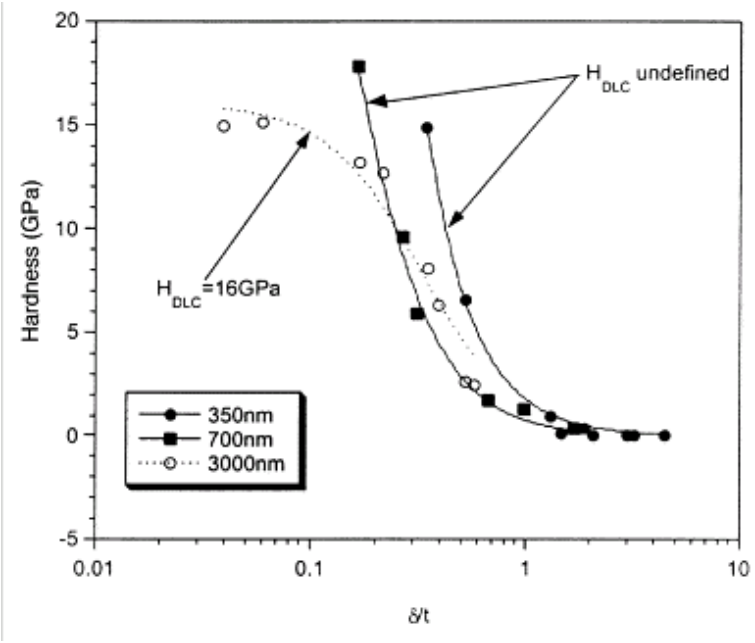


Figure 5-1 Increase in hardness due to the presence of three different thicknesses of DLC on aluminium as a function of normalised indentation depth (Bull and Korsunsky, 1998)

The research found that, the hardnesses of coatings of around 3 μm thickness were affected by the substrate hardness if the ratio of indentation depth to coating thickness was greater than 0.1. The ratios of indentation depth to coating thickness for the majority of coatings in this research were greater than 0.1. Therefore, it was expected that the substrate hardness would have a slight effect on measured coating hardness. Results from tests on the CrN/Graphit-iC multilayer systems deposited in batch 3 (Figure 4-16 (a)), showed that the substrate hardness (comparing M42 and 440C substrates of HV = 946 ± 2 kg f mm^{-2} and HV = 476 ± 7 kg f mm^{-2} respectively) had a slight effect on the hardness of coatings, with a reduction in hardness being seen for coatings deposited on the softer 440C substrates.

Using a fixed bilayer period of 100 nm and varying the architecture of the multilayers, it was expected that an increase in CrN would result in an increased hardness and vice versa due to the high hardness recorded of CrN (HV = 1707 kg f mm^{-2}) (Figure 4-5). This was confirmed by the results (Figure 4-16). Coatings with a CrN/Graphit-iC λ100 nm (3:1) multilayer ratio showed a hardness of around HV = 1448 kg f mm^{-2}

compared to that of the λ100 nm (1:1) multilayered coating (HV = 1388 kg f mm^{-2}) and λ100 nm (1:3) multilayered coating (HV = 1133 kg f mm^{-2}).

The results have shown that, when using the same bilayer period, a variation in architecture can affect the coating properties, meaning the option of tailoring a coating to have specific properties is possible. The effect of multilayer architecture on the hardness and scratch resistance of the coatings was seen to be more dominant than the effect of substrate hardness (Figure 4-16).

5.1.2 Effect of multilayering, multilayer architecture and substrate hardness on the scratch resistance of coatings

It was expected that multilayering and using a thinner bilayer period would result in a coating with higher scratch resistance due to an increase in coating deformation resistance and the multilayer interfaces acting as crack tip deflectors due to differences in shear modulus of the individual layers, improving the resistance of the coating to crack propagation. Plastic deformation and interfacial debonding is also expected to occur at the multilayer interfaces in preference to the coating/substrate interface (Holmberg et al., 1998; PalDey and Deevi, 2003; Mellor, 2006; Cabrera et al., 2011). It was also expected that coatings deposited on a softer substrate would provide a lower scratch resistance due to less load support being provided by the substrate, resulting in higher substrate deformation under load, which could result in cracking of the coating (Holmberg et al., 1998; Matthews et al., 1998; Stallard, 2005).

Multilayering was seen to be an effective tool in creating a coating with high scratch resistance, with the general trend showing that the smaller the bilayer period the higher the coating scratch resistance and therefore the higher the adhesion. Such behaviour is generally attributed to the multilayer interfaces deflecting micro-crack movements due to differences in shear modulus of the individual layers, improving the resistance of the coating to crack propagation (Holmberg et al., 1998; PalDey and

Deevi, 2003; Mellor, 2006; Cabrera et al., 2011). FIB SEM was carried out on a scratch scar to investigate this (Figure 4-37); however, no cracks were observed. The CrN + Graphit-iC coating showed a higher scratch resistance than all coatings. This could be attributed to the thick, hard CrN layer providing load support for the top Graphit-iC layer.

In all cases, coatings deposited on the softer substrate provided a lower scratch resistance as expected (Figure 4-16 (a)). This is attributed to higher substrate deformation of the softer substrate under load resulting in coating cracking and earlier coating failure (Holmberg et al., 1998; Matthews et al., 1998; Stallard, 2005). From the results it can be suggested that a harder substrate is preferable for development of a coating with high hardness and scratch resistance.

The scratch resistance was also affected by multilayer architecture; both CrN/Graphit-iC λ100 nm (1:3) and λ100 nm (3:1) multilayer coatings exhibited lower values of scratch resistance compared to the λ100 nm (1:1) multilayered coating. The reason for the decrease in scratch resistance for coatings with a 3:1 and 1:3 architecture is not well understood.

This shows that multilayering can be an effective tool in producing a coating with high hardness and high adhesion; although the monolayer CrN coating showed the highest hardness out of all coatings, all λ20 nm multilayered coatings provided a higher scratch resistance (between 28 N to 36 N increase in total failure load) compared to monolayer CrN.

5.1.3 Effect of multilayering and multilayer architecture on the microstructure of coatings

It was discovered that the coatings intended to be monolayer CrN and CrN/Graphit-iC multilayer (λ600 nm) were instead Cr_2N and Cr_2N/Graphit-iC, unlike the CrN/Graphit-iC (λ100 nm & λ20 nm) coatings which were as requested. The CrN and CrN/Graphit-iC multilayer (λ600 nm) coatings (Figure 4-3 (a & c)) showed a preferred

orientation of diffraction peaks in the {-1-1-1} plane of the Cr_2N phase at 42.6° 2θ, whereas the CrN + Graphit-iC and CrN/Graphit-iC multilayer (λ100 nm & λ20 nm) coatings (Figure 4-3 (b, d & e)) showed a preferred orientation of diffraction peaks in the {2 0 0} plane of the CrN phase at 43.3° 2θ. This difference in composition could be attributed to the different methods used to produce the λ100 nm & λ20 nm coatings compared to the λ600 nm coatings. To produce the coatings with a bilayer period of 600 nm, the multiple layers are produced by ramping the targets (alternating the power) up and down at appropriate intervals, whereas, for the λ100 nm & λ20 nm coatings, the multiple layers are developed by rotating the samples at a fixed speed between the different targets. This could also explain the diffraction peaks in the {1 5 1} plane of the chromium carbide phase at 44.2° 2θ for the CrN/Graphit-iC (λ600 nm) coating.

5.1.4 Effect of multilayering and multilayer architecture on the wear behaviour of coatings during sliding wear tests

It was expected that multilayering materials with Graphit-iC would increase the wear resistance of the coatings due to the reduction in friction through the development of a lubricious tribofilm, created by wear of the Graphit-iC and the increased resistance to crack propagation due to crack tip deflection at multilayer interfaces (Meletis et al., 1995; Holmberg et al., 1998; Grill, 1999; Wiklund et al., 1999; PalDey and Deevi, 2003; Stallard, 2005; Mellor, 2006; Holmberg et al., 2007; Cabrera et al., 2011; Olofsson et al., 2011). Whilst all PVD coatings exhibited lower wear depths than the reference Cr plate, in general, multilayering did not improve the wear resistance of coatings compared to monolayer and dual layer coatings (Figure 4-7).

The CrN + Graphit-iC coating exhibited the lowest (or very low) wear depths, ball wear rates and friction coefficients in almost all tests (Figure 4-7, Figure 4-8 & Figure 4-15). This suggests that, in general, multilayering does not increase the wear resistance of the coating or decrease the friction coefficient when compared to

monolayer coatings, as suggested in the literature (Cabrera et al., 2011). However, adding a top layer of Graphit-iC to a hard CrN layer does significantly improve the coatings wear properties. As seen from the hardness results (Figure 4-5), CrN exhibited the highest hardness out of all coatings (HV = 1707 kg f mm^{-2}). The higher wear resistance, scratch resistance and lower friction of the CrN + Graphit-iC coating, compared to the rest of the coatings, could be attributed to the load support provided by the hard CrN layer and the thick Graphit-iC top layer providing a lubricious tribofilm resulting in a low friction coefficient (Olofsson et al., 2011). A schematic cross-sectional diagram of the ball on a multilayer coating during sliding wear tests is shown in Figure 5-2.

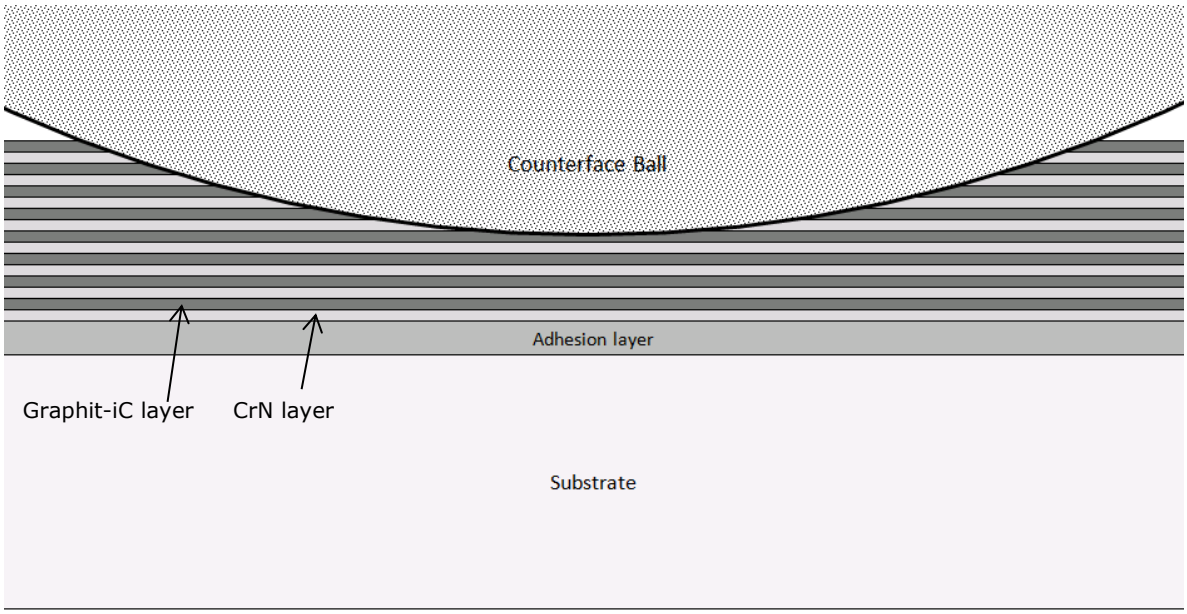


Figure 5-2 Cross-sectional schematic of coating and counterface ball during sliding wear tests

During sliding wear tests on multilayer coatings, the counterface ball is in contact with both Graphit-iC and CrN layers. The results here suggest that the CrN reduces the ability of the Graphit-iC to form a lubricious tribofilm. This was observed by the smaller transfer layers on the counterface balls tested against CrN/Graphit-iC coatings compared to CrN + Graphit-iC coatings (Figure 4-9 & Figure 4-10). As the Graphit-iC

is softer than the CrN, it wears more quickly. The resulting contact is presented in a schematic shown in Figure 5-3.

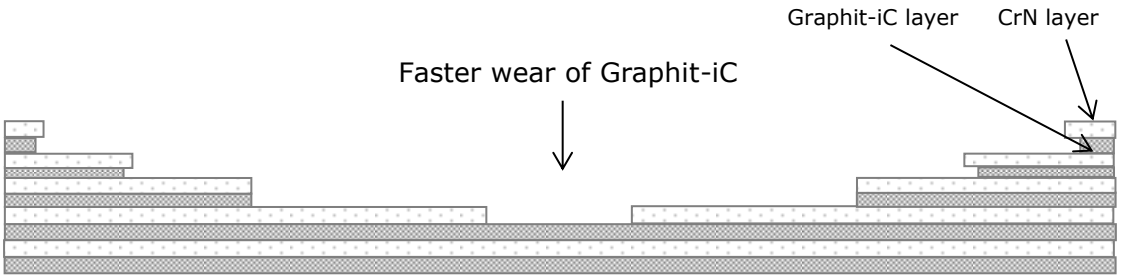


Figure 5-3 Schematic of the point of contact of the counterface ball on the coating

During steady-state wear, variation in material wear rates of the two materials is not possible. It has been suggested (Engqvist and Axén, 1999) that over a prolonged period of wear, the different phases in a multilayer system must adapt to the same wear rates. To fulfil this condition, additional removal mechanisms occur, which prefer the removal of the more wear resistant phase, resulting in a higher wear rate of the CrN compared to that of a single phase monolayer CrN, thus, resulting in a higher wear rate and friction coefficient of the multilayer coatings. However, the CrN can support the majority of the load and therefore be dominant in terms of the friction.

It was expected that changing the multilayer architecture to contain a higher amount of CrN in CrN/Graphit-iC multilayer coatings would increase the wear resistance of the coatings. Pin-on-disc tests were conducted on coatings against Ø3/8" WC-6%Co balls at sliding speeds of 0.05 m s^{-1} for 5700 revolutions, at both 10 and 40 N normal loads. Both the CrN/Graphit-iC λ100 nm (1:3) & λ100 nm (3:1) multilayer coatings showed higher wear depths (lower wear resistance) compared to the λ100 nm (1:1) coating at both loads (Figure 4-17). This could be attributed to the lower scratch resistances of the coatings (Figure 4-16 (b)); however, delamination was only seen for the λ100 nm (1:3) and λ100 nm (1:1) coatings at 40 N load (Figure 4-21 (d & f)). Therefore the reason for the decrease in wear resistance of the λ100 nm (1:3) and λ100 nm (3:1) coatings compared to the λ100 nm (1:1) coating is not well understood.

The CrN/Graphit-iC λ100 nm (1:1) coating exhibited wear depths even lower than that of the dual layered CrN + Graphit-iC coating. This is due to the local support provided by the CrN which reduces the wear rate of the Graphit-iC by reducing the contact pressure. All coatings exhibited significantly lower wear rates and counterface ball wear rates compared to Cr plate. This is because the Cr plate cannot provide a lubricious tribofilm, unlike the Graphit-iC, and has a high friction coefficient resulting in high energy dissipation and therefore higher wear.

In all cases, for batch 3 PVD coatings, the wear rates and counterface ball wear rates were very low (less than 2.18 x 10^{-15} m^3 N^{-1} m^{-1} and 4.2 x 10^{-17} m^3 N^{-1} m^{-1} respectively).

5.1.5 Effect of substrate hardness on the wear behaviour of coatings during sliding wear tests

It was expected that a substrate with lower hardness would result in a coating with lower wear resistance due to higher substrate deformation under load and therefore, coating cracking (Holmberg et al., 1998; PalDey and Deevi, 2003; Mellor, 2006; Cabrera et al., 2011). All PVD coatings exhibited lower wear depths than the reference Cr plate (Figure 4-7 (a & b)). At 10 N load (Figure 4-7 (a)), coatings deposited on 304L and 440C substrates generally showed similar wear depths as well as similar counterface ball wear rates (Figure 4-8), although a trend was seen on the 304L and M42 substrates indicating that a smaller bilayer period resulted in an increase in ball wear rate which could be attributed to the higher hardness of the coatings. At 40 N load (Figure 4-7 (b)), coatings deposited on 304L substrates resulted in the highest wear depths (Figure 4-7); in contrast, coatings deposited on M42 substrates generally exhibited the lowest wear depths (Figure 4-7) and counterface ball wear rates (Figure 4-8) for all coatings due to lower substrate deformation (Holmberg et al., 1998; PalDey and Deevi, 2003; Mellor, 2006; Cabrera et al., 2011). The lower counterface wear rate for coatings deposited on M42 substrates could also be

attributed to the lower surface roughness of the M42 substrates (~40 nm Ra) in comparison with the 440C and 304L substrates (~350 nm Ra). From the top surface SEM images of the wear scars (Figure 4-11 & Figure 4-12), smoothing of the Graphit-iC layers was observed (Figure 4-13); however, little wear could be seen on the coatings. The results showed that, in general, a harder substrate results in a coating with higher wear resistance and lower counterface wear rate. This is attributed to the lower load support offered by the softer substrates, resulting in substrate deformation and coating cracking. The increase in coating wear for those deposited on softer substrates also results in an increase in counterface wear due to coating fragments acting as abrasives and an increase in areas of exposed substrate resulting in higher wear (Holmberg et al., 1998; PalDey and Deevi, 2003; Mellor, 2006; Cabrera et al., 2011).

5.1.6 Effect of counterface ball material on the wear behaviour of coatings during sliding wear tests

Pin-on-disc tests were carried out at a sliding speed of 0.05 m s^{-1} for 5700 revolutions, at 10 and 40 N normal loads against Ø3/8" Stellite 20 balls (HV = 740 ± 10 kg f mm^{-2}) and Ø3/8" WC-6%Co balls (HV = 1700 ± 10 kg f mm^{-2}). It was expected that the Stellite balls would experience more wear than the WC-6%Co balls due to their lower hardness. The wear rates of the Stellite counterface balls were higher than those of the WC-6%Co balls in all tests (Figure 4-25) as expected. Wear tests carried out against the softer Stellite balls generally resulted in lower wear depths on monolayer and dual layer coatings, compared to tests against WC-6%Co balls, but higher wear depths on multilayered coatings (Figure 4-24). This could be attributed to the different wear modes occurring when testing against a ball of different composition, the higher ball wear rates for the softer Stellite 20 balls, resulting in more ball wear fragments and the generally higher wear rates and friction coefficients of multilayer coatings (Figure 4-24 (a & b)), as explained in section 5.1.4,

due to the different phases in a multilayer system adapting to the same wear rates (Engqvist and Axén, 1999), resulting in the CrN supporting the majority of the load, therefore, being dominant in terms of the friction and increasing the wear rate of the coating and counterface (Figure 4-25). The CrN and CrN/Graphit-iC λ100 nm (1:1) coatings resulted in the highest ball wear rates at both 10 and 40 N (Figure 4-25 (a & b)) due to the high hardness of the coatings (Figure 4-5 (a) & Figure 4-16 (a)). It is clear that the dual layered CrN + Graphit-iC coating gives the lowest ball wear rate out of all coatings. When tested against a Stellite ball, the CrN + Graphit-iC coating exhibited similar wear depths to the monolayer CrN (Figure 4-24); however, a large reduction in wear was seen for the counterface (Figure 4-25) as well as a reduction in friction coefficient (Figure 4-31) due to the formation of a lubricious tribofilm from the Graphit-iC top layer as can be seen from the top surface SEM images (Figure 4-11) (Meletis et al., 1995; Grill, 1999; Wiklund et al., 1999; Stallard, 2005; Holmberg et al., 2007; Olofsson et al., 2011). The Cr plate exhibited very low wear when tested against a Stellite 20 ball, however high wear when tested against a WC-6%Co ball, thus highlighting the importance of selecting a counterface which truly represents the service conditions of the coating.

5.2 Friction Coefficient

5.2.1 Effect of multilayering on the friction coefficients of coatings during sliding wear tests

It was expected that multilayering Graphit-iC with CrN would result in a coating with a lower friction coefficient than CrN due to the reduction in friction through the development of a lubricious tribofilm, created by wear of the Graphit-iC (Meletis et al., 1995; Holmberg et al., 1998; Grill, 1999; Wiklund et al., 1999; PalDey and Deevi, 2003; Stallard, 2005; Mellor, 2006; Holmberg et al., 2007; Cabrera et al., 2011; Olofsson et al., 2011). In contrast to observations made elsewhere (Cabrera et al.,

2011), multilayering was not seen to offer an effective way to reduce the coefficient of friction, and in most cases an increase in friction coefficient was observed (Figure 4-15) compared to the monolayer CrN and dual layer CrN + Graphit-iC coatings. It has been suggested that this can be attributed to the higher wear rates and increase in material removal mechanisms as explained in Figure 5-2 & Figure 5-3 resulting in surface roughening and abrasive particles.

However, all PVD coatings exhibited lower friction coefficients than the reference Cr plate. The dual layered CrN + Graphit-iC coating exhibited the lowest friction coefficient out of all coatings at both 10 N and 40 N loads. This could be attributed to the thick (2.4 μm) Graphit-iC top layer providing a lubricious tribofilm (Meletis et al., 1995; Grill, 1999; Holmberg et al., 2007; Olofsson et al., 2011).

5.2.2 Effect of multilayer architecture on the friction coefficient of coatings during sliding wear tests

Three CrN/Graphit-iC multilayer systems were investigated with bilayer periods and material ratios of λ100 nm (3:1), λ100 nm (1:1) and λ100 nm (1:3) on 440C substrates. Pin-on-disc tests were carried out against Ø3/8" WC-6%Co balls at sliding speeds of 0.05 m s^{-1} for 5700 revolutions, at 10 and 40 N normal loads. The coating with the most Graphit-iC (λ100 nm (1:3)) exhibited the lowest friction coefficient out of all multilayer coatings (Figure 4-23), as expected, due to the higher amount of Graphit-iC resulting in increased lubrication from the tribofilm developed (Meletis et al., 1995; Grill, 1999; Wiklund et al., 1999; Stallard, 2005; Holmberg et al., 2007; Olofsson et al., 2011). This coating resulted in lower friction coefficients than CrN in both 10 N and 40 N tests. However, the CrN/Graphit-iC λ100 nm (3:1) coating, despite having a larger fraction of the higher friction CrN, also exhibited a lower friction coefficient than the λ100 nm (1:1) coating (which showed the highest friction coefficient for all PVD coatings from batch three), in both 10 N and 40 N tests. SEM images of the wear scars on the CrN/Graphit-iC λ100 nm (1:1) coating after sliding

wear tests at 40 N load (Figure 4-21 (d)) showed more delamination both inside and surrounding the wear track compared to the 3:1 (Figure 4-21 (b)) and 1:3 (Figure 4-21 (f)) coatings. The CrN/Graphit-iC λ100 nm (1:1) coating also exhibited the highest scratch resistance out of the multilayer systems (Figure 4-16 (b)), as well as the lowest wear depth of all CrN/Graphit-iC multilayer coatings (Figure 4-17); therefore, the reason for the larger amount of delamination of this coating in 40 N tests is not well understood.

The CrN/Graphit-iC λ100 nm (3:1) coating exhibited a low initial friction at 10 N (Figure 4-22 (a)), attributed to the Graphit-iC top layer. The friction then increased throughout the test due to the exposure of the CrN layers, resulting in a final friction coefficient of around 0.23. However, at 40 N (Figure 4-22 (b)), the friction coefficient showed a smaller increase in friction coefficient throughout the test resulting in a final friction coefficient of around 0.15. This could be attributed to the higher load resulting in a faster generation of the lubricious tribofilm as SEM images revealed a smooth wear track (Figure 4-21 (a & b)) (Liu et al., 1996).

The friction coefficients of the CrN/Graphit-iC λ100 nm (1:3) multilayer coatings remained steady throughout both 10 N and 40 N tests, at around 0.1 (Figure 4-22 (e & f)). This low and steady friction coefficient is attributed to the higher percentage of Graphit-iC in the multilayer system. Some minor delamination of the Graphit-iC top layers was seen from SEM images of the wear tracks (Figure 4-21 (e & f)); however the majority of the wear tracks appeared smooth.

Although using a different multilayer ratio decreased the friction coefficient compared to the CrN/Graphit-iC λ100 nm (1:1) coating, the dual layer CrN + Graphit-iC coating still resulted in the lowest friction coefficient out of all coatings, at both 10 N and 40 N (Figure 4-23). This means that whilst the friction coefficient of a multilayer coating can be tailored through multilayer architecture, the dual layer system still provided the lowest friction.

5.2.3 Effect of substrate hardness on the friction coefficient of coatings during sliding wear tests

Pin-on-disc tests were carried out against a Ø3/8" WC-6%Co ball at 10 and 40 N normal loads for coatings deposited on 304L, 440C and M42 substrates. In all tests, all PVD coatings resulted in lower friction coefficients than the relevant uncoated substrates as well as the reference Cr plate (Figure 4-15). At 10 N normal load (Figure 4-15 (a)), the friction appeared to be affected by the coating material more than the substrate. In general, the friction of CrN/Graphit-iC multilayer coatings was higher for coatings deposited on softer 304L and 440C substrates compared to those deposited on M42 substrates. This could be attributed to the lower load support offered by the softer substrates for the thin hard coatings, resulting in substrate deformation and coating cracking, forming wear debris and allowing the CrN to dominate the friction coefficient (Holmberg et al., 1998; PalDey and Deevi, 2003; Mellor, 2006; Cabrera et al., 2011). As the coatings are very hard (Figure 4-5), they require a hard substrate for load support. This suggests that the friction may also be controlled by the ratio of coating hardness to substrate hardness. In addition, the lower friction coefficients for coatings deposited on M42 substrates could also be attributed to the lower surface roughness of the M42 (44 ± 4 nm Ra) compared to the 304L and 440C substrates (343 ± 40 nm Ra).

At 40 N normal load (Figure 4-15 (b)), the CrN/Graphit-iC multilayered (λ600 nm & λ100 nm) coatings on M42 substrates gave very low friction coefficients (around 0.05) compared to the λ20 nm multilayered coating (around 0.13). This could be attributed to the thicker Graphit-iC top layers on the λ600 nm & λ100 nm multilayered coatings, providing a more substantial tribofilm, giving lower friction for a longer period of time (Olofsson et al., 2011).

5.2.4 Effect of counterface ball material on the friction coefficient of coatings during sliding wear tests

It was expected that tests against the Stellite 20 balls would result in less wear than the WC-6%Co balls due to their lower hardness, therefore a closer investigation into the friction coefficient could be executed. In most cases, at 10 N normal load (Figure 4-30 (a)), the Stellite balls resulted in lower friction coefficients than the WC-6%Co balls. However, at 40 N load (Figure 4-30 (b)), the Stellite ball resulted in higher friction coefficients for the CrN/Graphit-iC multilayer systems, CrN and the uncoated 440C substrate. This could be attributed to the higher wear of the stellite balls, due to their lower hardness, resulting in a rougher counterface surface as well as ball wear fragments which could act as abrasives, increasing the wear rate and friction coefficient. In all cases, the CrN + Graphit-iC coating exhibited the lowest friction coefficients out of all coatings at both 10 N and 40 N (Figure 4-31 (a & b)).

The CrN/Graphit-iC λ100 nm (3:1) and (1:1) coatings exhibited higher friction coefficients than the monolayer CrN when tested at 40 N against a Stellite ball (Figure 4-31 (b)). This could be attributed to the mechanisms described in Figure 5-2 & Figure 5-3. In contrast, for the CrN/Graphit-iC λ100 nm (1:3) coating, the development of the lubricious tribofilm was promoted due to the lower percentage of CrN (and higher percentage of Graphit-iC) in the coating, resulting in a lower friction coefficient (Figure 4-22).

Results showed that, by changing the multilayer architecture to contain an increased percentage of Graphit-iC can result in a lower and steadier friction. This was seen when tested against both a Stellite and WC-6%Co ball (Figure 4-31). However, the wear resistance of the coatings appeared dependent on the counterface (Figure 4-24) as tests against a WC-6%Co ball showed an improved wear resistance of the CrN/Graphit-iC λ100 nm (1:3) coating in comparison to the CrN + Graphit-iC coating, however, the opposite was seen when tested against a Stellite 20 ball.

SEM images of the wear tracks (Figure 4-29 & Figure 4-28) revealed that the CrN and CrN + Graphit-iC coatings exhibited the least wear. Delamination of Graphit-iC layers

was seen on wear tracks of the CrN/Graphit-iC λ100 nm (1:3) multilayer coating. This could be attributed to the lower percentage of CrN, therefore lower load support offered by the 1:3 coating compared to the CrN/Graphit-iC λ100 nm (1:1) and (3:1) coatings (Figure 4-16 (a)), resulting in coating cracking and delamination under load. The CrN/Graphit-iC λ100 nm (3:1) coating exhibit no delamination suggesting the coating is hard wearing; however, the friction is dominated by the CrN as explained in section 5.1.4. The delamination of Graphit-iC from the CrN/Graphit-iC λ100 nm (1:1) coating appeared to have little effect on the friction coefficient as the friction was dominated by the CrN, however, an increase in ball wear was observed (Figure 4-18). The results show that the counterface ball material can have some effect on the friction coefficient, however, the same trends are generally seen regarding frictional behaviour and multilayer architecture.

5.2.5 Summary

Multilayering was seen to be an effective tool in creating a coating with high hardness and scratch resistance, with the general trend showing that the smaller the bilayer period the higher the coating hardness and scratch resistance. This is attributed to higher residual stresses and the multilayer interfaces deflecting micro-crack movements due to differences in shear modulus of the individual layers, improving the resistance of the coating to crack propagation (Holmberg et al., 1998; PalDey and Deevi, 2003; Mellor, 2006; Cabrera et al., 2011)

From the results, it is apparent that multilayering does not provide a better wear resistance compared to that of monolayer CrN. However, a top layer of Graphit-iC on a CrN coating can significantly reduce the wear rate of the coating and counterface as well as provide a low friction coefficient. The reason for the increase in wear rate for multilayer coatings could be attributed to the materials in the system adapting to have the same wear rate through increased wear of the material with the highest wear rate in that system (Engqvist and Axén, 1999).

Coatings generally showed a higher wear resistance and lower friction coefficient when deposited onto a harder substrate due to less substrate deformation under load, therefore, less cracking of the coating (Holmberg et al., 1998; Matthews et al., 1998; Stallard, 2005).

Multilayer architecture can be used to produce coatings with specific tailored properties; however, a dual layer CrN + Graphit-iC coating will still provide a lower friction coefficient and higher scratch resistance. The wear depth of coatings appeared to be more dependent on load than multilayer architecture. The counterface ball wear rate was seen to be equally dependant on multilayer architecture, load and coating wear rate.

Some coatings exhibited entirely different wear characteristics dependant on the counterface ball type, this highlights the importance of using a counterface and testing conditions which mimic those of the application intended for the coating.

For a wear resistant coating with low friction and high scratch resistance, a dual layer CrN + Graphit-iC coating, or a Graphit-iC top layer coating with a hard (HV = 1600 kg f mm^{-2}) underlayer is advised on a hard substrate.

5.3 Coatings Intended to be Corrosion and Scratch Resistant

5.3.1 Effect of multilayering, substrate surface finish and deposition conditions on the hardness of coatings.

It was expected that multilayering would result in coatings with a higher hardness compared to related monolayer coatings due to the Hall-Petch effect (Holmberg et al., 1998; Matthews, 2003; PalDey and Deevi, 2003; Mendibide et al., 2004; Mendibide et al., 2006; Zhang et al., 2009; Cabrera et al., 2011; Sprute et al., 2014).

From the hardness results (Figure 4-5 (a) & Figure 4-35 (a)), it was seen that multilayering increased the hardness of coatings compared to their relevant monolayer and dual layer coatings and hardness was seen to increase with decreasing bilayer period.

The effect of substrate surface roughness appeared to have little effect on the coatings hardness (Figure 4-62 (a)). Some variation was seen for the multilayer IN625/Cr (λ100 nm) coating. The coating deposited on a polished substrate exhibited a slightly higher hardness (HV = 86 kg f mm^{-2} higher) than the coating deposited on a 1200 grit surface finish substrate. The higher hardness of the coating deposited on a polished substrate could be attributed to the higher compressive residual stresses (Figure 4-57), as such stresses can retard crack propagation and increase fracture toughness (Holmberg et al., 1998; PalDey and Deevi, 2003; Mellor, 2006).

5.3.2 Effect of multilayering, substrate surface finish and deposition conditions on the scratch resistance of coatings

It was expected that multilayering and using a thinner bilayer period would result in a coating with higher scratch resistance due to an increase in coating deformation resistance and the multilayer interfaces acting as crack tip deflectors due to differences in shear modulus of the individual layers, improving the resistance of the coating to crack propagation (Holmberg et al., 1998; PalDey and Deevi, 2003; Mellor, 2006; Cabrera et al., 2011). It was also expected that coatings deposited on finer substrate surface roughnesses would exhibit a higher scratch resistance due to a reduction in growth defects which can act as stress raisers and result in higher friction and localised loss of adhesion (Brandl and Gendig, 1996; Ries et al., 1997; Cunha and Andritschky, 1999; Jehn, 2000; Lewis et al., 2006; Altun and Sen, 2007; Čekada et al., 2007; Panjan et al., 2009; Hoche et al., 2011; Panjan et al., 2012; Panjan et al., 2013).

decrease in frictional force at the indenter contact due to a higher load-carrying capacity and higher resistance to cracking (Lee et al., 1996). It was expected that intermediate etching would result in an increase in scratch resistance due to a reduction in defect density (Jehn, 2000; Fenker et al., 2002).

The scratch results (Figure 4-5 (b) & Figure 4-35 (b)) showed that, for all multilayer systems, a smaller bilayer period resulted in an increased scratch resistance with all λ20 nm coatings showing a higher scratch resistance than the relevant monolayer coating. All multilayer coatings provided a higher scratch resistance compared to the relevant dual and monolayered coatings.

The effect of substrate surface roughness appeared to have little effect on both the hardness and scratch resistance of the monolayer coatings (Figure 4-62 (a & b)). The reason for the lower scratch resistance of the λ20 nm coating on a 440C substrate compared to the λ100 nm is not well understood, as on an M42 substrate the λ20 nm coating exhibited a total failure load of >100 N compared to the λ100 nm which exhibited a total failure load of 87 N.

The IN625/Cr λ20 nm multilayered coating delaminated from the polished substrate after deposition. This could be attributed to the lower scratch resistance of the λ20 nm coating on a 440C substrate (Figure 4-62 (b)) and the higher residual stress in coatings deposited on polished substrates (Figure 4-57).

Some variation was observed for the scratch resistance of certain coatings when using different process conditions (Figure 4-63 (b)), however, no patterns were observed and in general, the overall variation was minimal.

5.3.3 Effect of multilayering, substrate surface finish and deposition conditions on the microstructure and residual stress of coatings

IN625 + Cr and IN625/Cr multilayer coatings (Figure 4-33) all showed a preferred orientation of diffraction peaks in the (1 1 1) plane of the nickel matrix phase at 43.4° 2θ and in the {1 1 0} plane of the chromium phase at 44.4° 2θ. The different substrate surface finishes and deposition conditions resulted in no change in the position of the diffraction peaks (Figure 4-52 to Figure 4-54); however, some peak broadening was observed for coatings deposited on 1200 grit or polished substrates and for coatings deposited under interrupted deposition conditions. This could be attributed to the slightly higher residual stresses observed in coatings deposited on finer substrate surface finishes and under interrupted conditions (Figure 4-57). Peak broadening was also observed for multilayer coatings; this is attributed to the smaller grain sizes of thin multilayers, rather than higher residual stresses (Holmberg, Matthews et al. 1998) as the residual stress exhibited by λ20 nm coating was lower than that of λ100 nm coatings (Figure 4-57). Multilayers generally exhibited lower compressive residual stresses for thinner bilayer periods. This could be attributed to microcracks between layers (observed in Figure 4-58) resulting in stress relief. However, it is not known if these cracks are present in the as deposited coating or if they are a result of stress relief during the thinning process of the TEM sample.

Coatings deposited on a substrate with a finer surface finish, and under intermediate etch conditions, exhibited an increase in coating residual stress (Figure 4-57) with all coatings exhibiting compressive residual stresses which in some cases led to coating cracking. Coatings were seen to have a polycrystalline structure (Figure 4-60).

5.3.4 Effect of multilayering, substrate surface finish and deposition conditions on the corrosion barrier performance of coatings

Multilayering was expected to result in coatings with higher corrosion resistance. Since the interfaces in a multi-layered structure are expected to block the path of the corrosion agents to the substrate by disrupting the structure of the coating and thus disrupting the defect growth through the coating (Holmberg et al., 1998; Jehn, 2000; Liu et al., 2001; PalDey and Deevi, 2003; Dobrzański et al., 2006; Mellor, 2006; Bobzin et al., 2012; Bobzin et al., 2013). It was also expected that a finer substrate surface finish would result in a coating with higher corrosion resistance as a finer surface finish has been shown to reduce defect density (Munemasa and Kumakiri, 1991).

Multilayering resulted in no significant improvement of the corrosion barrier performance of the coatings (Figure 4-38), suggesting that for the systems selected, the concepts proposed in the literature of multilayering disrupting the pathway for defects (Holmberg et al., 1998; PalDey and Deevi, 2003; Mellor, 2006) are not applicable; the defects were seen to pass through the coating regardless of multilayers.

This lack of disruption upon multilayering may depend upon the combination of materials chosen, IN625 and chromium. Both possess cubic structures (face-centered cubic (1 1 1) and body-centered cubic (1 1 0) respectively), resulting in good potential for epitaxial growth (with the closest-packed directions on the closest-packed planes having similar inter-atom spacings). It is possible that the mechanical and structural

properties of the two materials were too similar to provide any benefit to the corrosion resistance through structure disruption due to multilayering.

Although multilayers did not improve the corrosion barrier performance, some improvement was seen for dual layered IN625+Cr coating (Figure 4-38). This could be attributed to the thickness of the coating (7 μm) (Table 4-1). It has been said that a thicker coating can provide a better corrosion resistance (Jehn, 2000). The reference nickel plate coating showed no corrosion for over 200 hours, whereas all PVD coatings corroded within 10 hours.

Coatings exhibited very localised corrosion (Figure 4-39). Cross sectional and top surface SEM (Figure 4-40 to Figure 4-42) indicated that, in general, the coatings themselves were not corroding; however, corrosive media was reaching the substrate through pores such as defects, pinholes and cracks in the coatings. EDX results indicated that the corrosion products were iron oxide and not oxide compounds of coating elements. The substrate then corroded and delaminated the coating, or the coating collapsed into the corroded substrate.

The corrosion barrier performance of the IN625/Cr λ100 nm multilayer coating (Figure 4-65) was significantly increased for coatings deposited on a polished substrate. The λ100 nm coating on a polished substrate prevented corrosion for the first eight hours in the first test and for the first three hours in the repeat test, using a different section of the same sample, showing that defects are sporadic and can vary in density across a coated sample. For the monolayer IN625 coating, an increase was seen in corrosion barrier performance for the coating deposited on a 1200 grit substrate compared to the coating deposited on a rough (WG) substrate (Figure 4-64). However, the coatings deposited on a polished substrate, and under intermediate etch conditions, exhibited no further improvement in corrosion barrier performance due to cracks in the coatings (Figure 4-67 (f)). These cracks could be attributed to the higher residual stresses in coatings deposited on polished substrates and under interrupted conditions (Figure 4-57). Interrupting the process and intermediate etching generally resulted in a greater defect density for all coatings

(Figure 4-69 to Figure 4-71). This could be attributed to dust or particles, which remain in the chamber even after cleaning, being moved during the pumping stage and landing on the sample surface or through weakening of the coating integrity due to ion induced defects and stress relaxation due to ion generated thermal spikes during the intermediate etch (Fenker et al., 2002).

In potentiodynamic tests, the IN625 coating on a rough substrate (WG) exhibit two very different results for two different sections of the same sample. This shows that defects are sporadic and defect density can largely vary across a coated sample. All coatings delaminated during potentiodynamic tests (Figure 4-76); however, the coatings showed no sign of corrosion. This provides further evidence supporting the theory that the corrosive media reaches the substrate through growth defects in the coating, this then delaminates the coating from the substrate.

5.3.5 Effect of multilayering, substrate surface finish and deposition conditions on the defect density in coatings

Growth defects occur from seeds during deposition (nucleation sites), which can occur from a variety of sources: the cleanliness of the deposition chamber, substrate surface roughness, foreign particle contamination and more. Rotation of the samples during deposition can also generate wear particles which act as seeds (Altun and Sen, 2007; Durst et al., 2008; Panjan et al., 2009; Panjan et al., 2013). The ion etch stage has also been known to create seeds (due to different etch rates) if the substrate is a non-homogenous material. Etching of coated parts in the chamber can also generate flakes and particles that can land on the substrate. (Altun and Sen, 2007; Durst et al., 2008; Panjan et al., 2009; Panjan et al., 2013).

Substrate surface roughness was shown to have a large impact on the defect density (Figure 4-69 to Figure 4-71) showing a reduction in defect density with decreasing surface roughness. In all cases, the coatings deposited on polished substrates exhibited the lowest number of defects. The defects that dominated were the 1-3 μm

and <1 μm defects. Interrupting the process and intermediate etching resulted in a greater number of defects which could be attributed to dust or particles being moved during the pumping stage and landing on the sample surface or through weakening of the coating integrity due to ion induced defects and stress relaxation due to ion generated thermal spikes during the intermediate etch (Fenker et al., 2002).

5.3.6 Summary

Multilayering was not seen as an effective tool for improving the corrosion resistance of coatings as often suggested in the literature (Holmberg et al., 1998; Jehn, 2000; Liu et al., 2001; PalDey and Deevi, 2003; Dobrzański et al., 2006; Mellor, 2006; Bobzin et al., 2012; Bobzin et al., 2013). Corrosive media was observed to travel through coating defects towards the substrate resulting in corrosion of the substrate followed by coating delamination, however, no corrosion of the coating was observed. Growth defects are sporadic and defect density can largely vary across a coated sample. Defects occur from seeds during deposition (nucleation sites), which can occur from a variety of sources such as the cleanliness of the deposition chamber, substrate surface roughness, foreign particle contamination and more (Altun and Sen, 2007; Durst et al., 2008; Panjan et al., 2009; Panjan et al., 2013).

Multilayers were not observed to disrupt the growth of defects. This could be attributed to the materials chosen, IN625 and chromium. Both possess cubic structures (face-centered cubic (1 1 1) and body-centered cubic (1 1 0) respectively), resulting in good potential for epitaxial growth.

It was found that the substrate surface finish played a large role in development of growth defects. A reduction in substrate surface finish showed a reduction in defect density across all coatings. Interrupting the coating process and intermediate etching showed no improvement in corrosion resistance of coatings and in most cases resulted in an increase in defect density due to dust or particles, which remain in the chamber even after cleaning, being moved during the pumping stage and landing on the

sample surface or through weakening of the coating integrity due to ion induced defects and stress relaxation due to ion generated thermal spikes during the intermediate etch (Fenker et al., 2002).

Multilayering was seen as an effective tool for increasing coating hardness and scratch resistance which could be attributed to the Hall-Petch effect or due to an increase in hardness to elastic modulus (Holmberg et al., 1998; Matthews, 2003; PalDey and Deevi, 2003; Mendibide et al., 2004; Mendibide et al., 2006; Zhang et al., 2009; Cabrera et al., 2011; Sprute et al., 2014). The effect of substrate surface roughness and deposition conditions appeared to have little effect on both the hardness and scratch resistance of coatings.

The IN625 + Cr and IN625/Cr multilayer coatings all showed a preferred orientation of diffraction peaks in the {1 1 1} plane of the nickel matrix phase at 43.4^{o} 2θ and in the {1 1 0} plane of the chromium phase at 44.4^{o} 2θ. Peak broadening was observed for coatings deposited on 1200 grit or polished substrates and for coatings deposited under interrupted deposition conditions. This could be attributed to the higher residual stresses in coatings deposited on finer substrate surface finishes and under interrupted conditions.

6 Conclusions

- Multilayering was seen within two PVD coating systems to be an effective tool in creating a coating with high hardness, with the general trend showing that the smaller the bilayer period the higher the coating hardness. This hardening is attributed to the Hall-Petch effect, relating the increase in coating hardness with the decrease in grain size.

- Multilayering was seen to be an effective tool in creating a coating with high scratch resistance, with the general trend indicating that higher coating scratch resistance was achieved as the bilayer period was reduced. Such behaviour is generally attributed to the multilayer interfaces deflecting micro-cracking due to differences in shear modulus of the individual layers, improving the resistance of the coating to crack propagation.

- Changing the multilayer architecture can affect the properties of the coatings. Using a fixed bilayer period of 100 nm, coating hardness was directly affected by the volume of the harder material (CrN) within that system, with an increase in hardness resulting from a higher fraction of the harder material.

- In all cases, coatings deposited on the softer substrate exhibited a lower scratch resistance and hardness. This is attributed to higher substrate deformation of the softer substrate under load. For scratch tests, this resulted in coating cracking and earlier coating failure.

- Whilst all PVD coatings exhibited lower wear depths than the reference chrome plate, in general, multilayering did not improve the wear resistance of PVD coatings compared to monolayer and dual layer PVD coatings. Multilayering was also not seen to offer an effective way to reduce the coefficient of friction,

and in most cases an increase in friction coefficient was observed. This is attributed to the different phases in a multilayer system receding in wear at the same rate, resulting in a higher wear rate of the CrN compared to that of a single phase monolayer CrN. This results in a higher wear rate and friction coefficient of the multilayer coatings; however, within the multilayers, the CrN supports the majority of the load (due to its higher wear resistance) and therefore dominates in terms of the coefficient of friction.

- The dual layer CrN + Graphit-iC coating exhibited the highest wear resistance and lowest friction coefficient of all the coatings examined. This is attributed to the load support provided by the hard CrN layer and the thick Graphit-iC top layer providing a lubricious tribofilm resulting in a low friction coefficient.

- The results showed that, in general, a harder substrate results in a coating with higher wear resistance and (as a result) a lower counterface wear rate. This is attributed to the lower load support offered by the softer substrates, resulting in substrate deformation and coating cracking. The increase in coating wear for those deposited on softer substrates also results in an increase in counterface wear due to coating fragments acting as abrasives and an increase in areas of exposed substrate resulting in higher wear.

- Using a fixed bilayer period of 100 nm and varying architecture of CrN and Graphit-iC multilayers, the results showed that changing the multilayer architecture to contain an increased percentage of the more lubricious Graphit-iC material can result in a lower and steadier friction. This was seen when tested against both a Stellite and WC-6%Co counterbodies.

- The substrate surface roughness appeared to have little effect on either the hardness or the scratch resistance of the monolayer coatings.

- Coatings exhibited very localised corrosion. No corrosion of the coating materials themselves was observed; however, corrosive media was reaching the substrate through defects such as pores, pinholes and cracks in the coatings which resulted in coating delamination as substrate corrosion proceeded.

- Multilayering resulted in no significant improvement of the corrosion barrier performance of the coatings, since growth defects were seen to grow from the substrate to the counting outer surface, regardless of any multilayering.

- The corrosion barrier performance of the IN625/Cr λ100 nm multilayer system was significantly increased for coatings deposited on a polished substrate. The λ100 nm coating on a polished substrate prevented corrosion for the first eight hours in the initial test and for the first three hours in the repeat test, using a different section of the same sample, showing that defects are sporadic and can vary in density across a coated sample.

- For the monolayer IN625 coating, an increase was seen in corrosion barrier performance for the coating deposited on a 1200 grit substrate compared to the coating deposited on a rough (WG) substrate. However, the coatings deposited on a polished substrate, and those deposited with an intermediate etch (an etch mid-way through the coating cycle, designed to disrupt defect growth) exhibited no further improvement in corrosion barrier performance due to stress related cracks in the coatings.

- Interrupting the coating process and intermediate etching during the coating process generally resulted in a lower corrosion barrier performance for all coatings and an increase in defect density. This could be attributed to dust or

particles (which remain in the chamber even after cleaning) being moved during the pumping stage and landing on the sample surface or through weakening of the coating integrity due to ion induced defects and stress relaxation due to ion generated thermal spikes during the intermediate etch.

- Substrate surface roughness was shown to have a large impact on the defect density showing a reduction in defect density with decreasing surface roughness. In all cases, the coatings deposited on polished substrates exhibited the lowest number of defects.

In summary, the benefits of multilayering indicated in the literature have not been observed in this work. In terms of coatings that combine durability with low friction, the coefficient of friction was dominated by that associated with the harder material (in this case, this was also the material with the highest coefficient of friction), and the durability was reduced, associated with more rapid degradation associated with the numerous interfaces (this observation was made despite increases in hardness and scratch resistance associated with the multilayering).

In terms of corrosion resistance, whilst the coatings themselves were corrosion resistant, the multilayering was not able to disrupt the growth defects from propagating across the individual layers. It is proposed that this is due to the similarity of the two materials chosen for the multilayers (Cr and IN625), and that multilayering should still be considered as a means of disruption of growth defects for improvement in corrosion resistance, but that materials need to be chosen which do not allow defect growth across the different materials (it is proposed that materials with very different crystal structures should be considered).

7 Future work

Recommendations for future work are as follows: -

1. In almost all wear tests, the dual layer CrN + Graphit-iC coatings provided the lowest coating and counterface wear rates as well as low friction coefficients. Therefore, further investigation into the benefits of dual layer coatings, using a self-lubricating top layer and a hard underlayer, compared to single and multilayer coatings for sliding wear applications would be beneficial.
2. Microcracks were observed between layers of the IN625/Cr λ100 nm multilayer coating when investigated using TEM, however, it was not known if these cracks were due to stress relief during the thinning of the sample. Therefore, further investigations are needed to determine whether these cracks exist in the bulk material. If the cracks are found to be in the bulk material, an investigation would need to be carried out regarding the effect this has on the coating properties.
3. To investigate the defect growth in multilayer coatings using materials with very different crystal structures to determine if defect growth can be disrupted and in turn develop a coating with good corrosion resistance and a better understanding of defect growth within PVD coatings.
4. Further investigations into the effect of substrate surface finish on the defect density of PVD coatings. Defect density was observed to decrease with decreasing surface finish, however, for some coatings; this resulted in stress related cracks. Therefore, an investigation into the effect of substrate surface finish and residual stress would be beneficial. It would be of interest to investigate the stress across different coating architectures, using materials of very different crystal structures, and on different substrate surface finishes.

8 Appendix

During this research, three different batches of coatings were produced. In each batch a duplicate coating was deposited in order to assess any variation in mechanical properties across different batches. The results of coating hardness and scratch resistance for coatings deposited in different batches are presented in Figure 8-1. Coatings were deposited under nominally identical conditions, however, variations in mechanical properties were observed. Due to this, care was taken in assessing the validity of any comparisons of results from coatings deposited in different batches. Although variations in mechanical properties across different batches were apparent, the same trends were observed. In all cases, a thinner bilayer period resulted in a higher hardness and a higher scratch resistance, regardless of differences in mechanical properties of coatings deposited in different batches. This difference in mechanical properties could be due to differences in defect density across coatings deposited in different batches. Defects can cause higher friction, voids, pitting corrosion and can act as stress raisers which can affect the coating properties. (Brandl and Gendig, 1996; Ries et al., 1997; Cunha and Andritschky, 1999; Jehn, 2000; Lewis et al., 2006; Altun and Sen, 2007; Čekada et al., 2007; Panjan et al., 2009; Hoche et al., 2011; Panjan et al., 2012; Panjan et al., 2013).

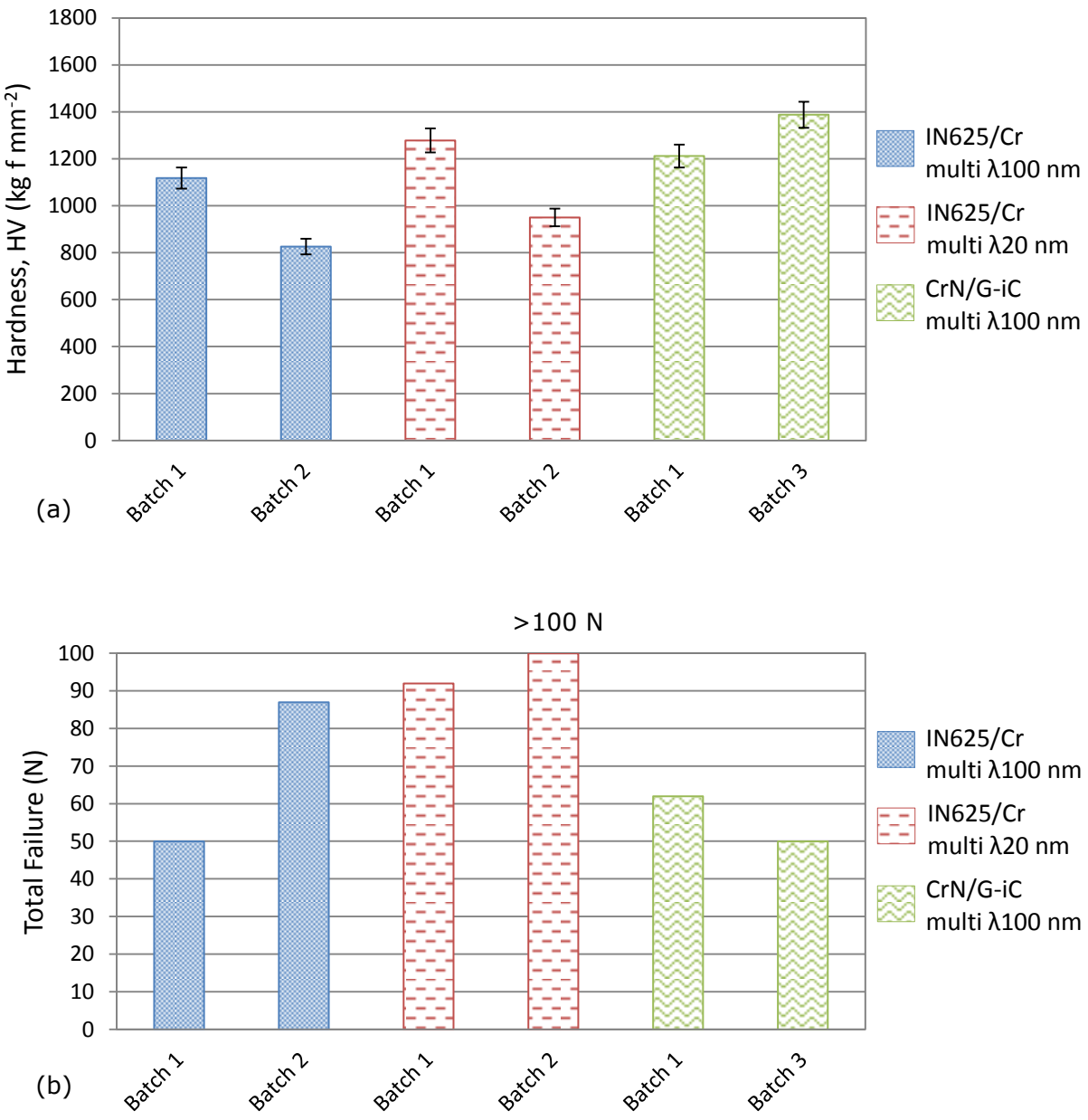


Figure 8-1 Variation in the mechanical properties (a) hardness (b) scratch resistance of repeat coatings deposited in different batches on M42 substrates (HV = 946 ± 2 kg f mm^{-2})

9 References

Abusuilik, S. B. and Inoue, K. (2013). Effects of intermediate surface treatments on corrosion resistance of cathodic arc PVD hard coatings. Surface and Coatings Technology, 237, 421-428.

Aihua, L., Jianxin, D., Haibing, C., Yangyang, C. and Jun, Z. (2012). Friction and wear properties of TiN, TiAlN, AlTiN and CrAlN PVD nitride coatings. International Journal of Refractory Metals and Hard Materials, 31, 82-88.

Altun, H. and Sen, S. (2007). The effect of PVD coatings on the wear behaviour of magnesium alloys. Materials Characterization, 58(10), 917-921.

Amiri, M. and Khonsari, M. (2010). On the thermodynamics of friction and wear - a review. Entropy, 12(5), 1021-1049.

ASTM (2015). G40-15. Standard Terminology Relating to Wear and Erosion. Annual Book of ASTM Standards. 03.02: 8.

Bayón, R., Igartua, A., Fernández, X., Martínez, R., Rodríguez, R. J., García, J. A., de Frutos, A., Arenas, M. A. and de Damborenea, J. (2009). Corrosion-wear behaviour of PVD Cr/CrN multilayer coatings for gear applications. Tribology International, 42(4), 591-599.

Blok, H. (1963). The flash temperature concept. Wear, 6(6), 483-494.

Bobzin, K., Bagcivan, N., Immich, P., Pinero, C., Goebbels, N. and Kramer, A. (2008). PVD - A success story with a future. Materialwissenschaft Und Werkstofftechnik, 39(1), 5-12.

Bobzin, K., Bagcivan, N., Theiß, S., Weiß, R., Depner, U., Troßmann, T., Ellermeier, J. and Oechsner, M. (2012). Influence of the Layer Architecture of DLC Coatings on Their Wear and Corrosion Resistance. International Journal of Materials Research and Advanced Techniques, 103(6), 774-782.

Bobzin, K., Bagcivan, N., Theiß, S., Weiß, R., Depner, U., Troßmann, T., Ellermeier, J. and Oechsner, M. (2013). Behavior of DLC coated low-alloy steel under tribological and corrosive load: Effect of top layer and interlayer variation. Surface and Coatings Technology, 215, 110-118.

Brandl, W. and Gendig, C. (1996). Corrosion behaviour of hybrid coatings. Thin Solid Films, 290–291, 343-347.

Bull, S. J. and Hainsworth, S. V. (1999). Time-dependent changes in the mechanical properties of diamond-like carbon films. Surface and Coatings Technology, 122(2-3), 225-229.

Bull, S. J. and Korsunsky, A. M. (1998). Mechanical properties of thin carbon overcoats. Tribology International, 31(9), 547-551.

Cabrera, G., Caicedo, J. C., Amaya, C., Yate, L., Muñoz Saldaña, J. and Prieto, P. (2011). Enhancement of mechanical and tribological properties in AISI D3 steel substrates by using a non-isostructural CrN/AlN multilayer coating. Materials Chemistry and Physics, 125(3), 576-586.

Camino, D., Jones, A. H. S., Mercs, D. and Teer, D. G. (1999). High performance sputtered carbon coatings for wear resistant applications. Vacuum, 52(1–2), 125-131.

Čekada, M., Panjan, P., Kek-Merl, D., Panjan, M. and Kapun, G. (2007). SEM study of defects in PVD hard coatings. Vacuum, 82(2), 252-256.

Chokethawai, K. (2008). Microstructural Evolution in Fe-Cr-B based Alloy Powder and Thermally Sprayed Coatings and their Wear Performance. Ph.D. thesis, University of Nottingham.

Cooke, K., Hampshire, J. and Teer, D. (2004). Variations on the Closed Field Unbalanced Magnetron Sputter Ion Platin Configuration. 1.

Costa, M. Y. P., Cioffi, M. O. H., Voorwald, H. J. C. and Guimarães, V. A. (2010). An investigation on sliding wear behavior of PVD coatings. Tribology International, 43(11), 2196-2202.

Creus, J., Idrissi, H., Mazille, H., Sanchette, F. and Jacquot, P. (1998). Improvement of the corrosion resistance of CrN coated steel by an interlayer. Surface and Coatings Technology, 107(2–3), 183-190.

Cullity, B. D. (1956). Elements of X-ray diffraction, Addison-Wesley Pub. Co. Reading, Mass.

Cunha, L. and Andritschky, M. (1999). Residual stress, surface defects and corrosion resistance of CrN hard coatings. Surface and Coatings Technology, 111(2–3), 158-162.

Cunha, L., Andritschky, M., Pischow, K. and Wang, Z. (1999). Microstructure of CrN coatings produced by PVD techniques. Thin Solid Films, 355–356, 465-471.

Czerwiec, T., He, H., Saker, A., Tran Huu, L., Dong, C., Frantz, C. and Michel, H. (2003). Reactive magnetron sputtering as a way to improve the knowledge of metastable F.C.C. nitrogen solid solutions formed during plasma assisted nitriding of Inconel 690. Surface and Coatings Technology, 174–175, 131-138.

PVD Chromium. (1990). Material Property Database. [online]. [Accessed 11 February 2015]. Available from http://www.mit.edu/~6.777/matprops/chromium.htm.

Depner, U., Ellermeier, J., Troßmann, T., Berger, C. and Oechsner, M. (2011). The Effect of Layer Structure on corrosion and Erosion Resistance of Thin PVD Multilayer Films. International Journal of Materials Research and Advanced Techniques, 102(8), 1014-1020.

Dobrzański, L. A., Lukaszkowicz, K., Mikula, J. and Pakula, D. (2006). Structure and corrosion resistance of gradient and multilayer coatings. Journal of Achievements in Materials and Manufacturing Engineering, 18(1-2), 75-78.

Dobrzański, L. A., Polok, M. and Adamiak, M. (2005). Structure and properties of wear resistance PVD coatings deposited onto X37CrMoV5-1 type hot work steel. Journal of Materials Processing Technology, 164–165, 843-849.

Donnet, C. and Erdemir, A. (2008). Tribology of Diamond-like Carbon Films: Fundamentals and Applications, Springer. New York.

Dörfel, I., Österle, W., Urban, I. and Bouzy, E. (1999). Microstructural characterization of binary and ternary hard coating systems for wear protection. Part I: PVD coatings. Surface and Coatings Technology, 111(2–3), 199-209.

Durst, O., Ellermeier, J. and Berger, C. (2008). Influence of plasma-nitriding and surface roughness on the wear and corrosion resistance of thin films (PVD/PECVD). Surface and Coatings Technology, 203(5–7), 848-854.

Durst, O., Ellermeier, J., Troßmann, T. and Berger, C. (2009). Erosion Corrosion of Graded Chromium Carbide Coatings in Multilayer Structure. Materialwissenschaft Und Werkstofftechnik, 40(10), 756-768.

Engqvist, H. and Axén, N. (1999). Abrasion of cemented carbides by small grits. Tribology International, 32(9), 527-534.

Erdemir, A. (2002). Friction and wear of diamond and diamond-like carbon films. Journal of Engineering Tribology, 216(Part J), 387-400.

Eyre, T. S. (1976). Wear characteristics of metals. Tribology International, 9(5), 203-212.

Fenker, M., Balzer, M., Jehn, H. A., Kappl, H., Lee, J. J., Lee, K. H. and Park, H. S. (2002). Improvement of the corrosion resistance of hard wear resistant coatings by intermediate plasma etching or multilayered structure. Surface and Coatings Technology, 150(1), 101-106.

Fenker, M., Balzer, M. and Kappl, H. (2006). Corrosion behaviour of decorative and wear resistant coatings on steel deposited by reactive magnetron sputtering – Tests and improvements. Thin Solid Films, 515(1), 27-32.

Field, S. K., Jarratt, M. and Teer, D. G. (2004). Tribological properties of graphite-like and diamond-like carbon coatings. Tribology International, 37(11-12), 949-956.

Fitzpatrick, M. E., Fry, A. T., Holdway, P., Kandil, F. A., Shackleton, J. and Suominen, L. (2005). Determination of Residual Stresses by X-ray Diffraction. Measurement Good Practice Guide No. 52,(2), 6-10.

Fry, C. (2013). Development of Magnesium-Based Multilayer PVD Coatings for Hydrogen Storage Applications. Ph.D. thesis, The University of Nottingham.

Gant, A. J. and Gee, M. G. (2009). Sliding wear corrosion of ceramics. Wear, 267(1–4), 599-607.

Grill, A. (1999). Diamond-like carbon: state of the art. Diamond and Related Materials, 8(2-5), 428-434.

Han, S., Lin, J. H., Guo, X. J., Tsai, S. H., Su, Y. O., Huang, J. H., Lu, F. H. and Shih, H. C. (2000a). The effect of Cr interlayer on the microstructure of CrN coatings on steel. Thin Solid Films, 377–378, 578-584.

Han, S., Lin, J. H., Tsai, S. H., Chung, S. C., Wang, D. Y., Lu, F. H. and Shih, H. C. (2000b). Corrosion and tribological studies of chromium nitride coated on steel with an interlayer of electroplated chromium. Surface and Coatings Technology, 133–134, 460-465.

Hans, M., Büchel, R., Grischke, M., Hobi, R. and Zäch, M. (2000). High-volume PVD coating of precision components of large volumes at low process costs. Surface and Coatings Technology, 123(2–3), 288-293.

Hoche, H., Schmidt, J., Groß, S., Troßmann, T. and Berger, C. (2011). PVD coating and substrate pretreatment concepts for corrosion and wear protection of magnesium alloys. Surface and Coatings Technology, 205, Supplement 2, S145-S150.

Hokao, M., Hironaka, S., Suda, Y. and Yamamoto, Y. (2000). Friction and wear properties of graphite/glassy carbon composites. Wear, 237(1), 54-62.

Holmberg, K., Matthews, A. and Ronkainen, H. (1998). Coatings tribology—contact mechanisms and surface design. Tribology International, 31(1–3), 107-120.

Holmberg, K., Ronkainen, H., Laukkanen, A. and Wallin, K. (2007). Friction and wear of coated surfaces — scales, modelling and simulation of tribomechanisms. Surface and Coatings Technology, 202(4–7), 1034-1049.

Hutchings, I. (1992). Tribology: Friction and Wear of engineering Materials, Elsevier. Oxford.

Jafarian, F., Amirabadi, H. and Sadri, J. (2015). Experimental measurement and optimization of tensile residual stress in turning process of Inconel718 superalloy. Measurement, 63, 1-10.

Jehn, H. A. (2000). Improvement of the corrosion resistance of PVD hard coating–substrate systems. Surface and Coatings Technology, 125(1–3), 212-217.

Jiang, J. and Arnell, R. D. (2000). The effect of substrate surface roughness on the wear of DLC coatings. Wear, 239(1), 1-9.

Jiang, J., Stott, F. H. and Stack, M. M. (1998). The role of triboparticulates in dry sliding wear. Tribology International, 31(5), 245-256.

Jianxin, D., Jianhua, L., Jinlong, Z., Wenlong, S. and Ming, N. (2008). Friction and wear behaviors of the PVD ZrN coated carbide in sliding wear tests and in machining processes. Wear, 264(3–4), 298-307.

Jisheng, E. (2002). An investigation of lubrication mechanisms and material removal of an alloy steel in sliding lubrication. Tribology Series, Elsevier. 40**,** 347-352.

Kamdi, Z., Shipway, P. H., Voisey, K. T. and Sturgeon, A. J. (2011). Abrasive wear behaviour of conventional and large-particle tungsten carbide-based cermet coatings as a function of abrasive size and type. Wear, 271(9–10), 1264-1272.

Kelly, P. J. and Arnell, R. D. (1997). Characterization studies of the structure of Al, Zr, and W coatings deposited by closed-field unbalanced magnetron sputtering. Surface and Coatings Technology, 97(1–3), 595-602.

Kelly, P. J. and Arnell, R. D. (2000). Magnetron sputtering: a review of recent developments and applications. Vacuum, 56(3), 159-172.

Kelly, P. J., Arnell, R. D., Ahmed, W. and Afzal, A. (1996). Novel engineering coatings produced by closed-field unbalanced magnetron sputtering. Materials & Design, 17(4), 215-219.

Laing, K., Hampshire, J., Teer, D. and Chester, G. (1999). The effect of ion current density on the adhesion and structure of coatings deposited by magnetron sputter ion plating. Surface and Coatings Technology, 112(1–3), 177-180.

Lee, H.-Y. (2004). Analysis of sliding wear mode on annealed steel by X-ray diffraction technique. Wear, 256(7–8), 657-663.

Lee, S.-C., Ho, W.-Y. and Lai, F. D. (1996). Effect of substrate surface roughness on the characteristics of CrN hard film. Materials Chemistry and Physics, 43(3), 266-273.

Leroy, C., Czerwiec, T., Gabet, C., Belmonte, T. and Michel, H. (2001). Plasma assisted nitriding of Inconel 690. Surface and Coatings Technology, 142–144, 241-247.

Lewis, D. B., Creasey, S. J., Wüstefeld, C., Ehiasarian, A. P. and Hovsepian, P. E. (2006). The role of the growth defects on the corrosion resistance of CrN/NbN superlattice coatings deposited at low temperatures. Thin Solid Films, 503(1–2), 143-148.

Lim, M.-K., Oh, S.-D. and Lee, Y.-Z. (2003). Friction and wear of Inconel 690 and Inconel 600 for steam generator tube in room temperature water. Nuclear Engineering and Design, 226(2), 97-105.

Liu, C., Bi, Q., Ziegele, H., Leyland, A. and Matthews, A. (2002). Structure and corrosion properties of PVD Cr-N coatings. Journal of Vacuum Science & Technology A: Vacuum, Surfaces, and Films, 20(3), 772-780.

Liu, C., Leyland, A., Bi, Q. and Matthews, A. (2001). Corrosion resistance of multi-layered plasma-assisted physical vapour deposition TiN and CrN coatings. Surface and Coatings Technology, 141(2–3), 164-173.

Liu, C., Leyland, A., Lyon, S. and Matthews, A. (1995). An a.c. impedance study on PVD CrN-coated mild steel with different surface roughnesses. Surface and Coatings Technology, 76–77, Part 2, 623-631.

Liu, Y., Erdemir, A. and Meletis, E. I. (1996). An investigation of the relationship between graphitization and frictional behavior of DLC coatings. Surface & Coatings Technology, 86-7(1-3), 564-568.

Lüdecke, C., Bossert, J., Roth, M. and Jandt, K. D. (2013). Physical vapor deposited titanium thin films for biomedical applications: Reproducibility of nanoscale surface roughness and microbial adhesion properties. Applied Surface Science, 280, 578-589.

Maeng, S., Axe, L., Tyson, T., Gladczuk, L. and Sosnowski, M. (2006). Corrosion Behavior of Magnetron Sputtered Alpha Ta Coatings on Smooth and Rough Steel Substrates. Surface & Coatings Technology, 200, 5717 - 5724.

Matthews, A. (2003). Plasma-based physical vapor deposition surface engineering processes. Journal of Vacuum Science & Technology A: Vacuum, Surfaces, and Films, 21(5), S224-S231.

Matthews, A., Jones, R. and Dowey, S. (2001). Modelling the deformation behaviour of multilayer coatings. Tribology Letters, 11(2), 103-106.

Matthews, A., Leyland, A., Holmberg, K. and Ronkainen, H. (1998). Design aspects for advanced tribological surface coatings. Surface and Coatings Technology, 100–101, 1-6.

Mattox, D. M. (2001). Physical vapor deposition (PVD) processes. Metal Finishing, 99, Supplement 1, 409-423.

Mattox, D. M. (2002). Physical vapor deposition (PVD) processes. Metal Finishing, 100, Supplement 1, 394-408.

McConnell, M. L., Dowling, D. P., Donnelly, N., Donnelly, K. and Flood, R. V. (1999). The effect of thermal treatments on the tribological properties of PVD hard coatings. Surface and Coatings Technology, 116–119, 1133-1137.

Meletis, E. I., Erdemir, A. and Fenske, G. R. (1995). Tribological characteristics of DLC films and duplex plasma nitriding/DLC coating treatments. Surface and Coatings Technology, 73(1–2), 39-45.

Mellor, B. G. (2006). Surface Coatings for Protection Against Wear, Woodhead Publishing. Cambridge.

Mendibide, C., Fontaine, J., Steyer, P. and Esnouf, C. (2004). Dry Sliding Wear Model of Nanometer Scale Multilayered TiN/CrN PVD Hard Coatings. Tribology Letters, 17(4), 779-789.

Mendibide, C., Steyer, P., Fontaine, J. and Goudeau, P. (2006). Improvement of the tribological behaviour of PVD nanostratified TiN/CrN coatings — An explanation. Surface and Coatings Technology, 201(7), 4119-4124.

Merl, D. K., Panjan, P., Čekada, M. and Maček, M. (2004). The corrosion behavior of Cr-(C,N) PVD hard coatings deposited on various substrates. Electrochimica Acta, 49(9–10), 1527-1533.

Mo, J. L. and Zhu, M. H. (2008). Sliding tribological behavior of AlCrN coating. Tribology International, 41(12), 1161-1168.

Moorthy, V. and Shaw, B. A. (2012a). Contact fatigue performance of helical gears with surface coatings. Wear, 276–277, 130-140.

Moorthy, V. and Shaw, B. A. (2012b). Effect of as-ground surface and the BALINIT® C and Nb–S coatings on contact fatigue damage in gears. Tribology International, 51, 61-70.

Munemasa, J. and Kumakiri, T. (1991). Effect of the surface roughness of substrates on the corrosion properties of films coated by physical vapour deposition. Surface and Coatings Technology, 49, 496-499.

Navinsek, B., Panjan, P. and Milosev, I. (1999). PVD coatings as an environmentally clean alternative to electroplating and electroless processes. Surface & Coatings Technology, 116, 476-487.

Navinšek, B., Panjan, P. and Milošev, I. (1997). Industrial applications of CrN (PVD) coatings, deposited at high and low temperatures. Surface and Coatings Technology, 97(1–3), 182-191.

Nilsson, M. and Olsson, M. (2011). Tribological testing of some potential PVD and CVD coatings for steel wire drawing dies. Wear, 273(1), 55-59.

Nordin, M., Herranen, M. and Hogmark, S. (1999). Influence of lamellae thickness on the corrosion behaviour of multilayered PVD TiN/CrN coatings. Thin Solid Films, 348(1–2), 202-209.

Ohana, T., Suzuki, M., Nakamura, T., Tanaka, A. and Koga, Y. (2004). Tribological properties of DLC films deposited on steel substrate with various surface roughness. Diamond and Related Materials, 13(11–12), 2211-2215.

Ohring, M. (1992). The Materials Science of Thin Films, Academic Press. San Diego.

Oliver, W. C. and Pharr, G. M. (2004). Measurement of hardness and elastic modulus by instrumented indentation: Advances in understanding and refinements to methodology. Journal of Materials Research, 19(1), 3-20.

Olofsson, J., Gerth, J., Nyberg, H., Wiklund, U. and Jacobson, S. (2011). On the influence from micro topography of PVD coatings on friction behaviour, material transfer and tribofilm formation. Wear, 271(9–10), 2046-2057.

Olofsson, U. and Olander, L. (2013). On the identification of wear modes and transitions using airborne wear particles. Tribology International, 59, 104-113.

Oskouei, R. H. and Ibrahim, R. N. (2011). The effect of a heat treatment on improving the fatigue properties of aluminium alloy 7075-T6 coated with TiN by PVD. Procedia Engineering, 10, 1936-1942.

PalDey, S. and Deevi, S. C. (2003). Single layer and multilayer wear resistant coatings of (Ti,Al)N: a review. Materials Science and Engineering: A, 342(1–2), 58-79.

Panjan, P., Čekada, M., Panjan, M. and Kek-Merl, D. (2009). Growth defects in PVD hard coatings. Vacuum, 84(1), 209-214.

Panjan, P., Čekada, M., Panjan, M., Kek-Merl, D., Zupanič, F., Čurković, L. and Paskvale, S. (2012). Surface density of growth defects in different PVD hard coatings prepared by sputtering. Vacuum, 86(6), 794-798.

Panjan, P., Gselman, P., Kek-Merl, D., Cekada, M., Panjan, M., Drazic, G., Boncina, T. and Zupanič, F. (2013). Growth defect density in PVD hard coatings prepared by different deposition techniques. Surface & Coatings Technology, 237, 349–356.

Panjan, P., Kek Merl, D., Zupanič, F., Čekada, M. and Panjan, M. (2008). SEM study of defects in PVD hard coatings using focused ion beam milling. Surface and Coatings Technology, 202(11), 2302-2305.

Prevéy, P. (1986). X-Ray Diffraction Residual Stress Techniques. Metals Handbook, 380-392.

Rai, S. K., Kumar, A., Shankar, V., Jayakumar, T., Bhanu Sankara Rao, K. and Raj, B. (2004). Characterization of microstructures in Inconel 625 using X-ray diffraction peak broadening and lattice parameter measurements. Scripta Materialia, 51(1), 59-63.

Rasmussen, A. J., Agüero, A., Gutierrez, M. and José Landeira Østergård, M. (2008). Microstructures of thin and thick slurry aluminide coatings on Inconel 690. Surface and Coatings Technology, 202(8), 1479-1485.

Regulation (EC) No 1907/2006 (2007). Concerning the Registration, Evaluation, Authorisation and Restriction of Chemicals (REACH), establishing a European Chemicals Agency, amending Directive 1999/45/EC and repealing Council Regulation (EEC) No 793/93 and Commission Regulation (EC) No 1488/94 as well as Council Directive 76/769/EEC and Commission Directives 91/155/EEC, 93/67/EEC, 93/105/EC and 2000/21/EC. 1907/2006**,** L136/133.

Ries, L. A. S., Azambuja, D. S. and Baumvol, I. J. R. (1997). Corrosion resistance of steel coated with Ti/TiN multilayers. Surface and Coatings Technology, 89(1–2), 114-120.

Rigney, D. A. (1988). Sliding Wear of Metals. Annual Review of Materials Research, 18, 141-163.

Robertson, J. (2002). Diamond-like amorphous carbon. Materials Science and Engineering: R: Reports, 37(4–6), 129-281.

Saker, A., He, H., Czerwiec, T., Li, X., Tran Huu, L., Dong, C., Michel, H. and Frantz, C. (2008). Reactive magnetron sputtering of Inconel 690 by Ar–N2 plasma. Thin Solid Films, 516(6), 1029-1036.

Singh, R. K., Xie, Z. H., Bendavid, A., Martin, P. J., Munroe, P. and Hoffman, M. (2008). Effect of substrate roughness on the contact damage of DLC coatings. Diamond and Related Materials, 17(6), 975-979.

Sprute, T., Tillmann, W., Grisales, D., Selvadurai, U. and Fischer, G. (2014). Influence of substrate pre-treatments on residual stresses and tribo-mechanical properties of TiAlN-based PVD coatings. Surface and Coatings Technology, 260, 369-379.

Sree Harsha, K. S. (2006). Principles of Physical Vapor Deposition of Thin Films, Elsevier. Oxford.

Stallard, J. (2005). The Tribological Behaviour of three Carbon-based Coatings, Tested in Air, Water and Oil Environments. Ph.D. thesis, The University of Nottingham.

Stallard, J., Mercs, D., Jarratt, M., Teer, D. G. and Shipway, P. H. (2004). A study of the tribological behaviour of three carbon-based coatings, tested in air, water and oil environments at high loads. Surface & Coatings Technology, 177, 545-551.

Stern, M. and Geary, A. L. (1957). Electrochemical Polarization: I . A Theoretical Analysis of the Shape of Polarization Curves. Journal of The Electrochemical Society, 104(1), 56-63.

Stott, F. H. (1998). The role of oxidation in the wear of alloys. Tribology International, 31(1–3), 61-71.

Stott, F. H. (2002). High-temperature sliding wear of metals. Tribology International, 35(8), 489-495.

Straffelini, G. and Gariboldi, E. (2007). Sliding behaviour of hard and self-lubricating PVD coatings against a Mg-alloy. Wear, 263(7–12), 1341-1346.

Suh, M.-S., Chae, Y.-H. and Kim, S.-S. (2008). Friction and wear behavior of structural ceramics sliding against zirconia. Wear, 264(9–10), 800-806.

Suresh Kannan, I. and Ghosh, A. (2014). Dry Machining of AA7075 by H-DLC Coated Carbide End Mill. Procedia Materials Science, 5, 2615-2621.

Thornton, J. A. (1974). Influence of apparatus geometry and deposition conditions on the structure and topography of thick sputtered coatings. Journal of Vacuum Science and Technology, 11(4), 666-670.

Thornton, J. A. (1977). High Rate Thick Film Growth. Annual Review of Materials Science, 7, 239-260.

Van Stappen, M., Stals, L. M., Kerkhofs, M. and Quaeyhaegens, C. (1995). State of the art for the industrial use of ceramic PVD coatings. Surface and Coatings Technology, 74–75, Part 2, 629-633.

Vesel, A., Drenik, A., Elersic, K., Mozetic, M., Kovac, J., Gyergyek, T., Stockel, J., Varju, J., Panek, R. and Balat-Pichelin, M. (2014). Oxidation of Inconel 625 superalloy upon treatment with oxygen or hydrogen plasma at high temperature. Applied Surface Science, 305, 674-682.

Voevodin, A. A., Rebholz, C., Schneider, J. M., Stevenson, P. and Matthews, A. (1995). Wear resistant composite coatings deposited by electron enhanced closed field unbalanced magnetron sputtering. Surface and Coatings Technology, 73(3), 185-197.

Wänstrand, O. (2000). Wear resistant low friction coatings for machine elements. Ph.D. thesis, Uppsala University.

Wen, C. Y., Guo, X. J., Huang, J. H. and Shih, H. C. (2000). Determination of the three-dimensional crystallographic misorientation in heterostructures by selected area diffraction (SAD) in cross-sectional TEM. Journal of Crystal Growth, 213(1–2), 150-156.

Wiklund, U., Wänstrand, O., Larsson, M. and Hogmark, S. (1999). Evaluation of new multilayered physical vapour deposition coatings in sliding contact. Wear, 236(1–2), 88-95.

Yang, Q., Senda, T., Kotani, N. and Hirose, A. (2004). Sliding wear behavior and tribofilm formation of ceramics at high temperatures. Surface and Coatings Technology, 184(2–3), 270-277.

Yang, S., Camino, D., Jones, A. H. S. and Teer, D. G. (2000). Deposition and tribological behaviour of sputtered carbon hard coatings. Surface and Coatings Technology, 124(2–3), 110-116.

Yang, S., Li, X., Cooke, K. E. and Teer, D. G. (2012). A study of TiMoN nano-multilayer coatings deposited by CFUBMSIP using DC and HIPIMS power. Applied Surface Science, 258(6), 2062-2067.

Yang, S., Li, X., Renevier, N. M. and Teer, D. G. (2001). Tribological properties and wear mechanism of sputtered C/Cr coating. Surface & Coatings Technology, 142, 85-93.

Zhang, Z. G., Rapaud, O., Allain, N., Mercs, D., Baraket, M., Dong, C. and Coddet, C. (2009). Microstructures and tribological properties of CrN/ZrN nanoscale multilayer coatings. Applied Surface Science, 255(7), 4020-4026.

Zhu, Z., Bai, S., Wu, J., Xu, L., Li, T., Ren, Y. and Liu, C. (2015). Friction and Wear Behavior of Resin/Graphite Composite under Dry Sliding. Journal of Materials Science & Technology, 31(3), 325-330.